





# TECTONIC, CLIMATIC AND PALEOCEANOGRAPHIC EVOLUTION OF THE SOUTHWESTERN SCOTIA ARC (ANTARCTICA)

# Cecilia Morales Ocaña







# TECTONIC, CLIMATIC AND PALEOCEANOGRAPHIC EVOLUTION OF THE SOUTHWESTERN SCOTIA ARC (ANTARCTICA)

#### Cecilia Morales Ocaña

Supervisors:
Carlota Escutia Dotti
Fernando Bohoyo Muñoz
Francisco José Jiménez Espejo

Departamento de Geociencias Marinas Instituto Andaluz de Ciencias de la Tierra (CSIC-UGR)

PhD Thesis 2024



The front cover photography was taken by Professor José Abel Flores during the POWELL 2020 Antarctic survey.
This PhD thesis has been carried out in the Department of Marine Geosciences at the Instituto Andaluz de Ciencias de la Tierra (IACT). Financial support was provided by a grant Formación de Personal Investigador FPI from the Spanish Ministerio de Economía y Competitividad with the grants PRE2018-084612 related to the project CTM2017-89711-C2-1-P.

El camino no era muy largo, pero hubo que vencer el vértigo

# Agradecimientos

Durante estos últimos años he estado muy bien acompañada por un montón de personas de las que he podido aprender tanto científicamente como personalmente, y que han ayudado a que hoy pueda concluir esta etapa de la mejor manera posible. En primer lugar, sin duda, mi agradecimiento más profundo y sincero es a mis directores de tesis, que han estado siempre conmigo al pie del cañón. Muchísimas gracias, Carlota, por tu infinita generosidad desde el primer momento que nos conocimos. Gracias por enseñarme y ayudarme tanto con tu constante optimismo, que hace que todo sea más fácil. El agradecimiento se extiende a toda tu familia, especialmente a Hans, por acogerme en infinidad de ocasiones y compartir sus conocimientos conmigo. Muchísimas gracias a Fernando y a Francis por estar siempre disponibles y enseñarme tanto, cada uno desde vuestra especialidad, logrando que haya podido abordar temáticas tan diferentes.

Que esté escribiendo las palabras que concluyen esta tesis es, sin duda, gracias a Lourdes y a Jesús. Con ellos empecé a dar los primeros pasitos en la investigación y aún hoy siguen ofreciéndome su apoyo y su cariño, imuchísimas gracias!

Todo el trabajo aquí reflejado es producto de la colaboración a lo largo de estos años con grandes investigadoras e investigadores con los que he tenido la suerte de trabajar. Muchísimas gracias a Estefanía, Javier, Adolfo, María, Carmen, Carlos, Marga, Julia y José Abel por el cariño y la ayuda que me habéis brindado. Also, many thanks to Amy Leventer, Johan Etourneau, Manon Sabourdy and Xavier Crosta for all the wisdom they provided. Special thanks to Johan and Manon for taking care of me during my stay in Bordeaux.

He tenido la suerte de poder compartir todo este proceso con mi compañerxs del IACT. Cuando tienes cerca a gente tan maja, todo es más fácil. Muchas gracias en especial a mi fiel compañero Álvaro por compartir el momento más ilusionante del día a día, comer al sol. Muchas gracias a Jon, Amira y África por venir a llenar el despacho de alegría. Muchísimas gracias a mis queridos Adri y Dimitris, que han sido ejemplo a seguir y apoyo fundamental en incontables momentos. No me olvido de Ana, Carolina y Juani. Muchísimas gracias por hacer más llevaderas las gestiones administrativas con vuestro buen hacer.

Esta tesis ha estado aderezada con la compañía de grandes amigxs que hacen todo mucho más divertido. Gracias a esta etapa, he tenido la suerte de incorporar a mi vida a un grupito de geologxs (algunxs con titulación y otrxs más que convalidado), a lxs que agradezco la perfecta combinación de fiesta y excursión. Muchas gracias también a lxs de siempre, por su incondicionalidad. A Delia y Sara por seguir a mi lado después de tanto tiempo. Y a Fran, por acompañarme en la distancia. Mi agradecimiento más especial es para Asier, por ser fuente de motivación y empuje siempre que ha hecho falta. Gracias por ilusionarte con mi trabajo muchas veces más que yo misma.

Por último, quiero agradecer a mi familia su apoyo incondicional y ánimos revitalizantes. En especial a la mejor hermana del mundo mundial por siempre querer ayudar, aunque no la deje tanto como ella

quisiera. A mi padre por ilusionarse con mis pequeños logros y a mi tía Merces por estar siempre alerta y atenta a cualquier necesidad.

Esta aventura acaba como empezó, a bordo del BIO Hespérides, que inesperadamente ya se siente un poco casa. ¡Qué alegría le daría saberlo a mi yo de hace 10 años! Muchísimas gracias a toda la gente con la que he compartido esta experiencia, por todo el cariño y los ánimos para acabar estos últimos momentos de la mejor manera. Mención especial a mis compis de guardia y al gym-team por las risas desestresantes y las tapitas de madrugada.

¡¡MUCHAS GRACIAS!!

#### Abstract

The opening of the Scotia Arc is a key event for the establishment of the Antarctic Circumpolar Current (ACC), a fundamental component of Earth's climate system. The ACC serves as a critical conduit for the transfer of heat, carbon dioxide, nutrients, chemicals, and various tracers across ocean basins. The gradual and intricate opening of the Scotia Arc, as continental fragments drifted apart, gave rise to multiple small sedimentary basins. At the southern boundary of the Scotia Arc, these basins served as primary channels for the flow of cold Antarctic waters from the Weddell Sea into the Scotia Sea, where they engage in complex interactions with the ACC. Despite their significance, our understanding of the distribution and temporal variability of water masses as the Scotia Arc developed remains limited. The South Orkney Microcontinent (SOM) is the largest continental remnant within the southern Scotia Arc, once part of the ancient land bridge connecting South America and Antarctica. The comprehensive analysis of its deep structure and sedimentary fill presents a significant opportunity to study the early phases of the Scotia Arc development and subsequent oceanic reorganization. To the west, the Bransfield Basin, located at the northernmost tip of the Antarctic Peninsula, stands as a key area for studying the variability of oceanic fronts and its impact on sedimentary processes.

In this context, this PhD thesis aims to: (1) Advance our understanding of the structural configuration of the South Orkney Microcontinent, linked to the tectonic evolution of the Scotia Arc. (2) Determine events recorded in the sedimentary fill of the southern SOM Basins, linked to understanding ocean current redistribution as the Scotia Arc opened. (3) Reconstruct the recent climatic variability of the oceanic fronts affecting the sedimentation in the Bransfield Basin.

To achieve these objectives, a multi-methodological approach has been implemented, including geophysical and sedimentological data analysis. As a result, this PhD thesis shows that the deep structural configuration of the SOM records the extensional forces during the early rifting phase from the Antarctic Peninsula. This process led to the development of four N-S elongated basins, exhibiting progressive deformation from east to west. Among these basins, the sedimentary deposits in the Bouguer and Eötvös basins reflect the influence of currents originating from the Weddell Sea as the SOM subsided as a consequence of the opening of the Powell Basin. Contour currents had a major influence in the southern margin of the SOM from the late Eocene to the middle Miocene. The cessation of the influence of these currents in the SOM is interpreted to be linked to the opening of the Jane and Scan Basins, diverting the flow towards the Scotia Sea. This agrees with previous studies that infer that the onset of the inflow of the Weddell Sea waters into the Scotia Sea occurred during the late Miocene. Furthermore, the results of this PhD thesis underscore the profound impact of contour currents sourced from the Weddell Sea and the Circumpolar Deep Water (CDW) on sedimentation patterns in the Bransfield Basin. Current intensity and phytoplankton variations are associated with different Southern Annular Mode (SAM) and El Niño-Southern Ocean Oscillation (ENSO) variability over the last millennium.

#### Resumen

La apertura del Arco de Scotia es un acontecimiento clave para el establecimiento de la Corriente Circumpolar Antártica (CCA), componente fundamental del sistema climático de la Tierra. La CCA es esencial en la transferencia de calor, dióxido de carbono, nutrientes, elementos químicos y diversos trazadores a través de las cuencas oceánicas por las que circula. La compleja y gradual apertura del arco de Scotia dio lugar a la apertura de pequeñas cuencas oceánicas a medida que los fragmentos continentales se separaban. En el límite meridional del arco de Scotia, estas cuencas sirvieron como canales para el flujo de las aguas frías antárticas procedentes del mar de Weddell hacia el mar de Scotia, donde interaccionan con la CCA. A pesar de la importancia de estos procesos, la comprensión sobre la distribución y variabilidad temporal de las masas de agua, a medida que se desarrollaba el arco de Scotia, sigue siendo limitada. El Microcontinente de las Orcadas del Sur (MOS) es el mayor vestigio continental de la antigua conexión entre Sudamérica y la Antártida. Situado en el sur del arco de Scotia, el análisis exhaustivo de su estructura profunda y relleno sedimentario representa una gran oportunidad para comprender mejor cómo fueron las primeras fases del desarrollo del arco de Scotia y la consecuente reorganización oceánica. Hacia el oeste, la cuenca de Bransfield, situada en el extremo más septentrional de la Península Antártica, se erige como un área clave para el estudio de la variabilidad de los frentes oceánicos y su impacto en los procesos sedimentarios.

En este contexto, esta tesis doctoral pretende: (1) Avanzar en el conocimiento de la configuración estructural profunda del MOS, vinculada a la evolución tectónica del arco de Scotia. (2) Determinar los acontecimientos registrados en el relleno sedimentario de las cuencas meridionales del SOM, vinculados a la redistribución de las corrientes oceánicas a medida que se abría el arco de Scotia. (3) Reconstruir la variabilidad climática reciente de los frentes oceánicos que tienen un impacto directo en la sedimentación en la cuenca de Bransfield.

Para alcanzar estos objetivos, se ha aplicado un enfoque multidisciplinar que incluye el análisis de datos geofísicos y sedimentológicos. Como resultado, esta tesis doctoral muestra que la configuración estructural profunda del MOS refleja las fuerzas extensionales que se produjeron durante las fases tempranas de la formación del arco de Sotia. Este proceso condujo al desarrollo de cuatro cuencas elongadas en dirección N-S en el dominio meridional del MOS, exhibiendo una deformación progresivamente mayor de oeste a este. Entre ellas, las cuencas de Bouguer y Eötvös que concentraron las mayores deformaciones, muestran una mayor extensión y profundidad, y albergan el registro sedimentario de mayor espesor. Los depósitos sedimentarios de estas cuencas reflejan una mayor influencia de corrientes de contorno procedentes del mar de Weddell a medida que el MOS se hundía, como consecuencia de la apertura de la cuenca de Powell. Esta influencia es máxima en el margen sur del MOS desde finales del Eoceno hasta el Mioceno medio. Posteriormente, el cese de la influencia de estas corrientes en el área de estudio está relacionado con la apertura de las cuencas Jane y Scan, que desviaron el flujo hacia el mar de Scotia. Esto concuerda con anteriores estudios que infieren el inicio de la afluencia de las aguas del mar de Weddell hacia el mar de Scotia

durante el Mioceno tardío. Además, los resultados de esta tesis doctoral subrayan el profundo impacto de las corrientes de contorno procedentes del mar de Weddell y de las aguas profundas circumpolares (CDW) en los patrones de sedimentación de la cuenca de Bransfield. La intensidad de las corrientes y las variaciones en el fitoplancton están asociadas a la variabilidad del Modo Anular del Sur (SAM) y de El Niño-Oscilación del Océano Austral (ENSO) a lo largo del último milenio.

# Table of contents

Abstract	<u>Page</u> i
Resumen	iii
Table of contents	1
Abbreviation index	5
Context and motivation	7
Hypotheses and objectives	9
Thesis layout	10
CHAPTER 1 – Introduction	15
1.1. Cenozoic history of climate and Antarctic Ice Sheet Evolution	15
1.2. Tectonic context of the opening of the Scotia Arc and the Drake Passage	18
1.3. Paleoceanographic evolution and present oceanographic setting	21
1.3.1. Teleconnections	23
1.4. Deep-water sedimentary processes	24
CHAPTER 2 – Materials and methods	29
2.1. Geophysical methods	29
2.1.1. Potential fields data: gravity and magnetic modeling	29
2.1.2. Seismic stratigraphic analysis	31
2.2. Sediment cores analyses	32
2.2.1. Ocean Drilling Program (ODP) Sites 695 and 696	32
2.2.2. Gravity cores	33
CHAPTER 3 – 3D Geophysical and geological modeling of the South Orkney Microcontinent (Antarctica): Tectonic implications for the Scotia Arc development	37
3.1. Introduction	37
3.2. Geological setting	38
3.3. Data and Methodology	42
3.3.1. Initial dataset	42
3.3.2. Modeling	43
<ul><li>3.3.2.1. Identification of the main geological boundaries as initial constraints</li><li>3.3.2.2. 2D geophysical modeling</li></ul>	43 45
3.3.2.3. 3D geological model. Geophysical forward modeling and joint-inversion	45

3.4. Results	47
3.4.1. Initial surfaces and 2D models	47
3.4.2. Gravity and magnetic response of the final 3D geological model	48
3.4.3. Sedimentary basins of the South Orkney Microcontinent	51
3.4.4. Characterization of the intrusive igneous rock body causing the PMA	52
3.4.5. Moho depth	52
3.5. Discussion	53
3.5.1. 3D geophysical and geological modeling as a suitable method to characterize and to understand deep structures	53
3.5.2. Structural heterogeneity of the South Orkney Microcontinent	55
3.5.3. Regional tectonic implications	57
3.6. Conclusions	58
CHAPTER 4 – Tectonic and climatic controls on the paleoceanographic evolution of the South Orkney Microcontinent (southern Scotia Arc, Antarctica)	63
4.1. Introduction	63
4.2. Geological and oceanographic setting	65
4.3. Materials and methods	67
4.3.1. Sedimentary data	67
4.3.2. Seismic data	67
4.3.3. Synthetic seismogram and age control	68
4.4. Results	68
4.4.1. Seismic stratigraphic analysis and correlation with ODP Sites 695 and 696	68
4.4.1.1. Age model	68
4.4.1.2. Seismic units, discontinuities and correlation with ODP Sites 695 and 696	69
4.4.2. Development of contourite depositional systems in the South Orkney Microcontinent	75
4.4.2.1. Depositional and erosive features	75
4.4.2.2. Spatial and temporal distribution of the contourite deposits	78
4.5. Interpretation and discussion	78
4.5.1. Early Eocene to Eocene-Oligocene Transition (EOT): SU5	79
4.5.2. Oligocene to early Miocene: SU4	80
4.5.3. Middle to late Miocene: SU3	81
4.5.4. Late Miocene to early Pliocene: SU2	82

	4.5.5. Early Pliocene to present: SU1	83
	4.6. Conclusions	84
Su	pplementary material to CHAPTER 4	87
	IAPTER 5 – Unraveling bottom current influence on diatomaceous contourite ifts in the Bransfield Strait (Antarctic Peninsula) throughout the past millennium	95
	5.1. Introduction	95
	5.2. Geological and oceanographic setting	96
	5.3. Materials and Methods	98
	5.3.1. Core location	98
	5.3.2. Core scanning, description, and sampling	99
	5.3.3. Grain-size analysis	99
	5.3.4. Diatom abundance and assemblage analysis	100
	5.3.5. Statistical analysis	100
	5.3.6. <sup>210</sup> Pb and <sup>14</sup> C dating	101
	5.4. Results	101
	5.4.1. Age model	101
	5.4.2. Sediment textures and structures	104
	5.4.3. Statistical analysis	108
	5.4.3.1. Principal component analysis	108
	5.4.3.2. Spectral analysis	109
	5.4.4. Sortable silt and flow speed reconstruction	110
	5.4.5. Diatom assemblage	110
	5.4.6. Proxies variability throughout the cores	111
	5.5. Discussion	112
	5.5.1. Interpretation of diatom, elemental ratio, and grain-size proxies	112
	5.5.2. influence of contour currents on sedimentation in the East Bransfield Basin	114
	5.5.3. Paleoenvironmental-related changes and paleoceanographic configuration	116
	5.6. Conclusions	119
	pplementary material to CHAPTER 5	123
CH	IAPTER 6 – General discussion and future perspectives	135
	<ul><li>6.1. The South Orkney Microcontinent key to Scotia Arc development and</li><li>Southern Ocean circulation</li><li>6.1.1 The South Orkney Microcontinent as a keystone in the development of</li></ul>	135 135
	the southern Scotia Arc	

6.1.2 The South Orkney Microcontinent as a keystone in the early oceanic connection between the Weddell and the Scotia Seas	137
6.2. Recent climatic variability from contourite deposits	139
Future perspectives	141
CHAPTER 7 – Conclusions	145
CÁPITULO 7 – Conclusiones	149
References	155

#### Abbreviation index

**AABW Antarctic Bottom Water** 

ACC Antarctic Circumpolar Current

**AMS** Accelerator Mass Spectrometry

AS **Analytic Signal** 

AB Airy Basin

BB **Bouguer Basin** 

**BBW Bransfield Bottom Water** 

**BDW Bransfield Deep Water** 

DB Discovery Bank

DvB **Dove Basin** 

CDS Contourite Depositional System

**CDW** Circumpolar Deep Water

**CRS** Chaetoceros Subg. Hyalochaete Resting Spores

CT-Scan **Computerized Tomography Scanning** 

EΒ Eötvös Basin

**EBB** Eastern Bransfield Basin

**ESR** East Scotia Ridge

**EOT Eocene-Oligocene Transition ENSO** El Niño-Southern Oscillation

FAD First Appearance Datum

GRD Gamma-Ray Density

HB Herdman Bank

**IODP** International Ocean Drilling Programm

iu **Instrumental Units** 

JB Jane Basin

**mCDW** 

mbsf Meters Below Sea Floor Meters Below Sea Level

mbsl

Modified Circumpolar Deep Water

MS Magnetic Susceptibility

**MSCL** Multi-Sensor Core Logger

MCS Multi-Channel Seismic Reflection

LAD Last Appearance Datum

LU Lithostratigraphic Unit PMA Pacific Margin Anomaly

PiB Pirie Bank

**PrB** Protector Basin

PC Principal Component

**PCA** Principal Component Analysis

**PB** Powell Basin

**SAM** Southern Annular Mode

SACCF Southern Antarctic Contour Current Front

**SDLS** Seismic Data Library System

**SShI** South Shetland Islands

SSI South Sandwich Islands

SSR South Scotia Ridge

SS Mean Sortable Silt

**SOM** South Orkney Microcontinent

**SOI** South Orkney Islands

**SST** Sea Surface Temperature

**SU** Seismic Unit

**ODP** Ocean Drilling Program

**TOPAS** Topographic Parametric Sonar

**TWTT** Two-Way Travel Time

U Scalar Flow Speed

XRF X-Ray Fluorescence

**WDMAM** World Digital Magnetic Anomaly Map

**WSDW** Weddell Sea Deep Water

yr cal BP year calibrated Before Present

#### Context and motivation

The opening of the Scotia Arc and, consequently, the Drake Passage marks a significant tectonic event that, together with the opening of the Tasman Gateway, contributed to the development of the Antarctic Circumpolar Current (ACC). The ACC is crucial in transporting heat, carbon dioxide, nutrients, and other tracers across the oceanic basins surrounding Antarctica. Estimates regarding the timing of the Tasmanian Gateway's final opening and deepening are reasonably well constrained to the Eocene-Oligocene Transition (EOT, ~34–33 Ma) (Stickley et al., 2004). However, estimates for the opening and deepening of the Drake Passage vary widely, ranging from the middle Eocene (~40 Ma) to the middle Miocene (~17 Ma) (Barker & Burrell, 1977; Livermore et al., 2007; Maldonado et al., 2014). These uncertainties result from the complex development of the Scotia Arc, where continental blocks gradually drifted eastward, resulting in progressively deeper oceanic passages until a complete opening occurred (Lagabrielle et al., 2009). Therefore, a comprehensive understanding of the timing of the processes involved in the development of the Scotia Arc is needed. This development was pivotal in reshaping oceanic configurations leading up to the present Southern Ocean configuration and potentially influencing Antarctic ice sheet dynamics.

This PhD thesis focuses on the study of the southwestern Scotia Arc (Fig. I), a critical boundary between the Weddell and Scotia seas. Along this boundary, the South Orkney Microcontinent (SOM) is the largest remaining continental crust block from the former land bridge connecting South America and Antarctica. Its current location results from its eastward drift away from the Antarctic Peninsula, which resulted in the opening of the Powell Basin (Eagles & Livermore, 2002). Based on very sparse data, it has been proposed that the SOM has a thinned crust intruded by Cretaceous-age igneous rocks, evidenced by a band of magnetic anomalies in the southern region (King & Barker, 1988). These anomalies connect to the large amplitude magnetic anomaly belt along the Antarctic Peninsula known as the Pacific Margin Anomaly (PMA) (Barker & Griffiths, 1972; Garrett et al., 1986/87). The continuation of the PMA across various continental blocks has facilitated the paleogeographic reconstructions of the ancient connection between the South American and Antarctic plates (Martos et al., 2014; Riley et al., 2023). Different phases of regional tectonic evolution have resulted in the development of two sets of sedimentary basins in the SOM (Busetti et al., 2001; King & Barker, 1988). In the northern SOM, an E-W elongated basin opened as a back-arc basin during the Late Cretaceous (King & Barker, 1988). In the southern SOM, N-S elongated basins opened as a consequence of the E-W extension associated with the opening of the Powell Basin (Eagles & Livermore, 2002; King & Barker, 1988). All these findings, however, are mostly based on the study of a single set of geophysical data (i.e., magnetic, gravimetric, or multichannel seismic reflection profiles). This thesis aims to thoroughly examine the crustal structure of the SOM, with the integration of all available geophysical data sets. This approach would enhance our understanding of the early stages of the Scotia Arc fragmentation.

Regarding the sedimentary infill of the SOM, a partial sampling was conducted during the Ocean Drilling Program (ODP) Leg 113 (Barker et al., 1988). The deepest sediments retrieved from Leg 113 at Site 696 were dated from the late Eocene and identified as inner-shelf terrigenous sediments

(Barker et al., 1988). The deposition of these sediments was suggested to occur while the SOM was still connected to the Antarctic Peninsula. The first indication of the detachment of the SOM from the Antarctic Peninsula is a condensed terrigenous glauconitic sediments interval dated at ~ 35.5 Ma and interpreted to result from the formation of a shallow gateway corresponding to a proto-Powell Basin (López-Quirós et al., 2021). Above, the absence of terrigenous sediment deposition during the middle Miocene indicates the complete separation of the SOM from the Antarctic Peninsula due to the formation of Powell Basin. The progressive opening of the Powell Basin and other ocean basins surrounding the SOM, including the Jane and Scan basins, allowed the connection between the water masses of the Weddell and Scotia Seas. This resulted in the redistribution of ocean currents leading to the present configuration (Maldonado et al., 2003). Previous work has reported the influence of the Weddell Basin thermal subsidence on the early arrival of currents from the Weddell Sea to the southern margin of the SOM (Huang et al., 2014). However, our understanding of the spatial and temporal changes in ocean current paths as the basins open remains extremely limited. This thesis aims to study the sedimentary fill of the SOM to determine the tectonic and climatic factors that led to the formation and distribution of deep water pathways between the Scotia Sea and the Weddell Sea.

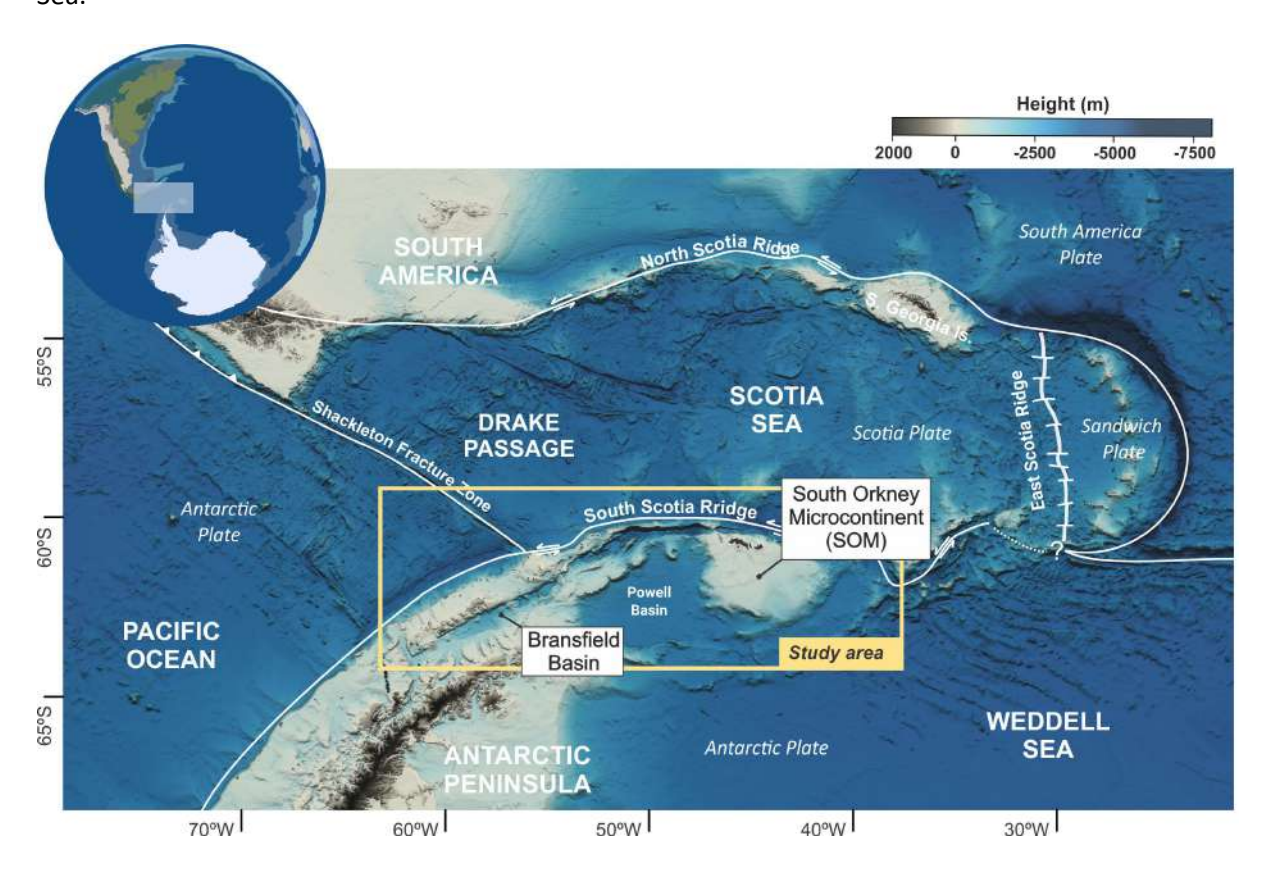


**Figure 1:** Regional map of the Scotia Arc. The PhD thesis focuses on the study of the South Orkney Microcontinent (SOM) and the Bransfield Basin, located in the southwestern area.

Once the Scotia Sea acquires its current oceanographic configuration, understanding the climatic impact on the Southern Ocean fronts is also relevant. In the southern Scotia Arc, the Bransfield Basin, located between the northern tip of the Antarctica Peninsula and the South Shetland Islands,

has been identified as a key location connecting the Scotia Sea and the Weddell Sea. Today, the basic circulation pattern in the Bransfield Basin consists of the interaction between relatively warm and fresh water from the Bellingshausen Sea and the ACC, and the relatively cold and salty water from the Weddell Sea (Wilson et al., 1999). The complex interaction between these water masses and the seafloor result in the formation of sediment drifts, identified using seismic reflection profiles (García et al., 2019; Liu et al., 2022). Based on the stacking patterns in these bottom contour current deposits, Liu et al. (2022) infer that ocean circulation in the Bransfield Basin began to resemble the present-day after the middle Pleistocene. Additional studies using marine sediment cores are needed to validate the contourite nature of these deposits and to better understand the connections between ocean fronts dynamics and various modes of climate variability, such as the Southern Annular Mode (SAM) and El Niño-Southern Ocean Oscillation (ENSO). The information gathered has the potential to provide valuable insights that can be used to make informed decisions in response to ongoing climate change.

# Hypothesis and objectives

The overall goal of this PhD thesis is to contribute to the understanding of the main tectonic events that led to the separation and subsidence of the South Orkney Microcontinent (SOM), the establishment of the subsequent paleoceanographic and paleoenvironmental evolution, and the impact of climate variability in the Southern Ocean fronts. Three hypotheses are established, each associated with a specific objective to achieve the overarching aim.

#### Research hypotheses:

- > The deep structure of the SOM, such as the boundaries between continental and oceanic crust, cortical thickness, and the position and geometry of its sedimentary basins, records the early stages and the tectonic evolution of the opening of the Scotia Arc.
- Paleoceanographic and paleoenvironmental changes forced by tectonic events related to the evolution of the Scotia Arc and/or Cenozoic climatic changes are preserved in the sedimentary infill of SOM and provide insights into the early ocean current pathways between the Weddell Sea and the Scotia Sea.
- Recent sediments from contourite deposits in the Bransfield Basin can provide information regarding the climatic influence on ocean fronts dynamics

#### Specific objectives:

- Characterize the deep structure of the SOM through 3D modeling of potential field data (i.e., gravity, magnetic anomalies) and multichannel seismic data to understand its role during the opening of the Scotia Arc.
- > Identify key thresholds in the paleoceanographic and paleoenvironmental evolution of the SOM through seismic stratigraphic analysis of its sedimentary infill dated by correlation with sedimentary records (i.e., ODP sites 695 and 696).

Reconstruct recent variability of the Southern Ocean fronts in the Bransfield Basin, key location between the Weddell and the Scotia seas, from sedimentological and geochemical analyses of sediment cores.

# Thesis layout

This thesis is organized into seven chapters:

#### CHAPTER 1: Introduction

This chapter presents an overview of the Cenozoic climate variability, the Antarctic ice-sheet evolution, and the Scotia Arc tectonic evolution, with particular attention to the southern sector. Also, Chapter 1 includes an overview of the oceanographic evolution since the opening of the Drake Passage and an introduction to deep water sedimentary processes, especially those related to the action of bottom contour currents.

#### CHAPTER 2: Material and methods

This chapter provides a general introduction to the materials and methods used in this thesis. Detailed methodological descriptions are provided in Chapters 3, 4, and 5.

### CHAPTER 3: 3D Geophysical and Geological Modeling of the South Orkney Microcontinent (Antarctica) - Tectonic Implications for the Scotia Arc Development

Cecilia Morales-Ocaña, Fernando Bohoyo, Carlota Escutia, Carlos Marín-Lechado, Carmen Rey-Moral, María Druet, Jesús Galindo-Zaldívar, Adolfo Maestro

Published in Tectonics, 28 March 2023; https://doi.org/10.1029/2022TC007602

This chapter presents a 3D model of the South Orkney Microcontinent (SOM), which characterizes the geometry of the sedimentary basins, the magnetic source of the Pacific Margin Anomaly, and the crustal thickness. The outlined structural features of the model can be linked to the significant E-W extension that the SOM experienced during the early stages of the Scotia Arc formation before the Powell Basin opened.

# CHAPTER 4: Tectonic and climatic controls on the paleoceanographic evolution of the South Orkney Microcontinent (southern Scotia Arc, Antarctica)

This chapter provides a detailed seismic stratigraphic analysis of the sedimentary infill of the SOM (Bouguer and Eötvös basins). A chronostratigraphic framework is provided for the five seismic units identified by correlation with Ocean Drilling Program (ODP) Sites 695 and 696. This allows for the interpretation of the timing and nature of regional paleoceanographic and paleoenvironmental events.

# CHAPTER 5: Unraveling bottom current influence on diatomaceous contourite drifts in the Bransfield Strait (Antarctic Peninsula) throughout the past millennium

This chapter presents a multiproxy analysis of Holocene sediment cores collected from the East Bransfield Basin. The results confirm the influence of varying intensity bottom contour currents affecting the organic matter content and sediment winnowing. A marked change at 600 cal yr BP points to increasing Circumpolar Deep Water intrusions into the East Bransfield Basin coincident with a regional warming trend in the eastern Antarctic Peninsula tendency and more variable SAM-positive and ENSO-negative phases.

#### CHAPTER 6: General discussion and future perspective

This chapter aims to integrate the findings in Chapters 3, 4, and 5 and to discuss them in a regional context by comparison with previous studies in the region. In addition, open questions and possible future research are briefly discussed.

#### CHAPTER 7: Conclusions

This chapter summarizes the final conclusions concerning the initial objectives addressed in this PhD thesis.



# CHAPTER 1

Introduction

# CHAPTER 1: Introduction

The Southern Ocean and Antarctica's cryosphere, which includes the ice sheet, ice shelves, and sea ice, significantly impact the global climate system. Among others, polar ice cover and ice sheet volume directly impact Earth's sea level and albedo, while shifts in atmospheric and oceanic currents modulate the distribution of heat and marine nutrients worldwide. At present, Antarctica is covered by two main ice sheets, the East Antarctic Ice Sheet (EAIS) and the West Antarctic Ice Sheet (WAIS) (Fig. 1.1). In addition, a smaller but distinct ice sheet covers the Antarctic Peninsula, the Antarctic Peninsula Ice Sheet (APIS) (Fig. 1.1). These vast ice sheets hold most of the Earth's fresh water and play a key role in regulating global sea level. If all Antarctic ice sheets melted, they would contribute to a sea level rise of approximately 58 m on a global scale (Fretwell et al., 2013). In recent decades, Antarctic glacier flow has accelerated, attributed mainly to warm, salty Circumpolar Deep Water (CDW) intrusions into the continental shelf and bed topography (Shen et al., 2018; Rignot et al., 2019; Smith et al., 2020). Especially threatened are the WAIS and APIS, where mass loss exceeds gains in recent decades (Rignot et al., 2019; Smith et al., 2020) (Fig. 1.1). Despite the importance of Antarctica and the Southern Ocean in the Earth's climate dynamics, the complex interaction between bedrock, cryosphere, ocean, and atmosphere remains poorly understood. However, this knowledge is indispensable for refining models that accurately depict ongoing changes and predict future trends in ice sheet and Southern Ocean behavior.

Geophysical and geological data can help us understand how interactions between the bedrock, ocean, and cryosphere have influenced the dynamics of the Southern Ocean and Antarctica's cryosphere in the past. Indeed, information obtained from land outcrops and drilled cores around Antarctica has led to a better understanding of the role of the geometry and nature of sedimentary basins, continental margins and paleotopographic configurations in the stability and dynamics of the Antarctic ice sheet (e.g., Colleoni et al., 2018; Cook et al., 2013; Hochmuth et al., 2020; Levy et al., 2019) and on the paleoceanographic variability (e.g., Hutchinson et al., 2019; Katz et al., 2011; Sijp et al., 2011; Toggweiler & Samuels, 1995). However, geological records around Antarctica remain limited due in part to the remoteness and inaccessibility of the continent. Thus, additional data and integrated studies that include solid Earth, ocean, and cryosphere processes from key areas of the Antarctic continental margin and Southern Ocean are needed.

#### 1.1. Cenozoic history of climate and Antarctic Ice Sheet Evolution

The Cenozoic era spans the last 65 million years and has witnessed complex changes in Earth's climate. During the Paleocene-Eocene Thermal Maximum (PETM, 55.8 Ma) and the Early Eocene Climatic Optimum (EECO, 51–53 Ma) (Fig. 1.2), the Earth's poles were warm and ice free (Huber et al., 2004; Zachos et al., 2001). Subtropical forests have been reported to exist in the Wilkes Land margin during peak greenhouse conditions (Pross et al., 2012). These forests were replaced by temperate forests around Antarctica in response to a global cooling trend that commenced around the end of the early Eocene (~ 50 Ma) (Francis et al., 2008; Pross et al., 2012). This cooling trend culminated with

an abrupt shift from a 'greenhouse' world to an 'icehouse' Earth during the Eocene-Oligocene Transition (EOT; ~34 - 33.6 Ma) (Zachos et al., 2001; Fig. 1.2). The EOT is marked by a two-step global shift in deep-sea  $\delta^{18}$ O isotopic record lasting ~ 790 kyr (Coxall et al., 2005; Hutchinson et al., 2020 and references therein) and representing a combination of deep-ocean cooling and growth in land ice volume (Lear et al., 2008; Zachos et al., 2008). During the EOT, the first ice sheet of continental dimensions grew in Antarctica. A long-held belief is that the growth of the ice sheet was forced by the breakup of the two last land bridges connecting Antarctica to South America and Australia, the Drake and the Tasman Gateways. Kennett (1977) postulated that, as these gateways opened and deepened, the development of the Antarctic Circumpolar Current (ACC) thermally isolated Antarctica, favoring the growth of a continental-size ice sheet. Numerical modeling indicates that only minor changes in the depths of the Tasmanian and Drake gateways are necessary to cause dramatic reorganization in ocean circulation patterns and Antarctic surface water temperatures (Sauermilch et al., 2022). Challenging this belief is the hypothesis that, while orbital forcing likely influenced the precise timing of the glaciation, the primary triggering mechanism was the cooling related to a decline in atmospheric CO<sub>2</sub> concentrations (e.g., DeConto & Pollard, 2003; Hutchinson et al., 2020). A recent study by Evangelinos et al. (2024) shows that an ACC like the modern one, thermally isolating the Antarctic continent, did not form until the middle Miocene (14 Ma). These results point to the paleogeographic changes related to gateways opening to have played a secondary role in the transition from a 'greenhouse' to an 'icehouse' world during the EOT.

After ice sheet expansion during the EOT, oxygen isotopic records from the Oligocene (33.6–23.3 Ma) point to highly variable climate conditions and ice sheet dynamics, paced by orbital variations (Liebrand et al., 2017; Palike et al., 2006; Fig. 1.2). During the late Oligocene (~26-23.5 Ma), a general warming trend is depicted by 1 ‰ long-term decrease in the benthic  $\delta^{18}$ O isotopic record (Liebrand et al., 2016; Zachos et al., 2001; Fig. 1.2). Late Oligocene sediments from the Wilkes Land margin show that the Antarctic continental ice masses and sea surface temperatures fluctuated considerably in response to this warming (Hartman et al., 2018; Hoem et al., 2021; Salabarnada et al., 2018). In addition, there are evidences of the intrusion of warm waters close to the Antarctic margin during some extremely warm late Oligocene interglacial periods, which resulted in the retreat of the ice sheet to the hinterland (Evangelinos et al., 2020; Hoem et al., 2021; Salabarnada et al., 2018).

Late Oligocene warming was followed by a second sharp shift in the oxygen isotopic record, coincident with the Oligocene–Miocene Transition (OMT,  $\sim$  23 Ma) and the Mi-1 event, characterized by a  $\sim$  1‰ positive excursion in marine benthic foraminiferal  $\delta^{18}$ O record (Zachos et al., 2001, 2008; Fig. 1.2). The OMT is associated with a large-scale Antarctic Ice Sheet expansion and cooling of the Southern Ocean sea surface temperatures by several degrees (DeConto et al., 2007). The early Miocene witnessed warm mean summer temperatures re-establishment, culminating in the Middle Miocene Climatic Optimum (MMCO; 17–14 Ma). During the MMCO, temperatures are reported to be 3 – 4  $^{\circ}$ C higher than present, marking the warmest conditions since the Eocene (Griener et al., 2015). The MMCO was succeeded by the Middle Miocene Climate Transition (MMCT; 14.2–13.8 Ma), with a general cooling trend that persisted until recent times (Mudelsee et al., 2014; Shevenell et al., 2004;

Zachos et al., 2001; Fig. 1.2). From MMCT to the present day, the Antarctic Ice Sheets are considered a permanent feature over the continent (Flower & Kennett, 1994). Nevertheless, the cooling trend has experienced interruptions marked by warm intervals, during which the ice sheet may have undergone significant variations in size. One notable period was the early Pliocene warm period (~ 5-3 Ma), characterized by widespread ocean warming and the prevalence of open water conditions around Antarctica (Cook et al., 2013; Escutia et al., 2009; Naish et al., 2009; Pollard & DeConto, 2009; Reinardy et al., 2015; Whitehead & Bohaty, 2003). During this period, Antarctic sediments document repeated retreat of the Antarctic ice sheets, with the collapse of the WAIS in the Ross Sea and the retreat in the Wilkes Subglacial Basin of the EAIS (Cook et al., 2013; Naish et al., 2009; Reinardy et al., 2015).

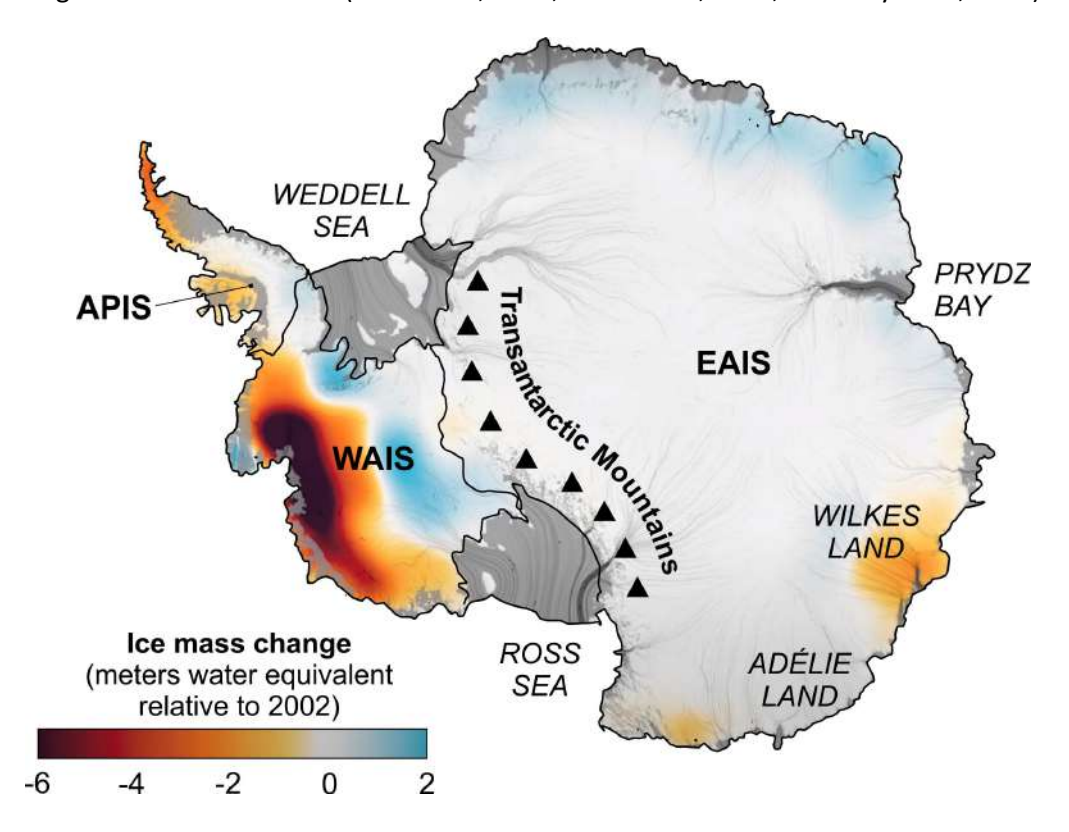


**Figure 1.1.** Antarctic ice mass loss in the period of 2002-2023. The three main Antarctic Ice Sheets are differentiated: East Antarctic Ice Sheet (EAIS), West Antarctic Ice Sheet (WAIS), and Antarctic Peninsula Ice Sheet (APIS). Data are obtained from GRACE and GRACE-FO satellites and published on nasa.gov.

In the Antarctic Peninsula, available records allow the reconstruction of the Antarctic Peninsula Ice Sheet (APIS) fluctuation through the Cenozoic. The existence of Eocene and early Oligocene glaciation is yet ambiguous and unconvincing (Ivany et al., 2006). The earliest unequivocal glaciogenic sediments on King George Island are from late Oligocene (Davies et al., 2012; Troedson & Riding, 2002). However, this would represent a temperate alpine-style glaciation rather than the full-scale development of an ice sheet (Davies et al., 2012). The oldest glaciomarine sediments recovered offshore the Antarctic Peninsula Pacific margin are dated in 9 Ma and record the history of multiple ice sheet advances and erosional episodes consistent with a persistent, yet dynamic, APIS (Barker et al., 1999; Bart & Anderson, 2000; Bart, 2001; Pudsey, 2002b). Over the past 5 Ma, the average size of the APIS and WAIS has grown, with periodic collapses of the WAIS in which a string of small ice sheets

remained (Davis et al., 2012). Moreover, during the warm early to mid-Pliocene, open ocean conditions may have occurred even during glacial periods (Hepp et al., 2006; Hillenbrand & Ehrmann, 2005; Pudsey & Howe, 2002; Williams et al., 2010).

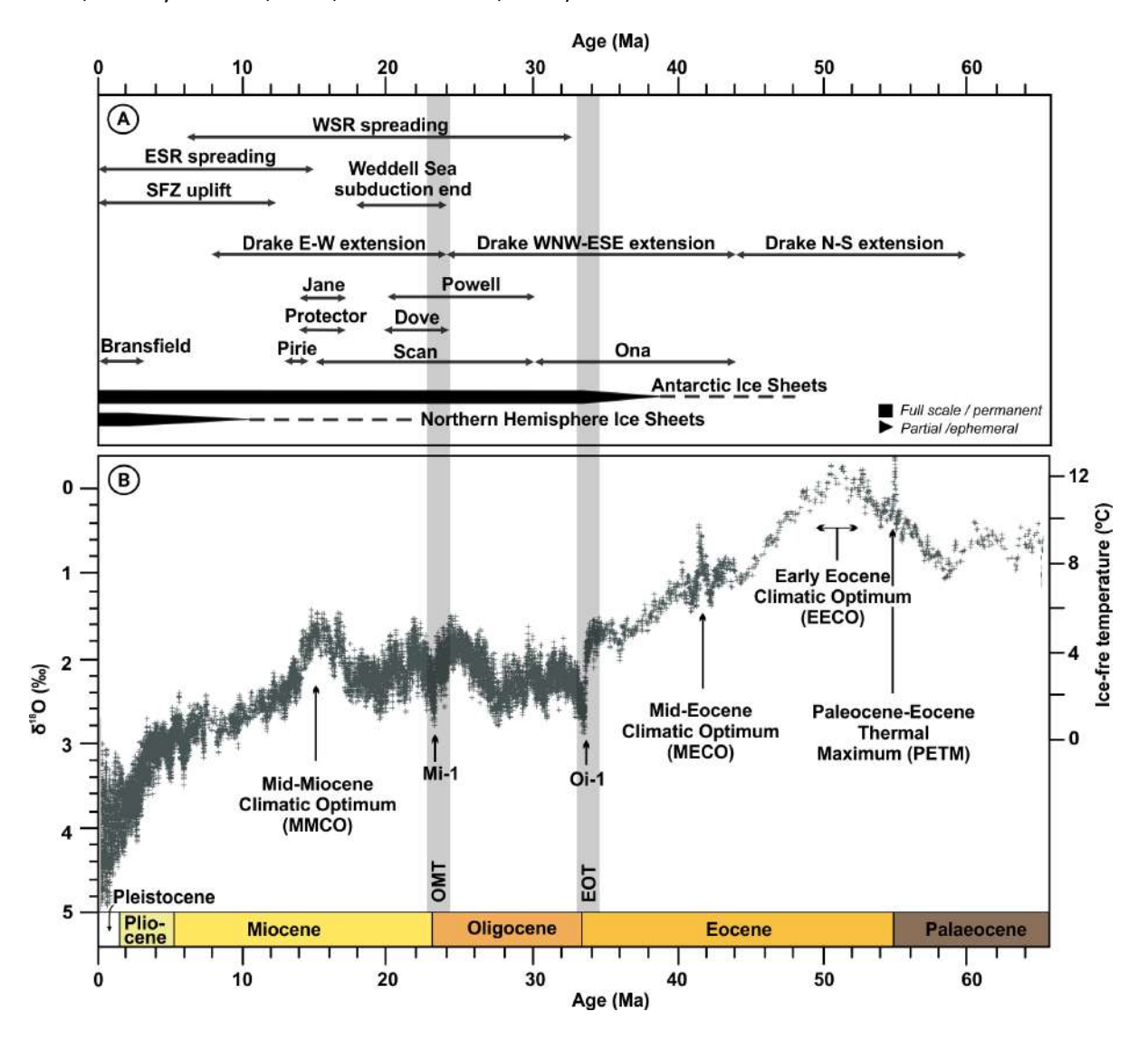


**Figure 1.2.** A) Timing of regional tectonic events, including the stress directions during the opening of the Drake Passage, the timing of the oceanic basin spreading in the southern Scotia Sea and northern Weddell Seas and the Antarctic ice sheet evolution (modified from Pérez et al., 2019). B) Stacked deepsea benthic foraminiferal oxygen isotope curve ( $\delta^{18}$ O records) and main climatic events during the Cenozoic (modified from Zachos et al., 2008).

#### 1.2. Tectonic context of the opening of the Scotia Arc and the Drake Passage

The Scotia Arc developed during the final phase of Gondwana fragmentation (Dalziel et al., 2013). The formation of the Scotia plate results from subduction of the South American plate below the Pacific margin, involving a rapid eastward roll-back of the subduction hinge (Barker et al., 2001). Today, subduction continues beneath the Sandwich Plate, forming the intra-oceanic volcanic arc of the South Sandwich Islands (van de Lagemaat et al., 2021; Fig. 1.3). The tectonic history of the Scotia Arc opening can be inferred by seafloor magnetic anomalies resulting from oceanic spreading, which

provide a timeline of the successive tectonic events. The opening of the Scotia Sea and Drake Passage led to the drift of a group of continental blocks to the east, accommodated by the development of two major ridges, the East and West Scotia Ridge (ESR and WSR; Fig. 1.3).

Seafloor magnetic anomalies allow dating on the western side of the ESR to C5C (17 Ma; Larter et al., 2003), and on the eastern side of the ESR to C4A (9.1 Ma; Larter et al., 2003). The WSR is an extinct mid-ocean ridge with well-defined symmetrical seafloor magnetic anomalies. These anomalies indicate that spreading span between chrons C10 or C12 (~28–30.5 Ma; Bohoyo et al., 2019; Eagles et al., 2005a; Livermore et al., 2005; Lodolo et al., 2006; Maldonado et al., 2014) and chron C3An (~6.1 Ma; Eagles et al., 2005). The southern boundary of the Scotia Sea, marked by the South Scotia Ridge (SSR; Fig. 1.3) is characterized by a group of small oceanic basins developed between small continental blocks that drifted apart (Barker, 2001). To the north of the SSR are located, from west to east, the Ona, Protector, Dove and Scan basins (Fig. 1.3). In Ona basin, the oldest seafloor magnetic anomalies correspond to chrons C10 or C12r (~32-28.5 Ma). The Protector Basin features N-S marine magnetic anomalies are linked to chrons C5Dn-C5ABr (17.5-13.6 Ma; (Galindo-Zaldívar et al., 2006; Schreider et al., 2018). Dove Basin has NNE-SSW-oriented marine magnetic anomalies corresponding to chrons C6Cn.2n-C6Ar (25.3-20.7 Ma; Schreider et al., 2018). The Scan Basin contains NNW-SSE anomalies from chrons C16n.1n-C11n.2n (35.7-29.5 Ma; Schreider et al., 2017). South of the SSR, the Jane Basin, located between Jane Bank and the South Orkney Microcontinent (SOM), has marine magnetic anomalies that formed during chrons C5Dn-C5ADn (17.5-14.2 Ma; Bohoyo et al., 2002). Finally, the Powell Basin, situated between the Antarctic Peninsula and the SOM, has an extinct spreading ridge with marine magnetic anomalies oriented NW-SE corresponding to chrons C11-C6AA (29.5-21.2 Ma; Eagles & Livermore, 2002).

Along the Antarctic Peninsula, elongated Cretaceous mafic rocks have been linked to the large amplitude magnetic anomaly belt that is known as the Pacific Margin Anomaly (PMA) (Garrett et al., 1986; Suriñach et al., 1997). The intrusion of the Cretaceous mafic rocks is related to the subduction of the former Phoenix Plate below the Pacific continental margin (Garrett, 1990). The PMAis well identified along the southern Scotia Arc in several of the continental blocks, including the South Orkney Microcontinent (Martos et al., 2014; Morales-Ocaña et al., 2023), the Discovery Bank, and the northern part of Herdman Bank and the Bruce Bank (Martos et al., 2014; Riley et al., 2023). The PMA anomalies can serve as valuable indicators for understanding the recent tectonic evolution of the area as its interruptions respond to later drifting processes (Martos et al., 2014; Morales-Ocaña et al., 2023).

One of the last tectonic events in the evolution of the Scotia Arc is the opening of the Bransfield Strait as an asymmetrical back-arc basin at 3.3 Ma (Galindo-Zaldívar et al., 2004). This event likely occurred due to two interacting processes. Firstly, the end of the oceanic spreading at the Phoenix-Antarctic Ridge in the middle Pliocene and the resulting roll-back mechanism caused the South Shetland Block to migrate northwestward. Secondly, the deformation linked with the Scotia/Antarctic plate boundary propagated along the southeastern boundary of the South Shetland

Block and reached the Bransfield Basin, resulting in its development (Galindo-Zaldívar et al., 2004). Extension in the Bransfield Strait is indicated by the lack of an oceanic crust (Eagles and Jokat, 2014 and references therein).

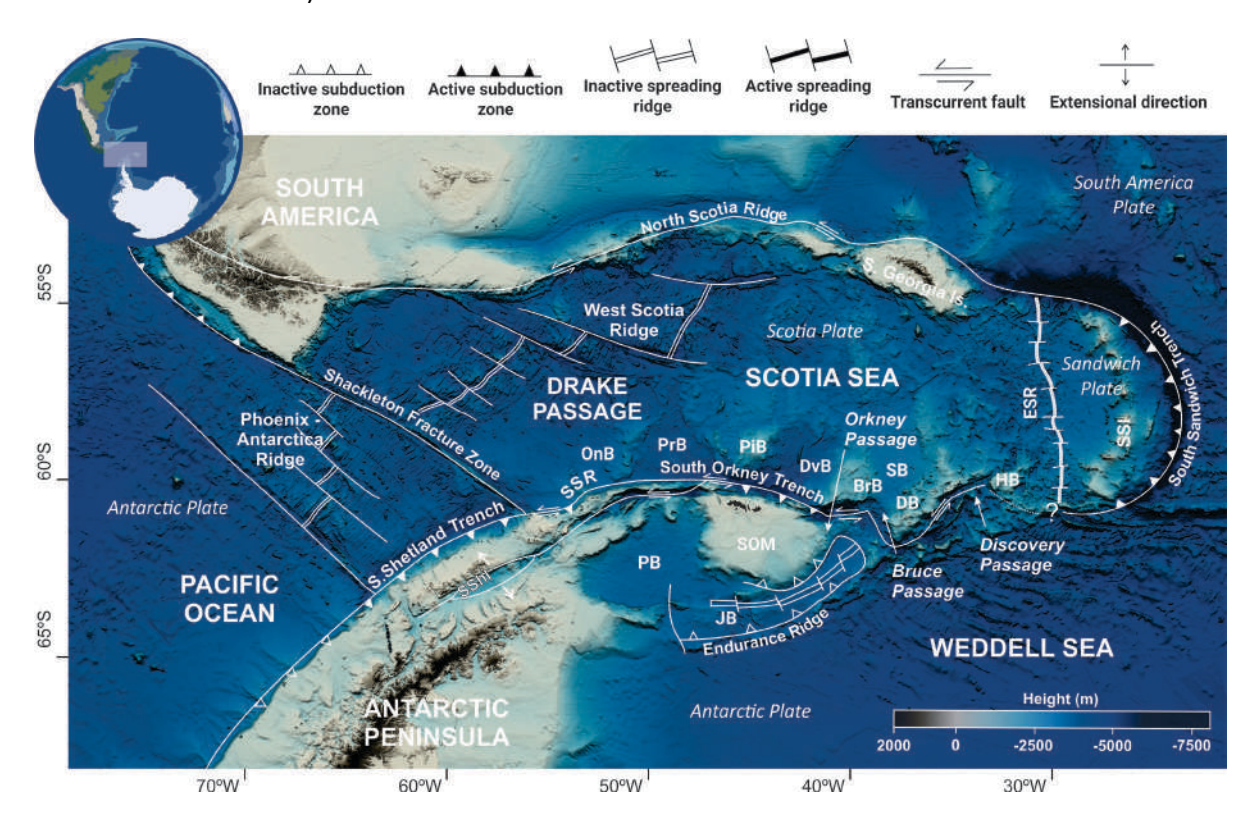


**Figure 1.3.** Tectonic setting of the Scotia Arc. Bathymetry from GEBCO 2020. BB: Bruce Bank; DB: Discovery Bank; DvB: Dove Basin; ESR: East Scotia Ridge; HB: Herdman Bank; JB: Jane Basin; OnB: Ona Basin; PB: Powell Basin; PiB: Pirie Bank; PrB: Protector Basin; SB: Scan Basin; SOM: South Orkney Microcontinent; SShI: South Shetland Islands; SSI: South Sandwich Islands; SSR: South Scotia Ridge.

#### 1.3. Paleoceanographic evolution and present oceanographic setting

The opening of the Drake Passage facilitated the confluence between the Weddell and Scotia seas. Due to its progressive opening, the exact timing of this confluence is still unknown. Based on the study of bottom contour current deposits imaged with swath bathymetry, multichannel and high-resolution seismic data, the initial incursion of the Weddell Sea Deep Water (WSDW) into the Scotia Sea is proposed to have occurred during the middle Miocene (Maldonado et al., 2003). This confluence only occurred once several passages along the South Scotia Ridge, such as Bruce, Orkney, and Discovery passages, were opened (Naveira Garabato et al., 2002; Schodlok et al., 2002; Fig. 1.3). The first incursion of the WSDW in the Scotia Sea is documented north of the South Scotia Ridge by a widespread unconformity of regional relevance, named Reflector-c, that records a major paleoceanographic reorganization (Hernandez-Molina et al., 2008; Maldonado et al., 2014). Above Reflector-c, depositional units document a complex history of current strengthening. After 8 Ma, the uplift of the Shackleton Fracture Zone in the Drake Passage forced the northward migration of ACC-related fronts (Martos et al., 2013). The ultimate opening of the Bransfield Strait at 3.3 Ma allowed

the interaction of the water masses from both domains as it occurs in the present. The establishment of contour current deposits in the Bransfield Basin has been inferred to occur since 0.2 Ma (Liu et al., 2022).

The position of the ACC fronts varies on time scales ranging from seasonal/interannual (Freeman et al., 2016; Gille, 2014) to orbital (Kemp et al., 2010; Scherer et al., 2008). At orbital time scales, geological records suggest that the ACC fronts were displaced northward during glacial intervals (Evangelinos et al., 2020; Salabarnada et al., 2018), while a poleward migration occurred during interglacial periods (Evangelinos et al., 2020; Salabarnada et al., 2018). Moreover, records of the warm late Oligocene interglacial periods relate the intrusion of relatively warm and saline Circumpolar Deep Water (CDW) close to the Antarctic margin (Evangelinos et al., 2020; Salabarnada et al., 2018). Intrusions of CDW are today associated with increased basal melting and thinning of ice shelves (Pritchard et al., 2012), resulting in accelerated ice stream flow, inland ice thinning, and retreat of the grounding line (Fretwell et al., 2013; Peck et al., 2015; Rignot et al., 2014; Tamsitt et al., 2021). Recent studies agree that during the late Oligocene and the earliest Miocene, a fundamentally different Southern Ocean was present, with a weaker proto-ACC frontal system than at present (Evangelinos et al., 2020; 2022; Hartman et al., 2018; Salabarnada et al., 2018; Sangiorgi et al., 2018). A strong ACC, similar to the present-day, did not exist until approximately 14 Ma (Evangelinos et al., 2024).

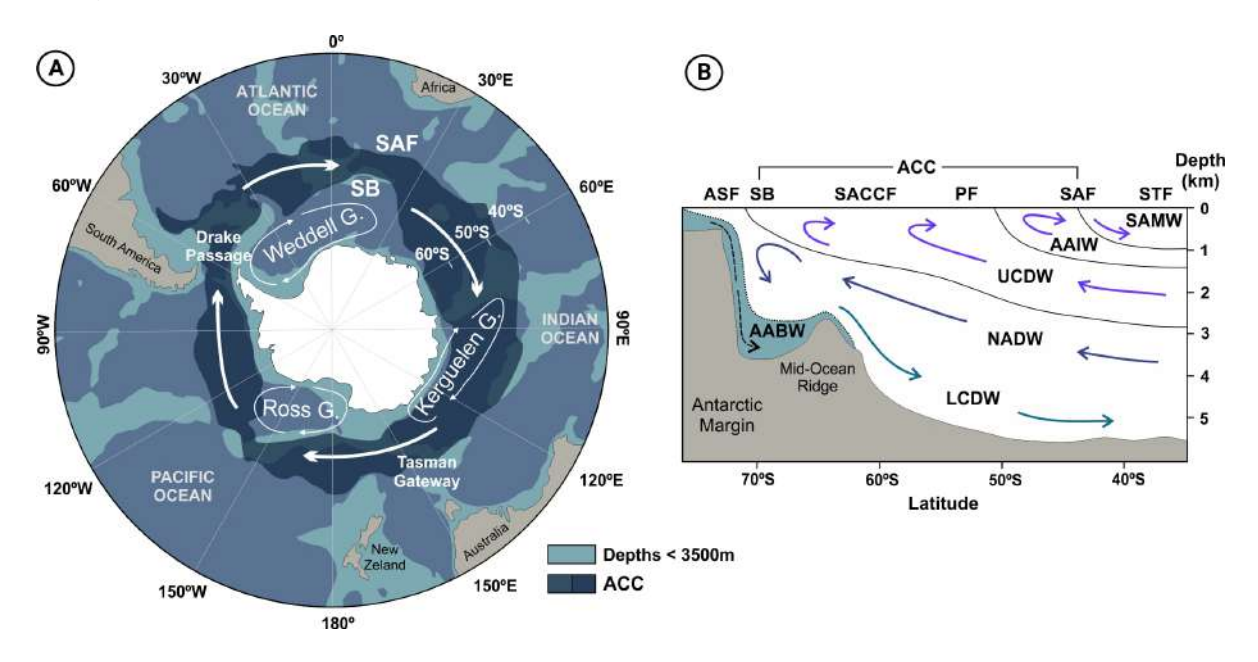


**Figure 1.4.** A) Main oceanographic elements of the Southern Ocean including: (i) the Antarctic Circumpolar Current (ACC) contained between the Subantarctic Front (SAF) and the Southern Boundary (SB); (ii) the Ross, Weddell and Kerguelen subpolar gyres. The general path for the ACC is from Orsi et al. (1995). The base chart is addapted from Carter et al. (2008). B) Schematic section of the main water masses and their meridional transport also adapter from Carter et al. (2008). Water masses are SAMW, Subantarctic Mode Water; AAIW, Antarctic Intermediate Water; UCDW, Upper Circumpolar Deep Water; LCDW, Lower Circumpolar Deep Water; NADW, North Atlantic Deep Water; AABW, Antarctic

Bottom Water. The Southern Ocean fronts are: ASF, Antarctic Slope Front; SB, Southern Boundary of the ACC; SACCF, Southern Antarctic Circumpolar Current Front; PF, Polar Front; SAF, Subantarctic Front; STF, Subtropical Front.

At present, the ACC connects the Atlantic, Indian, and Pacific oceanic basins, links the deep and shallow layers of the ocean, and has a strong influence on global ocean circulation, climate, biogeochemical cycles, and the Antarctic Ice Sheet (Rintoul, 2018; Fig. 1.4A). The main flow of the ACC concentrates four primary fronts characterized by enhanced gradients of water properties: (1) the Southern Boundary of the ACC (SB), (2) the Southern Antarctic Circumpolar Current Front (SACCF), (3) the Polar Front (PF), and (4) the Subantarctic Front (SAF) (Orsi et al., 1995; Sokolov & Rintoul, 2009; Fig. 1.4B). It is possible to determine the location of the fronts by their temperature and salinity parameters that can be associated with specific water masses. Occupying the intermediate to deep layers of the ACC, the CDW is the most extensive water mass in the Southern Ocean, ranging from 1,400 to 4000 meters deep (Orsi et al., 1995: Fig. 1.4B). It comprises two main water masses: (1) The Upper Circumpolar Deep Water (UCDW) and (2) the Lower Circumpolar Deep Water (LCDW) (Fig. 1.4B). The LCDW result of the interaction between the ACC with the North Atlantic Deep Water (NADW) (Fig. 1.4B). The LCDW retains the high-salinity signature of the NADW and rises at the continental slope, contributing to the renewal of deep circulation (Foster & Carmack, 1976; Jacobs, 2004; Orsi et al., 1999; Fig. 1.4B). Dense water formed over the Antarctic continental shelf rapidly descends into the deep ocean, spreading throughout the global ocean as Antarctic Bottom Water (AABW), the deepest water mass in the Southern Ocean (Orsi et al., 1999; Fig. 1.4B). About 80% of the AABW is generated by supercooling and brine rejection, mainly from Weddell Sea, Ross Sea and Adélie Land. The Weddell Sea Bottom Water (WSBW) is the coldest and most voluminous component of the AABW (Foldvik et al., 2004; Gordon, 2009).

#### 1.3.1. Teleconnections

The distribution of currents in the Southern Ocean is currently sensitive to atmospheric phenomena, mainly the Southern Annular Mode (SAM) and El Niño–Southern Oscillation (ENSO). These two modes affect the distribution of the CDW in the Antarctic Peninsula (Fig. 1.5). During SAM-positive phases, the belt of Southern Westerly Winds (SWW) strengthens and contracts towards Antarctica, resulting in drier weather in Patagonia and increased CDW upwelling onto the Antarctic Continental Shelf (Fig. 1.5A). In SAM-negative phases, the weaker belt of SWW moves northwards towards the equator, bringing cold, wet weather to Patagonia and causing a decrease in CDW upwelling on the Antarctic Continental Shelf (Damini et al., 2022; Renner et al., 2012; Fig. 1.5B). Although apparently remoter, the ENSO also impacts the Antarctic climate variability, particularly in terms of interannual sea ice variations across the Ross, Amundsen, Bellingshausen, and Weddell Sea (Simpkins et al., 2012). During ENSO-positive phases (El Niño), warm air from lower latitudes moves towards the polar region, resulting in a high-pressure center over the Amundsen Sea and cold air from Antarctica to the open ocean in the Weddell Sea, creating dipole anomalies in these two regions simultaneously (Yuan, 2004; Fig. 1.5C). During this phase, northerly winds are weaker on the western

Antarctic Peninsula, causing the SACCF and SB to shift towards the north and less CDW to move into the Bransfield Strait (Ruiz Barlett et al., 2018). Conversely, the northwesterly winds are stronger during ENSO-negative phases (La Niña) (Fig. 1.5D). Thus, the SACCF and SB shift towards the Antarctic Peninsula, resulting in more CDW moving into Bransfield Strait (Ruiz Barlett et al., 2018). The effects of ENSO and SAM events are amplified when they are in phase, i.e., SAM-positive with ENSO-positive phases and SAM-negative with ENSO-negative phases. For example, during ENSO-positive and SAM-positive phases, the advection of CDW into Bransfield Strait is even stronger, which is associated with the weakening of the transport of shelf waters along the west Antarctic Peninsula (Ruiz Barlett et al., 2018).

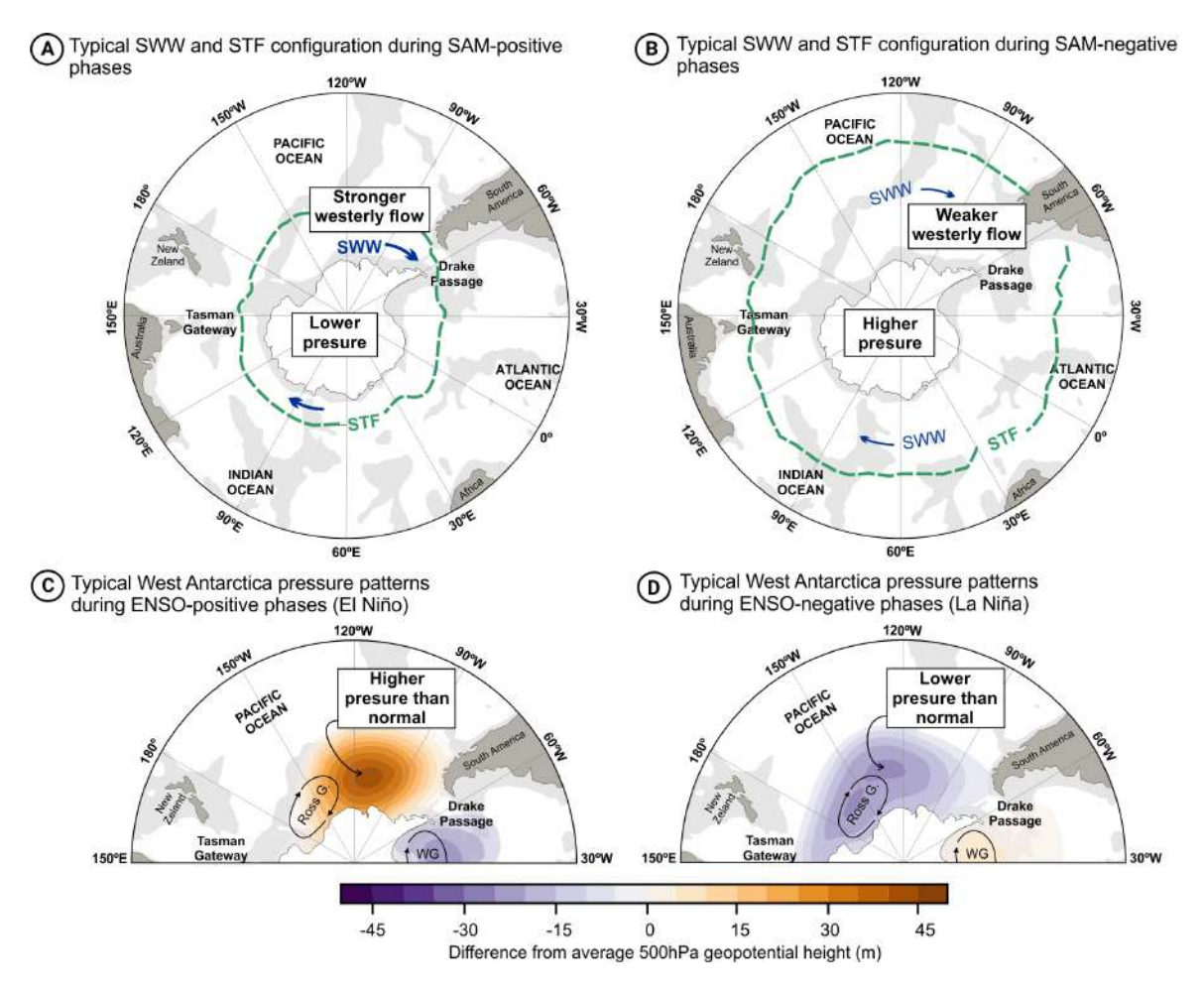


**Figure 1.5.** A) Pressure pattern during ENSO-positive phase. B) Pressure pattern during ENSO-negative phase (adapted from figure by Emily Becker in climate.gov). C) Configuration of the Southern Westerly Winds (SWW) and the Subtropical Front (STF) during SAM-positive phases. D) Configuration of the Southern Westerly Winds (SWW) and the Subtropical Front (STF) during SAM-negative phases (modified from Lee et al. (2019).

In the Antarctic Peninsula region, the air-sea-ice system responds strongly to the ENSO forcing, resulting in the Antarctic Dipole climatic mode that produces an out-of-phase relationship between sea ice and surface temperature anomalies in the South Pacific and South Atlantic (Yuan, 2001). During ENSO-positive phases, warm temperature anomalies and reduced sea ice anomalies

occur in the Pacific sector of the Antarctic and the opposite response in the Atlantic sectors of the Antarctic (Yuan, 2004).

#### 1.4. Deep-water sedimentary processes

Sedimentary processes in deep-water marine settings include pelagic/hemipelagic settling, gravity-driven downslope and along-slope sedimentary processes. Pelagic/hemipelagic sedimentation is a process of vertical settling of biogenic material (phytoplankton and zooplankton) and a varying amount of terrigenous material through the water column to the seafloor (Stow & Smillie, 2020; Stow & Tabrez, 1998). Gravity-driven down-slope processes are responsible for the transfer of sediment from marginal areas to the deep sea. They include submarine slides, slumps, cohesive debris flows, and turbidite flows (Mulder & Alexander, 2001; Shanmugam, 2016). Along-slope sedimentary processes include contour currents deposits, and wind- and internal tide-driven currents deposits, playing an important role in sediment erosion, redistribution and preferential deposition (Rebesco et al., 2014; Stow et al., 2002; Stow & Smillie, 2020). Each of these sedimentary processes forms distinct deposits (hemipelagites, turbidites, mass transport deposits, contourites, drifts, etc.). However, the interplay among these processes is common in the natural system. Deciphering which process predominates can be difficult, as they often overlap as part of a continuum (Rebesco et al., 2014; Stow & Smillie, 2020). In this PhD thesis, the dominant sedimentary processes studied are along-slope processes interacting with pelagic/hemipelagic sedimentation, with minor preservation of gravity flows.

The interaction between bottom contour currents and the seafloor results in contourite deposits, the identification of which remains a challenge. Contourites show a wide range of grainsizes, composition, and preserved sedimentary structures. Contourites commonly results in wellsorted sediments, due to affecting reworking processes and the winnowing of finer grained material delivered to the deep sea as pelagites/hemipelagites and or gravity flows (Rebesco et al., 2014). Contourites can be studied using a wide variety of oceanographic, geophysical and sedimentological techniques. The initial recognition of a contourite deposit in the marine setting can be done by means of seismic profiles based on distinct mounded/drift morphologies, and internal reflection configurations (Rebesco & Stow, 2001; Fig. 1.6A). In addition, the upper and lower boundaries of the drift often display low-angle downlap reflectors onto the basal unconformity (Faugères et al., 1999; McCave & Tucholke, 1986; Rebesco & Stow, 2001; Fig. 1.6A). The interpretation of seismic facies relies heavily on seismic acquisition and processing and, therefore, may not be a "stand-alone" diagnostic tool. Sedimentologically, a common contourite sequence separate the deposits into five divisions (C1 to C5), with a typically bigradational pattern resulting from an increase followed by a decrease in the current intensity ( Stow & Faugères, 2008; Fig. 1.6B). However, it is common that in the geological record the ideal sequence is only partially preserved (Stow & Faugères, 2008). Contourites can provide important insights into changes in the ocean circulation patterns, current velocities, oceanographic history and basin interconnectivity.

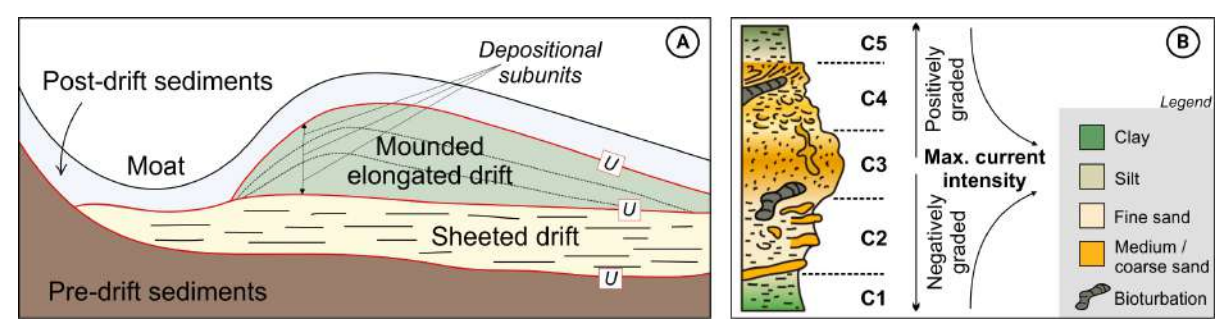


**Figure 1.6.** A) Conceptual model of principal seismic characteristics of contourite deposits, modified from Nielsen et al. (2008) from the original figure in Stow et al. (2002). B) Standard facies model of a contourite sequence, linked to variations in contour current velocity, modified from Salabarnada (2020) based on the original figure from Gonthier et al. (1984).

Additionally, the morphology of the contourites and their relative position to the slope can indicate the current flow direction considering the influence of Coriolis force in the southern hemisphere, which deflects along-slope bottom currents towards the left, resulting in higher energy and velocity on that side (Fig. 1.7A). As a result, sediments are eroded on the left and deposited on the right where the flow velocity is lower (Fig. 1.7B and 1.7C). Elongation is generally parallel or subparallel to the margin (Faugères et al., 1999; Fig. 1.7B and 1.7 C).

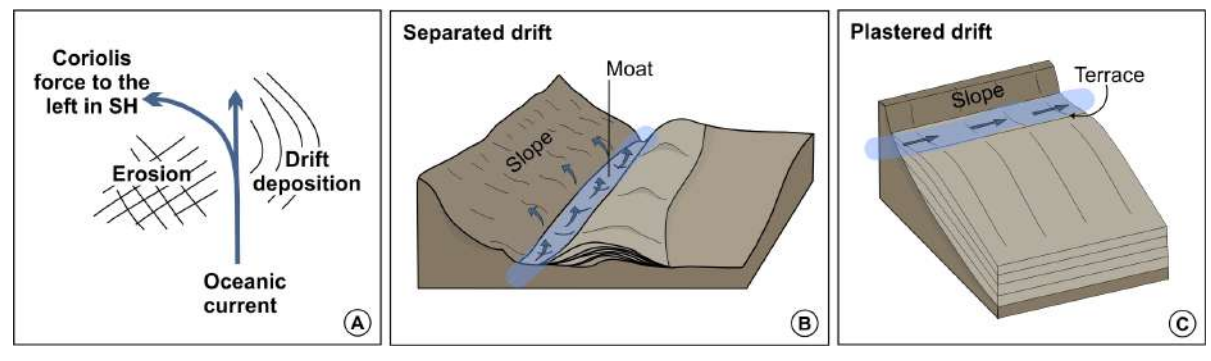


**Figure 1.7.** A) Sketch map showing how the Coriolis force in the Southern Hemisphere affects the contourite deposition (adapted from Salabarnada, 2020). Sketch of the deposition of a separated drift (B) (modified from Faugères et al., 1999) and a plastered drift (C) in the southern hemisphere (addapted from Rodrigues et al., 2020).



# CHAPTER 2

Materials and methods

# CHAPTER 2: Materials and methods

This chapter presents a brief description of the different geophysical and sedimentological data sets used during this PhD thesis (Fig. 2.1) and the methodologies applied to address the research objectives (Table 2.1). A multiproxy approach was conducted to fulfil each of the proposed objectives listed in the Hypotheses and Objectives section. Table 2.1 shows the methods used for each of the chapters in the thesis pointing to what analysis have been performed by the PhD candidate and which analyses have been performed by collaborators. The integration of all proxies has been conducted in the frame of this PhD thesis. An overview to the fundaments of the methodologies and adapted work flows applied are discussed in this chapter, however, detailed aspects of the used methodologies are described in their respective chapters (Chapters 3, 4, and 5).

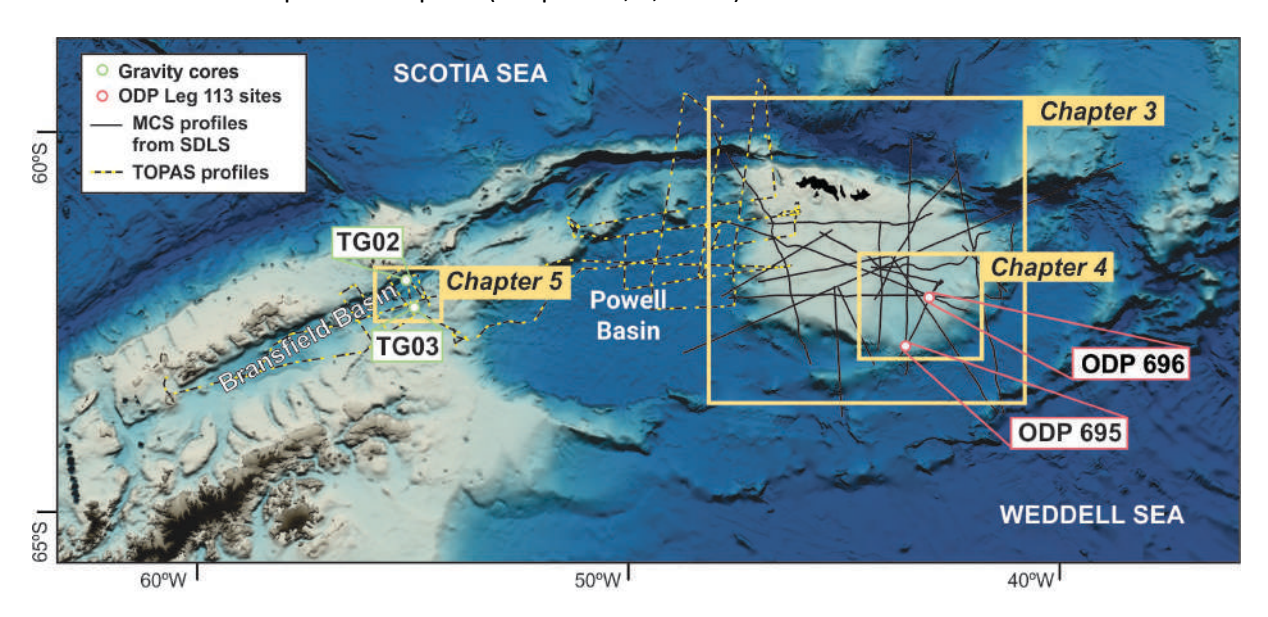


**Figure 2.1.** Overview map of the study area of the PhD thesis. Available MCS profiles from the Seismic Data Library System (SDLS) and TOPAS profiles are located, together with sediment cores from ODP Leg 113 and gravity cores collected during Powell2020 cruise.

# 2.1. Geophysical methods

#### 2.1.1. Potential fields data: gravity and magnetic modeling

Gravity and magnetic methods assess changes in the Earth's gravity and magnetic fields. Gravity prospecting is based on the variation of the gravity acceleration as a result of lateral density contrasts. A gravity anomaly can be defined as the difference between the gravity value measured in a point and the theoretical gravity value expected for that point according to its geographical position and a standard homogeneous model of the Earth (Keary et al., 2002). The gravity anomalies employed in this thesis are converted from geoid height measurements made with satellite altimetry (CryoSat-2 and Jason-1), available from the open database of TOPEX (Sandwell et al., 2014).

Magnetic anomalies are the result of variations in the total Earth's magnetic field strength, usually referred as the total magnetic intensity (TMI). Its variation is the result of variations in rock

magnetism, which is mostly controlled by magnetic susceptibility (Keary et al., 2002). The TMI data used in this thesis were extracted from the open database of World Digital Magnetic Anomaly Map (WDMAM) that compile data form airborne surveys at a constant nominal survey height, research vessel magnetometer traverses at sea, and observations from earth-orbiting satellites (Lesur et al., 2016).

		Chapter 3 3D Modelling of the SOM	Chapter 4 Seismic stratigraphic analysis of the SOM	Chapter 5 Ocean current variability in the Bransfield Basin
le s	2D gravity and magnetic modeling	~		
Geophysical methods	3D gravity and magnetic modeling	~		
9	Seismic stratigraphic analysis	✓	✓	
-B	Grain size analysis			<b>√</b>
Sedimentological methods	Core scanning (XRF, Physical properties and CT-Scan)			<b>√</b>
met	Diatom counting and assemblage			<b>√</b>
Sed	Age model		Revised	✓

**Table 2.1.** Specific methodologies used in each chapter of the PhD thesis. The boxes colored in gray indicate the methods addressed by other researchers.

Modeling the gravity and magnetic anomalies is a cost-effective methodology for subsurface surveying, especially suitable for remote areas like Antarctica where direct methods might not be feasible. Forward and inverse modeling are two different techniques for analyzing geophysical data. In forward modeling, the model parameters are adjusted iteratively until the best adjust between the observed and the computed anomaly is obtained. With inverse modelling, or inversion, the iterative modeling process is automated with the drawback of geophysical non-uniqueness. Due to the non-uniqueness of gravity and magnetic modelling, the modeled structure is not necessarily the true structure. For that reason, during 2D and 3D modeling, joint gravity and magnetic modeling in both forward and inversion has been implemented to obtain the better geologically plausible model of the South Orkney Microcontinent (SOM; see Chapter 3).

The analytic signal (AS) is the total gradient applied to potential field data at a certain location (x, y) and given by:

$$AS(x,y) = \sqrt{\left(\frac{\partial f}{\partial x}\right)^2 + \left(\frac{\partial f}{\partial y}\right)^2 + \left(\frac{\partial f}{\partial z}\right)^2}$$

Where, f is the magnetic or gravity potential field. The resulting signal show its maximum ridges matching the edges of the source prism, revealing its geometric form. Applied to TMI data, the

AS is effective methodology for delineating the geological boundaries of a magnetic source (Doo et al., 2009).

# 2.1.2. Seismic stratigraphic analysis

Multichannel seismic reflection (MCS) profiles are widely used to enable the imaging of subsurface structures and strata. The available MCS profile on the SOM were obtained from the Seismic Data Library System (SDLS), which works under the auspices of Scientific Committee on Antarctic Research to provide open access to all MCS data collected south of 60°. The different cruises that collected the data from the SOM used for this PhD thesis are listed in Table 2.2, with the technical details for their acquisition. Figure 2.1. shows the grid of seismic profiles in the SOM analyzed for this PhD thesis. In the 3D model presented in Chapter 3, MCS lines were used throughout the SOM to determine the acoustic basement as a first approach of the boundary between the upper crust and sedimentary fill. In Chapter 4, MCS profiles were used to study the stacking patterns and morphosedimentary characteristics of the sedimentary infill of the SOM. Additionally, in Chapter 5, very high-resolution seismic reflection profiles from Topographic Parametric Sonar (TOPAS) collected onboard the Spanish R/V Hespérides during the Powell2020 oceanographic cruise in the Bransfield Basin were analyzed. This technique allows the imaging of the first up to 100 m of sedimentary cover.

Survey	Year	Country	Source Type	Receiver Type	Top Bandwidth
BAS845	1993	UK	Four air guns (capacity 8.5 L)	Sercel sn-358, 48-channel TELEDYNE streamer 2400 m	250 Hz top- bandwidth multi- channel seismic reflection systems
TH87	1996	Japan	Two water guns (capacity 13.1 L)	DFS-V, 24-channel, 600 m ministreamer	250 Hz top- bandwidth multi- channel seismic reflection systems
IT91	1991	Italy	Two air guns (capacity 45.16 L)	Sercel sn-358, PRAKLA- SEISMOS analog cable, with 120-channel, 25 m intertrace	250 Hz top- bandwidth multi- channel seismic reflection systems
IT89	1989	Italy	Two air guns (capacity 45.16 L)	Sercel sn-358, PRAKLA- SEISMOS analog cable, with 120-channel, 25 m intertrace	250 Hz top- bandwidth multi- channel seismic reflection systems

**Table 2.2.** Summary of the cruises that collected Multichannel Seismic Data (MCS) across the South Orkney Microcontinent (SOM) and survey characteristic of the MSC profiles acquisition parameters when available used in Chapters 3 and 4.

The analysis and interpretation of MCS profiles was performed with Kingdom Suite software. Seismic interpretation followed the basic analytical methods of seismic stratigraphy (e.g., Payton, 1977) consisting of three main steps: (1) subdivision of seismic sections into sequences of reflections that are interpreted as genetically related sedimentary sequences, (2) analysis of seismic facies, and (3) interpretation of depositional environments.

Genetically related sedimentary sequences typically comprise a set of concordant strata that are discordant with the underlying and overlying sequence, usually bounded by angular unconformities that variously represent overlap, downward overlap, top overlap, or erosion (Fig. 2.2). Once the boundary of seismic sequences has been interpreted, the analysis of seismic facies is based on reflection geometries and seismic attributes (i.e., amplitudes, continuity, frequency). By grouping parameters into mappable seismic facies, depositional processes and environments, erosion, and uncorrected paleotopography can be interpreted. The overall external geometry and association of seismic facies units (e.g., in sheets, wedges, mounds) are also relevant to interpreting depositional processes and environment.

#### 2.2. Sediment cores analyses

# 2.2.1. Ocean Drilling Program (ODP) Sites 695 and 696

Sites 695 and 696 were collected in the southeast margin of the SOM, during Leg 113 of the Ocean Drilling Program (ODP) in 1987 (Barker et al., 1988). Site 695 (62° 23.476' S, 43° 27.095' W) is located at 1300 m water depth (Fig. 2.1). This site was continually cored to a depth of 341.1 meters below sea floor (mbsf) with a core recovery of 74.6%. The oldest sediments from Site 695 were dated late Miocene. Site 696 (61° 50.945' S, 42° 55.984' W) was drilled at 650 water depth. The total drilled depth was 645 mbsf, with 55% recovery. The oldest sediments were dated from the late Eocene.

To optimize the tie between ODP Sites and MCS profiles in Chapter 4, a synthetic seismogram was calculated based on density and velocity data from the Leg 113 Initial Reports (Barker et al., 1988). The product of the density and P-wave velocity of a medium yields the acoustic impedance. The variation in acoustic impedance between two media results in a reflection coefficient, which, multiplied by an assumed source wave through a horizontal layered model, represents the equivalent of the seismic response (Kearey et al., 2002; Fig. 2.3).

New direct sedimentological analyses were not implemented in Sites 695 and 696 during this PhD thesis. However, available data published by Baker et al. (1988) were used to provide the necessary information to analyze the MCS profiles. The chronostratigraphy in Barker et al. (1988) has been updated to the biostratigraphic zonation for the Southern Ocean following Weber et al. (2019) zonations, as it has been revised since the time of Leg 113. The revised age model is provided in Chapter 4 and allowed to constrain the ages of the interpreted seismic units. Finally, we have considered the shipboard descriptions and interpretations of the lithostratigraphic units at both Sites

695 and 696 (Barker et al., 1988), together with other studies in the SOM, to help interpret the evolution of the SOM and depositional setting.

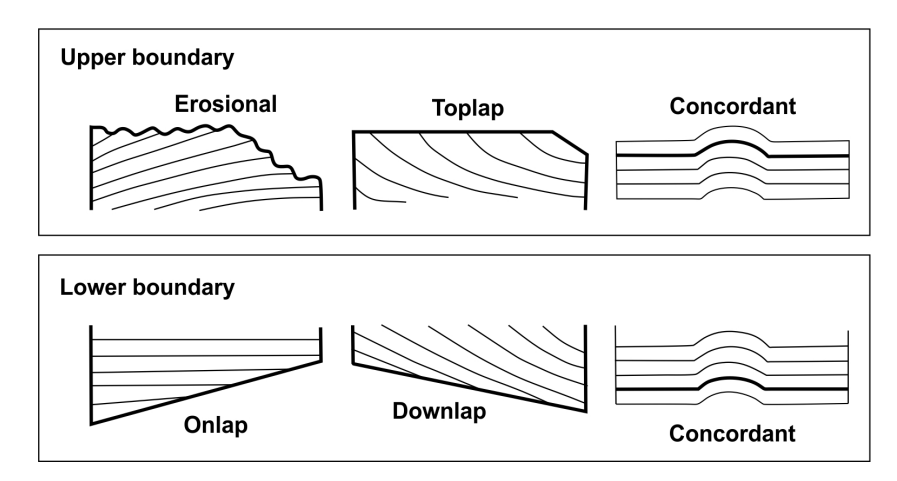


**Figure 2.2.** Seismic terminology used in sequence-stratigraphic analysis for seismic terminations in relation with the upper and the lower boundary (Sheriff 1980).

#### 2.2.2. Gravity cores

Gravity cores TG02 (61° 39.293' S, 55° 7.651' W) and TG03 (61° 59.189' S, 55° 0.442' W) analyzed in Chapter 5 were collected in the East Bransfield Basin (EBB) during the POWELL2020 cruise on board the Spanish R/V Hespérides (Fig. 2.1). A gravity core consists of a 5-meter-long spear attached to a total weight of 700 kg used to collect sediment samples from the ocean floor. Once released from the support, the deployment and retrieval process is carried out at an average speed of about 50 meters per minute. The TOPAS profiles were used to determine the location of deployment of the gravity cores. Cores TG02 and TG03 were retrieved from mounded morphologies in areas previously described as influenced by contour-current deposition (García et al., 2019; Liu et al., 2022). However, it is worth noting that the R/V Hespérides does not have a Dynamic Positioning System. Thus, sediment core sampling faces the challenge of maintaining its position during the collection process for up to two hours at depths of up to 2000 m. However, the spatial coverage of the imaged mounded deposits was thought to guarantee the retrieval of the targeted sediments.

A multiproxy analysis of cores TG02 and TG03 was performed (Table 2.1). Non-destructive core scanning included: (1) Computed tomography scanning (CT-Scan) of whole cores; (2) High-resolution digital imaging and physical properties analysis (i.e., gamma-ray density, magnetic susceptibility, resistivity, and P-wave velocity) in the archive half of the core and 0.5 cm sampling resolution; and (3) high-resolution X-Ray Fluorescence (XRF) at 1 cm sampling resolution in the same archive half of the core. In addition, discrete grain size analysis and biostratigraphic and ecological characterization of diatoms were performed on samples taken approximately every 10 cm. CT-Scan images were obtained with a Hitachi ECLOS 16 Multislice CT at the Veterinary Teaching Hospital Rof Codina. High resolution images, physical properties and XRF data were obtained from split cores using different Geotek equipment at the Instituto Geológico y Minero de España (IGME). High resolution

images are captured with the Geoscan IV Core Imaging System. The physical properties and XRF data are acquired with the Multi-Sensor Core Logger equipment.

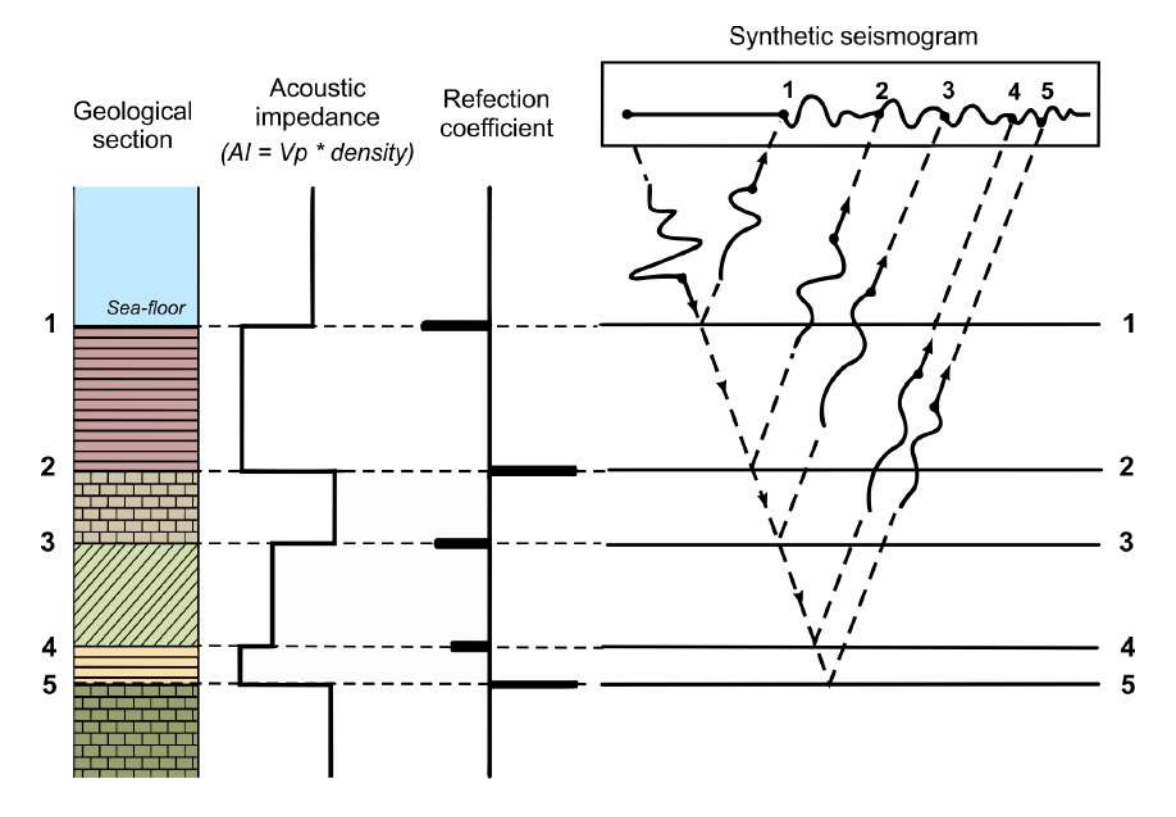


**Figure 2.3.** Schematic diagram of a synthetic seismogram construction modified from Kearey et al. (2002)

The grain size analysis was carried out by laser diffraction using the Malvern Mastersizer 2000 equipment at the University of Bordeaux during the research stay required to obtain the International Mention. Both the bulk sample and the sortable silt fraction (10-63  $\mu$ m) were analyzed. The methodology used to obtain the sortable silt fraction included the removal of carbonate, organic matter, and biogenic silica content. Firstly, two grams of each sample were dried in the oven at 40°C for 24 hours. For the carbonate content removal, samples were flooded with HCl until no CO₂ emission occurred. When the reaction was completed, the samples were diluted in purified water. After centrifugation, the pellet was rinsed, dried, and weighed to determine the carbonate percentage. To remove the organic matter content, samples were treated with H<sub>2</sub>O<sub>2</sub> in bath-marie at 65° C for 6 hours. Subsequent reactions occur at room temperature for several days, with periodic addition of H<sub>2</sub>O<sub>2</sub>. The percentage of organic matter is then estimated as described in the previous step. The last step involves the removal of biogenic silica. Treatment with sodium hydroxide (NaOH) in a sealed tube, with subsequent water bath sessions, removes the biogenic silica. Finally, the percentage of biogenic silica is also estimated after microscopic examination to ensure the absence of biogenic silica components. Both bulk samples and the resulting samples free of carbonate, organic matter and biogenic silica are introduced into the equipment, passing through a focused laser beam. The particles scatter light at an angle that is inversely proportional to their size. The results are statistically treated with the GRADISTAT package (Blott & Pye, 2001).



# CHAPTER 3

3D geophysical and geological modeling of the South Orkney Microcontinent (Antarctica) - Tectonic implications for the Scotia Arc development

Morales-Ocaña, C., Bohoyo, F., Escutia, C., Marín-Lechado, C., Rey-Moral, C., Druet, M., Galindo-Zaldívar, J., & Maestro, A. (2023). 3D Geophysical and Geological Modeling of the South Orkney Microcontinent (Antarctica): Tectonic Implications for the Scotia Arc Development. *Tectonics*, 42(4), 1–20. https://doi.org/10.1029/2022TC007602

CHAPTER 3: 3D geophysical and geological modeling of the South Orkney Microcontinent (Antarctica): Tectonic implications for the Scotia Arc development

# **Abstract**

The opening of the Scotia Arc resulted in the final breakup of the land bridge between South America and the Antarctic Peninsula. The South Orkney Microcontinent (SOM) constituted part of this former connection and it is now the largest continental block in the Southern Scotia Arc. We present the first 3D model of the SOM that, given its strategic position and characteristics, allows us to advance the knowledge of the tectonic processes involved in the development of the Scotia Arc. Due to the scarcity of reliable geological data, the initial approximation of the deep structure of the SOM was supported by the calculation of three main geological boundaries from geophysical data: the acoustic basement, the boundary of the magnetic anomaly source and the Moho depth. The 3D model was built, refined and validated by forward modeling and joint inversion of gravity and magnetic data. We have accurately defined the geometry of the sedimentary cover, determined the geometry of the intrusive igneous body causing the Pacific Margin Anomaly (PMA) and mapped the heterogeneity of the crustal thickness. These structural features show a clear relationship to each other and are consistent with an important E-W extension to the east of the SOM during early stages of the Scotia Arc formation, prior to the opening of the Powell Basin.

# 3.1. Introduction

The origin of the Scotia Arc lies in the early stages of the fragmentation of the supercontinent Gondwana during the late Mesozoic (Dalziel et al., 2013), which culminated in the separation between South America and the Antarctic Peninsula, thus opening the Drake Passage (Barker and Burrell, 1977). The South Orkney Microcontinent (SOM) is the largest continental block in the South Scotia Arc, located between the Scotia and the Antarctic plates. Previous work has postulated the SOM to be the final continental link between the Antarctic Peninsula and South America (Lawver et al., 1985). Paleogeographic reconstructions place the SOM adjacent to the eastern Antarctic Peninsula and close to South America before the opening of the Scotia Arc and the Drake Passage (Livermore et al., 2005; Dalziel et al., 2013; Eagles and Jokat, 2014; van de Lagemaat et al., 2021). However, many uncertainties remain as to when and how the dispersion of the continental blocks occurred in the Scotia Arc (Riley et al., 2022). These uncertainties in turn, prevent accurate paleoceanographic reconstructions of the earliest connection between the Pacific and Atlantic Oceans and hinder confident understanding of the implications for global ocean circulation and climate.

Previous works carried out in the study area, although scarce, have defined the main structural characteristics of the SOM: i) The geometry of the sedimentary basins of the SOM from geophysical data facilitated the recognition of two structural trends (i.e. a younger N-S overlying an older E-W trend) (King and Barker, 1988; Busetti el at., 2000). ii) The continuity of a large amplitude magnetic anomaly belt - the Pacific Margin Anomaly (PMA) - along the dispersed continental fragments of the

Scotia Arc, allowed the reconstruction of the former connection between the SOM and the Antarctic Peninsula (Barker and Griffiths, 1972; Garrett et al., 1986/87; Eagles and Livermore, 2002; Martos et al., 2014). iii) The crustal thickness below the SOM has been described as unusually thin as an expression of the extensional tectonic regime it has undergone (King and Barker, 1988). So far, those works have characterized these features separately resulting in a limited understanding of the origin and evolution of the SOM.

The aim of this study is to improve the resolution of the aforementioned structural features of the SOM and to interrelate their geometries to reveal new insights into the tectonic processes operating during the different stages of the Scotia Arc formation, from the Mesozoic to the present. 3D modeling represents a powerful tool that facilitates the integration of different geological and geophysical datasets (Mallet et al., 2002; Wu et al., 2005; Calcagno et al., 2008) and allows to characterize large geological structures in data-poor regions such as Antarctica. We present the first 3D geophysical and geological model of the SOM and its surroundings by gravity and magnetic forward modeling and joint inversion. The model has been constrained by three main geological boundaries: the acoustic basement inferred from multichannel seismic reflection (MCS) profiles, the PMA source boundary and the Moho. The model resolves the complex geological structure of the SOM, including refinement of the geometry of the sedimentary basins, the magnetic source of the PMA and the variation of the crustal thickness, providing new insights into the tectonic evolution of the SOM.

# 3.2. Geological setting

The SOM is located in the southern branch of the Scotia Arc and is the largest continental block in the area (nearly 70.000 km2). At present, the SOM is integrated in the Antarctic plate and its northern margin constitutes an active segment of the boundary between the Scotia and Antarctic plates (Fig. 3.1).

The tectonic evolution of the SOM since the Mesozoic has been inferred by the analysis of lineaments and brittle structures measured in rock outcrops in the South Orkney Islands, the only exposed part of the microcontinent (Trouw et al., 1997, Maestro et al., 2013). Trouw et al. (1997) established up to five phases of deformation. In the early Mesozoic (phases 1-3), the SOM was still attached to the Antarctic Peninsula and the deformation was north-south trending as a response to the subduction of the former Phoenix plate beneath the Gondwana margin (Barker et al., 1991). During late Jurassic (phase 4), the opening of the Rocas Verdes Basin (154 Ma) produced an important N-S crustal extension that has been related to the first stages of the Gondwanaland breakup (Barker et al., 1991). Simultaneously with the Rocas Verdes Basin opening, the Antarctic Peninsula started a rotation relative to East Antarctica. There is no consensus on the sense of rotation, since for some authors it is clockwise and for others counterclockwise (Barker and Dalziel, 1983; Dalziel, 1984; Eagles and Eisermann, 2020; van de Lagemaat et al., 2021). The Cenozoic history of the SOM produced a phase of brittle faults of horizontal extension (phase 5) that has been related with opening of the Powell Basin and the development of the Scotia Arc (Trouw et al., 1997). The opening of the Scotia

Arc after 50 Ma and consequently, the opening of the Drake Passage, caused the drift of the different continental blocks, including the SOM (Livermore et al., 2007).

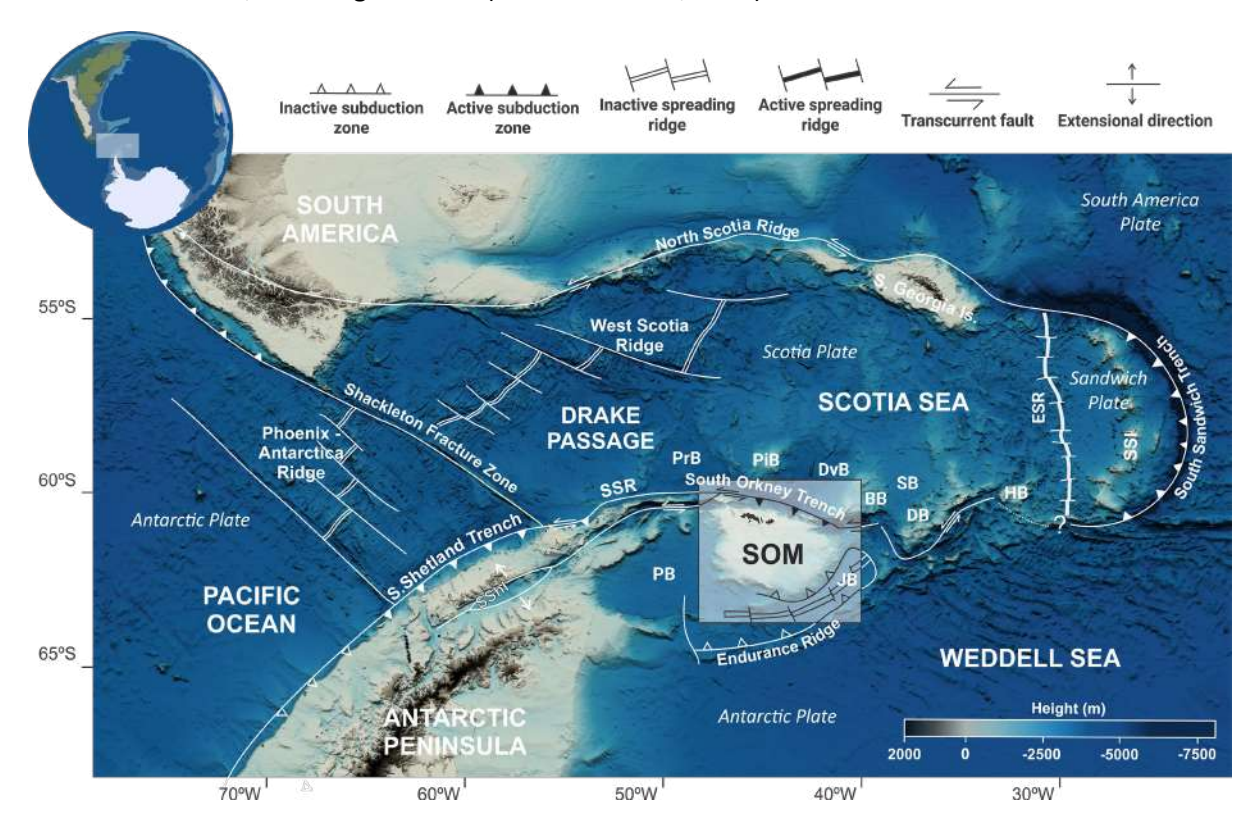


**Figure 3.1**. Tectonic setting of the Scotia Arc. Bathymetry from GEBCO 2020. BB: Bruce Bank; DB: Discovery Bank; DvB: Dove Basin; ESR: East Scotia Ridge; HB: Herdman Bank; JB: Jane Basin; PB: Powell Basin; PiB: Pirie Bank; PrB: Protector Basin; SB: Scan Basin; SOM: South Orkney Microcontinent; SShI: South Shetland Islands; SSI: South Sandwich Islands; SSR: South Scotia Ridge.

The current location of the SOM with respect to the Antarctic Peninsula is the result of the seafloor spreading in Powell Basin, dated between 29 and 21 Ma according to Eagles and Livermore (2002) and between 38 and 29 Ma according to Schreider et al. (2022). Garret et al., (1986/87) proposed a 30°counterclockwise rotation to reconstruct the position of the SOM to when it was attached to the Antarctic Peninsula. Another approach to the reconstruction of the former connection between the SOM and the Antarctic Peninsula was performed by Eagles and Livermore (2002) by applying palinspastic adjustments to the shape of the SOM guided by the gravity signals of the Newton, Airy, Bouguer and Eötvös basins.

As a consequence of the tectonic evolution in the area, the SOM presents four margins with distinctive morphologies, sediment distributions and different crustal structures (King and Barker, 1988). The northern margin of the SOM corresponds with a curved segment of the plate boundary between the Antarctic and the Scotia plates. Today, this plate boundary is a zone of sinistral transpression (Bohoyo et al., 2007; Civile et al., 2012), which concentrates the current seismic activity in the area (Fig. 3.2). The western margin of the SOM represents a passive margin connected to the oceanic Powell Basin. Catalán et al. (2020) identified the ocean-continent boundary between Powell Basin and SOM describing a transition zone with extended and intruded continental crust between

them (Fig. 3.2). The southern and eastern margins are bounded by the oceanic Jane Basin. Seafloor magnetic anomalies indicates that the subduction of the Weddell Sea spreading center beneath the southeastern SOM could have caused the development of the Jane back-arc Basin between 17.6 and 14.4 Ma, after the end of the subduction of the Weddell Sea, tentatively dated at 20 Ma (Bohoyo et al., 2002).

The knowledge of the deep structure of the SOM is still limited. As a first approach to the deep crustal structure, Harrington et al. (1972) performed a N-S seismic refraction profile west of the South Orkney Islands with results limited to the upper layers. The considerable extension undergone by the SOM resulted in an unusually thin crust (King and Barker, 1988). This major extension is evidenced by the presence of NNW-SSE trending normal faults in the southern portion of the SOM that bound the basins located in the area (King and Barker, 1988). Different authors have modeled the crustal thickness: King and Barker (1988) infer 21 km, Kavoun and Vinnikovskaya (1994) between 14-26 km, and Busetti et al. (2001) model around 25 km. King and Barker (1988) computed simple isostatic gravity models across the SOM, resulting in most of the SOM considered to be in isostatic equilibrium except the northern margin. The positive isostatic anomaly in the northern SOM reflects an uplift of the area, most likely related to an active strike-slip movement along the northern margin (King and Barker, 1988). In terms of crustal composition, outcrops in South Orkney Islands indicate that the upper continental crust consists mainly of low-grade metamorphic rocks of Paleozoic to Cretaceous age, intruded by bodies of igneous rocks of Cretaceous age. (Dalziel et al., 1984; King and Barker, 1988; Rodríguez-Fernández et al., 1997; Maestro et al., 2013). Barber et al. (1991) dredged rock from around Powell Basin and the margins of the SOM and differentiated between two groups of samples. The first group, from the east and west margins of the SOM, was described as hydrothermally altered subalkaline basalts, radiometrically dated with ages between 70 and 85 Ma (stars in Fig. 3.2). The second group corresponds to samples from the western margin of the Powell Basin, which include alkali basalts with ages between 47.7 and 49 Ma and Pliocene/Recent.

Throughout the Antarctic Peninsula, long wavelength, high-intensity magnetic anomalies have been described as the Pacific Margin Anomaly (PMA) or the West Coast Magnetic Anomaly (Renner et al., 1982; Garret, 1990). Subsequent studies have shown the continuity of this belt in multiple continental fragments - including the SOM - which allows the reconstruction of the continental blocks position in the late Mesozoic (Martos et al., 2014). The source of this anomaly is likely the presence of linear batholiths of basic-intermediate composition, probably gabbro (Garrett et al. 1986/87), produced by the subduction of the Pacific margin below the Gondwana margin (Garrett and Storey, 1987; King and Barker 1988; Suriñach et al., 1997). Large intrusive bodies with varying magnetic susceptibilities and thicknesses have been modeled to explain the PMA along the Antarctic Peninsula and the SOM. They are considered to have a maximum thickness between 11 km (Garrett et al., 1986/87, Martos et al., 2014) and 20 km (Harrington, 1972). Maximum magnetic susceptibilities used for modeling also vary in a wide range: from 0.006 to 0.8530 SI (Harrington, 1972; Martos et al., 2014). Below the SOM, it has been proposed that the source of the magnetic anomaly may have been

alternative caused by intrusive bodies resulting from the subduction of the Weddell Sea beneath the microcontinent (Bohoyo et al., 2002).

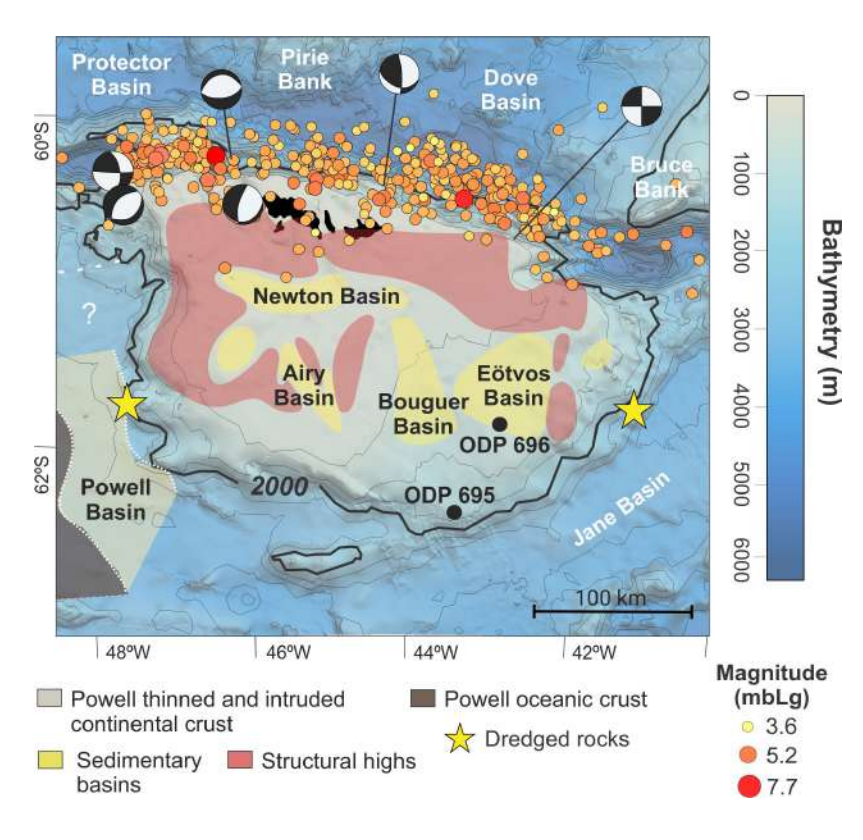


**Figure 3.2**. *Geological setting* of the SOM. Historical seismicity was extracted from the USGS earthquake catalogue. Earthquake focal mechanisms after Bohoyo et al. (2007). Position of the sedimentary basins and structural basement highs after Busetti et al. (2000). Powell Basin crustal zones were differentiated in Catalán et al. (2020). Location of the Ocean Drilling Program (ODP) Sites 696 and 695 is also pointed. The location of dredged rocks around the SOM by Barber et al. (1991) is shown with stars.

The sedimentary basins in the SOM were first described by King and Barker (1988) using gravity anomalies that depict values below 40 mGal. However, the gravity data shown in that work did not cover the westernmost part of the SOM. Busetti et al. (2000) refined the position of these basins by analyzing seismic reflection data. The orientations of the basins coincide with two main structural domains: (1) An E-W orientated graben south of the islands, the so-called Newton Basin, filled with more than 4 km of sediments (Harrington, 1972) and associated with the Mesozoic forearc setting (King and Barker, 1988). (2) N-S orientated grabens, located in the southern part of the SOM, the Airy, Bouguer and Eötvös basins. Their formation is associated with east-west extension related to the separation of the SOM from the Antarctic Peninsula (King and Barker, 1988). The sedimentary infill of the SOM basins has been targeted by the Ocean Drilling Program (ODP) Leg 113 (Barker et al., 1988) that recovered sediment cores at Sites 695 and 696 (Fig. 3.2). Site 695 reached upper Miocene sediments, while Site 696 recovered sediments spanning from the Eocene to the Quaternary (Barker et al., 1988). Recovered sediment cores record the evolution of the SOM from when it was attached to the Antarctic Peninsula to its present position. Before late Eocene (~37.6-35.5 Ma), locally sourced terrigenous sediments recovered at Site 696 are associated with the SOM still close to the Antarctic Peninsula (López-Quirós et al., 2021). The decrease in the input of these proximal sediments to the Site 696 is interpreted to indicate the separation between the SOM and the Antarctic Peninsula as a result of the proto-Powell Basin opening (López-Quirós et al., 2021). A terrestrial cooling phase at the latest Eocene (35.5 Ma) is also linked to the opening of the Powell Basin (Thompson et al., 2022).

#### 3.3. Data and Methodology

This section describes the initial geophysical data used and the methodology leading to the construction of the 3D model validated by forward and joint inversion of gravity and magnetic data.

#### 3.3.1. Initial dataset

Bathymetric data of the study area has been extracted from the GEBCO 2020 database (GEBCO Compilation Group, 2020), which includes the IBCSO database (Arndt et al., 2013), with a cell resolution of 500 m (Fig. 3.3A). The bathymetry of the SOM ranges from < 500 meters below sea level (mbsl) in the northern and the western area, deepening to the SE where the platform reaches depths up to 1500 mbsl. The South Orkney Islands emerge towards the NNW limit of the SOM. To the north, the edge of the microcontinent is marked by the Orkney Trench, which deepens to up to 5500 mbsl, along the South Scotia Ridge. The other margins show smoother slopes, reaching 3000 mbsl. The 2000 mbsl isobath (Fig. 3.3A) has been considered to be representative of the continental area of the SOM, and has therefore been used as a visual reference in the figures throughout the work.

Multichannel seismic reflection (MCS) profiles cover most of the SOM (Fig. 3.3A). The Seismic Data Library System (SDLS) provides an open database including profiles carried out by the Italian National Institute of Oceanography (OGS, 1989 and 1991), the Russian Polar Marine Geosurvey Expedition (PMGE, 1994), the British Antarctic Survey (BAS, 1985) and the Antarctic Spanish program (SCAN, 2001 and 2004). SDLS profiles were complemented by recently obtained MCS data collected by the Antarctic Spanish Program during the POWELL2020 cruise. The penetration of the MCS ranges from 4 to 8 seconds in TWTT (two-way travel time), allowing to image the acoustic basement in most cases.

The global GEMMA earth crustal model (Reguzzoni and Sampietro, 2015) offers a first approximation to the Moho depth in the area (Fig. 3.5C). This model is calculated from GOCE satellite gravity data that provides a global estimation of the mean Moho depth with a resolution of 0.5°. The GEMMA model shows a maximum Moho depth of 32.5 km under the central south area of the SOM and thins towards the edges of the SOM, reaching depths between 20 and 25 km. Below the oceanic crust of the Powell, Jane, Protector and Dove basins, the Moho is modeled at depths between 11 and 15 km. GEMMA model describes a significantly deeper Moho than modeled in previously published work (King and Barker, 1988; Kavoun and Vinnikovskaya, 1994; Busetti et al., 2001).

The gravity anomaly data (Fig. 3.3C) used for modeling were compiled from the global marine gravity database from Sandwell et al. (2014), and represents a free-air gravity dataset with 1-minute grid resolution. This global marine gravity model achieves twice the accuracy of previous models by enhancing existing data with new radar altimeter measurements from the CryoSat-2 and Jason-1 satellites (Smith and Sandwell, 1997; Sandwell et al., 2014). Gravity free-air anomaly values range from -230 to +240 mGal. A continuous east-west band of negative anomalies at the north of the SOM, from -80 to -230 mGal, coincides with the Orkney Trench. The highest positive anomaly values ranging from 150 to 240 mGal, are found in the north of the SOM, where the South Orkney Islands are located. In

the inner part of the SOM, free-air anomaly values ranging between 15 and 50 mGal,  $\sim$  40 mGal below the adjacent areas, can be highlighted (Fig. 3.3C) related to the sedimentary basins (King and Barker, 1988; Busetti et al., 2000). In addition, we calculated the complete Bouguer gravity anomaly (Fig. 3.3D) form the free-air gravity dataset. For Bouguer plate correction we used a Bouguer density of 1.64 (2.67gr/cm3 as the mean crustal density and 1.03 g/cm3 as water density). For terrain correction we used the bathymetry of Dickens et al. (2013) for local correction, which improves the resolution to 300 m on the continental shelf, and GEBCO for regional correction. The complete Bouguer gravity data allow to distinguish more clearly the position of the sedimentary basins and the boundary between the continental crust of the SOM and the adjacent oceanic crust.

Magnetic data were extracted from the World Digital Magnetic Anomaly Map (WDMAM) (Fig. 3.3B), a global near-surface magnetic data compilation grid with a cell size resolution of 5 km (Lesur et al., 2016). The WDMAM database is composed of marine and terrestrial data. The data used in this work are mainly marine and therefore referenced to sea level. A band of positive magnetic anomalies is observed in the SSW-NNE direction over the SOM, reaching +700 nT in the center of the SOM. This band depicts continuously over most of the microcontinent, showing a discontinuity over the Bouguer sedimentary basin, where a relative minimum is observed.

# 3.3.2. Modeling

The building of a robust 3D geologic model of the SOM based only on the available data is not feasible due to their scarcity. Therefore, we choose three main geological boundaries as initial constraints to reduce the multiplicity of the modeling results: 1) the acoustic basement depth, 2) the PMA source boundary, and 3) the Moho. The estimation of these boundaries deduced from geophysical data, together with the bathymetry, have been used as constraints for 2D geological models, which in turn are the basis for the construction of the 3D model. The 3D geological model of the SOM has been improved and validated by forward modeling and joint inversion of potential fields.

# 3.3.2.1. Identification of the main geological boundaries as initial constraints

As a first approach to the boundary between the sedimentary infill and the continental basement of the SOM, we mapped the acoustic basement from MCS profiles. The acoustic basement was manually identified and picked in the KINGDOM Suite software along each MCS profile (Fig. 3.3A). The resulting depth grid (Fig. 3.5A) is achieved through a double time-to-depth conversion, assigning velocities of 1460 m/s and 2200 m/s (King et al., 1997) to the water and sediment layers, respectively.

The analytic signal (AS) has proven to be an effective tool for locating geological boundaries of the magnetic source bodies (Dentith & Mudge, 2014; Doo et al., 2009). The AS is defined as the square root of the sum of squares of the data derivatives in the x, y, and z directions (Roest et al., 1992; Roest & Pilkington, 1993). In this study, we calculate the AS from the WDMAM magnetic anomaly data using the GRIDASIG GX module of the Oasis Montaj software in order to locate the edges of the PMA source (Fig. 3.5B).

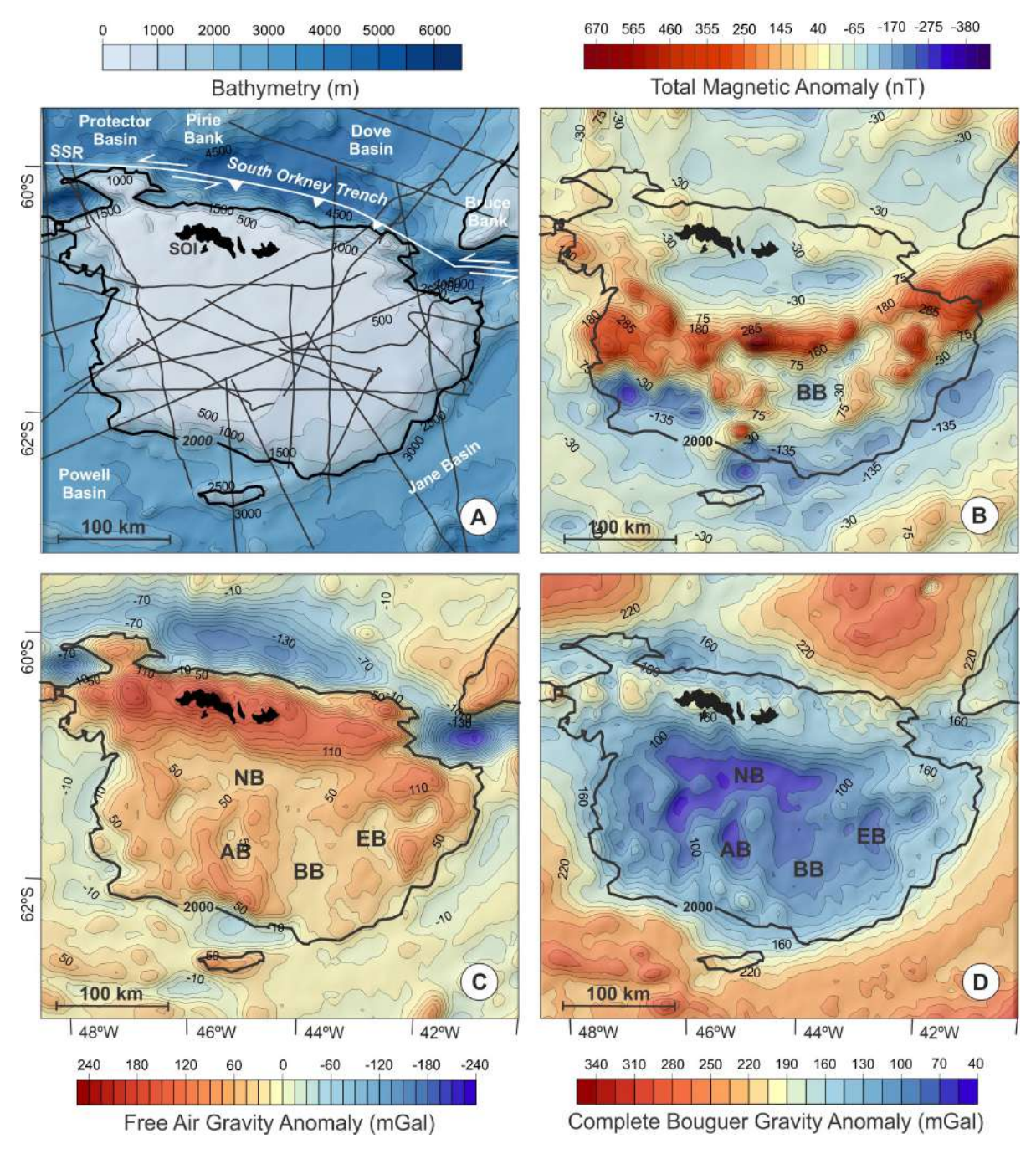


**Figure 3.3**. Initial dataset used: A) GEBCO bathymetry (GEBCO Compilation Group, 2020) with SDLS and POWELL2020 MCS profiles. B) WDMAM total magnetic anomaly map with contour lines every 50 nT (Lesur et al., 2016). C) Free-air gravity anomaly map with contour lines every 15 mGal (Sandwell et al., 2014). D) Calculated complete Bouguer gravity anomaly map with contour lines every 15 mGal. The 2000 m isobath is highlighted as a visual reference.

The global GEMMA model (Reguzzoni & Sampietro, 2015) is a useful first reference model for crustal thickness variation (Fig. 3.5C). However, the Moho depth below the SOM extracted from this model seems to be overestimated compared to the results previously described in the literature (King & Barker, 1988; Kavoun & Vinnikovskaya, 1994; Trouw et al., 1997). As a second approach, we have calculated the depth of the Moho below the SOM under isostatic equilibrium conditions (Fig. 3.5D).

We assess the theoretical isostatic root using the AIRYROOT GX module of Oasis Montaj based on the USGS algorithm by Simpson et al. (1983). This program calculates a Moho depth -the root- using the bathymetric grid, a crust-mantle density contrast and a compensation depth. We use the density contrast calculated from the difference between estimated densities of the mantle (3.3 g/cm3) and the crust (2.67 g/cm3): 0.63 g/cm3. The compensation depth has been assumed at 27 km, as the thickness of the continental crust has been described in previous works to be no more than 26 km (see section 2). For our study, we consider only the results in areas below the SOM since the values used for its calculation were based on continental crust (Fig. 3.5D).

#### 3.3.2.2. 2D geophysical modeling

The GM-SYS software (Gemperle et al., 1991), implemented in the Geosoft Oasis Montaj software, allows the building of 23/-D models. The modeling takes into account the influence of adjacent bodies orthogonal to the profile for a defined extent (Northwest Geophysical Associates, 2004). For ease of reading, we refer to the models simply as 2D. We carried out 2D models of potential field data in order to locate the geological units of the SOM in depth. The main challenge in potential field modelling is that multiple sources with varying geometry and properties can fit the observed anomalies equally well. Due to the high reliability of the MCS data, 2D gravity models were fitted along fifteen selected nearly rectilinear seismic profiles (blue lines in Fig. 3.4A). To avoid edge effects, the profiles were extended to the limits of the selected study area. During 2D modeling, bathymetry was imported as a fixed surface. The calculated depth of the acoustic basement was considered a reliable surface in the areas with good quality of the MCS profiles (i.e. the Bouguer and Eötvös basins mainly) (dotted line in Fig. 3.5E). In the remaining modeled area, the acoustic basement was considered as a tentative input data. The Moho depth -isostatic and GEMMA- and the extent of the magnetic bodies were considered as guiding initial data. Once the gravity anomaly has been fitted along all selected seismic profiles, the gravity and magnetic anomalies are simultaneously fitted along five profiles (red lines in Fig. 3.4A) perpendicular to the dipole (Fig. 3.3B). In the case of magnetic anomalies, we only assign a magnetic susceptibility value to the batholith in order to adjust the low frequency anomalies. This allows to improve the geometry of the intrusive igneous rock body that cause the PMA. The aim of the modeling along the 2D profiles was to provide simple input surfaces for the 3D model, which resulted in a poorer fit of the anomalies.

# 3.3.2.3. 3D geological model. Geophysical forward modeling and joint-inversion

To define the geological structure of the SOM, we transfer the geological contacts from the 2D models to the corresponding vertical sections in Geomodeller software (Intrepid Geophysics) (Fig. 3.4B). The 3D model extent is 440 km in the E-W direction, 410 km in the N-S direction and 40 km deep. Geomodeller builds the model using the principles of potential-field interpolation method (Lajaunie et al., 1997; Calcagno et al., 2008). Due to the irregular distribution of the 2D models (see Fig. 3.4A), the first 3D model portrayed many inconsistencies. To solve this, we created an additional grid composed of evenly spaced N-S and E-W vertical sections (Fig. 3.4B), where the structures were

projected to ease the modification of the interfaces of the lithological units. The interpolation of all imported data constitutes our initial 3D geological model, the 'a priori' 3D model (Fig. 3.4B).

Geophysical forward modeling and inversion were implemented to refine the 'a priori' 3D model. Forward modeling computes the gravity and magnetic response taking into account uniform petrophysical properties values. Joint inversion discretizes the geological model into a 3D matrix of voxels. In this study, voxels have an extension of 10 km in xy directions. In the z-direction, the software allows to define a voxel geometry in which the cell size can vary with depth. The cell size in z-direction has a fixed value above a certain boundary. Below this boundary, the cell size increase by a defined factor. In this case, we set a cell size of 200 m from the sea level to 20 km depth. Below 20 km depth, this value starts to increase by a factor of 1.3 ending in a last cell with a size in z-direction of 4.65 km. For each voxel, the software can modify the petrophysical properties (i.e. density and magnetic susceptibility) and/or lithological boundaries according to defined probability functions. In addition, the user can set the degree of freedom allowed to the software (very tight, moderate or loose) for each boundary between lithological units (Calcagno et al., 2008). Inversions that we carried out ran for two million iterations. Throughout the modeling process, the bathymetry was established as a fixed surface. The acoustic basement was also considered fixed in those areas where it could be defined with confidence (i.e. Bouguer and Eötvos basins).

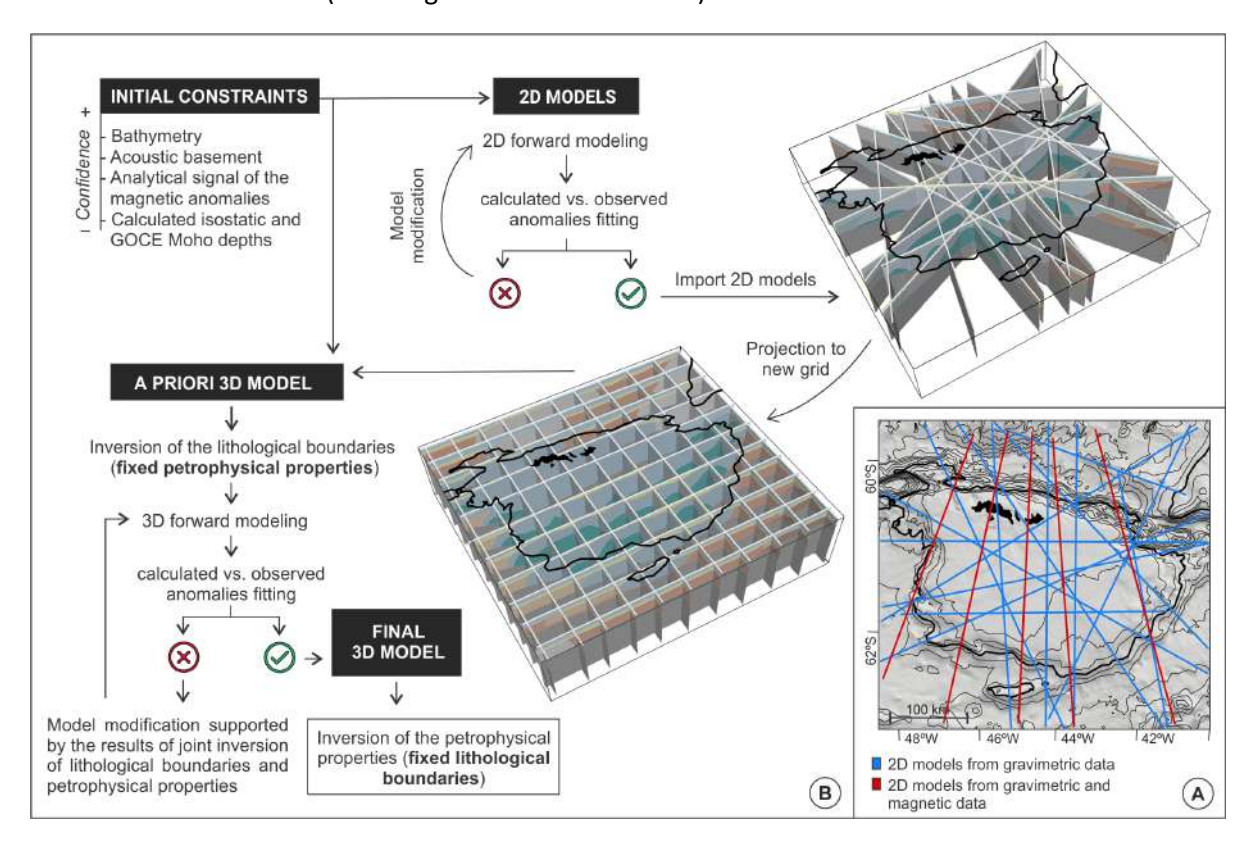


**Figure 3.4**. A) Location of 2D models. In blue, the position of the gravity anomaly models, which correspond to the location of the dense network of MCS profiles extended to the limits of the modeling area. In red, the position of the profiles where simultaneous gravity and magnetic anomaly modeling has been performed. B) Summary of the workflow followed for the modeling. Initial constraints were considered during 2D and 3D modeling.

In a first stage, the goal was to obtain a geologically robust model that conforms to the regional geodynamic framework, especially in the areas not covered by the 2D models. For this purpose, we performed a joint inversion with fixed petrophysical properties and moderate degree of freedom allowed for lithological boundaries to improve the geometry of the model "a priori". (Fig. 3.4B). The geologically consistent proposed changes that improved the adjustment were accepted. To refine the geometry of the model in detail, forward modeling was best suited. In areas where differences between computed and observed data were localized, the lithological boundaries were modified by trial-and-error to improve the fit. This process was complemented with several joint inversions of the lithological boundaries and petrophysical properties simultaneously and with equal weighting of probability functions for both. The inversion returns changes in lithological boundaries and the most likely distribution of petrophysical properties. The final geometry was reached when the applied changes no longer significantly improved the forward modeling result. At this point, the final model represents the geological structures realistically and does not present inconsistencies. The last stage consists of an inversion of the petrophysical properties with fixed geometry of the different lithological units (Fig. 3.4B). After the last stage of the inversion process (Fig. 3.4B), a more realistic configuration of the density variability and magnetic susceptibility is achieved (Fig. 3.6F and 3.7F). The RMS error of the misfits between the observed and calculated anomaly is substantially improved compared to forward modeling (see section 3.4.2).

#### 3.4. Results

The results obtained during the modeling include: the geological boundaries used as constraints (see section 3.2.1), the fit achieved in the 2D and 3D models and the geometry of the final 3D geological model. In this section we have highlighted the three main surfaces that will be discussed below.

# 3.4.1. Initial surfaces and 2D models

The acoustic basement depth, calculated from seismic data, ranges from 382 mbsl at the northern SOM to 9000 mbsl in the Orkney trench and provides a first approximation to the location and geometry of the sedimentary basins (Fig. 3.5A). The reliability of the grid is limited to areas with good MCS data coverage (Fig. 3.3A). For example, the greatest acoustic basement depths within the continental shelf coincide with well surveyed position of the Bouguer (4200 mbsl) and Eötvös (3500 mbsl) basins. Instead, the less surveyed area of the Airy Basin images a small depocenter surrounded by basement highs. To the west, another small depocenter is observed. The Newton basin is not recognized due to the poor quality of seismic profiles in this area.

The AS amplitude calculated from magnetic anomalies ranges from 0 to 0.2 nT/m (Fig. 3.5B). Higher AS amplitude corresponds to bodies closer to the surface whereas lower amplitude might correspond to bodies placed either at greater depth or to the absence of magnetic bodies (Hsu et al., 1998). The highest AS amplitude is located in the center of the SOM. We consider AS amplitudes > 0.01 nT/m to frame the source of the magnetic anomalies. This area has been delimited as the most likely location of the PMA source (Fig. 3.5B). According to the results, the intrusive igneous rock body

causing the PMA (also called batholith this work) would be sited in the southern half of the microcontinent, extending to Bruce Bank.

The depth of the Moho calculated under isostatic equilibrium (Fig. 3.5D) shows a crustal thickness that reaches 27 km below the islands. The crust thins towards the SE, where the bathymetry deepens, resulting in a Moho depth of 24 km below the Eötvös and Bouguer basins. This result contrasts with the global GEMMA earth crustal model (Reguzzoni and Sampietro, 2015) (Fig. 3.5C), where the maximum depth of the Moho of 31.5km was located in the central area of the SOM and decreases toward the edges.

These three initial constraints provide the basis for the 2D modeling. Figure 5E shows one of the five 2D models realized fitted to the gravity and magnetic anomalies. The RMS error between the observed and calculated magnetic anomaly is 46 nT, within a range of the observed magnetic anomaly between -176 nT and 370 nT. For the gravity anomalies, the RMS error along this profile is of 15 mGal, and the minimum and maximum observed gravity anomalies are -140 mGal and 139 mGal, respectively. RMS errors present similar values for all the 2D models carried out.

# 3.4.2. Gravity and magnetic response of the final 3D geological model

The final 3D geological model produces a gravity and magnetic response in forward modeling (Fig. 3.6B and 3.7B) taking into account homogeneous petrophysical properties for each lithological unit (Table 1). During the inversion process, these fixed values are allowed to vary in a controlled range (Table 1). The fixed values used for the forward modelling and the ranges of variation used in the inversion modelling are chosen after the empirical values in Telford (1990) and values previously used in models near the study area (Busetti et al., 2001; Bohoyo, 2004; Galindo-Zaldívar et al., 2006). The inversion of these petrophysical properties produced an improved gravity and magnetic response (Fig. 3.6C and 3.7C).

The free-air gravity computed anomaly in the final forward modeling ranges from -185 mGal to 161 mGal while the observed anomaly data ranges between -219 mGal to 220 mGal. The misfits range between ±75 mGal. The forward model is able to describe the main features of the free-air anomalies, but the RMS error is still relatively large with 23.3 mGal. Larger differences can be observed at the northern boundary of the model, the Jane Bank, the contact between the SOM and Bruce Bank, and around the South Orkney Islands (Fig. 3.6E). During modeling, the misfit values around the South Orkney Islands were expected to be high because the altimeter-derived gravity close to them is unreliable and over them it is absent. Within the SOM, the misfits were up to +50 mGal, being the southwest and the northeast border of the SOM the most conflictive areas. After the last stage of the inversion process, the variability applied to the density values resulted in a considerable improvement of the free-air gravity anomalies. At this point, the computed anomaly ranges between -189 mGal and 164 mGal and the misfit values range between -53 mGal and 60 mGal. The RMS error reduced to 15.8 mGal. It is noteworthy that the largest misfits in the forward were scattered over all the modeled area.

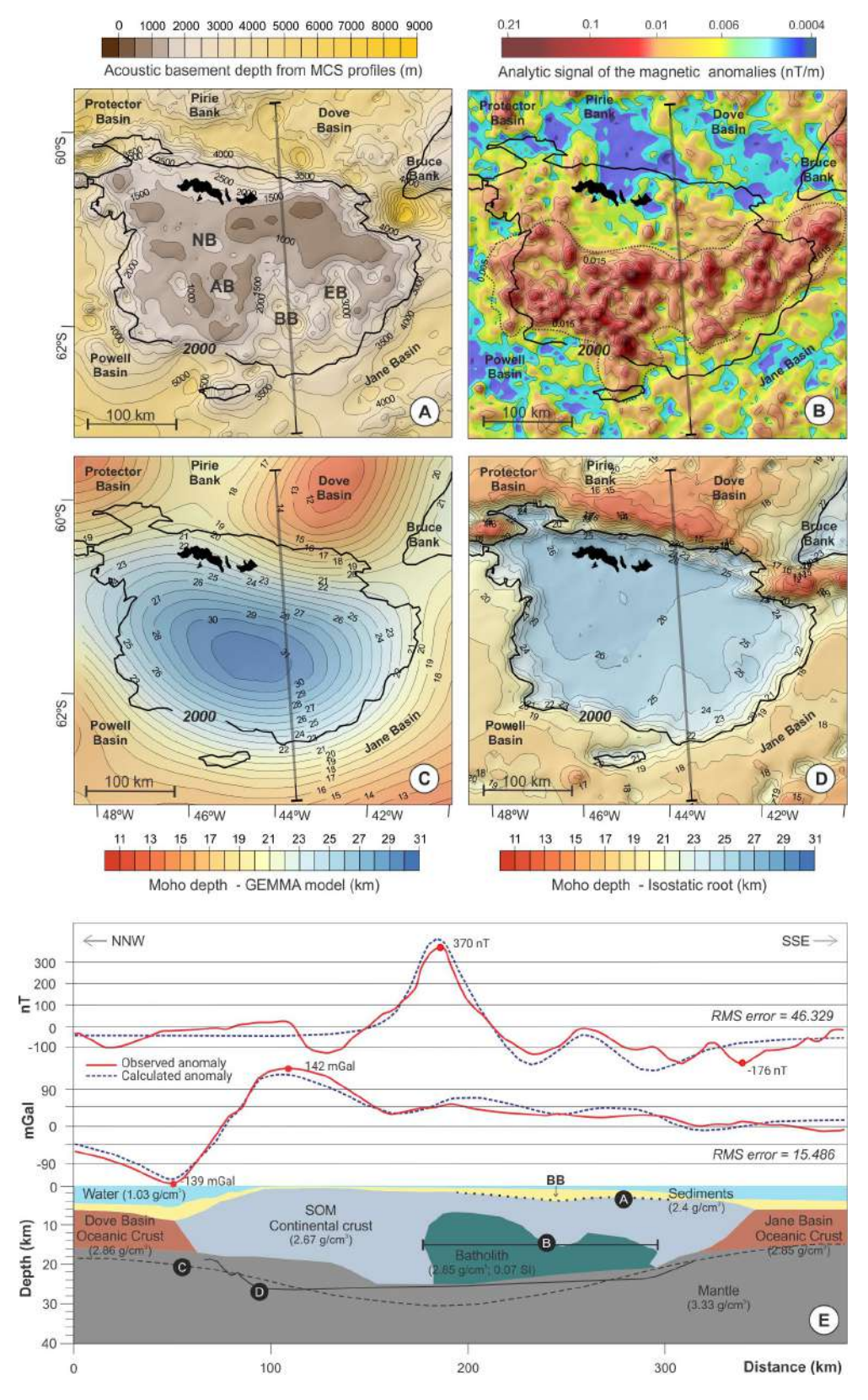


**Figure 3.5.** A) Acoustic basement depth derived from MCS profiles with contour lines every 500m. The sedimentary basins are named by their acronyms: AB: Airy Basin; BB: Bouguer Basin; EB: Eötvös Basin. B) Analytic signal of the total magnetic anomaly with contour lines every 0.005 nT/m. The most probable zone for the presence of the batholith is outlined in dotted line. C) Depth of the Moho from the GEMMA global model (Reguzzoni and Sampietro, 2015). Contour line every kilometer. D)

#### **CHAPTER 3**

Calculated Moho depth assuming an isostatic equilibrium. Contour line every kilometer. E) Gravity and magnetic adjustment of a N-S oriented 2D model. The location of the profile is shown in Fig. 3.5 A-D. The acoustic basement, the extent of the PMA source and the GEMMA and Isostatic Moho are projected over the profile and labeled A-D. BB: Bouguer Basin.

	Forward		Inversion	
Lithological unit	Density (g/cm³)	Magnetic Susceptibility (SI)	Density variation (g/cm³)	Magnetic susceptibility variation (SI)
Water	1.03	-	1.03	-
Sediments	2.4	-	2.4 ± 0.1	-
Oceanic Crust (Dove, Protector, Jane, Powell basins)	2.85	0.03	2.85 ± 0.075	0.03 ± 0.007
Continental Crust (Pirie Bank, Bruce Bank, SOM)	2.7	0.007	2.7 ± 0.04	0.007 ± 0.004
Oceanic Crust (Weddell Sea)	2.9	0.03	2.9 ± 0.075	0.03 ± 0.007
Jane Bank	2.83	0.05	2.8 ± 0.07	0.05 ± 0.015
Thinned And Intruded Continental Crust (Powell Basin)	2.8	0.03	2.8 ± 0.02	0.03 ± 0.02
Intrusive body	2.88	0.07	2.88 ± 0.07	0.07 ± 0.05
Mantle	3.33	0	3.33 ± 0.035	0

**Table 3.1**. Petrophysical properties of the lithological units used for the 3D forward and inversion modeling.

After inversion, the greatest misfits are at the edges of the model, outside the SOM (Fig. 3.6F). Figure 3.6D shows two histograms representing the distribution of misfits for forward and inversion modeling. The bars correspond to 10 mGal intervals with the same range and colors as the misfit color scale. The percentage of voxels with a misfit between 5 and -5 mGal improve from 14.5% to 37% after inversion (Fig. 3.6D). This, together with the improvement of RMS errors provide good reliability in the model when discussing the results.

For the magnetic anomalies, we could not achieve a desirable adjustment. The forward response of the final 3D model ranges from -220 nT to 514 nT (Fig. 3.7B) while the observed anomaly data ranges from -286 nT to 647 nT (Fig. 3.7A), with an RMS error of 91.8 nT. After the last stage of the inversion process, the RMS reduces to 77 nT, which is still far from acceptable. In this case, moreover, the distribution of the misfits did not significantly improve after the inversion (Fig. 3.7D). With a voxel dimension of 10 km in the xy direction, the high frequencies of magnetic anomalies were difficult to fit. Although the RMS error values were very high, the morphology of the computed

anomalies and the position of the maximum values show a good match with the observed anomalies (Fig. 3.7A, B and C).

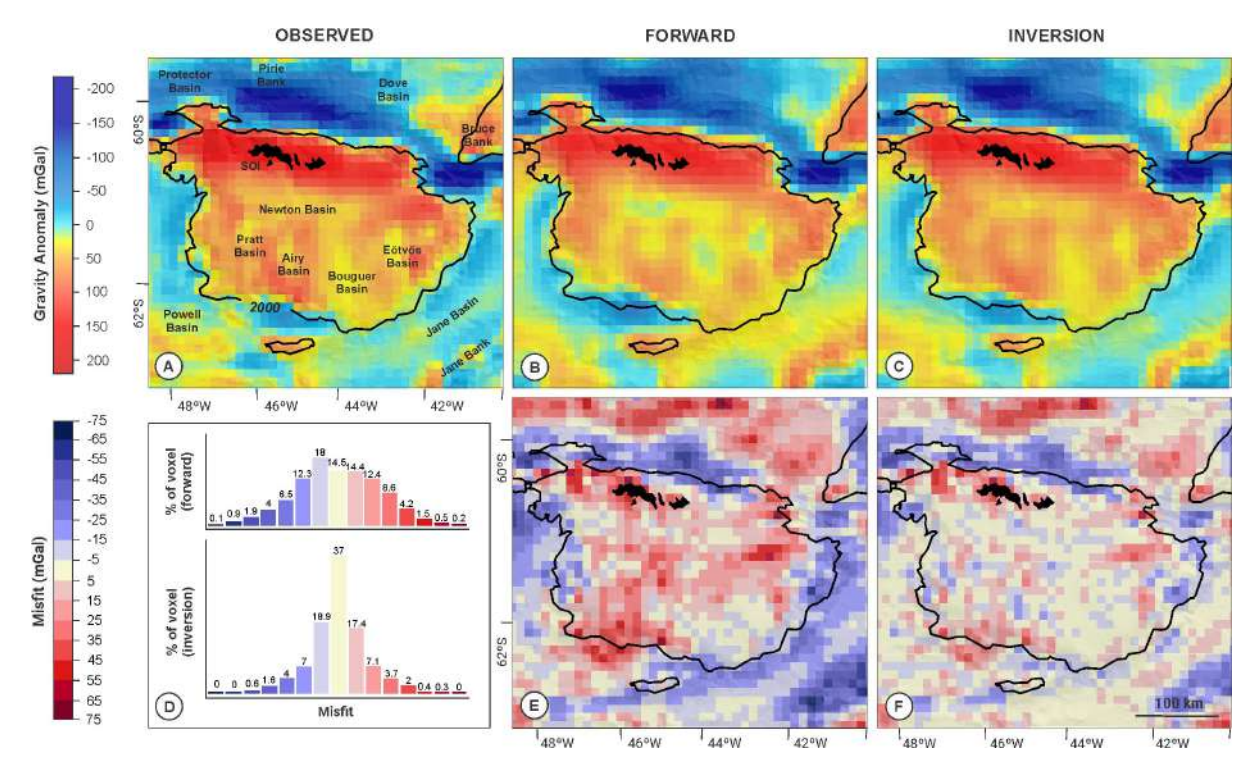


**Figure 3.6**. A) Observed free-air gravity anomalies. Anomaly ranges may vary slightly from the original satellite data due to the gridding simplification. B) Forward calculated gravity response of the final 3D model. C) Gravity response of the final 3D model with inverted density values. D) Histogram of misfit distribution in Fig. 3.6E (above) and Fig. 3.6F (below). E) Misfit between forward gravity response and observed anomalies. F) Misfit between inverted and observed gravity anomalies.

# 3.4.3 Sedimentary basins of the South Orkney Microcontinent

The final geometry of the 3D model enables the analysis of the complete sedimentary cover of the SOM. These results are more reliable within the continental area of the SOM, associated in this work to the 2000 m isobath (Fig. 3.8A). To the north, the Newton Basin extends in an E-W direction for about 150 km and is 20 km wide. The depocenter is located at its western end and it is filled with a 3.5 km thick sediment cover. The morphology of the northern and southern boundaries of the Newton basin results in a boudinage shaped basin (Fig. 3.8A). In the southern area, the Airy, Bouguer and Eötvös basins have a N-S orientation (Fig. 3.8A). According to the modeling results, the Airy Basin is framed by basement highs and has an ellipsoidal shape of 17 x 30 km, with a central depocenter accumulating 2.1 km of sediments. To the west of the Airy Basin, another elongated N-S basin is distinguished. Since it is sufficiently large, we tentatively name it Pratt Basin in this work (Fig. 3.8A). Pratt Basin is about 70 km long and 25 km wide with a maximum sediment thickness of 2.4 km in the northern area. Eötvös and Bouguer basins are located in the southeastern part of the SOM where the bathymetry is deeper. Both basins are separated by a relative basement high and widen southeast. Sedimentary thickness in the Bouguer Basin reaches 2.9 km. Eötvös Basin has a thickness of 2.8 km in

its deepest area. To the east of this basin, there is another depocenter, which is 2.1 km thick. The ODP Site 696 was drilled in the southern edge of the Eötvös Basin (Fig. 3.2) where, according to the model, the basin accumulates 1.6 km of sediments.

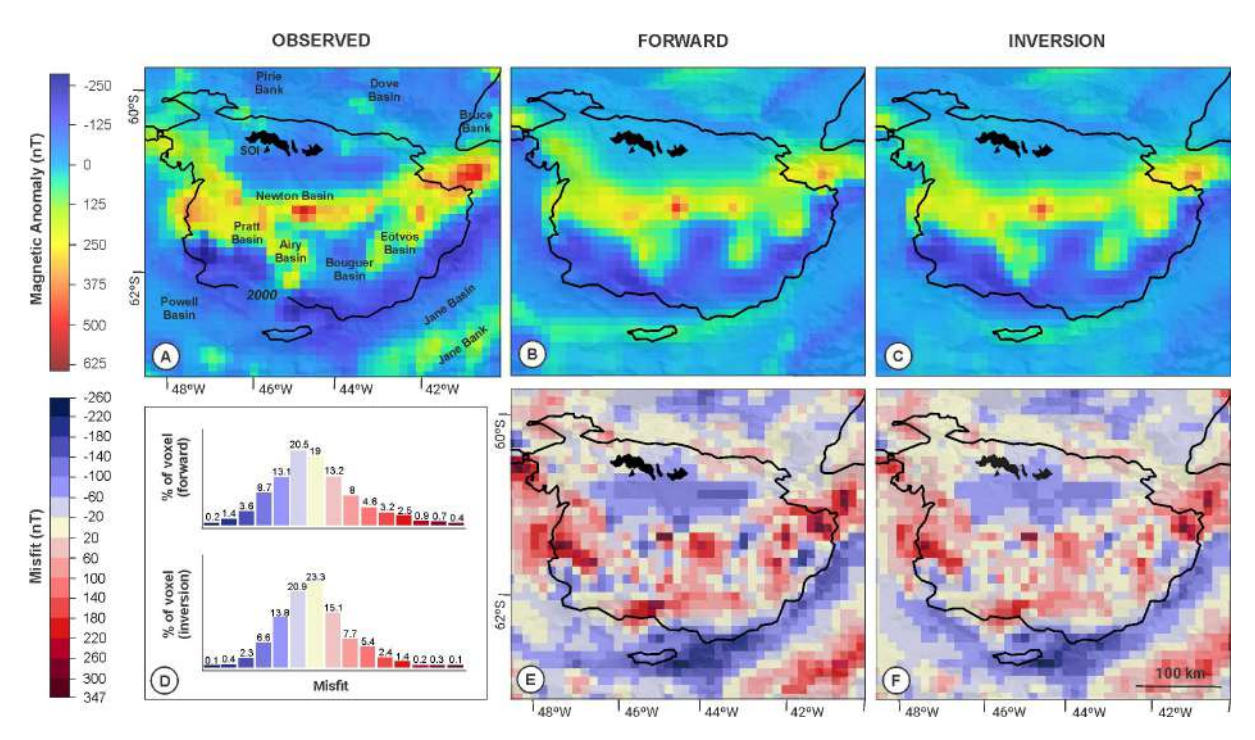


**Figure 3.7**. A) Observed WDMAM magnetic anomalies. B) Forward calculated magnetic anomalies of the final 3D model. C) Calculated magnetic anomalies of the final 3D model with inverted magnetic susceptibilities. D) Histogram of the misfit distribution in Fig. 3.7E (above) and Fig. 3.7F (below). E) Misfit between forward magnetic and observed anomalies. F) Misfit between inverted and observed magnetic anomalies.

# 3.4.4. Characterization of the intrusive igneous rock body causing the PMA

The modeled body of intrusive igneous rock causing the PMA, also called batholith in this work, is located in the southern area of the SOM and present variable thickness (Fig. 3.8B). The maximum thicknesses are found in the central SOM, matching the area of basement highs surrounding the Airy Basin. In this area, the body portrays thickness between 15 and 20 km, where the magnetic maximum is also located. It is an elongated magnetic province about 130 km wide that extends throughout the southern part of the SOM and continues eastwards out of the modeling area. The body ends at the edge of the Powell Basin. The interruption of the batholith coinciding with the position of the Bouguer and Eötvös basins is noteworthy.

#### 3.4.5. Moho depth

Although we considered two different models of Moho depth (the global GEMMA model and the calculated isostatic Moho depth) as a starting point, the result of the 3D modeling (Fig. 3.8C) shows that both were overestimated. The result of the Moho depth derived from the 3D model below the oceanic crust of Protector, Dove, Powell and Jane basins ranges from 10 to 13 km. This depth increases

to 18 km under the Pirie and Bruce Bank continental blocks. Under the continental area of the SOM, three zones can be distinguished: (1) the northern sector, where the Moho depth ranges between 15 and 20 km; (2) the south-western sector, where the greatest crustal thickness places the Moho at 26.5 km; and (3) the south-eastern sector, characterized by the shallowing of the Moho to 17.5 km depth, coinciding with the modeled interruption of the batholith.

McKenzie (1978) first introduced the stretching factor  $\beta$  to describe the formation of intracontinental rift basins by rapid stretching of the lithosphere. The stretching factor  $\beta$  has also been used to define the extension occurring in the whole crust (Zhang et al., 2008; Chen, 2014). The stretching factor  $\beta$  can be calculated through formula  $\beta$  =ct<sub>0</sub>/ct<sub>now</sub>, of which, ct<sub>0</sub> is the original thickness of the crust, and ct<sub>now</sub> is the thickness of present crust (Alvey et al., 2008). A thinned crust presents higher values of stretching factor  $\beta$ . To produce a sedimentary basin filled with 4.5 km of sediments requires a stretching factor  $\beta$  of about 2 (McKenzie, 1978). We have calculated an estimation of the stretching factor  $\beta$  from the model results. To do this, we need to assume the original thickness of the crust. Garret (1990) performed two-dimensional models of the crustal structure of the Antarctic Peninsula that described a crustal thickness of about 30 km. If we take this value as the assumed original thickness of the SOM crust,  $\beta$  would have a value of 1.13 for the south-western sector of the SOM, and a value of 1.71 for the south-eastern sector.

#### 3.5. Discussion

The results derived from the 3D model provides improved insight into the geological structure and evolution of the South Orkney microcontinent which have tectonic implications for the early stages of the Scotia Arc development.

# 3.5.1. 3D geophysical and geological modeling as a suitable method to characterize and to understand deep structures

The 3D geological model of the SOM was built by combining acquired geophysical data and calculated data of its deep structure with gravity and magnetic data. The approximation in depth of the different geological contacts prior to modeling has allowed the results to be geologically consistent. After the joint inversion of the petrophysical properties of the final 3D geological model, there were differences between the fit achieved in the gravity and the magnetic anomalies. In the case of the gravity anomalies, the RMS error achieved is 15.8 mGal. Given the complexity of the area and the relative simplicity of the model in terms of lithological units involved, we consider that the final geometry and the distribution of density values represent the SOM structure in a realistic way. In contrast, the fit to the magnetic anomalies is not satisfactory, presenting a RMS error of 77 nT. However, the approximation to the shape of the magnetic anomalies was quite accurate (Fig. 3.7C). In fact, we believe that it was decisive to take into account the AS of the magnetic anomalies as a guide during the modeling process. This permitted to delineate the PMA source. If the magnetic component had not been taken into account, the gravity anomalies could have been misinterpreted, as the batholith is dense and very bulky. The final range of densities attributed to the batholith is

within the range of densities of gabbros (2.70 - 3.11 g/cm3 in Telford, 1990), which is the composition previously described in the literature (Garrett et al. 1986/87).

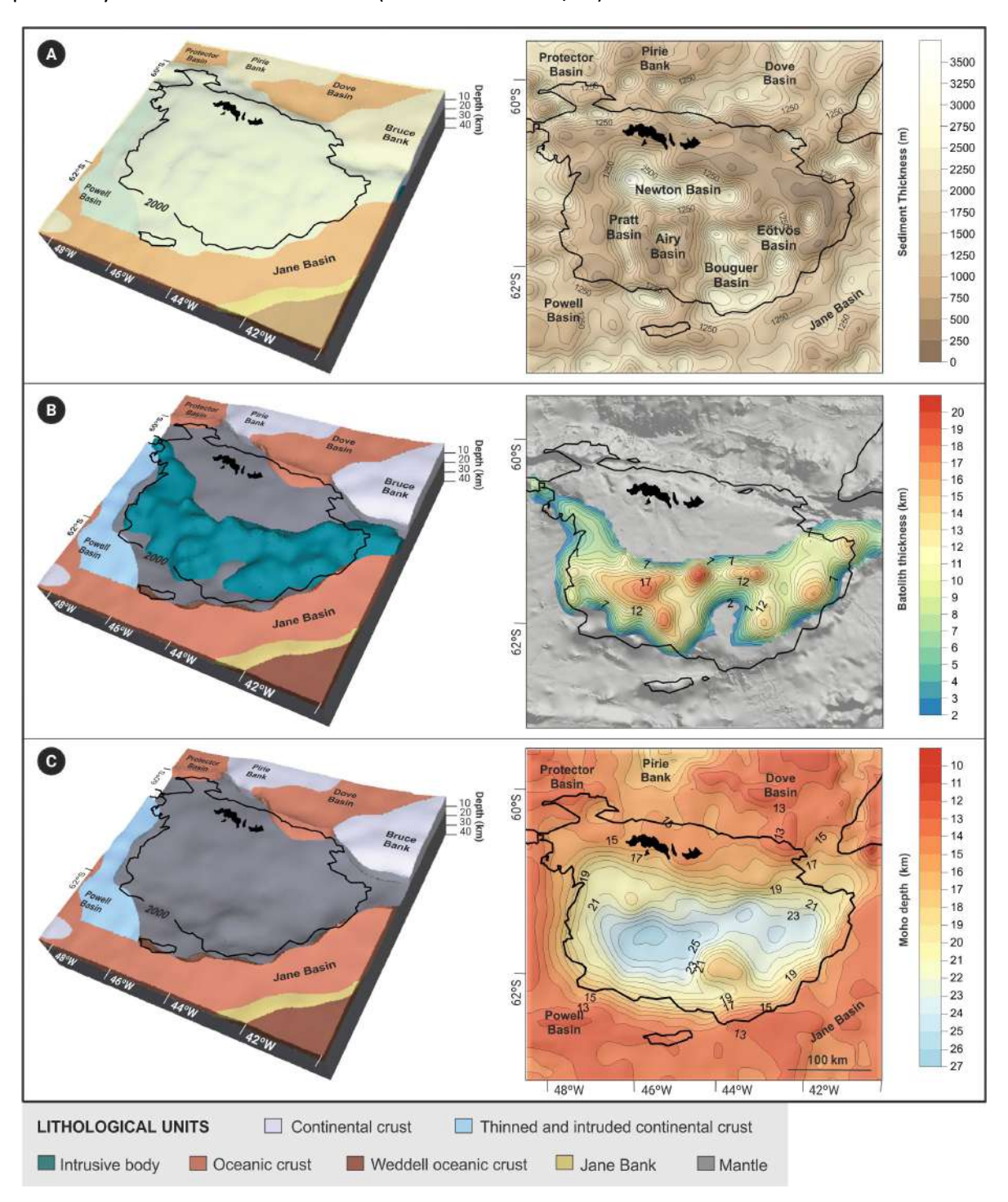


**Figure 3.8**. Main results derived from the 3D modeling. For better visualization, 3D volumes and contour maps are shown for each unit of interest: A) Sedimentary cover thickness. The volume of the 3D sedimentary cover is shown with transparency. Contour lines every 250m. The 1500m isopach is highlighted. B) Batholitic complex. Contour lines every kilometer. C) Moho depth. Contour lines every kilometer. The vertical exaggeration of the 3D model is 2.

The modeling carried out in this study proved to be very effective for the characterization of the sedimentary cover. Most of the SOM sedimentary basins were previously located by King and Barker (1988) and roughly described by Busetti et al. (2000). In the present study, by combining the analysis of the available seismic profiles with the gravity modeling, the position and geometry of the basins has been determined more precisely and the total sediment fill thickness has been estimated for the first time. The Eötvös, Bouguer and Airy basins are easily identifiable from seismic data and their depths can be mostly estimated directly. To the west of the Airy Basin, another elongated N-S basin, here named Pratt Basin, is noteworthy. This basin was not identified in the previous description of the SOM sedimentary infill of King and Barker (1988) due to lack of gravity data coverage in this area. However, they analyzed a seismic profile in the surroundings of this basin (profile "E" in King and Barker, 1988) and described the presence of normal faults and sedimentary fill. Busetti et al. (2000) mapped the basin depocenter (Fig. 3.2) but its shape could not be delimited. Similarly, a small basin to the east of the Eötvös Basin was included as part of the Eötvös Basin in the work of King and Barker (1988), but our results show that it is another disconnected basin (Fig. 3.8A). On the other hand, the sparse coverage of the Newton Basin with seismic profiles leads to an underestimation of the sediment thickness. In fact, gravity anomalies reveal that Newton Basin might be deeper than initially observed. Based on the model, sediment thickness in the Newton Basin is up to 3.5 km, which is closer to the more than 4 km described by Harrington et al. (1972) by means of the seismic refraction profile performed west of the South Orkney islands.

# 3.5.2. Structural heterogeneity of the South Orkney Microcontinent

The crustal thickness heterogeneity of the SOM is consistent with a complex tectonic evolution. According to the results derived from the model, we can distinguish three zones (Fig. 3.9A). The northern third of the SOM, zone 1 in Fig. 3.9A, clearly shows a crustal thinning. The difference in Moho depth between the model results (Fig. 3.8C) and the theoretical calculation under isostatic equilibrium conditions (Fig. 3.5D) in this area is up to 10 km. However, this difference is much smaller in the southern SOM. This is consistent with the conclusion reached by King and Barker (1988) that the continental block of the SOM is mostly in isostatic equilibrium except for the northern part. The most likely reason, given the position of the northern margin, is an uplift of the northern sector of the SOM, related to the active strike-slip movement with compressive character along this South Scotia Ridge segment (Bohoyo et al., 2007).

Early Cretaceous intrusive igneous rock bodies produced major crustal growth on the western Antarctic Peninsula and they are an important component of the continental crust in the area (Vaughan et al., 1998). Likewise, in the southern half of the SOM, the crust is thickened by the presence of the batholith (Fig. 3.9). King and Barker (1988) in the description of the tectonic fabric of the southern portion of the SOM, identified two extensional systems separated by a central horst representing the only portion not affected by stretching. Based on our results, however, we distinguished two zones in the southern area of the SOM (Fig. 3.9A). The zone 2 (Fig. 3.9A), to the west, concentrates the greatest crustal thickness, which may therefore have been less affected by

#### **CHAPTER 3**

extensional processes. In zone 3 (Fig. 3.9A), to the east, the absence of the batholith coincides with an extreme crustal thinning that must be the result of further extension of this zone (Fig. 3.9A). This extension is also recorded by the bathymetry since the southeastern part of the SOM is where the deepest water depth is located (Dickens et al., 2014). Thus, we conclude that the whole south sector is affected by extensional tectonism, with increasing intensity towards the east.

The differentiation between zone 2 and zone 3 (Fig. 3.9A) is also reflected in the position of the sedimentary basins and its relation with the thickness variation of the batholith. The discontinuity observed in the batholith match the location of the most important sedimentary basins, the Bouguer and Eötvös basins (Fig. 3.9B). The opening of the narrower Airy and Pratt basins also coincides with regions of an evident thinning of the batholith (Fig. 3.9B). In addition, the horsts surrounding the Airy basin are located where the batholith is thickest (Fig. 3.9B). Therefore, we interpret that the batholith has thinned as a result of the opening of the N-S elongated basins that even produced its fracturing under the Bouguer and Eötvos basins. Moreover, the E-W extension affecting the SOM and leading to the opening of the N-S elongated sedimentary basins (Pratt, Airy, Bouguer and Eötvös) seems to have been greater in zone 3. The estimated values for the stretching factor can be related to the thicknesses of the sedimentary basins in these areas. Zone 3, with the greatest stretching factor  $\beta$  of 1.71 corresponds to the Bouguer and Eötvös basins that accumulate up to 2800 m of sediments. Zone two, with an estimated stretching factor  $\beta$  value of 1.13, has a sedimentary thickness of up to 2400 m in the Pratt basin. This configuration could be associated with an extensional process that began east of the SOM and migrated westward later.

The E-W extensional regime must have affected the entire SOM in a similar way. However, it is noteworthy that no features associated with this extension are well observed in the northern area. One possibility is that the Newton Basin was originally smaller than present and the E-W extension enlarged its geometry, creating the boudinage pattern that is shown by the 1500 m sediment isopach (Fig. 3.8A). Otherwise, the two domains (north and south) should be separated by a tectonic feature, such as a strike-slip fault, which decouples the deformation. In the southern SOM, however, deformation appears to be coupled throughout the crustal thickness, taking into account the abovementioned correlation between shallow and deep features. This could be conditioned by the rheology of the different layers of the lithosphere. The depth at which the lithosphere changes from brittle to ductile behavior, the "brittle-ductile transition" of Kirby (1983) is greater in basic rocks than in acidic rocks (Ranalli and Murphy, 1987). Therefore, the basic nature of the batholith could have facilitated its fracturing together with the opening of the N-S elongated basins.

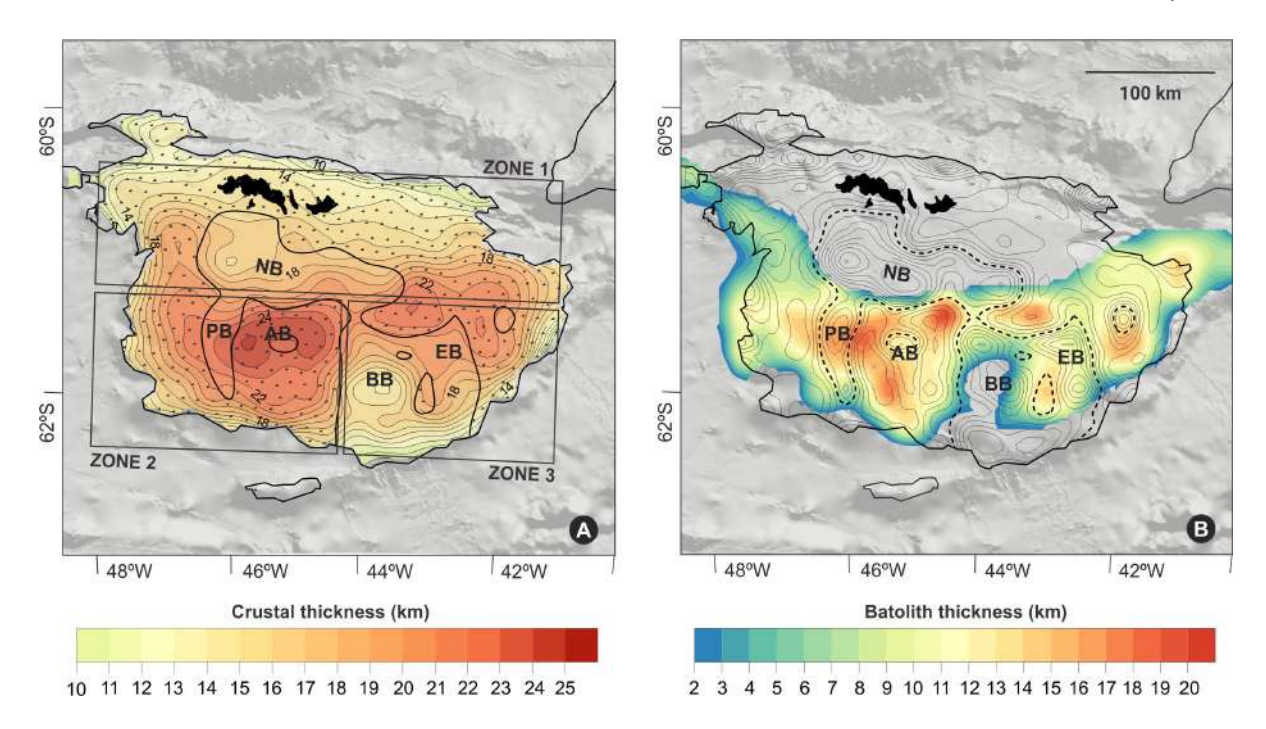


**Figure 3.9**. A) Differentiated zones in the SOM according to the thickness of the crust. The dotted area frames the structural highs according to the model results. B) Superposition of batholith thickness variation and location of the sedimentary basins. The 1500 m isopach of the sedimentary cover is highlighted to delimitate the sedimentary basins. Sedimentary basins are identified by their acronyms: AB: Airy Basin; BB: Bouquer Basin; EB: Eötvös Basin; PB: Pratt Basin.

# 3.5.3. Regional tectonic implications

The results derived from the model have implications for the tectonic processes involved in the formation of the sedimentary basins of the SOM. Previous works interpreted the Newton Basin as an intra- or fore-arc Cretaceous basin based on the compatibility between the direction of extension and the orientation of the intrusive basic igneous body causing the PMA (King and Barker, 1988; Eagles and Livermore, 2002). Our model results are compatible with the interpretation of the Newton Basin as a fore-arc basin originated during the Late Cretaceous, contemporary with the emplacement of the batholith (Fig. 3.10A). The boudinage pattern in the 1500 m isopach of the Newton basin (Fig. 3.8A) could be related to the prolongation of the extension of the N-S elongated basins northward or be the result of E-W extension of basement.

The results obtained from the 3D modeling and some geological assumptions allow us to propose a relative age for the opening of the Bouguer, Eötvös and Airy Basin, which would also apply to the Pratt Basin identified in this work. The correlation between the thinning and fragmentation of the batholith with the position of the N-S elongated basins (Pratt, Airy, Bouguer and Eötvös) (Fig. 3.9B) leads us to assume a basins formation age younger than the intrusion. To further constrain the age of formation of these basins, we turn to the sedimentary record recovered from the ODP Site 696, drilled on the Eötvös Basin (Barker et al., 1988). The deepest sedimentary section of ODP Site 696 is attributed to the late Eocene (~37.6–35.5 Ma). Below the lowest sediments recovered at ODP site 696, our model and seismic data show that there are further 955 m sediments to reach the basement. The similarity

#### **CHAPTER 3**

between the late Eocene depositional environment and sediment composition of SOM and Seymour Island suggested to López-Quirós et al. (2021) that the SOM was sourced by sediment from the Antarctic Peninsula, to which it was still attached or in close proximity at that age. Interpolating the sedimentation rate of ~4 cm/kyr calculated for the lower sediments recovered from ODP Site 696 (López-Quirós et al., 2021) to the additional unsampled sediment thickness below the site, we could assign an age of about 58 Ma for the sediments resting directly above the basement. However, this age is speculative as sedimentation rates can be expected to have changed over time. More reliable sedimentation rates are calculated from the Seymour Island formations, which span from the Cretaceous to Eocene. In Seymour Island, sedimentation rates in sedimentary units older than 37.6 Ma range between 5.5 cm/kyr and 7.6 cm/kyr (Amenábar et al., 2020; Montes et al., 2019a; Bijl et al., 2013a). If we consider similar sedimentation rates for SOM sediments older than late Eocene at Site 696, we could attribute ages between 45 and 50 Ma to the deepest sediments of the Eötvös Basin.

In this time frame, the initial development of the N-S elongated basins may be related to an early stage of the Scotia Arc formation before or around 50 Ma (Fig. 3.10B). We interpret the differential deformation observed between the eastern and western sectors of the southern part of the SOM (Fig. 3.9A) to be result of a great extensional stress to the east of the SOM, rather than two extensional systems separated by a central horst (King and Barker, 1988). The extension must have started east of the SOM, maybe linked to Weddell subduction below the east side of the Arc (Fig. 3.10) and migrated westwards thereafter. A clear disconnection between the SOM and the Antarctic Peninsula has been interpreted at 35.5 Ma, during a Proto-Powell formation stage (López-Quirós et al., 2021; Thompson et al., 2022). However, the opening of the Powell Basin may have begun earlier. The alkali basalts dredged from the Antarctic Peninsula margin conjugated to the western SOM have Eocene age (47.7 and 49 Ma) (Barber et al., 1991). These dates fit within the proposed range for the start of sedimentation in the Eötvös Basin, suggesting that regional extension indeed affected the SOM and Powell Basin simultaneously. We postulate that a proto-Powell Basin existed parallel to the Pratt, Airy, Bouguer and Eötvös basins (Fig. 3.10B), which subsequently developed in a last stage finally becoming oceanic. The opening of the N-S elongated basins fits into a regional history of extensional deformation that begins with thick crust that as it extends thins in multiple places in a "core complex" mode. Subsequently, extension focuses on the Powell basin that deepens and widens to produce a crustal neck prior to seafloor extension.

#### 3.6. Conclusions

The integration of observed and calculated geological and geophysical information with geophysical modeling of gravity and magnetic data has allowed the development of the first detailed geological 3D model of the SOM. The results of the modeling enable to link the deep structure of the SOM with its tectonic evolution. The following conclusions can be summarized from the research described above:

- 3D geophysical and geological modeling reveals as the most powerful tool for integrating different datasets to characterize large geological structures in regions with scarce direct data as Antarctica.
- In the absence of well distributed seismic information, 3D modeling of gravity anomalies enables to accurately define the geometry of sedimentary basins. In this work we have been able to determine the depth of the Newton Basin and define the existence of a well-developed sedimentary basin, the Pratt Basin.
- The N-S elongated basins (Pratt, Airy, Bouguer and Eötvös) were formed due to a great extensional stress during early stages of the Scotia Arc opening. Newton Basin could be slightly deformed and extended during the N-S elongated basin formation.
- The style of deformation undergone by the SOM is conditioned by the rheology of its different layers. The rheology of the batholith linked to its basic nature could have facilitated its brittle deformation coupled with the opening of the N-S elongated basins.
- The interrelated deformation observed in the structural features of the SOM suggest that the south-eastern area of the SOM has been the most affected by the eastwards tectonic extension. Extensional stress was greatest to the east of the SOM in the early stages of the Scotia Arc fragmentation, propagating westward thereafter.
- The Powell Basin may have been another N-S elongated basin to the west of the Pratt Basin, which may have progressed at a later stage, leading to its oceanization.

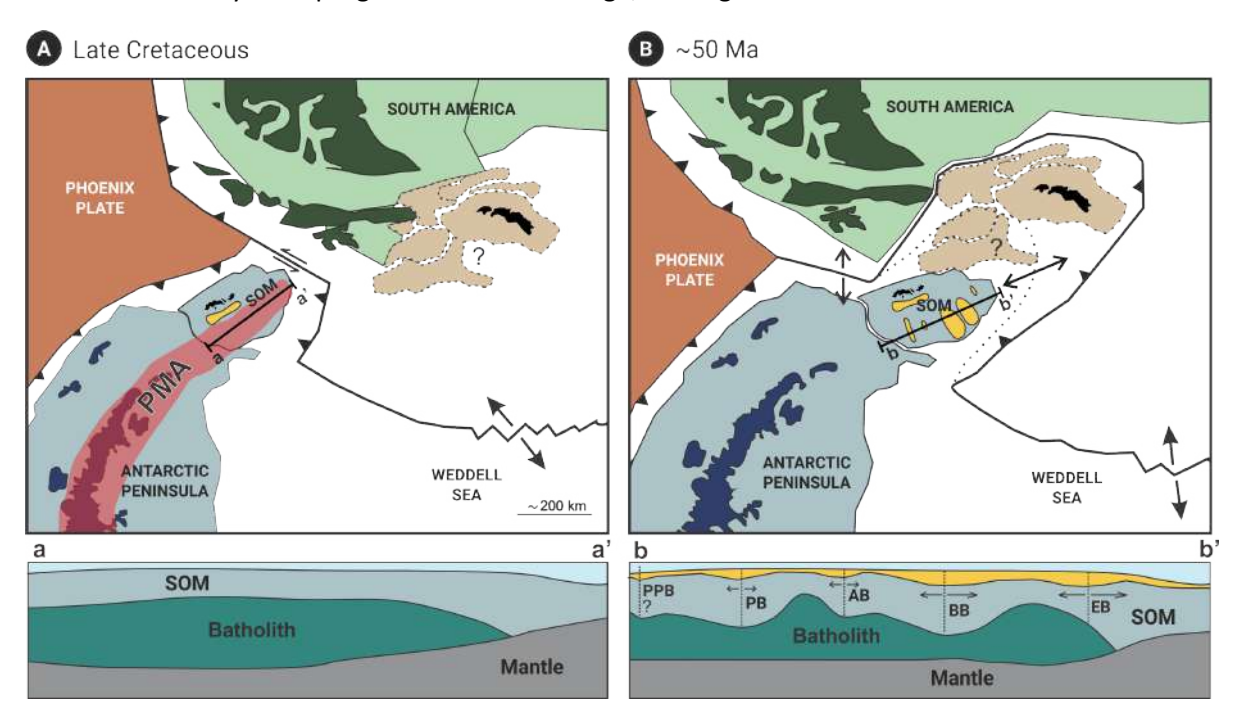


**Figure 3.10**. Sketch of the different phases of the SOM tectonic evolution. A) Late Cretaceous: Subduction of the Phoenix Plate below the Antarctic Peninsula producing the intrusion of the batholitic complex. B) Around 50 Ma: Beginning of the extension to the east of the SOM that causes the opening

# **CHAPTER 3**

of the N-S elongated basin. AB: Airy Basin; BB: Bouguer Basin; EB: Eötvös Basin; PB: Pratt Basin; PPB: Proto-Powell Basin. Kinematic reconstruction after van de Lagemaat et al. (2021).

# **Acknowledgments**

We thank Dr. Graeme Eagles and another anonymous reviewer who helped improving the manuscript with their very constructive comments. We would like to thank also to Professor Jonathan Aitchison and Dr. Augusto Rapalini the for their editorial handling of the manuscript. This research was funded by the Spanish Ministry of Science and Innovation through the coordinated project TASDRACC (CTM2017-89711-C2-1P and CTM2017-89711-C2-2P), cofounded by the European Union through FEDER funds.

The WDMAM compilation of magnetic anomalies used in this work is available at: http://wdmam.org/. Free-air gravity data database can be found at: https://topex.ucsd.edu/. The seismicity data is available at the USGS earthquake catalogue: https://earthquake.usgs.gov/. This research used data provided by the Scientific Committee on Antarctic Research (SCAR) Seismic Data Library System (SDLS) accessible on the website: http://sdls.ogs.trieste.it/. Finally, the GEBCO bathymetric data is provided at: https://download.gebco.net/.



# CHAPTER 4

Tectonic and climatic controls on the paleoceanographic evolution of the South Orkney Microcontinent (southern Scotia Arc, Antarctica)

CHAPTER 4: Tectonic and climatic controls on the paleoceanographic evolution of the South Orkney Microcontinent (southern Scotia Arc, Antarctica)

# **Abstract**

The opening and deepening of the Drake Passage, framed in the development of the Scotia Arc, facilitated the establishment of the Antarctic Circumpolar Current, which significantly influenced Earth's climate history. The opening of small oceanic basins at the southern Scotia Arc are today essential conduits for the exchange and interaction of deep water masses. However, the complex tectonic evolution of the Scotia Arc limits the reconstruction of when and how these ocean current conduits developed over time. The South Orkney Microcontinent (SOM) is located in the southern Scotia Arc and stands as one of the largest continental blocks resulting from the separation of South America and the Antarctic Peninsula. This breakup gave birth to the Powell Basin, which together with the margins of the SOM, today constitutes one of the main paths for water mass exchange between the Weddell and the Scotia seas. Given its key location, studying the sedimentary cover of the SOM can provide new insights into early paleoceanographic reorganization before and during the opening of the surrounding oceanic basins. In this work, the sedimentary infill of the SOM has been analyzed using multichannel seismic reflection profiles. The spatial and temporal distribution of five main seismic units has been defined, and a formation age has been attributed to them by correlation with Ocean Drilling Program Sites 695 and 696. We show that the southern margin of the SOM records the onset of the influence of contour currents from the Weddell Sea in the late Eocene, with a major development of contourite deposits during the early and middle Miocene. The influence of contour currents in the SOM is favored by continued subsidence as the Powell Basin developed, followed by the early opening stages of the Jane Basin. The cessation of contour current influence in the study area coincides with the onset of widespread development of contourite deposits in the Scotia Sea basins. We interpret this shift in contourite deposition to correspond with the full opening of basins around the SOM, such as Jane and Scan Basins, favoring the establishment of the Weddell-Scotia Sea connection. After the middle Miocene, sedimentation in the SOM suggests the proximity of an ice sheet extending into the continental shelf, coinciding with the reported timing for the establishment of more permanent ice sheet in the Antarctic Peninsula region at around 5 Ma.

#### 4.1. Introduction

The tectonic opening of the Drake Passage and the Tasman Gateway caused the removal of the two last major land barriers surrounding Antarctica. Their opening and deepening played a pivotal role in facilitating the establishment of the Antarctic Circumpolar Current (ACC), which in time favored the thermal isolation of Antarctica and ultimately contributed to the development of the first Cenozoic continental Antarctic ice sheet (e.g., (Dalziel, 2014; Kennett, 1977). The timing of the opening and deepening of the Tasman Gateway is well constrained at around 35 Ma (Stickley et al., 2004). In contrast, there is an ongoing debate about when precisely the Drake Passage opened and deepened,

ranging from the middle Eocene (~ 40 Ma) to the middle Miocene (~17 Ma) (Dalziel et al., 2013; Eagles & Jokat, 2014; Maldonado et al., 2014; Scher & Martin, 2006). The uncertainties surrounding the opening and deepening of the Drake Passage stem, in part, from the intricate development of the Scotia Arc. During its opening, the development of small ocean basins between the southern Scotia Sea and the northern Weddell Sea resulted in pathways for establishing deep-water circulation (Maldonado et al., 1998; Naveira-Garabato et al., 2002). However, there is still limited knowledge of the timing and the role of these pathways in the changing paleoceanographic configuration. As a result, although a proto-ACC may have existed either since the late Eocene or the Oligocene (Lyle et al., 2007; Sarkar et al., 2019), a robust, deep-reaching ACC comparable to the present did not emerge until the Miocene (Evangelinos et al., 2020, 2022, 2024; Salabarnada et al., 2018; Sangiorgi et al., 2018).

The intrusion of the northward outflow of the Weddell Sea Deep Water (WSDW) in the Scotia Sea resulted in a regional paleoceanographic reorganization that is reflected in ocean-current-related sedimentation producing extensive contourite deposits in the basins located north of the South Scotia Ridge (Maldonado et al., 2006; Martos et al., 2013; Pérez et al., 2019), mainly developing since 14-8 Ma (Pérez et al., 2021; Weber et al., 2019). Paleoceanographic reconstructions in the Weddell Sea report changes in paleobathymetry related to thermal subsidence affecting Antarctic Bottom Water (AABW) distribution during the middle Miocene (Huang et al., 2014, 2017). Additionally, an increase in bottom current intensity along the entire Antarctic margin of the Weddell Sea occurred from  $\sim$  15 to 5 Ma (Michels et al., 2002). These studies indicate that the opening of oceanic passages between the Weddell Sea and the southern Scotia Sea played a crucial, though largely unknown, role in continuously reshaping current paths, ultimately influencing today's deep-water circulation through the Drake Passage (e.g., Naveira-Garabato et al., 2002).

At the southwestern Scotia Sea, the separation between Antarctica and South America resulted in the drifting of the South Orkney Microcontinent (SOM) to the east, which led to the opening of the Powell Basin (Catalán et al., 2020; Eagles & Livermore, 2002; King & Barker, 1988). There is little knowledge regarding how the paleogeographic and paleobathymetric changes, as the SOM surrounding basins opened, forced the redistribution of ocean water masses in this area. The SOM contains several large sedimentary basins (Busetti et al., 2001; King & Barker, 1988; Morales-Ocaña et al., 2023), two of them drilled during the Ocean Drilling Program (ODP) Leg 113: Sites 695 and 696 (Barker et al., 1988). Recovered sediments from Site 695 were dated Miocene and younger and the older sediments from 696 were assigned an Eocene age (Barker et al., 1988). These two sites provide an opportunity to improve our limited knowledge regarding the development of pathways as the SOM separated from the Antarctic Peninsula. In this study, we extend the chronostratigraphic and paleoenvironmental information recorded in sediments from Sites 695 and 696 through the available multichannel seismic (MCS) profiles across the Bouguer and Eötvös basins, the largest sedimentary basins of the SOM (Morales-Ocaña et al., 2023). We provide an age for the different seismic units, which allows us to determine the timing of the onset of the influence of ocean currents in the SOM margins and their evolution as the SOM subsided and widespread glaciation was established.

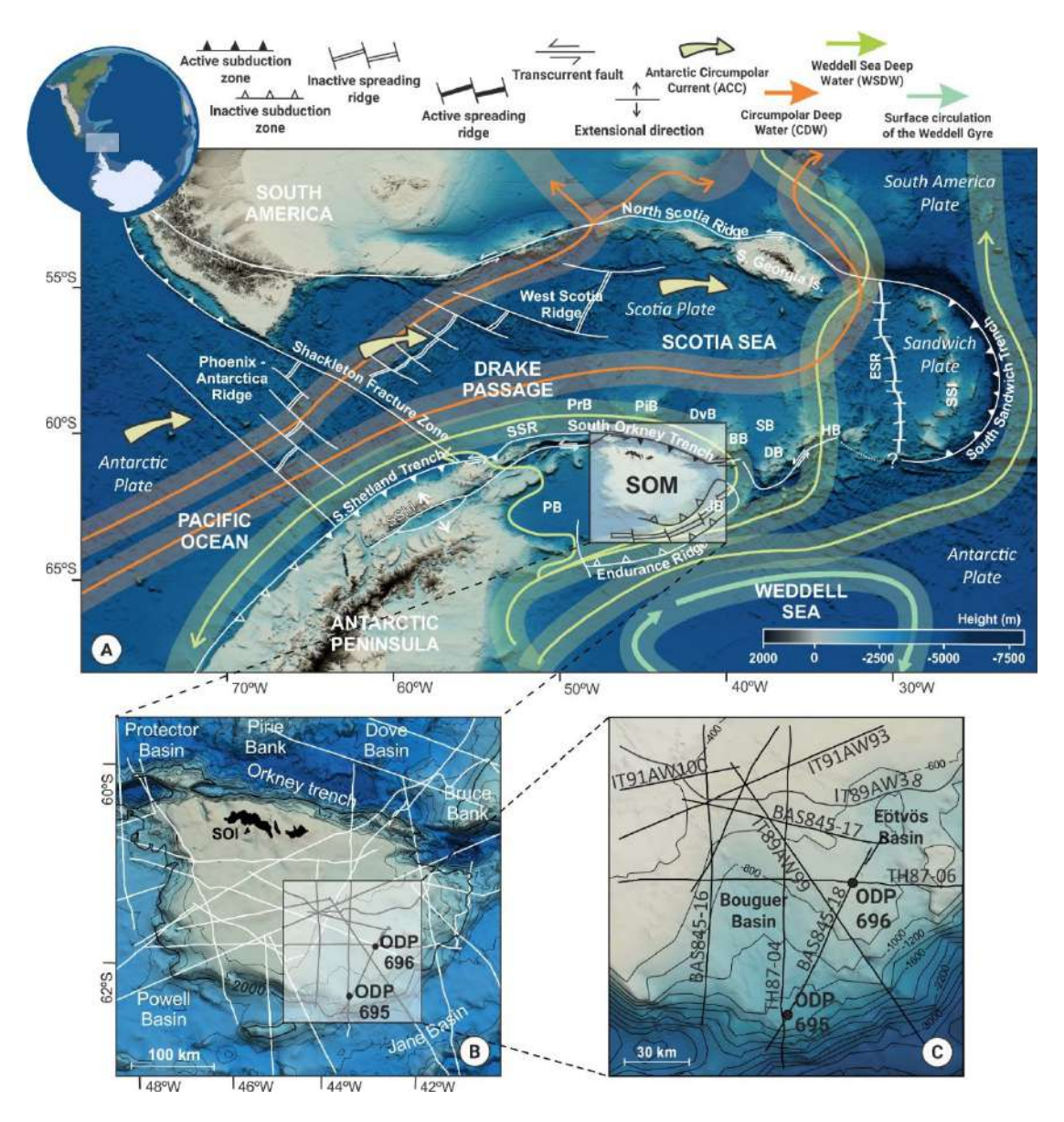


**Figure 4.1.** A) Tectonic and oceanographic setting of the South Orkney Microcontinent (SOM). Bathymetry from GEBCO 2020. BB, Bruce Bank; DB, Discovery Bank; DvB, Dove Basin; ESR, East Scotia Ridge; HB, Herdman Bank; JB, Jane Basin; PB, Powell Basin; PiB, Pirie Bank; PrB, Protector Basin; SB, Scan Basin; SOM, South Orkney Microcontinent; SShI, South Shetland Islands; SSI, South Sandwich Islands; SSR, South Scotia Ridge. The main currents affecting the Drake Passage are adapted from Hernández-Molina et al. (2006). B) All SDLS multichannel seismic (MSC) profiles available in the area. SOI, South Orkney Microcontinent. C) Southeastern sector of the SOM. Solid lines are the MSC profiles analyzed in this study. Contour lines for the bathymetry are each 200 m.

# 4.2. Geological and oceanographic setting

The evolution of the Scotia Arc caused the drift of different continental blocks and the opening of small oceanic basins in the southern Scotia Sea (Bohoyo et al., 2019; Livermore et al., 2007; Pérez et al., 2019). These oceanic basins were crucial in redistributing deep water flow as their physiography determines the primary pathways (Maldonado et al., 2005). The study of their sedimentary fill using

seismic profiles has allowed a better understanding of their evolution, marked by five to eight major discontinuities (Maldonado et al., 2014; Pérez et al., 2019). These discontinuities, named from bottom to top, Reflector- g to a', have sometimes been correlated from basin to basin and interpreted to represent important tectonic or oceanographic events (Maldonado et al., 2006; Pérez et al., 2019). Among them, Reflector-e and c are widely distributed and represent major regional changes (Pérez et al., 2019). Reflector-e has been interpreted to record a regional switch in tectonic extension, from NW-SE west Scotia spreading to E-W east Scotia spreading (Pérez et al., 2014, 2019). Reflector-c marks a change in the oceanographic setting that has been interpreted to be caused by the establishment of the connection between Scotia and Weddell seas resulting in the development of a more vigorous intermediate and deep circulation (Hernandez-Molina et al., 2008; Maldonado et al., 2006; Pérez et al., 2019). Until recently, Reflector-e and Reflector-c were assigned estimated ages of 17.2 and 12.6 Ma, respectively, based on the magnetic anomalies of the igneous oceanic crust and inferred sedimentation rates above the basement of the Scotia Sea (Maldonado et al., 2003, 2005, 2006). Recent findings from the International Ocean Discovery Program (IODP) Expedition 382 revealed sediments above and below a hiatus to be 8.4 and 14.2 Ma, respectively (Weber et al., 2019). This hiatus is now linked to Reflector-c and as a result, the timeframe for the development of this unconformity is now more confidently constrained (Pérez et al., 2021; Weber et al., 2019). Above Reflector-c, well-developed sediment drifts describe a prevailing current towards the northwest associated with the flow of Weddell Sea Deep Water (WSDW) through the Scotia Sea (Maldonado et al., 2006, 2014; Martos et al., 2013; Pérez et al., 2014, 2017). Also, sediment drift development over the eastern rise of the Antarctic Peninsula has been related to the intensification of the Antarctic Bottom Water (AABW) formation in the Weddell Sea and the Weddell Gyre during the middle Miocene (Huang et al., 2017).

The SOM is the largest continental block in the southern Scotia Arc (Fig. 4.1A). The SOM underwent great extensional stress during the early stages of the Scotia Arc development prior to the opening of the surrounding oceanic basins (King & Barker, 1988). As a result, a set of N-S elongated basins (Pratt, Airy, Bouguer, and Eötvös) opened in the southern domain of the SOM in the early Eocene (Morales-Ocaña et al., 2023). Among these basins, the Bouguer and the Eötvos basins show the most extensive sedimentary fill, with 2.9 and 2.8 km of thickness in their deepest area, respectively. The formation of these basins results from significant E-W deformation within the southeastern area of the SOM, resulting in crustal thinning (Morales-Ocaña et al., 2023). This fact is also evident in the bathymetric data, where the Bouguer and Eötvös Basins exhibit the greatest seafloor depths within the SOM, exceeding 600 meters below sea level (mbsl) (Figs. 4.1B and 4.1C) (Dickens et al., 2014). The separation of the SOM from the Antarctic Peninsula led to the opening of the Powell Basin (Catalán et al., 2020; Eagles & Livermore, 2002; King & Barker, 1988; López-Quirós et al., 2021). At the southeastern margin, the Jane Basin opened as a back-arc basin. This has been inferred to take place between 17.4 and 14.4 Ma, after the end of the Weddell Sea subduction below the SOM inferred to occur at 19.5 Ma (Bohoyo et al., 2002; Livermore et al., 2005). However, there is little knowledge regarding how the opening of the surrounding basins of the SOM (e.g. Protector,

Dove, Scan, Powell and Jane basins; Fig. 4.1A) impacted the redistribution of ocean water masses in this area.

# 4.3. Materials and methods

# 4.3.1. Sedimentary data

Ocean Drilling Program (ODP) Leg 113 drilled sites 695 and 696 in the southern Bouguer and western edge of the Eötvös basins, respectively (Barker et al., 1988) (Figs. 4.1B and 4.1C). Site 695 penetrated 341 meters of sediments spanning from the late Miocene to the present. Shipboard sediments recovered from Site 695 were divided in three lithostratigraphic units differentiated by changes in the abundance of biosiliceous components. The biosiliceous component increases from bottom (Lithostratigraphic Unit III and II) to top (Lithostratigraphic Unit I), with diatoms comprising 70-80% of the sediment during the early and middle Pliocene (Barker et al., 1988). Site 696 drilled 645 meters of sediments from the late Eocene to the present, with its sequence divided into three parts and seven lithostratigraphic units, also showing variations in biosiliceous content (Barker et al., 1988). The lower part (Lithostratigraphic Unit VII) is dominated by terrigenous and authigenic sediments (Barker et al., 1988) that record shallow deposition in a shelf environment when the SOM was still connected to the Antarctic Peninsula margin (López-Quirós et al., 2021). The middle part (Lithostratigraphic Units VI, V, and IV) is rich in biosiliceous sediments, with diatoms comprising up to 90% (Barker et al., 1988), likely due to reduced terrigenous-sourced sediment following SOM isolation from the Antarctic Peninsula as the Powell Basin opened (López-Quirós et al., 2021). The upper part (Lithostratigraphic Units I, II, and III) is again dominated by terrigenous components, with a gradual increase in diatom abundance (up to 70%) toward the top.

This study utilizes sediment ages from both Sites 695 and 696 to constrain the age of seismic units defined in the SOM. Since ODP Leg 113, advancements in Southern Ocean biostratigraphy have led to shifts in First Appearance Datum (FAD) and Last Appearance Datum (LAD) ages for some species, necessitating adjustments to shipboard age assignments for sections younger than the early Miocene. We incorporated updated biostratigraphic zonations following the proceedings of IODP Expedition 382 (Weber et al., 2019).

#### 4.3.2. Seismic data

A network of Multi-Channel Seismic (MCS) reflection profiles was obtained from the Scientific Committee on Antarctic Research (SCAR) open-source database Seismic Data Library System (SDLS, http://sdls.ogs.trieste.it). Seismic interpretation was conducted using HIS Kingdom Suite software. Nine studied MCS profiles (BAS845-16, BAS845-17, BAS845-18, TH87-04, TH87-06A-B, IT89AW99, IT89AW38, IT91AW93, and IT91AW100; Fig. 4.1C) were acquired in four oceanographic campaigns using different acquisition methods. In order to homogenize the profiles, we referenced them to the same ocean floor using the bathymetry compilation in Dickens et al., (2014). For that purpose, the bathymetry depth was transformed to two-way travel time (TWTT), assuming a sound water velocity of 1460 m/s.

#### **CHAPTER 4**

Seismic interpretation followed basic analytical methods of seismic-stratigraphy (e.g., Payton, 1977). The analysis focused on the southeastern part of the SOM, where the basement reaches greater depths (Morales-Ocaña et al., 2023), and reflectors show continuity. Major stratigraphic discontinuities were identified as high amplitude reflectors constituting local unconformities. The thickness and depth of seismic units and discontinuities are presented in seconds (two-way travel time, TWTT) due to uncertainties associated with depth conversion. Interpolation between profiles allowed mapping of seismic units and inferring the regional distribution of sediments. It should be noted that the presented paleobathymetries do not include restauration for the effect of subsidence since the backstripping method has not been applied. The criteria for seismic interpretation of morphologies and internal configurations of contourite depositional systems (CDS) have been performed following the methods described by Faugères et al. (1999), Rebesco et al. (2014), Rebesco & Stow (2001) and Stow et al. (2002). When possible, the current direction is interpreted following these same references, considering the deflection towards the left of the currents and deposition to the right due to the Coriolis effect in the southern hemisphere.

# 4.3.3. Synthetic seismogram and age control

To assign ages to seismic units and extend the results of drilled sequences regionally, we correlated seismic interpretations with Sites 695 and 696 using a synthetic seismogram constructed from velocity and density log data available from ODP Leg 113 (Fig. 4.2; Barker et al., 1988). Density and velocity data allow calculation of acoustic impedance variability in both cores. Synthetic seismograms were constructed using the SynPAK module in Kingdom Suite software to provide the best possible tie between borehole data and seismic profiles for core-log-seismic correlation.

# 4.4. Results

# 4.4.1. Seismic stratigraphic analysis and correlation with odp sites 695 and 696

# 4.4.1.1. Age model

Table 4.1 presents the updated ages from the original biostratigraphic ages of sites 695 and 696 (Barker et al., 1988), following the biostratigraphic zonation employed during Expedition 382 (Weber et al., 2019). Revised Eocene to Miocene ages for sediments obtained from Site 696 are also included, as previously updated by various authors (Houben et al., 2011, 2013, 2019; López-Quirós et al., 2021).

Section	Depth (m)	Fossil taxa	Previous age	Updated age (based on)				
	695							
	Radiolarian							
113- 695A-20X, CC, through - 26X, CC 113-695A-27X, CC to 113-695A-30X,	160 to 215 215 to 255	LAD Prunopyle titan to FAD Helotholus vema FAD Helotholus vema to LAD Lychnocanium grande	Lower Upsilon Zone (Barker et al., 1988)  Upper Tau Zone (Barker et al., 1988)	3.48 to 4.59 Ma (This study) 4.59 to 5 Ma (This study)				
CC 113-695A-40X, CC - 4IX, CC	325 to 341	LAD Cycladophora spongothorax	Uppermost part of the C. spongothorax (Barker et al., 1988)	> 9.20 Ma (This study)				

**Table 4.1.** Updated shipboard ages for sediments obtained from Sites 695 and 696 based on current biostratigraphic zonation. Ages previously updated by various authors are also shown.

#### 4.4.1.2. Seismic units, discontinuities, and correlation with ODP 695 and 696

The correlation between MSC profiles and Sites 695 and 696 has allowed us to assign and age to the seismic units and to ground-truth the paleoenvironmental interpretations based on of seismic data (Fig. 4.2). Four major seismic discontinuities can be distinguished in the stratigraphic record above the acoustic basement, named D4 to D1 from older to younger. These discontinuities, together with the acoustic basement and the seafloor are bounding five seismic (SU5 to SU1, from bottom to top; Figs. 4.2, 4.3 and 4.4).

Seismic Unit 5 (SU5) encompasses all sediments between the acoustic basement and the D4 discontinuity. This unit displays heterogeneous reflector amplitude and continuity, with parallel and discontinuous internal reflectors that are locally truncated by the D4 unconformity (Fig. 4.3). SU5 thickness varies, being minimum over structural highs and maximum in the Bouguer Basin depocenter, where it reaches up to 2.2 s TWTT (Fig. 4). In western edge of the Eötvös Basin, the deepest sampled sediments obtained at Site 696, dated as late Eocene correlates with the uppermost part of SU5 (Figs. 4.2, 4.3 and 4.5). These sediments comprise two of the Lithostratigraphic Units (LU) described on shipboard during ODP Leg 113: LU VIID (from the bottom of the Site, at 645.6 mbsf, to 606.9 mbsf), dominated by organic-rich sandy mudstone facies, and LU VIIC (606.9 to 569.7 mbsf) composed of glaucony-bearing packstone facies (Barker et al., 1988; López-Quirós et al., 2019, 2021). Sediments below and above the unconformity D4 are dated 34.1 and 33.6 Ma, respectively (López-Quirós et al., 2021). Therefore, the interval comprising unconformity D4 contain the record of the Eocene-Oligocene Transition (EOT).

Section Depth (m) Fossil taxa		Fossil taxa	Previous age	Updated age (based on)		
696						
Diatoms						
113-696B-25R,	280 to	LAD Nitzschia	Late Miocene (Barker	11.7 Ma		
CC -27R, CC	300	denticuloides	et al., 1988)	(This study)		
113-696B-47R, CC	490 to 500	LAD  Denticulopsis maccollu  mii	Middle Miocene (Barker et al., 1988)	14.3 Ma (This study)		
113-696-50R-	521.91	FAD	14.4 Ma	16.5-16.7		
	to	Denticulopsis maccollu	(Gersonde & Burckle,	(López-Quirós et al., in		
2W, 26-29	521,08	mii	1990)	prep)		
	1	Radio	larian			
113-696B-11R - 165- Presence of boundary 12R, CC 175 Lithomelissa stigi (Barker et al., 1988)			9.3- 9.8 Ma (This study)			
		Dino	cysts			
113-696B -51R- 2W, 51-53	531.81	Invertocysta tabulata	Undefined	< 23.5 Ma (López-Quirós et al., in prep)		
113-696B -53R-	551.7 -	FAD Chiropteridium	Hadafia ad	<33.6 Ma		
3W, 80	552.7	Galea	Undefined	(Houben et al., 2012)		
113-696B -55R-	568.82 -	FAD	Undefined	33.6 Ma		
1W, 62-117	569.39	Malvinia escutiana	Undefined	(Houben et al., 2013)		
113-696B -55R- 3W, 75-147	571.16 - 571.95	FAD Stoveracysta kakanuie nsis	Undefined	34.1 Ma (Houben et al., 2013)		
Calcareous nannofossils						
113-696B -58R-	593.57	FAD Reticulofenestra	about 35-38 Ma	~35.5 Ma		
1W		oamaruensis	(Barker et al., 1988)	(Houben et al., 2019)		
113-696B - 60R-	616.70	FAD	35.2-37.8 (Barker et al.,	36.27 Ma		
1W	616.78   Istmolithus recurvus 1988)		1988)	(Houben et al., 2019)		
113-696B -62R-	642.62	FAD Reticulofenestra	Late Eocene (Barker et	< 37.61 Ma		
6W	643.62	bisecta	al., 1988)	(Houben et al., 2019)		

**Table 4.1 (cont.).** Updated shipboard ages for sediments obtained from Sites 695 and 696 based on current biostratigraphic zonation. Ages previously updated by various authors are also shown.

Seismic Unit 4 (SU4) lies above D4 and exhibits an overall tabular morphology (Figs. 4.3, 4.4 and 4.5). Its thickness is generally constant around 50 ms TWTT but becomes thinner or locally disappears towards the north of the study area (Figs. 4.3 and 4.4). The thickness of SU4 locally increases in two areas: at the shelf break in the southern edge of the SOM, where a mounded morphology reaches up to 200 ms TWTT (Fig. 4.3), and in the northeastern area, where the unit

reaches up to 100-200 ms TWTT, coinciding with the presence of a mounded morphology (Figs. S4.2, S4.3 and S4.4 in supplementary materials). Based on the correlation with Site 696, SU4 comprises sediments assigned to LU VIIB (569.7 to 548.9 mbsf) and LU VIIA (548.9 to 529.8 mbsf) (Fig. 4.2). At Site 696, LU VIIB consists of claystone and limestone facies, and LU VIIA comprises rhythmically interbedded sandy mudstone facies with glauconite-bearing sandstone beds (Barker et al., 1988; López-Quirós et al., 2020). SU4 is bounded at its top by a high impedance reflector, discontinuity D3, which coincides with the top of LU VIIA. Available ages at 531.81 mbsf and 521.49 mbsf just below and above D3, are < 23.5 Ma and 16.5-16.7 Ma, respectively (López-Quirós et al., in prep). This implies SU4 spans from the Oligocene to the early Miocene (Fig. 4.2).

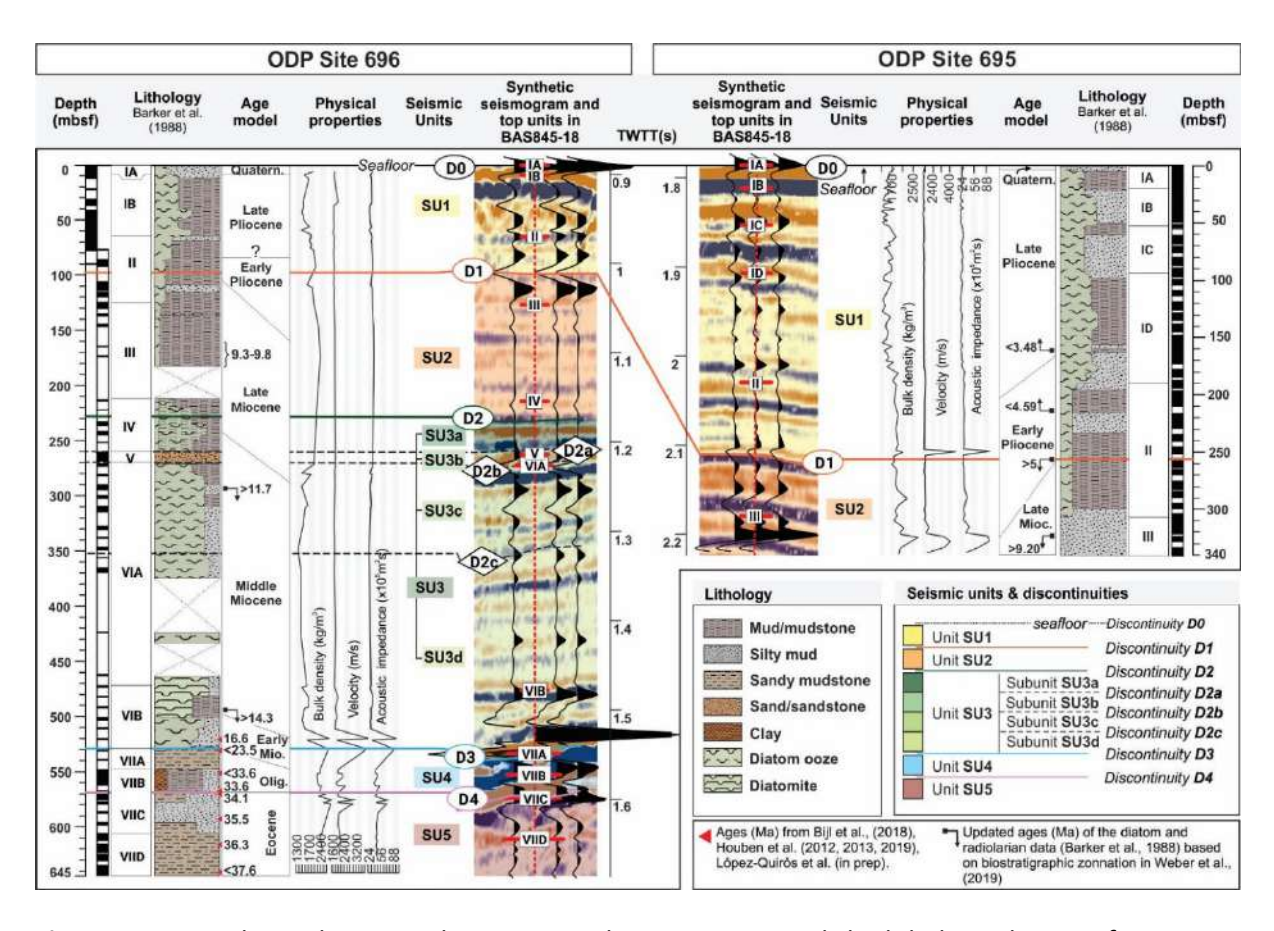


**Figure 4.2.** Correlation between the interpreted seismic units and the lithological units of ODP Sites 695 and 696 (Barker et al., 1988). The correlation is supported by the synthetic seismogram built from acoustic impedance contrast calculated from core physical properties (bulk density and velocity) (Barker et al., 1988).

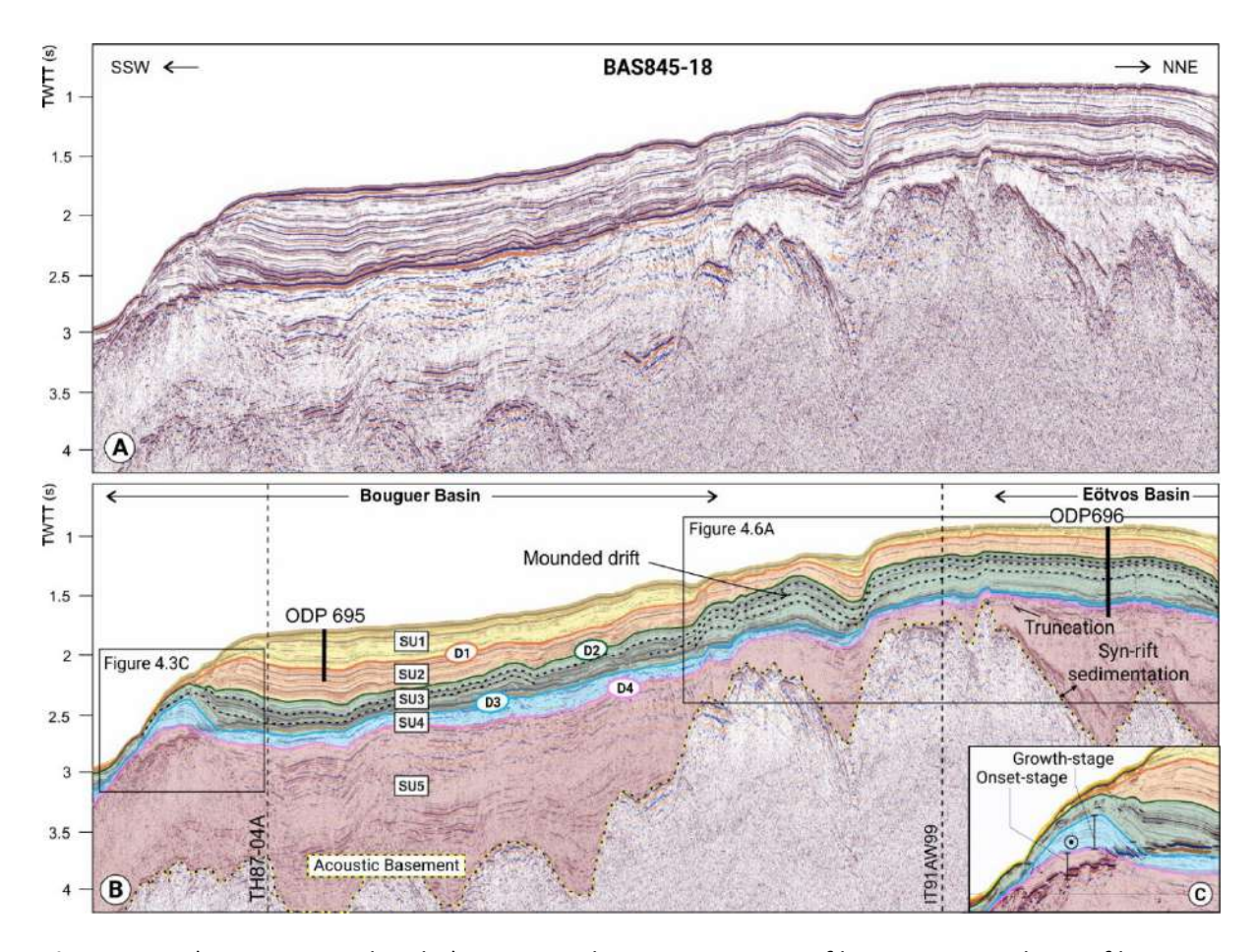


**Figure 4.3.** A) Uninterpreted and B) interpreted SSW-NNE MSC profile BAS845-18. This profile crosses both ODP Sites 695 and 696. C) Close up of the shelf break mounded drift deposits showing the different stages in its development. Location of the profile is shown in Figure 4.1C.

Seismic Unit 3 (SU3) develops above discontinuity D3 and presents highly variable thickness throughout the study area. Thickness increases markedly within mounded morphologies that form around the structural highs bounding the Bouguer and Eötvös basins. From bottom to top, we distinguish four subunits, SU3d, SU3c, SU3b, and SU3a, delimited by reflectors D2c, D2b, and D2a (Figs. 4.2 and 4.6). The subunits are differentiated based on strata/reflector terminations and seismic facies changes, associated to variations in the morphology and spatial distribution of the mounded deposits. Together, SU3d and SU3c reach up to 340 of the 390 ms TWTT, which is the maximum thickness measured in SU3 (Fig. 4.6). SU3b locally records a shift in the spatial distribution of the mounds, with reflectors onlapping the mounded deposits of the lower subunits (Fig. 4.6). SU3a subunit fills the previously formed moats. SU3 correlates with the LU VIB, LU VIA, LU V, and almost all of LU IV of Site 696. The lower LU VIB marks a change in sedimentation at Site 696 with an increase in the abundance of diatoms, with intervals of diatom oozes containing up to 90% of diatoms. LU VIB consists of lithified diatomite and mud-bearing diatomite and coincides with the lower part of the SU3d, where higher impedance contrast reflectors are observed (Fig. 4.2). The upper part of SU3d is characterized by transparent facies, unfortunately this section corresponds to an interval of no core recovery in LU VIA (Fig. 4.2). SU3c correlates to the upper part of LU VIA, which is composed of diatom ooze and mudbearing diatom ooze. SU3b corresponds in the sedimentary record to a thin LU V, composed of coarsegrained sand interpreted as a turbidite (Barker et al., 1988). SU3a correlates with almost all the LU IV, which is also composed of diatom ooze and mud-bearing diatom ooze. The D2 discontinuity constitutes the upper boundary of SU3 and does not present an overall great impedance contrast. Its definition is based on the onlap or downlap terminations of reflectors against the mounded morphologies (Figs. 4.2 and 4.6). Based on the age model, SU3d comprises strata from the early to middle Miocene, SU3c spans the middle Miocene and possibly the earliest late Miocene, SU3b strata ages range from the latest middle to the late Miocene, and SU3a strata are late Miocene in age. At the top, unconformity D2 develops during the early late Miocene.

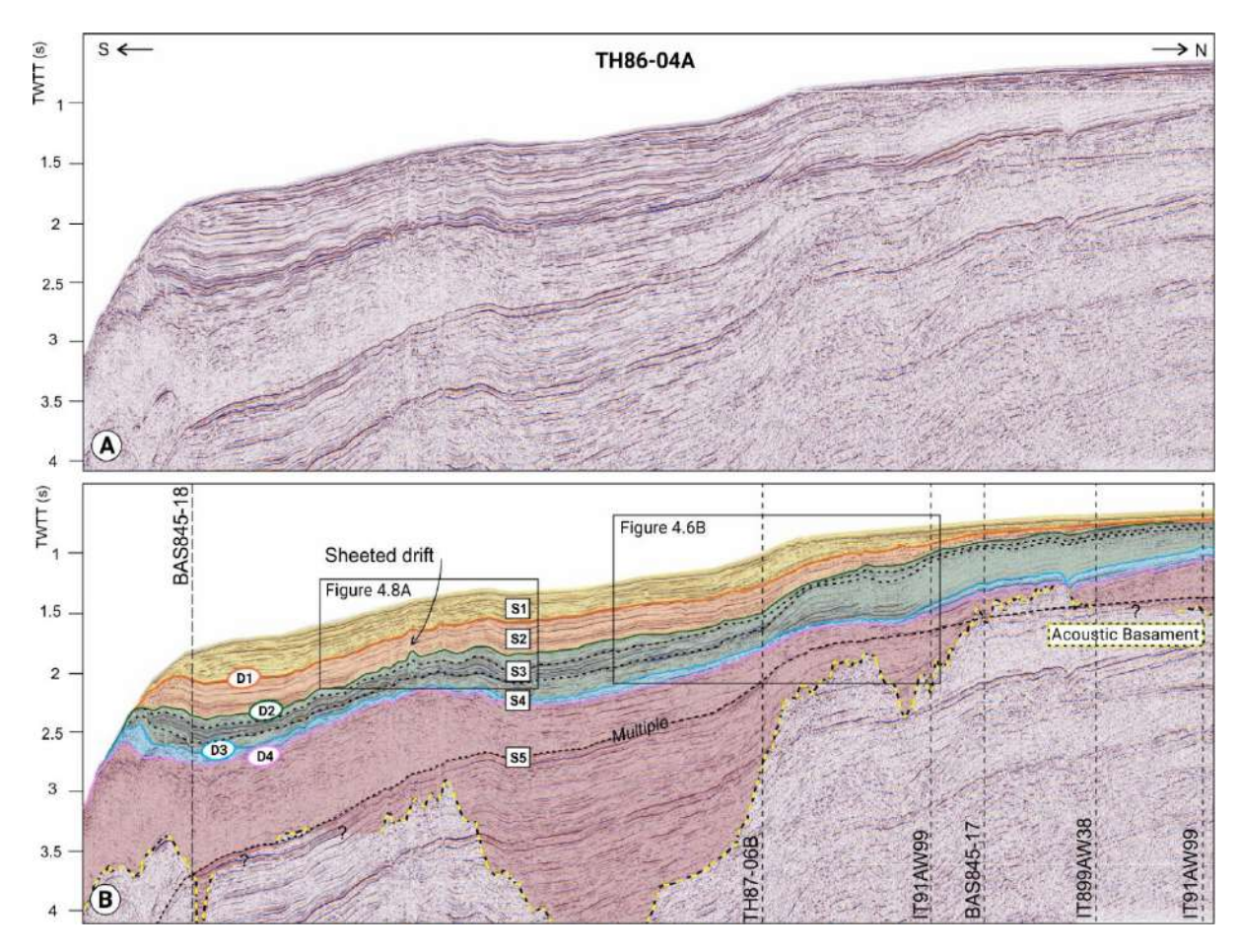


**Figure 4.4.** A) Uninterpreted and B) interpreted MSC profile TH86-04A, orientated N-S. Location of the profile is shown in Figure 4.1C.

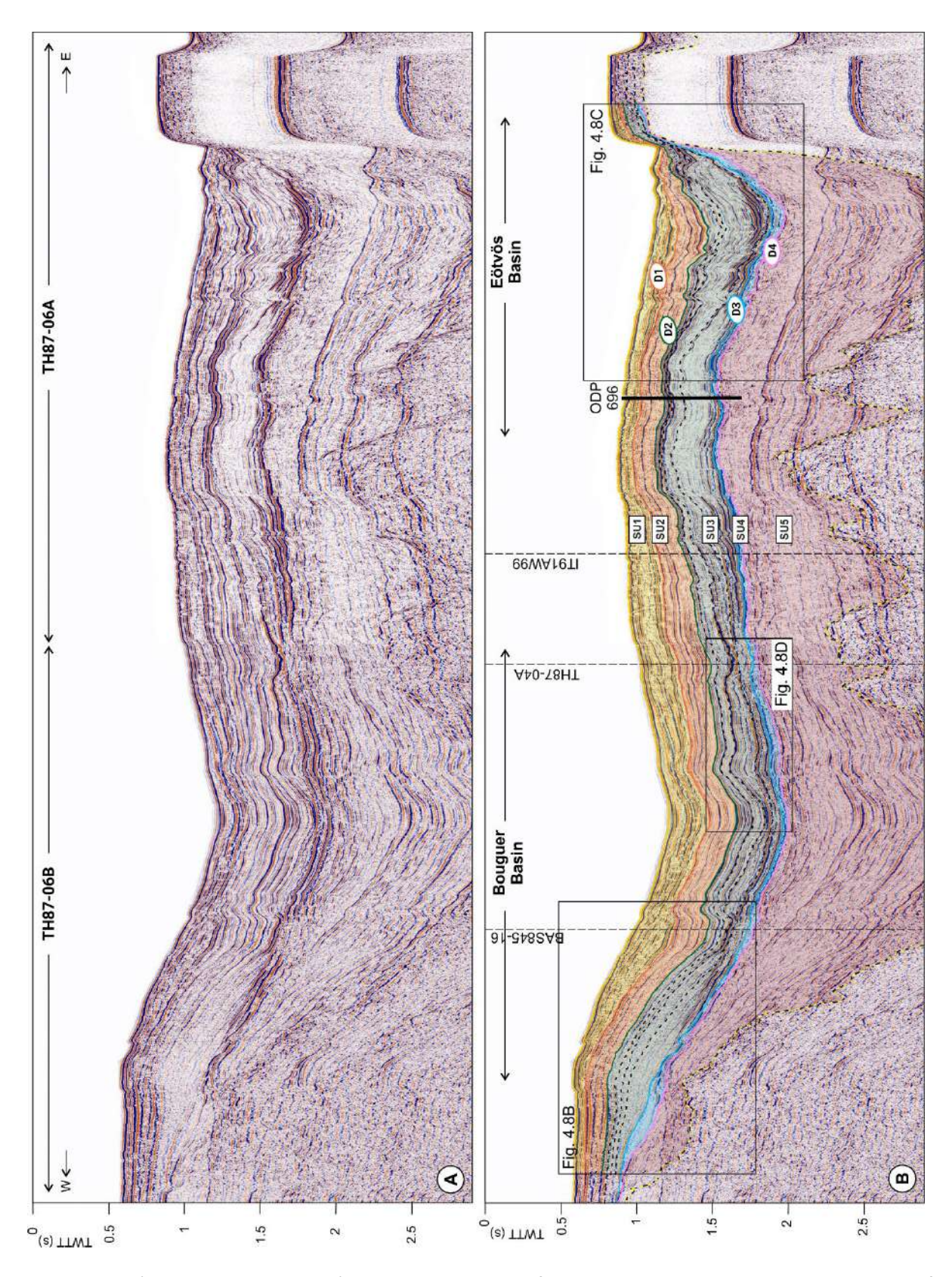


**Figure 4.5.** A) Uninterpreted and B) interpreted MSC profile TH87-06AB, orientated E-W. Location of the profile is shown in Figure 4.1C.

Seismic Unit 2 (SU2) lies above D2 and is characterized by a nearly homogeneous thickness of about 200 ms TWTT throughout most of the study area, thinning towards the north. SU2 is characterized by parallel/subparallel continuous reflectors that do not develop the large mounded morphologies that characterized previous seismic units, although wavy reflectors can be distinguished (Figs. 4.3, 4.4 and 4.5). Strata within SU2 has been drilled by both Sites 695 and 696. At Site 695, SU2 correlates with the half bottom of LUII and LU III (Fig. 4.2). At Site 696, SU2 correlates with the upper part of the LU IV, the LU III, and the lower part of the LU II (Fig. 4.2). At both sites, the deposition of this unit is marked by a distinct decrease in the biosiliceous components. SU2 comprises predominantly silty and clayey mud combined with some diatom-bearing mud. The top of SU2 is marked by discontinuity D1, which does not present an overall great impedance contrast. Based on the age model from Site 695, the D1 unconformity is bounded by sediments below and above that have been dated between >5 Ma and 4.59 Ma, respectively (Fig. 4.2).

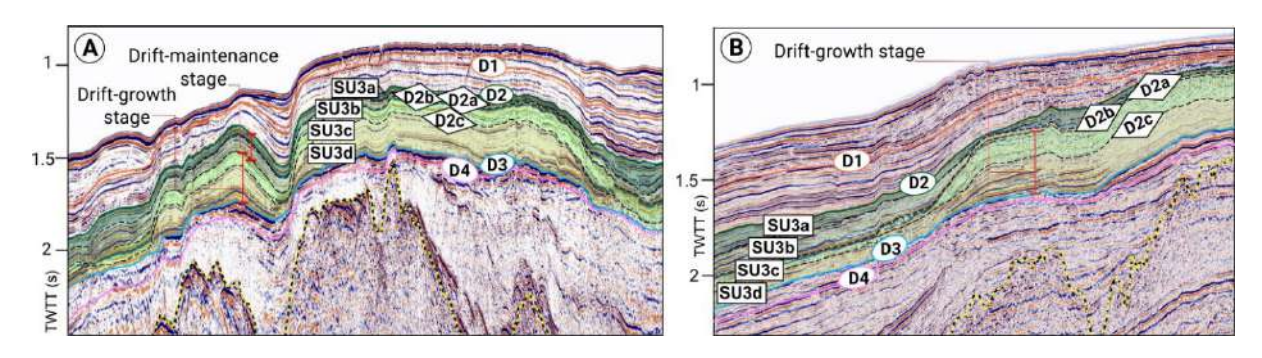


**Figure 4.6.** Subunits identified within Seismic Unit 3 (SU3). The location of the MCS profiles are highlighted in Figs. 4.3 and 4.4.

SU1 develops between D1 and the seafloor and is characterized by a wedge-shaped morphology with maximum thickness at the shelf edge, also thinning towards the north. SU1 inner reflectors are continuous and generally concordant with the previous unit. Local downlap or onlap reflector terminations against D1 are observed developing mounded morphologies, although less developed than in SU3 (Fig. 4.3 and 4.7). SU1 correlates with the LUII and LUI at Site 695 and the upper part of LU II, and the LU IB and LU IA at Site 696. At both sites, sediments record an increase in diatom abundance up to 70% along this unit, generally poorly preserved (Barker et al., 1988).

# 4.4.2. Development of contourite depositional systems in the South Orkney Microcontinent

# 4.4.2.1. Depositional and erosive features

The studied sedimentary fill studied above D4 exhibits distinctive characteristics of sediments deposited under the influence of along slope bottom currents, resulting in the formation of contourite depositional systems (CDS) (Stow et al., 2002; Hernández-Molina et al., 2003; Rebesco, 2005). A CDS includes a variety of erosive and depositional features (Faugères et al., 1999; Rebesco et al., 2014). The main erosional features in the CDS are the moats associated with the formation of sediment drifts (Fig. 4.8). The predominant depositional features in the study area include elongated mounded drifts

and sheeted drifts, based on the classification of Faugères et al. (1999), Stow et al. (2002); Rebesco et al. (2014), and Stow & Faugères (2008) (Fig. 4.8).

Seismic Units		Geometry	Internal configuration	Age	Seismic Discontinuities	Reflection termination	
SU1		Tabular shape, relatively homogeneous thickness (~ 200-300 ms), thining towards the north. Mounded morphologies and erosional features locally founded	Medium to high amplitude, subparallel to irregular relflections	Early Pliocene to present	Seafloor 🧷	Concordant Onlap/ Downlap/ Concordant	
		Tabular shape, homogeneous thickness (~ 200 ms)	Medium to high amplitude, parallel to subparallel reflections	Middle / Late Miccene to Early Pliocene  Between 11.7	Low impedance contrast	Concordant	
	*SU3a			- 9.8 Ma	D2a	Toplap Onlap	
SU3-	+SU3b +SU3c	Mounded morphologies Great thickness variability (up to ~ 400 ms), major during SU3d y SU3C	Medium to high amplitude continous reflections	Early Miocene to Middle / Late Miocene	Lateral	Toplap Onlap Toplap Downlap	
	→ SU3d	• • • • • • • • • • • • • • • • • • • •	••••	Between 23.5	D2c	Toplap Downlap	
s	U4	Tabular shape, general low thickness (~ 50 ms), except in the northern edge (~ 100-200 ms) and in the southern shelf-break (~ 200 ms)	Medium to high amplitude, irregular to continous reflections	- 16.5 Ma Early to Late Oligocene / Early Miocene Between 33.6	Great impedance contrast, continuous at regional scale	Toplap	
SU5		Heterogeneous shape, conditioned by the basement Locally wedging morphologies	Low to high amplitude, irregular to continous reflections	- 34.1 Ma  Early to Late Eocene	Locally shows great impedance The continuity is sometimes lost  Basement	Toplap / truncation	

**Figure 4.7.** Seismic character (i.e. external geometry and internal seismic facies) of the main seismic units (SU1 - SU5), their bounding discontinuities (D1 - D4 and the seafloor), and the reflection terminations that defines them. Also shown are the ages assigned to SU5-SU1. Acoustic basement age estimation after Morales-Ocaña et al. (2023)

Elongated mounded drifts laterally change their seismic expression, allowing to differentiate between plastered, separated, and patched drifts based on their reflection configuration and terminations (Fig. 4.7):

- a) Plastered drifts are here defined as a type of elongated mounded drift that develops against a gentle slope. It displays an asymmetric shape with a flat terrace at the top. Their internal configuration is characterized by relatively continuous subparallel reflectors of medium-to-high amplitude that exhibit an up-slope migration and down slope downlap reflection terminations.
- b) Separated drifts develop separated from an adjacent slope by a distinct moat, where the principal flow is focused. The internal seismic reflectors are medium-to-high in amplitude, with onlap/downlap reflector terminations onto the basal discontinuity. The up up-slope progradation results in the associated moat migration.

c) Patch drifts develop away from the slope. Their internal reflectors are medium-to-high in amplitude that downlap onto the basal discontinuity. Moats on both sides of the mound characterize the observed patch drifts.

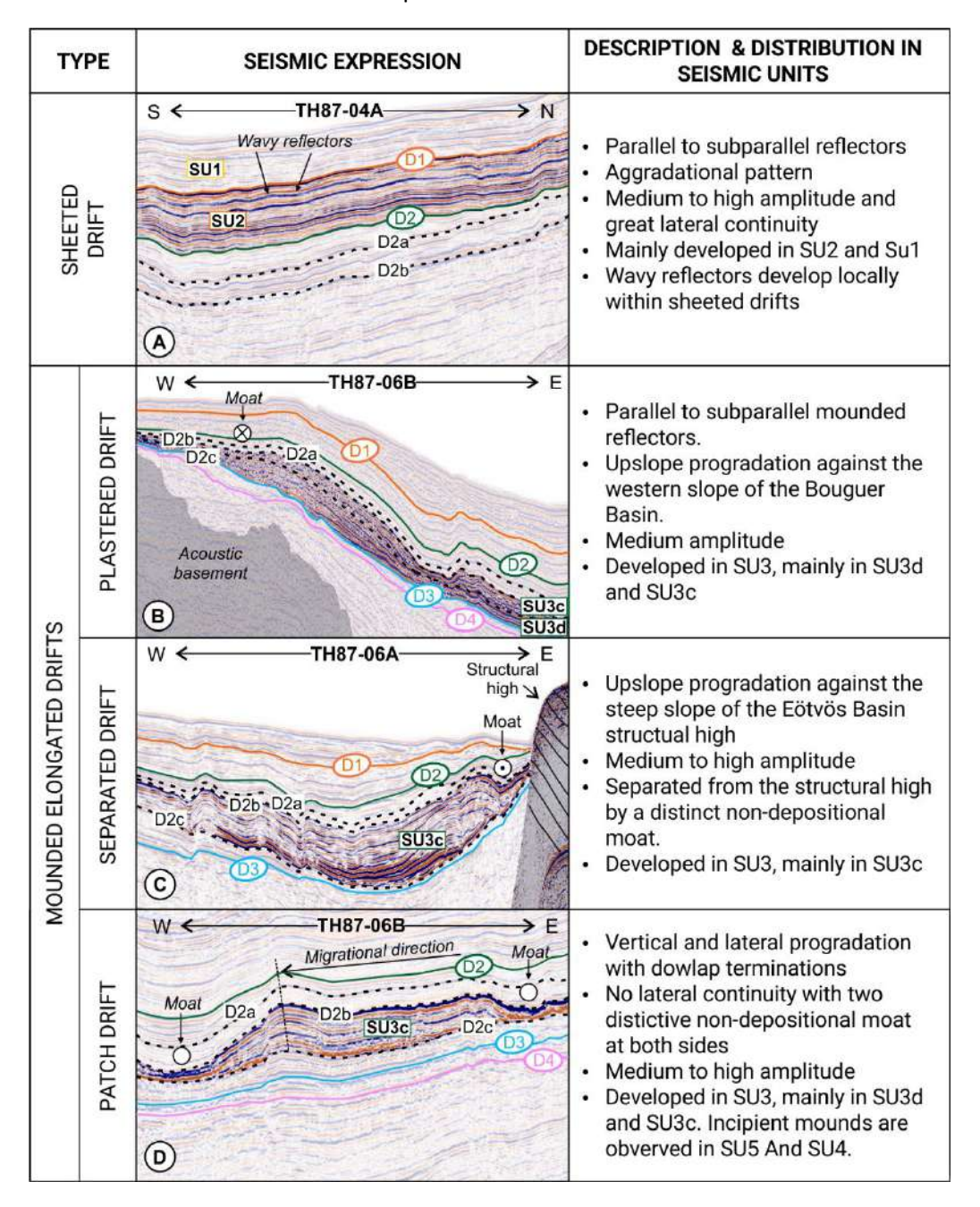


**Figure 4.8.** Classification scheme and examples for contourite deposits identified in the SOM based on Rebesco et al. (2014).

The sheeted drifts display an aggrading pattern with parallel medium-to-high amplitude reflectors extending over large areas (Figs. 4.4 and 4.8). These characteristics make them difficult to differentiate from other deep-water sediments such as pelagic, hemipelagic, distal turbidites, or sediments resulting from mixed deep-water processes. In this study, we classified the deposits as

sheeted drifts due to the presence of wavy reflections in some locations, indicating bottom-current influence during deposition.

# 4.4.2.2. Spatial and temporal distribution of the contourite deposits

The distribution of the contourite deposits observed in the southeastern SOM is neither spatially nor temporally homogeneous. Two CDS with distinct evolutionary stages (i.e. drift-growth and maintenance stages) have been identified based on Rebesco et al. (1996). CDS1 comprises a mounded drift located on the continental shelf-break of the southern edge of the study area (Figs. 4.3C, and 4.9C), and another mounded drift situated over the structural high between the Bouguer and Eötvös basins at the northern edge (Fig.4. 9C and Figs. S4.2, S4.3 and S4.4 in supplementary materials).

The onset of the shelf-break mounded drift predates D4, occurring in the uppermost part of SU5 with the development of a plastered drift (Fig. 4.3C). However, significant growth of the mound occurs above D4 during the deposition of SU4 (Fig. 4.3C). The mounded drift in the northern area, although insufficiently characterized due to limited data, likely corresponds to an elongated patch mounded drift (Figs. S4.3 and S4.4 in supplementary materials).

Discontinuity D3 separates the development of localized mounded drifts of CDS1 from widespread drifts of CDS2, developed during the deposition of SU3. CDS2 consists of different sediment drifts positioned around the structural highs bounding the Bouguer and Eötvös basins. The onset of the CDS2 mounded morphologies occurs during SU3d. During deposition of SU3c mounds continue to grow, not only aggrading over the previous subunit but also expanding laterally, involving the preservation and slight enhancement of the elevation of the drifts (Fig. 4.6). These two sub-units, SU3d and SU3c, represent the main drift-growth stage, reaching thicknesses up to 340 ms TWTT (Fig. 4.6). SU3b exhibits variable thickness. On top of previous mounded deposits, this subunit mainly constitutes a drift-maintenance stage (Fig. 4.6). However, the sealing of previous mounded morphologies is locally observed (Fig. 4.6B). SU3a is the thinnest among all SU3 subunits. Its nearly constant thickness is only interrupted by the local growth of isolated and small mounded deposits. D2 discontinuity seals the CDS2.

Within the identified mounded drifts, the direction of current-related flow can be inferred in two cases: a plastered drift against the western Bouguer margin indicates a northward flowing current, while a separated drift against the eastern Eötvös margin suggests a southward flowing current.

# 4.5. Interpretation and discussion

Revised shipboard chronologies from Sites 695 and 696, based on updated biostratigraphic zonation, offer an up-to-date seismic-stratigraphic framework. Sediment core-to-seismic tie in the Bouguer and Eötvös basins records the early Eocene to present tectonic, climatic, and paleoceanographic evolution of the SOM. Our results indicate that the southern margin of the SOM has been influenced by bottom currents since at least the late Eocene. Progressive deepening of the SOM due to the opening of the Powell Basin and the subsidence of the Weddell Basin likely favored

an increased contour current influence over the SOM, resulting in the widespread development of mounded elongated drifts during the middle Miocene. The cessation of contourite drift development in the Bouguer and Eötvös basins coincides with the reported onset of contourite drift development in the southern Scotia Sea (~10-12 Ma) (Maldonado et al., 2005; Martos et al., 2013; Pérez et al., 2019, 2021). This section discusses the results of each unit in the regional tectonic, climatic, and paleoceanographic context.

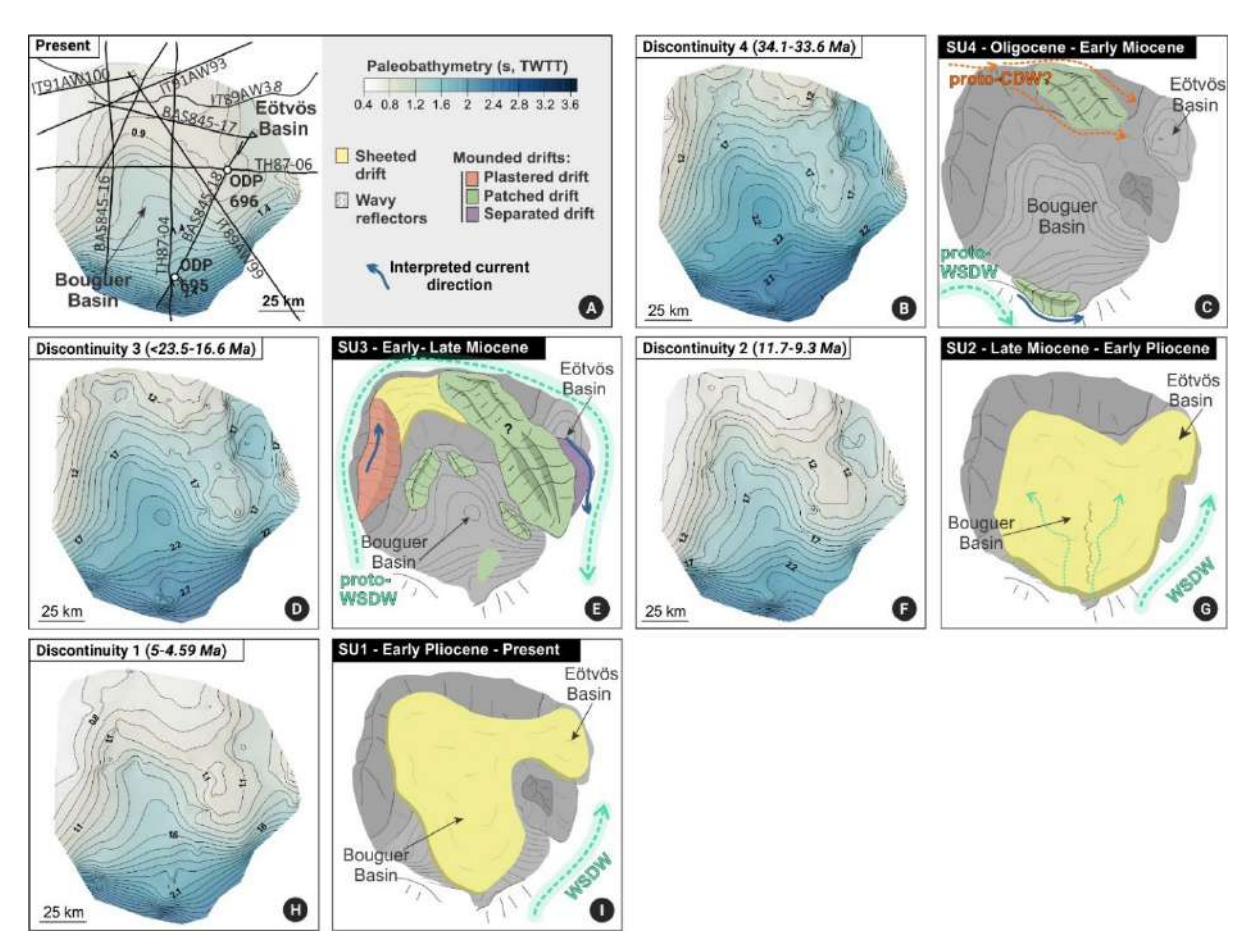


**Figure 4.9.** A) Present seafloor bathymetry in seconds TWTT and location of analyzed MCS profiles. B, D, F and H) Paleobathymetric maps of the discontinuities D4, D3, D2 and D1 respectively. C, E, G and I) Schematic morpho-sedimentary maps displaying the main depositional features formed during SU4 to SU1, respectively. When possible, current directions have been interpreted.

# 4.5.1. Early Eocene to Eocene-Oligocene Transition (EOT): SU5

SU5 corresponds to the sedimentary sequence between the acoustic basement and the discontinuity D4. The correlation between Site 696 and the seismic data is only possible for the upper 75 m of SU5 (Fig. 4.2). However, this unit also encompasses an underlying sedimentary sequence of about 955 m below the bottom of Site 696 (Morales-Ocaña et al., 2023). We interpret SU5 as capturing the tectonic history of the SOM since the opening of the N-S elongated basins, estimated at 45 - 50 Ma based on recent tectonic reconstructions (Fig. 4.10A) (Morales-Ocaña et al., 2023). Above the basement, which most likely includes pre-rift sediments, wedge-shaped sediments with onlapping

reflectors are interpreted as the syn-rift deposits (Fig. 4.3). The heterogeneous and deformed sedimentary fill above these wedges likely constitute the late syn-rift sediments. Above them, locally truncated reflectors by the D4 discontinuity constitutes the post-rift unconformity that formed during the EOT between 34.1 Ma and 33.6 Ma.

The upper 75 m of the SU5, spanning from <37 to 34 Ma, contains a significant amount of locally derived detrital material from exposed parts of the SOM, as described by López-Quirós et al. (2021) (Fig. 4.2). In this stage of the Scotia Arc evolution, the SOM constituted a passive margin with a paleo-water depth shallower than today (López-Quirós et al., 2019, 2021). The SOM remained attached to the Antarctic Peninsula, starting its separation as the Powell Basin opened during the latest Eocene (Barker et al., 1988; López-Quirós et al., 2021). In this context, the main contourite drift of CDS1 develops locally along the southeastern margin of the SOM following a WSW-ENE direction along the shelf-break (Fig. 4.3 and 4.9C). The onset and incipient growth stages of CDS1 to occur during the late Eocene (> 34.1 Ma) influenced by a contour current originating from the Weddell Sea, based on the plastered morphology of the drift (Figs. 4.3C and 4.9C). The onset of the development of this drift could have been favored by the initial subsidence of the SOM during the earliest stages of the opening of the Powell Basin at ~35.5 Ma (López-Quirós et al., 2021). Ongoing subsidence has also been reported in the Weddell Basin around 34 - 28 Ma, allowing Weddell Sea sourced current to reach the southeastern shelf break of the SOM (Huang et al., 2014). In addition, vigorous wind-driven westward circulation in the Weddell Sea during the latest Eocene (~36.2-35.8 Ma) has been reported from Site 696 sediments (Hojnacki et al., 2022; Houben et al., 2019).

# 4.5.2. Oligocene to ~ early Miocene: SU4

SU4 is the thinnest of all the seismic units and is very homogeneous, as shown by the subtle differences in the calculated paleobathymetries of the unconformities bounding this unit (Fig. 4.9B and 4.9D). This unit hosts the preserved record of the entire Oligocene and possibly sediments from the earliest Miocene (Fig. 4.2). We infer a combination of tectonic and climatic processes in the development and ultimate preservation of the SU4 strata. At Site 696, the recovery of sediments belonging to SU4 was poor. Recovered sediments showed a change towards finer-grained sediments (Barker et al., 1988) compared to those recovered from the top of SU5. This change has been previously attributed to ongoing subsidence at the SOM as the Powell Basin continued to open (Lopez-Quirós et al., 2021). In addition, regional glacial terrestrial and marine deposits in King George and Seymour Islands, respectively, have been interpreted to record major cooling episodes with glacier ice extending beyond the coast during the Oligocene (26.7 Ma) and the earliest Miocene (21.8 Ma) (Ivany et al., 2006; Smellie et al., 2021). The interplay between glacial dynamics and ongoing subsidence during the deposition of SU4 could explain the overall low thickness of this seismic unit in the SOM. Similar processes in the Antarctic Wilkes Land margin have been interpreted for the development of a large hiatus, including tectonic subsidence as the Tasman Gateway opened and major erosion by the ice sheet during the EOT (Escutia et al., 2011; Escutia & Brinkhuis, 2014).

Despite the low overall thickness in SU4, two mounded drifts on the southern margin and northern edge mark the development of the CDS1. Ongoing subsidence of the SOM in the early stages of the opening of the Powell basin during SU4 deposition would have placed its southern edge at a greater depth. This could have caused a relative displacement of the water masses affecting the area, allowing the mounded drift to experience its greatest growth. The climatic influence in the development of this mounded drift cannot be ruled out. The intensification of the Weddell Sea Gyre due to widespread glaciation in the southern Antarctic Peninsula and West Antarctica around 33.2 Ma (Hojnacki et al., 2022) might have favored the growth of this mounded drift. This timing coincides with the deposition of organic-rich sediments at Site 696, which have been interpreted to record enhanced upwelling at the southern SOM shelf margin (López-Quirós et al., 2021). However, contour currents from the Weddell Sea affecting the southern margin hardly explain the development of the mounded drift at the northern edge of the study area. This shallow contourite deposition in the north Bouguer Basin (Fig. 4.9C) could be related to a branch of a proto-Circumpolar Deep Water flowing eastward through the SOM. Although the details and intensity of paleocurrent circulation in the Drake Passage-Scotia Sea are still subject to speculation at this period (e.g., Livermore et al., 2007; López-Quirós et al., 2021), this possibility agrees with dynamic features such as topographic flow direction as shown in the proposed conceptual model (Fig. 4.10B).

#### 4.5.3. Middle to late Miocene: SU3

SU3 marks the onset of the widespread development of contourite drifts within the Bouguer and Eötvös basins (CDS2), representing a major shift in the sedimentary deposition from the previous units in the study area. The regional tectonic context may have played an essential role in the redistribution of currents that led to the development of drifts. The SOM might have further continued its deepening as the Powell Basin completed its opening at 21.2 Ma (Eagles & Livermore, 2002). After the end of the Weddell Sea subduction below the SOM (19.5 Ma; Bohoyo et al., 2002; Livermore et al., 2005), the spreading of the Jane Basin (17.4-14.4 Ma; Bohoyo et al., 2002) could cause additional subsidence of the SOM. These processes are in the context of a regional deepening of the Weddell Basin, which northwestern edge deepened about 0.5–1 km since the Oligocene (Huang et al., 2014). All this together might progressively allow the intrusion of deeper water masses from the Weddell Sea into the Bouguer and Eötvös Basins during the middle Miocene. The contourite drifts of SU3 are mainly associated with underlying basement-controlled structures (Fig. 9E), pointing to basin morphology as the main control in bottom current deposition. The inferred current directions from the plastered and separated drifts (see section 4.2.2) are consistent with a clockwise current entering the Bouguer and Eötvös basins from the Weddell Sea (Fig. 4.9E and 4.10C).

Sediments from Site 696, coeval to the deposition of the CDS2 contourite drifts, are mainly composed of diatoms, which account for up to 90% of the sediments (Barker et al., 1988) (Fig. 4.2). The change in lithology from the previous unit is reflected by a strong peak in the acoustic impedance, which correlates with the high amplitude reflectors that locally characterize D3 (Fig. 4.2). The significant development of the contourite drifts during SU3 could be favored by the high productivity

and the fairly constant high sedimentation rates (Barker et al., 1988). Increased productivity is coherent with open water conditions inferred from sediments recovered by the SHALDRIL II (Shallow Drilling on the Antarctic Continental Margin) expedition located in the conjugated margin of the Antarctic Peninsula during the middle Miocene (Tibbett et al., 2022). No permanent sea ice has been described during the middle Miocene in the northernmost part of the Antarctic Peninsula, although widespread sea ice would occur during winter months (Anderson et al., 2011a). Indeed, major West Antarctic ice sheet or Antarctic Peninsula ice sheet were absent from the Middle Miocene to the early part of the Late Miocene (Chow & Bart, 2003; Kennett & Barker, 1990). However, a possible first expression of the northward expansion of the West Antarctic and Antarctic Peninsula ice sheets can be related to the presence of ice-rafted dropstones in Site 696 from 366 mbsf to the top of the core (Barker et al., 1988). This depth roughly coincides with the boundary between SU3d and SU3c (Fig. 4.2). These two subunits together report the higher thickness within the mounded drifts. Seismic subunits SU3b and SUa (<11.7 Ma - > 9.8 Ma) are locally observed either maintaining the growth of existing mounded drifts (Fig. 4.6A), or starting the burial phase of the CDS2 (Fig. 4.6B). The less growth of these mounds during SU3b and SU3a and an increased presence of ice-rafted dropstones could indicate the onset of the cooling trend in the study area.

# 4.5.4. Late Miocene to early Pliocene: SU2

Starting in the late Miocene, SU2 is characterized by predominating aggradational deposits, although wavy reflectors are locally present. This suggests a change in the current regime in the SOM, with likely weaker bottom currents compared to the previous unit. High and fairly constant sedimentation rates are described during this time period (Barker et al., 1988). The correlation of SU2 with sites 695 and 696 reveals a drastic sedimentary change with respect to SU3, with the replacement of the biosiliceous fraction by a large increase in the detrital component. We relate this increase in detrital input to the onset of the northward expansion of the West Antarctic and Antarctic Peninsula ice sheets and perennial sea ice, which has been reported to begin during the late Miocene (Anderson et al., 2011; Bart et al., 2005; Levy et al., 2019). Therefore, this unit could be associated with the onset of a more persistent, yet dynamic, ice sheet over the South Orkney Islands. Supporting this notion, ice-rafted dropstones of all sizes are commonly present in sediments from Site 696 within SU2 (Barker et al., 1988).

Interestingly, the burial of CDS2 by D2, sometime between 11.7 and 9.8 Ma, is generally concurrent with the regional discontinuity of the Reflector-c in the southern Scotia Sea, dated between 14.2 and 8.4 Ma (Maldonado et al., 2006; Pérez et al., 2021; Weber et al., 2019). Sedimentation above the Reflector-c shows significant drift development, representing the onset of the influence of bottom currents in the Scotia Sea (Hernández-Molina et al., 2006; Maldonado et al., 2006; Pérez et al., 2019). The onset of this major change in the oceanic circulation pattern has been interpreted to be controlled by the northward inflow of Weddell Sea Deep Water (WSDW) into the Scotia Sea, interacting for the first time with the Circumpolar Deep Water (CDW) (Maldonado et al., 2003, 2006; Pérez et al., 2014, 2017, 2019). Therefore, we postulate that the cessation of contour

current deposition within the SOM results from the oceanographic reorganization as Jane and Scan basins formed at the southern Scotia Sea. Indeed, the complete opening of the Jane Basin, which ends at 14 Ma, would help the canalization of the WSDW towards the Scan Basin channeled through Orkney Passage and Bruce Passage (Hernandez-Molina et al., 2007; Fig. 4.10D).

#### 4.5.5. Early Pliocene to present: SU1

SU1 starts developing around 5-6 Ma and lasts until the present. During the deposition of this last unit, the regional tectonic configuration was similar to the present, with the main pathways for the ocean currents around the SOM already open (Fig. 10F). Therefore, observed sedimentation changes are attributed mainly to climatic changes. While SU2 was characterized by its tabular shape with scattered wavy reflectors, SU1 is locally characterized by erosional channels (Fig. 4.7), fill sequences (Fig. S4.5), and local plaster drifts (Fig. 4.3). Sediments from Site 696 record an increase in the biosiliceous component relative to the previous unit. However, diatom assemblages are reported to be poorly to moderately preserved compared to the excellently preserved diatoms of the SU3 (Gersonde & Burckle, 1990). We interpret this change as likely driven by the establishment of more permanent and stable ice sheets in the Antarctic Peninsula in the early Pliocene (approximately 5.3–3.6 Ma) (Anderson et al., 2011). By this time, the Bouguer and Eötvös Basins would be close to the maximum extension of the grounded ice sheet, which has been estimated to be correlated with the 300-350 m bathymetric contour lines (Dickens et al., 2014) (Fig. 4.10E). In this context, SU1 seismic and sedimentary data are coherent with a proximal glaciomarine setting.

#### 4.6. Conclusions

The interpretation of the available MCS profiles and the correlation with the chronostratigraphic information from Sites 696 and 695 in the Bouguer and Eötvös Basins have allowed us to determine the timing of the onset of ocean currents in the southern margins of the SOM and their evolution.

- We identify five seismic units that are interpreted to record different phases in the tectonic, climatic, and paleoceanographic evolution of the region. Tectonic and climatic controls might interplay role within the studied deposits until the early Pliocene when climatic influence became the main controlling factor.
- Evidence of bottom-current activity has been observed, for the first time, since the Late Eocene, mainly restricted to the shelf-break, identified as CDS1 in this study. This activity is coherent with the influence of a proto-Weddell flow that would reach the southern margin of the SOM. The deepening of the SOM, resulting of its separation from the Antarctic Peninsula and the Powell Basin formation, placed the southern margin to progressively greater depths likely facilitating the widespread development of these mounded drifts, characterized as CDS2. The inferred current direction is coherent with a clockwise circulation in the basins that emplace the contour current deposits mainly associated with the basement highs surrounding the basins.

- The cessation of major current influence in deposition at the middle Miocene (~11.7-9.8 Ma) coincides with the onset of the major development of contourite drifts in the Scotia Sea (~8-14 Ma). This suggests to us that a major re-organization of current pathways occurred as a result of the onset of the intrusion of Weddell Sea Deep Water into the Scotia Sea favored by the full opening of the surrounding basins (e.g., Jane and Scan basins).
- The onset of more persistent glaciations becoming stable at 5.3–3.6 Ma near the SOM points to the study area being in a more proximal setting, also supported by the local observation of erosive features.

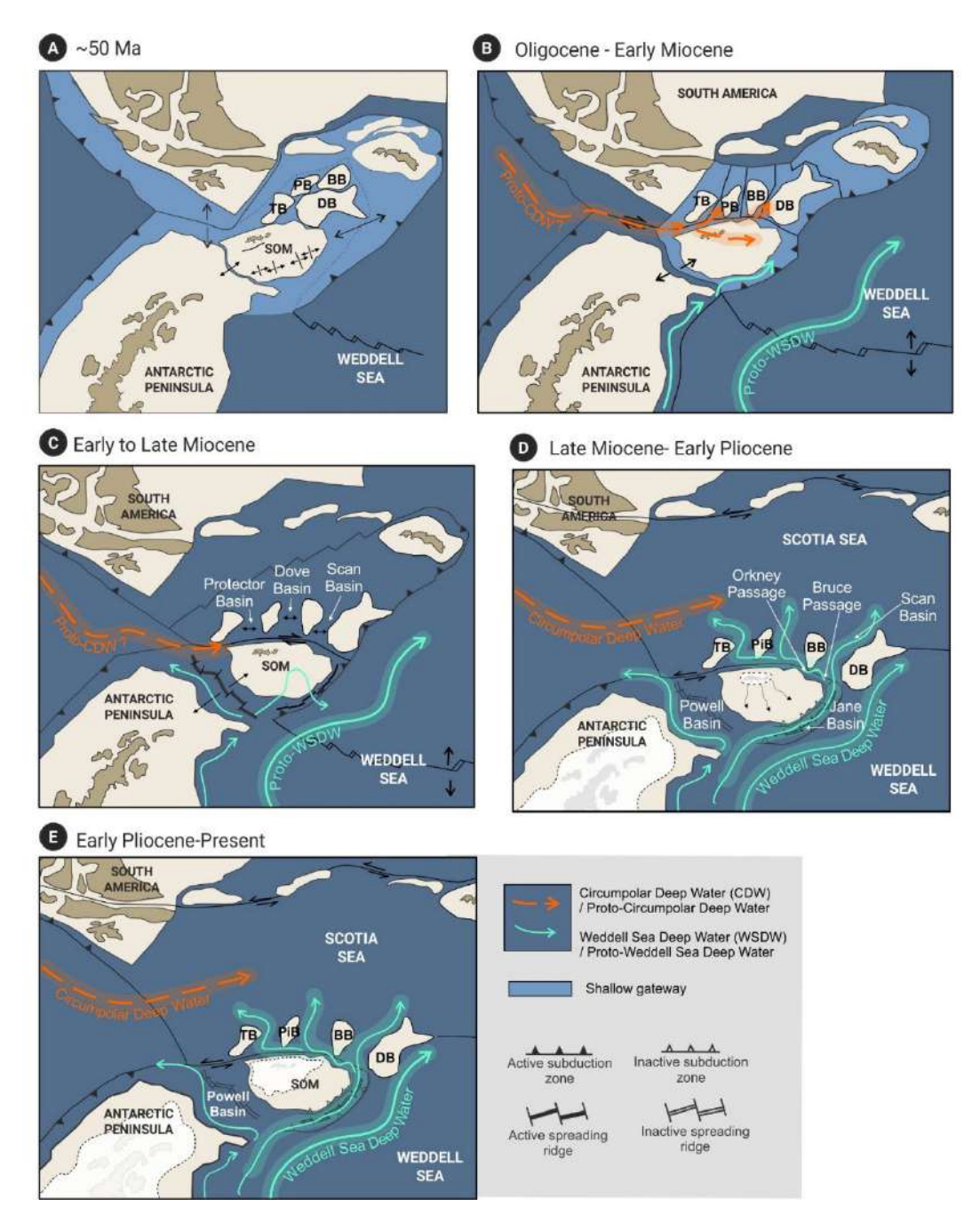


**Figure 4.10.** Schematic paleogeographic and paleoceanographic reconstruction for the five evolutionary phases presented in this study.



Supplementary material to

CHAPTER 4

# Supplementary material to CHAPTER 4

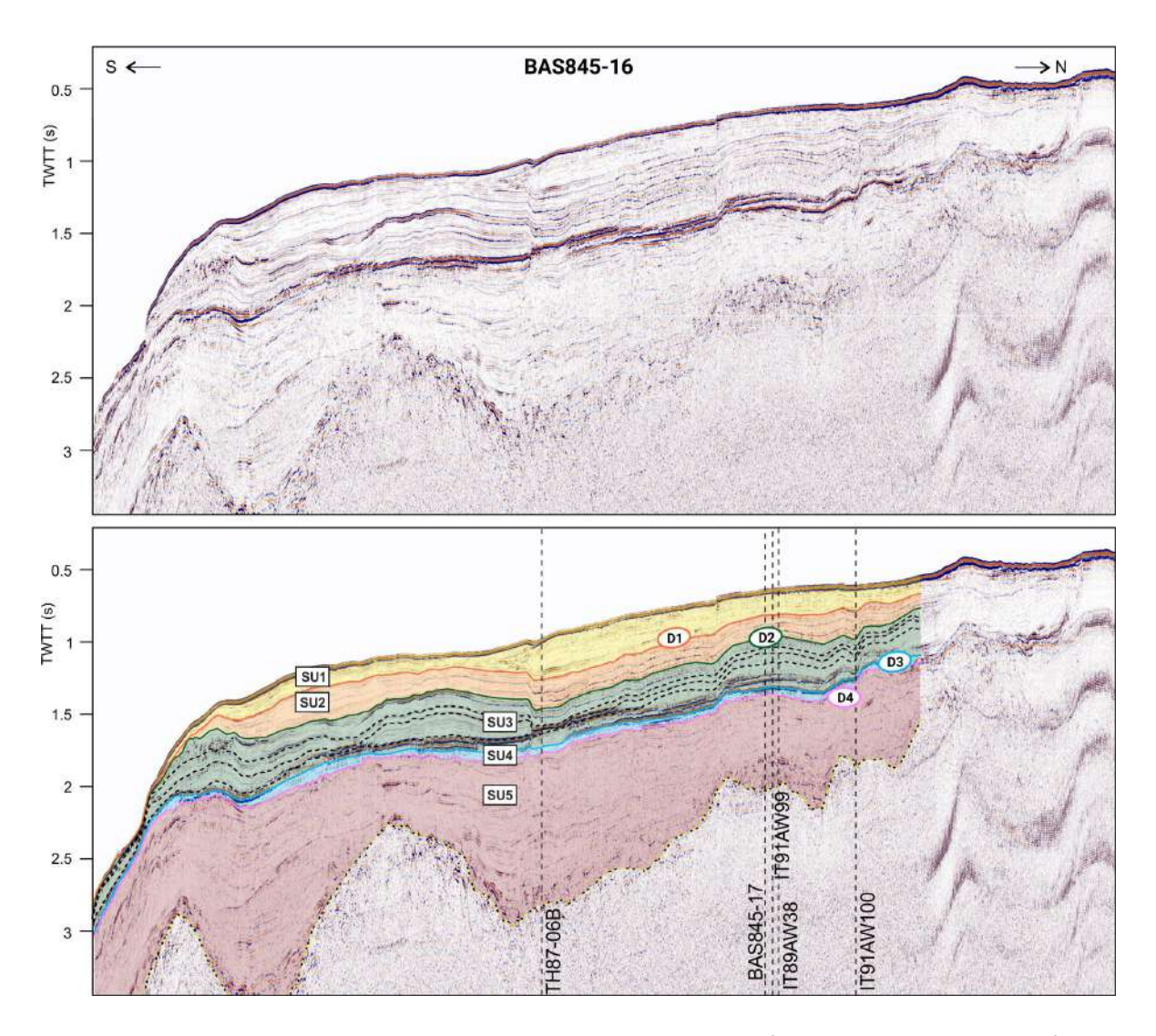


**Figure S4.1**. Uninterpreted and interpreted S-N orientated MSC profile BAS845-16. Location of the profile is shown in Figure 4.1C.

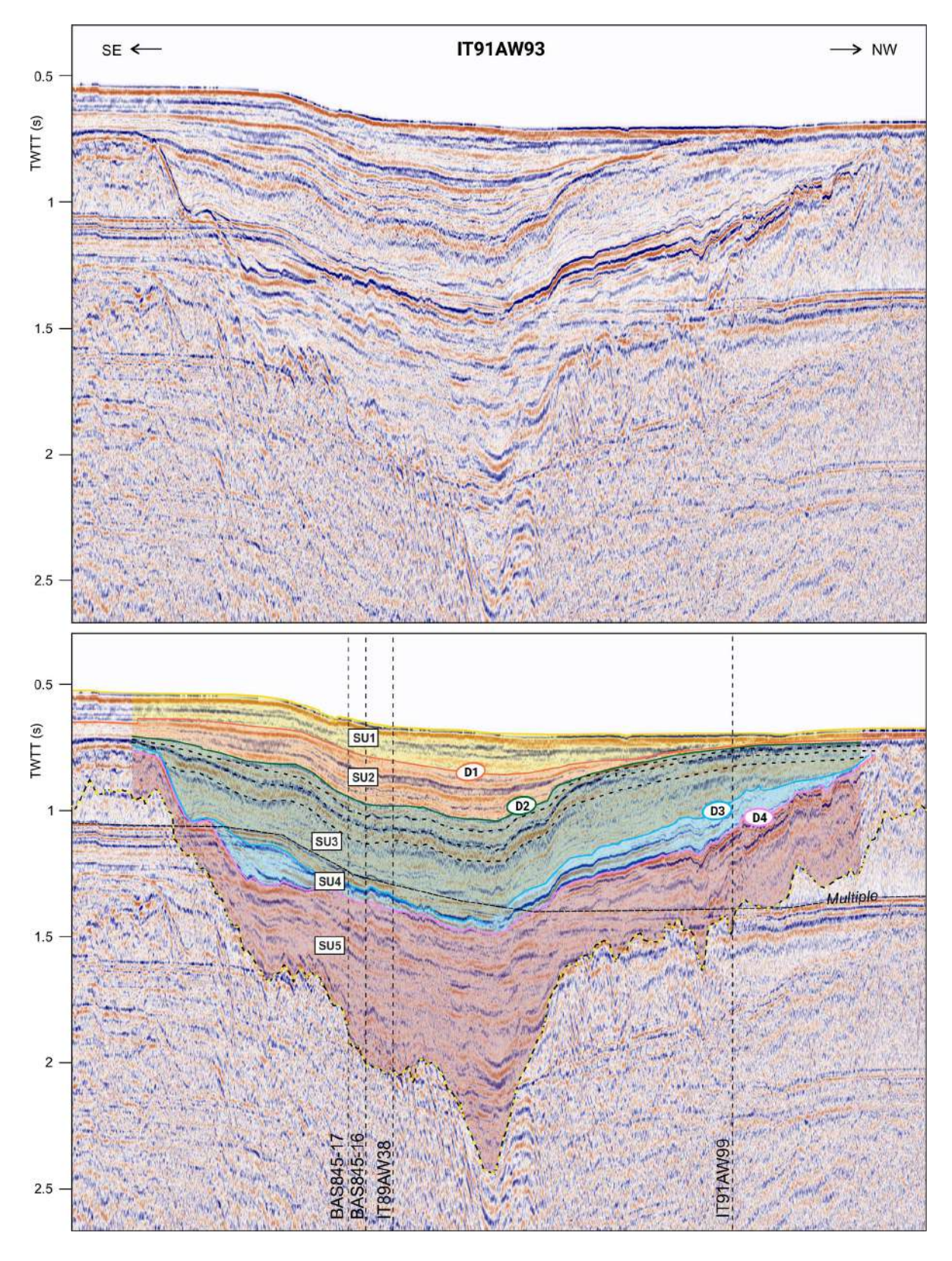


**Figure S4.2**. Uninterpreted and interpreted SE-NW orientated MSC profile IT91AW93. Location of the profile is shown in Figure 4.1C.

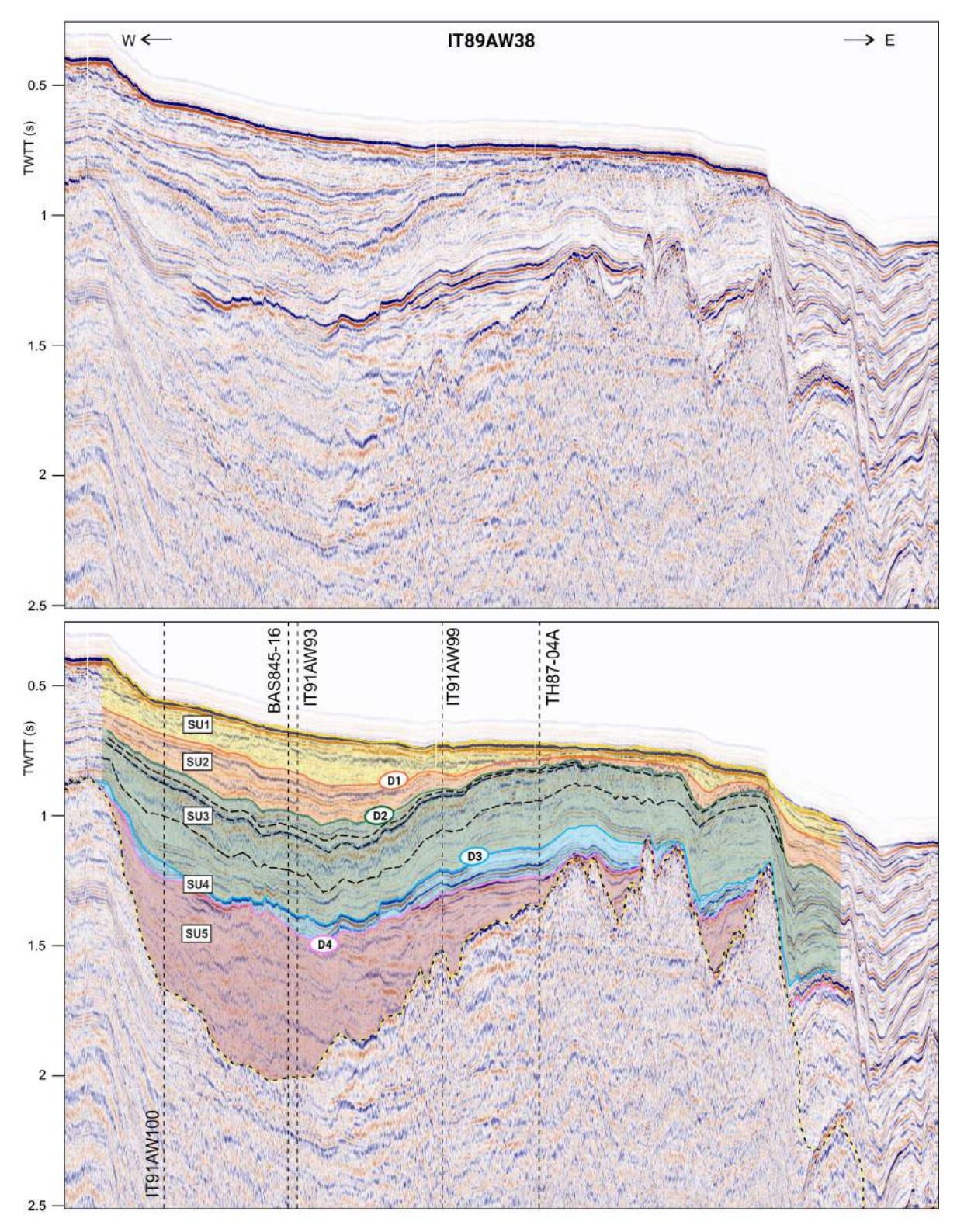


**Figure S4.3** Uninterpreted and interpreted W-E orientated MSC profile IT89AW38. Location of the profile is shown in Figure 4.1C.

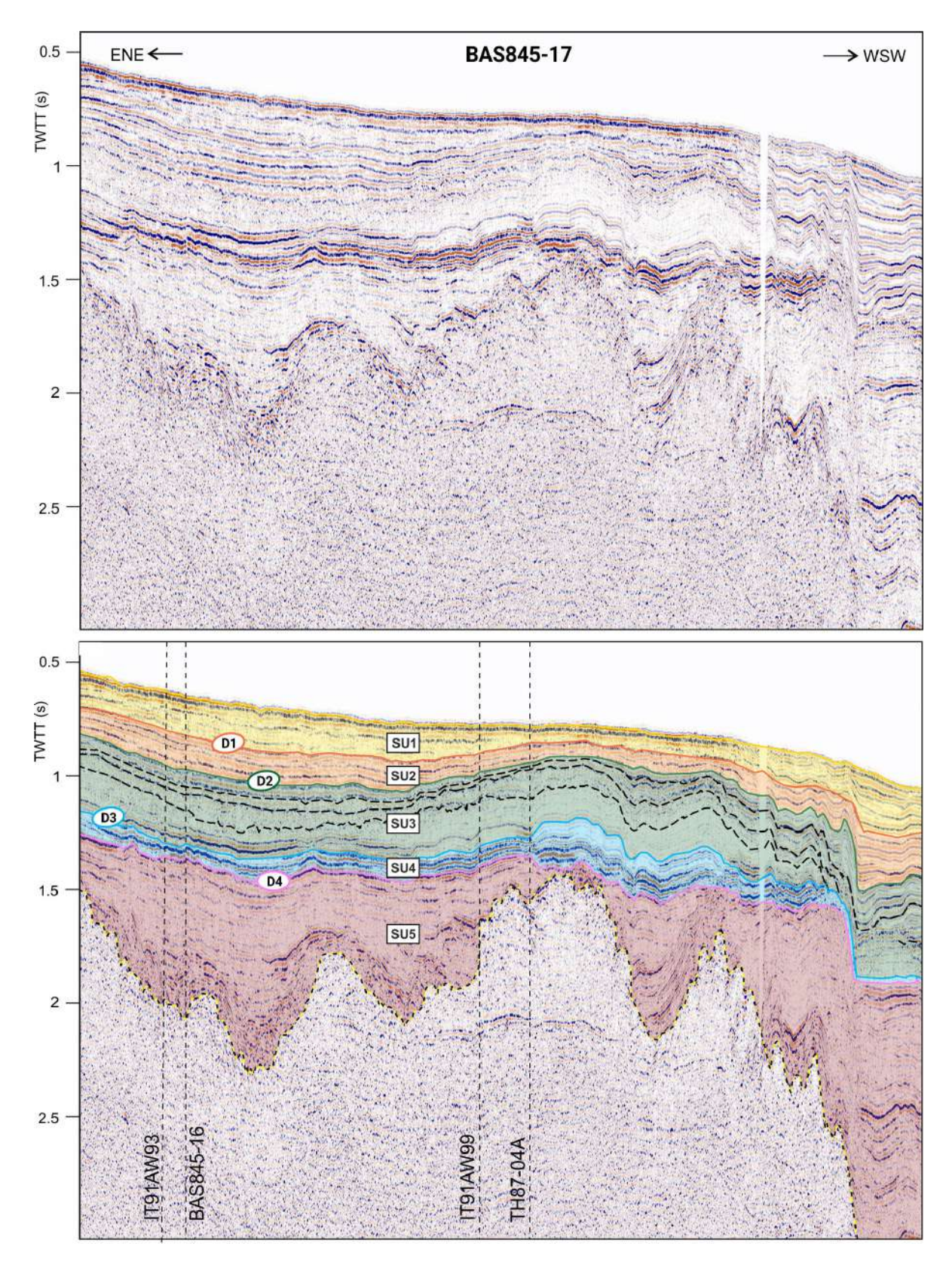


**Figure S4.4** Uninterpreted and interpreted ENE-WSW orientated MSC profile BAS845-17. Location of the profile is shown in Figure 4.1C.

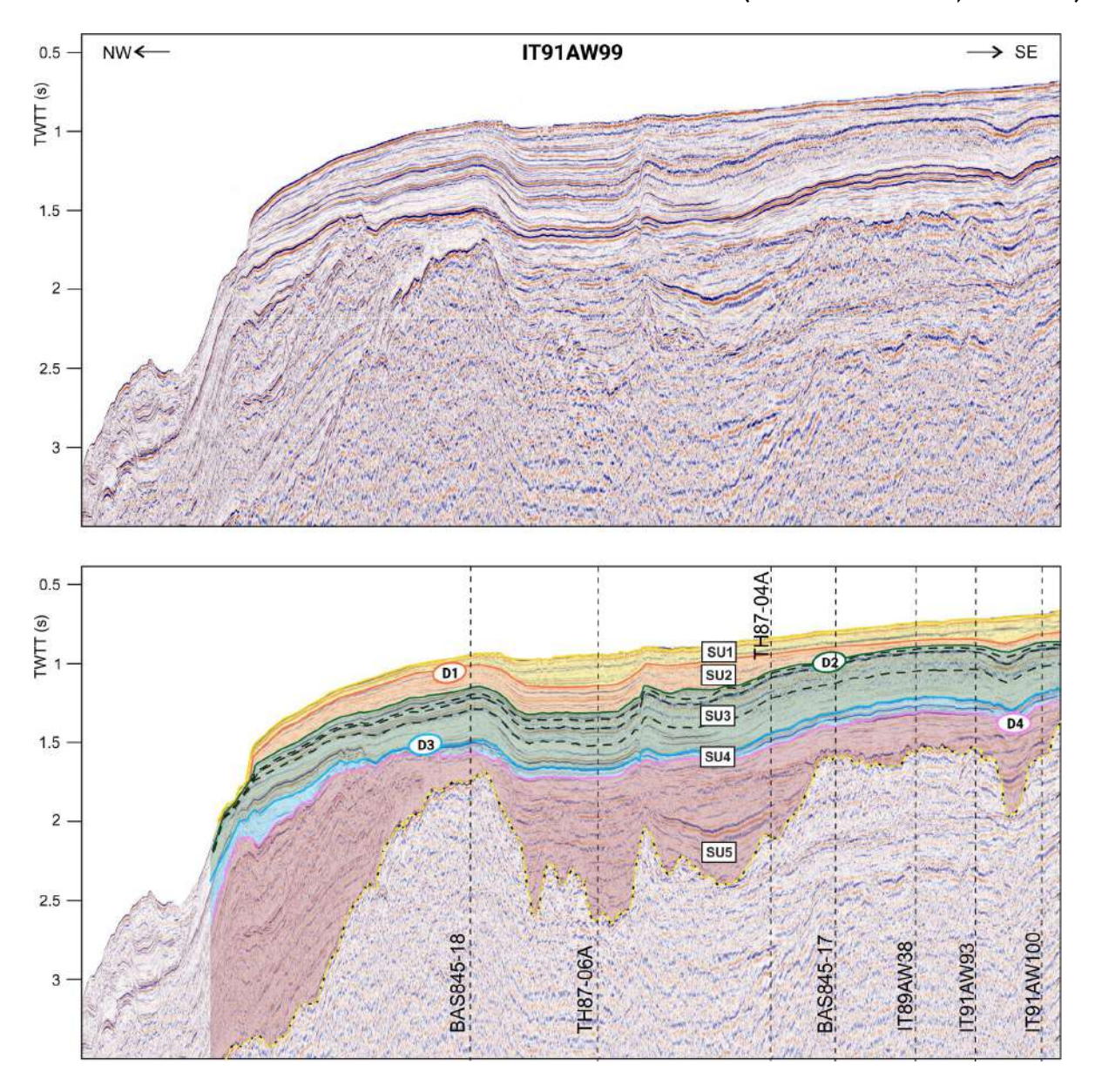


**Figure S4.5**. Uninterpreted and interpreted ESE-WNW orientated MSC profile IT91AW100. Location of the profile is shown in Figure 4.1C.

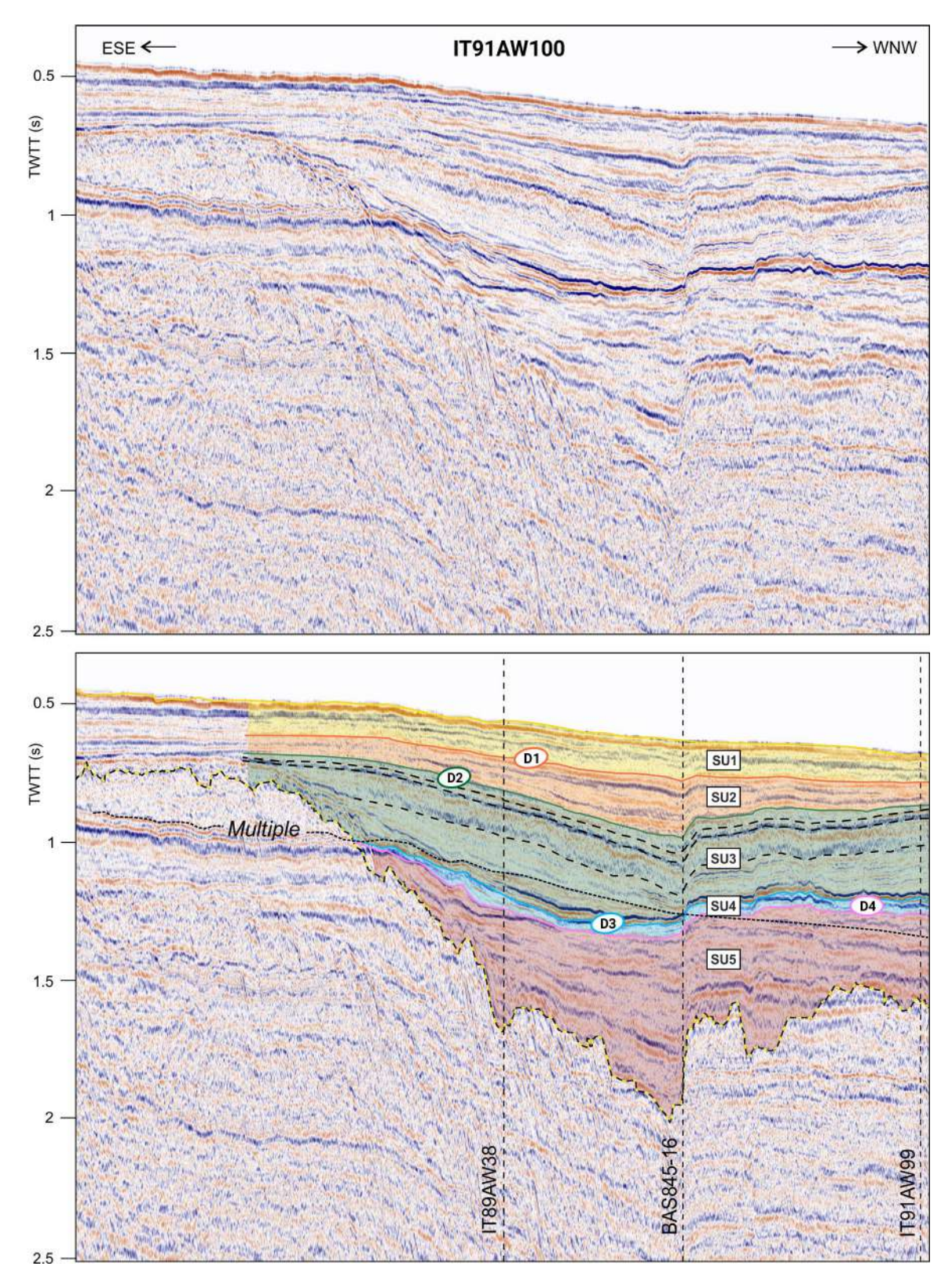


**Figure S4.6**. Uninterpreted and interpreted ESE-WNW orientated MSC profile IT91AW100. Location of the profile is shown in Figure 4.1C.



# CHAPTER 5

Unraveling bottom current influence on diatomaceous contourite drifts in the Bransfield Strait (Antarctic Peninsula) throughout the past millennium

CHAPTER 5: Unraveling bottom current influence on diatomaceous contourite drifts in the Bransfield Strait (Antarctic Peninsula) throughout the past millennium

# **Abstract**

The Antarctic Peninsula is one of the Antarctic regions that has been severely affected by ongoing climate warming. The Bransfield Basin, located at the northern tip of the Antarctic Peninsula, is influenced by complex interactions between oceanographic frontal systems, coastal influence, and sensitivity to large-scale atmospheric circulation patterns. Here, we report findings from two welldated cores retrieved from two mounded deposits located in the deep basin and on the southern flank of the East Bransfield Basin. Our aim is to better understand the effect that climate variability has in frontal system migrations and bottom currents in this region during the past millennium. Multiproxy analyses in these sediments confirms the influence of bottom contour currents in the development of the mounded deposits. Three distinct facies are interpreted to record increasing bottom current intensity from Facies 1 (finely laminated organic rich sediments) to Facies 3 (apparently non-laminated coarse silts). Varying bottom current intensities strongly influence the fluctuations in organic matter content as well as sediment winnowing/sorting during the deposition of the diatomaceous contourite drifts. A marked environmental change at 600 cal yr BP towards more open water conditions coincides with an increase in detrital material that is interpreted to result from meltwater processes linked to the retreat of ice sheet/glaciers. This change includes the first appearance of Facies 3 linked to the presence of Fragilariopsis kerguelensis. This points to Circumpolar Deep Water intrusions into the Bransfield Basin, enhanced by a tendency towards more variable SAM-positive phases and La Niña conditions, and regional warming trend in the eastern Antarctic Peninsula.

#### 5.1. Introduction

Among Antarctic margins, the Antarctic Peninsula has been the most rapidly warming region over the past decades (Jones et al., 2016; Vaughan et al., 2003). There, both atmosphere and ocean warming have strong impacts on the vulnerability of the regional ice sheets (Bentley et al., 2009; Smith et al., 1999). Additionally, marine-based ice shelves are exposed to ocean heat flux, especially where the Antarctic Circumpolar Current (ACC) is closest to the Antarctic continent (Gille et al., 2016) allowing the warm Circumpolar Deep Water (CDW) to intrude on the continental shelves and melt the ice shelves (Dinniman et al., 2012; Nakayama et al., 2018; Pritchard et al., 2012; Rignot et al., 2019). In the Antarctic Peninsula region, the warm CDW enters the Bransfield Strait from the south while the cold Weddell Sea Surface Water enters from the north (Wilson et al., 1999). Sediments from the Bransfield Strait are therefore ideal to study the past interaction between these two water masses, which transport depends on the variability of the regional fronts (Gordon & Nowlin, 1978; Whitworth et al., 1994).

At present, the CDW shows significant variability within the Bransfield Basin from year to year (Gordon et al., 2000; Gordon & Nowlin, 1978; Wilson et al., 1999). Its average contribution to the Eastern Bransfield Basin (EBB) deep water masses varied between 35 to 55% between 2004 and 2019 according to Damini et al. (2022), although other authors have pointed to its absence or weak presence (Gordon & Nowlin, 1978; Wilson et al., 1999). The deep waters variability in the Bransfield Basin is linked to regional atmospheric patterns related to a complex interconnection between El Niño-Southern Oscillation (ENSO) and the Southern Annular Mode (SAM) climate modes (Damini et al., 2022; Dotto et al., 2016; Gordon et al., 2010). During positive phases of the SAM and negative phases of ENSO, stronger westerly winds shift the position of the Southern Antarctic Circumpolar Current Front and the Southern Boundary of ACC towards the Antarctic Peninsula (Damini et al., 2022; Dotto et al., 2016). The opposite trends are observed during SAM-negative phases and ENSO-positive phases.

The variability of deep water in recent decades is relatively well known from instrumental climate records of the Southern Ocean. However, sedimentary records from the Bransfield Basin are essential to study its past variability and how it affected Antarctic climate and cryosphere dynamics. Particularly useful are laminated sedimentary records containing a seasonal to decadal resolution record. On Antarctic margins, laminated sediments are associated with contourite deposits. Contourites are defined as sediments deposited by the persistent action of bottom currents (Stow et al., 2002). These deposits have been particularly useful for past sea ice/ice sheet and ocean front dynamic reconstructions (Camerlenghi et al., 2001; Escutia et al., 2011; Escutia & Brinkhuis, 2014). To provide robust reconstructions, it is essential to understand how these currents affect the burial and preservation of paleoenvironmental indicators in the sediments (Bahr et al., 2014; Salabarnada et al., 2018).

To elucidate the effect of different deep water masses on sedimentation in the Bransfield, we collected two late Holocene marine cores (TG02 and TG03) from the EBB. The two cores were strategically taken in two different contourite depositional systems (García et al., 2019) located at different depths in order to capture the action of different bottom currents entering the Basin, but close enough (about forty kilometers apart) to record common regional paleoenvironmental variability. The multidisciplinary study of the two cores included the analysis of physical properties, Computed Tomography Scans, major element composition by X-Ray Fluorescence scanning, grain size (both bulk and sortable silt portion), and diatom assemblages at different resolutions. The age control was developed from radiocarbon dates on bulk sediments along the cores and radioactive lead (210Pb) on core tops. Three different facies related to changes in bottom current intensity and ventilation in the EBB are characterized that are linked to ENSO/SAM variability during the last millennium.

# 5.2. Geological and oceanographic setting

The Bransfield Basin is located north of the Antarctic Peninsula, in the confluence zone between the northwestern Weddell Sea and the southern Scotia Arc (Fig. 5.1). The Bransfield Basin is a back-arc basin whose opening is related to the slab rollback of the former Phoenix Plate that began

about 3.3 Ma ago (Galindo-Zaldívar et al., 2004; Jabaloy et al., 2003). This basin is divided into a West, a Central, and an East basins that are separated by sills shallower than 1,500 m (Gordon & Nowlin, 1978). The Central Bransfield Basin (CBB) and EBB are the largest and deepest (Fig. 5.1). CBB presents a smooth bathymetry, while the EBB is narrower and divided, in turn, into three separate troughs (Gràcia et al., 1997). This complex topography controls ocean circulation in the Bransfield Basin, restricting influence from the surrounding ocean (Gordon & Nowlin, 1978).

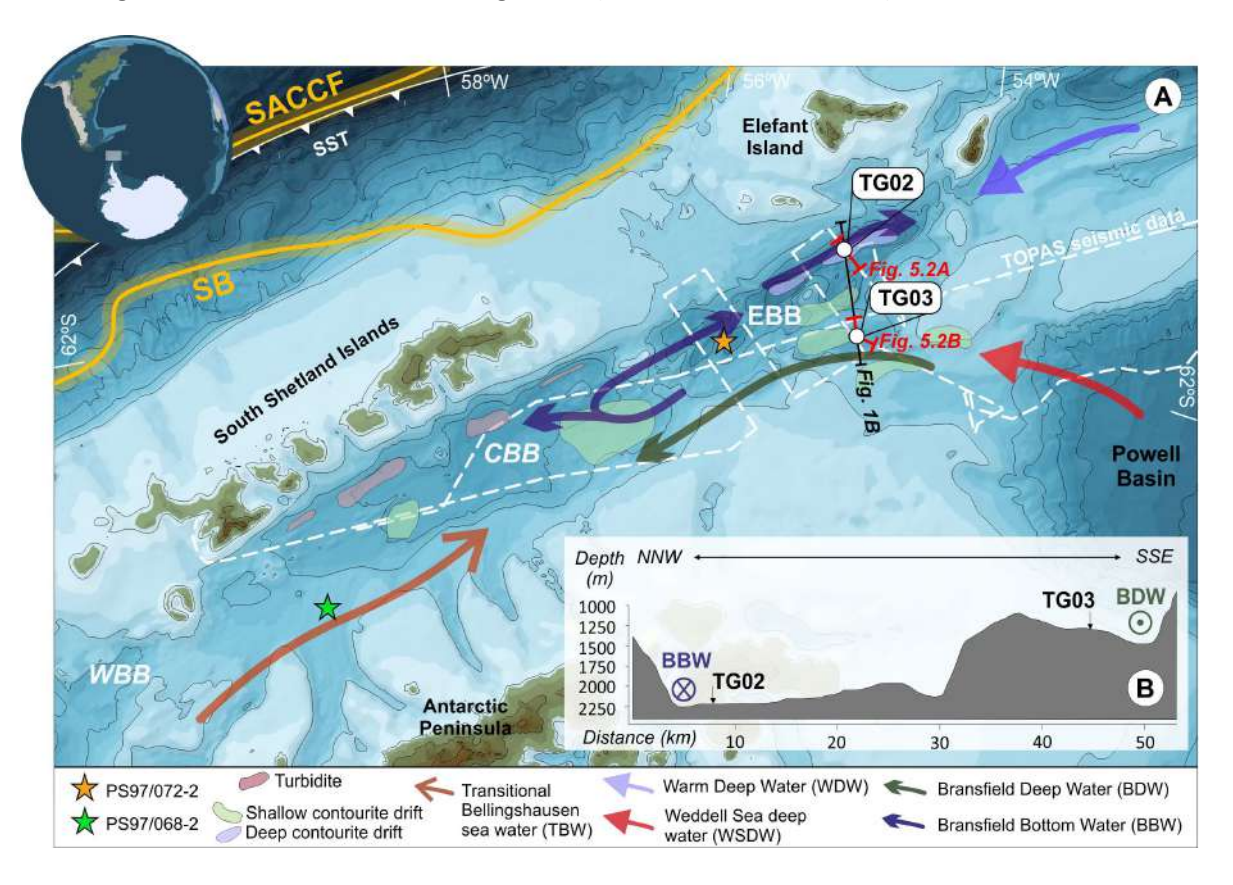


**Figure 5.1.** A) Geographic and oceanographic setting of the study area. The bathymetry was extracted from GEBCO 2019. Gravity cores TG02 and TG03 are located in the Eastern Bransfield Basin (EBB). CBB and WBB stand for Central Bransfield Basin and Western Bransfield Basin, respectively. Colored arrows represent the ocean currents in the area inferred by Liu et al. (2022). Turbidites and contourite drifts identified by Liu et al. (2022) using MCS data are shown by: red shaded areas for turbidites, and purple and green shaded areas for the deep and shallow contourite depositional systems of the EBB, respectively. The core PS97/072-2 and PS97/068-2 are positioned with stars (Vorrath et al., 2020). B) Bathymetric profile of a transect between TG02 and TG03.

At present, the Bransfield Basin receives distinct water masses from the Bellingshausen Sea, the ACC, and the Weddell Sea (Liu et al., 2022). The CBB and EBB show significant differences between their deep and bottom waters (Wilson et al., 1999). The CBB traps denser water than the EBB due to the sinking of well-preserved shelf water from the Weddell Sea in that region and its better ventilation (Dotto et al., 2016). The bottom waters of the CBB are colder and denser than the EBB bottom waters, despite being 500 m shallower, with a minimum temperature of -1.76°C (Wilson et al., 1999). However, the EBB bottom waters may have a more complex origin and stratification. Wilson et al.

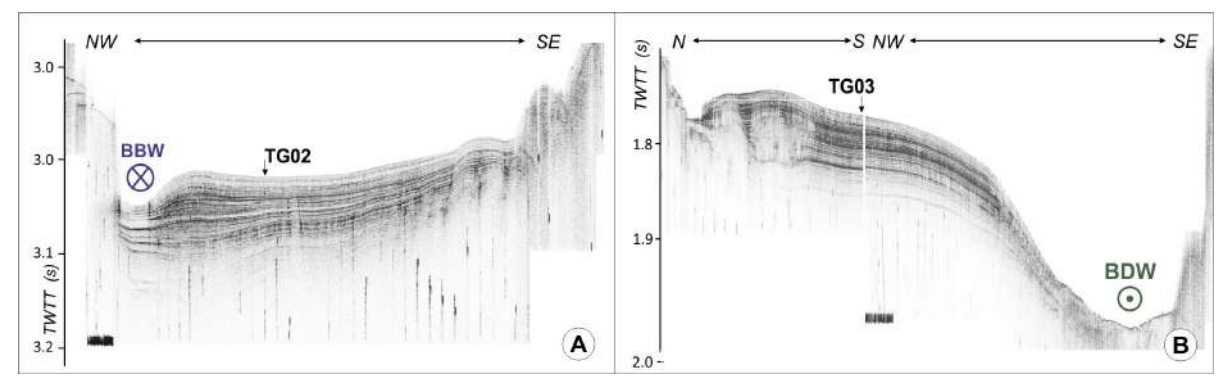
(1999) state that while the bottom waters of the CBB appears to be the product of a single process, EBB bottom waters results from a mixture of (1) Central Basin sill water, (2) Weddell Sea sill water, and (3) Weddell Sea bottom water and/or Central Basin Bottom Water. Among these, the Weddell Sea sill water is the predominant end-member (40%–60%) throughout most of the EBB, but Central Basin sill water contributes the most to the deepest EBB subbasins, where it reaches 50%.

Figure 5.1, illustrates the depositional bodies identified in the Bransfield Basin by Liu et al. (2022). While reports of turbidites exist along the northern margin of the CBB, the prevailing deposits consist of contourites. This depositional bodies result from the interplay between various water masses with the complex seafloor topography of the Bransfield Basin (Ercilla et al., 1998; García et al., 2009; Liu et al., 2022). A shallow contourite depositional system develops in the southern flank of the CBB and the EBB by the influence of the Bransfield Deep Water (BDW) (Liu et al., 2022), which core is located at a depth of 750 m (Dotto et al., 2016; Gordon et al., 2000; Fig. 5.1). The bottom part of the EBB is occupied by a deep contourite depositional system associated with the Bransfield Bottom Water (BBW) (García et al., 2019), with its core situated at a depth of 1750 m (Dotto et al., 2016; Gordon et al., 2000; Fig. 5.1). These two contourite depositional systems are inferred to develop since the middle Pleistocene (0.7–0.9 Ma) (Liu et al., 2022).

# 5.3. Materials and methods

## 5.3.1. Core location

Two gravity cores (TG02 and TG03) were collected from the EBB,  $\sim$  40 km apart (Fig. 5.1), during the POWELL2020 cruise on board the R/V Hespérides (Fig. 5.1). TG02 is located in the northeastern bottom EBB (Fig. 5.1; 61° 39.293' S, 55° 7.651' W) at a depth of 2225 m below sea level (mbsl) and collected 383 cm of sediment. TG03, located at the southern flank of the EBB (Fig. 5.1; 61° 59.189' S, 55° 0.442' W) at a depth of 1300 mbsl, recovered 437 cm of sediment. The two sites, TG02 and TG03, were strategically selected from the deep and shallow contourite depositional systems (García et al., 2019; Liu et al., 2022), respectively, guided by high-resolution Topographic Parametric Sonar PS 18 (TOPAS) images taken also during the POWELL2020 cruise (Fig. 5.2A and 5.2B).



**Figure 5.2.** TOPAS profiles that cross the TG02 (A) and TG03 (B) respectively. The direction of the BBW and BDW currents are inferred form García et al. (2019) and Liu et al. (2022). Position of the profiles is shown in Figure 5.1.

## 5.3.2. Core scanning, description, and sampling

Computerized Tomography scanning (CT-Scan) was conducted on whole cores using clinical equipment (Hitachi ECLOS 16 Multislice CT) at the Veterinary Teaching Hospital Rof Codina of Lugo (Galicia, Spain) following Mena et al. (2015) acquisition protocol. CT-Scan was used to detect density changes by analyzing small-scale stratigraphic changes and internal structures of the sediment cores (Duliu, 1999; Fouinat et al., 2017; Mena et al., 2015). The shown CT-Scan images share the same relative color scale for both cores. A modified color scale was used in areas where colors were saturated.

Whole cores were split into two working halves. One working half was used to conduct a detailed visual core description on both cores, focusing on sedimentary textures and structures (i.e., lamination, bioturbation, sediment contacts), following the methods detailed in Escutia et al. (2011). On the archive half, high-resolution digital images in visible light were obtained using the Geotek Geoscan IV high-resolution camera at the Spanish Geological Survey (IGME, Spain). Physical properties (magnetic susceptibility, gamma-ray density, electrical resistivity, and P-wave velocity) were also measured on the archive half of the split core surface at 1 cm resolution using the Geotek Multi-Sensor Core Logger (MSCL) at the Spanish Geological Survey (IGME, Spain). In this work, the interpretation is focused on the gamma-ray density (GRD), which is complementary to high-resolution CT-scan images, and on magnetic susceptibility (MS) data. GRD data provide a high-resolution bulk density record, indicating lithology and porosity changes (Blum, 1997). MS data can be used to detect the amount of magnetic material in the sediment (Robinson, 1992).

Major element composition was also measured on the archive half of the split cores surface using Geotek MSCL-X-ray fluorescence (XRF) at the IGME. The scan was performed at 0.5 cm intervals during two separate runs. For the first run, a 1 mm window size detector resolution was selected, in which two beams were measured: beam 1 (Al - Ni) at 10 kV and beam 2 (Fe - U) at 40 kV. For the second run, a 10 mm window size was selected, in which 3 beams were measured: beam 1 (Al - Ni) at 10 kV, beam 2 (Fe - U) at 40 kV, and beam 3 (Cd - Ba) at 50 kV. Increasing the detector's window size improves the quality of the received beads for the less common elements, mainly Ba-oriented. XRF and MSCL data recorded from uneven core surface areas were not taken into account due to their low reliability.

## 5.3.3. Grain-size analysis

Samples for grain size analysis were taken from each core at approximately 10 cm intervals. In total, we measured 64 samples in TG03 and 55 in TG02 at the Sedimentology Laboratory of the University of Bordeaux. For this work, we were interested in the grain size distribution of both the bulk sample and the detrital fraction. To obtain the detrital fraction, each sample was treated with 1-2 ml HCl 37%, 20ml  $H_2O_2$ , and 20 ml NaOH (1M) to eliminate the carbonates, organic matter, and biogenic silica fractions, respectively. The grain size distribution of each sample (bulk and detrital) was measured using a Malvern Instruments Mastersizer hydro2000G. The output data were then

processed using the GRADISTAT package (Blott & Pye, 2001). We followed the Folk & Ward (1957) geometric classification in µm for sorting, skewness, and kurtosis analysis.

Within the detrital fraction, we focus on the analysis of the sortable silt (10-63  $\mu$ m, SS), which is the fraction most easily remobilized by the action of currents (McCave et al., 1995). The weighted mean size of the sortable silt fraction (denoted by  $\overline{SS}$ ) has been used as a proxy to assess changes in bottom flow speed in deep-sea sediments, assuming that the sediment is controlled by current sorting during deposition, with a coarser mean size when the flow is stronger (McCave et al., 1995; McCave & Hall, 2006). To test whether the sediment deposits of our studied cores confirm to this assumption and obtained values are suitable for reconstructing flow speed, we followed the methodology of MacCave & Hall (2006). In current-sorted regime, a positive correlation between  $\overline{SS}$  and the 10 to 63- $\mu$ m fraction percentage (SS%) exist. In that case, the current flow speed (U) variation along the cores can be obtained following the equation calibrated for the Scotia-Weddell Sea region:  $\overline{SS}=0.59U+12.23$  (McCave et al., 2017).

#### 5.3.4. Diatom abundance and assemblage analysis

Slides for quantitative analysis were made via a settling technique that produces a random distribution of specimens (Warnock & Scherer, 2014). Norland Optical Adhesive #61 was the mounting media. Quantitative analyses of the diatom composition were completed on 60 samples from TG03 and 45 samples from TG02. All the samples were examined at 1000X on an Olympus CX31 or BX60 microscope. As in other sediment cores in the area (e.g. Barcena et al., 1998; Vorrath et al., 2020), Chaetoceros subg. Hyalochaete (resting spores and vegetative valves) (CRS) were extremely abundant. Therefore, to evaluate the relative contribution of the remaining assemblage, we counted diatom valves other than CRS, a commonly used technique (e.g., Sjunneskog & Taylor, 2002). At least 400 specimens were counted per slide along non-overlapping transects. We focused on species or groups with abundances >2% for interpretation. We have selected those with environmental significance for their interpretation in the set of species observed.

## 5.3.5. Statistical analysis

To elucidate which factors influence the geochemical composition of the sediment, Principal Component Analysis (PCA) of the XRF data was conducted using the PAST version 4.04 software package (Hammer et al., 2001). As a preliminary step, the element counts obtained from the XRF analysis were normalized using Z-score normalization. This involves subtracting the mean from each count and dividing it by the standard deviation. We only used elements with robust signal quality to run the PCA, including Si, K, Ca, Ti, Mn, Fe, Br, Rb, Sr, Zr, and Ba (The Al was neglected due to its small counts).

Spectral analyses were conducted to detect sedimentary cycles using the REDFIT (Schulz & Mudelsee, 2002) package in PAST 4.04 statistical software (Hammer et al., 2001). Several datasets from both cores were tested to identify which dataset records the best signal. Only MS data in TG02 core offered a clear cycle variability, allowing the detection of relevant frequencies. We used an

oversampling factor of 2 for the Fourier transform, three segments with a 50% overlapping, and a rectangle window with no Montecarlo setting. Only those frequency peaks that are above 99% significance were considered. The inverse value of the detected frequency is equal to the temporal occurrence of this cycle. Subsequently, using the QAnalySeries program (Kotov & Pälike, 2018), the original data is filtered according to the relevant frequency detected.

# 5.3.6. <sup>210</sup> Pb and <sup>14</sup>C dating

The chronology of TG02 and TG03 cores is based on <sup>210</sup>Pb and <sup>14</sup>C measurements in bulk sediment samples. Activities of <sup>210</sup>Pb and <sup>137</sup>Cs were measured at EPOC department at the Université de Bordeaux using a semi-planar germanium detector (EGSP 2200-25-R, EURYSIS Mesures; Schmidt et al., 2014). Activities are expressed in mBq/g and errors correspond to one standard deviation counting statistics. Samples were taken every centimeter over the first 10 cm and every 5 cm from 10 to 30 cm, on 1 cm thick sediment slices taken. The sedimentation rate was calculated using the Constant Flow: Constant Sedimentation (CF: CS) model (Bonotto & García-Tenorio, 2014).

For <sup>14</sup>C dating, 14 samples in TG02 and 12 samples in TG03 were carved at fairly regular intervals, where sedimentation appeared to be continuous (triangles in Figs. 5.4 and 5.5). These samples were measured in the MICADAS (Mini radioCarbon Dating) AMS (Accelerator Mass Spectrometry) system at the Salamanca University. The dating was duplicated for each sample, taking into account the average value (Tables S5.1 and S5.2 in supplementary materials). The errors correspond to one standard deviation counting statistics. Among the <sup>14</sup>C dated samples, four from TG02 and one from TG03 (grey circles in Fig. S5.1 in supplementary materials) greatly deviate from the main tendency the other samples show. These samples were discarded from the age model, supported by observations in CT-Scan images confirming the coincidence with small ripples or denser intervals with higher terrigenous supply (see Figs. 5.4 and 5.5).

The calibration of the selected  $^{14}$ C ages was performed using the package rBacon (Blaauw & Christen, 2013) and taking into account the following criteria: (1) Conventional  $^{14}$ C ages were calibrated using the Marine20 curve following the procedure recommended for Holocene samples, that includes a 400 yr correction. (2) An additional regional difference of  $802 \pm 97$  yr was applied from averaging the three closest Marine Reservoir Ages (MRA) to our core locations from the online database http://calib.org/marine (Stuiver & Reimer, 1993). Therefore, the final reservoir age ( $\Delta$ R) correction is 1202 yr, a value commonly used in the Antarctic margins (Crosta et al., 2021; Ingólfsson et al., 1998). At top core, the difference between the  $^{210}$ Pb ages and  $^{14}$ C ages was used to estimate the dead carbon fraction. Regional deviation from the global reservoir and dead carbon fraction were used as priors in rBacon.

## 5.4. Results

# 5.4.1. Age model

In TG02 and TG03, the <sup>210</sup>Pb data confirmed the presence of sub-recent sediment at the top of the cores. However, the complete Pb decay curve was not recovered. <sup>137</sup>Cs data present background

#### **CHAPTER 5**

noise values and cannot be used to identify nuclear tests performed in the 1960s. In TG03, the <sup>210</sup>Pb<sub>xs</sub> at the surface was 24.3 mBq/g (Fig. S5.1 in supplementary material), which is much lower than Pb activities in nearby multi-cores (Masqué et al., 2002; Vorrath et al., 2020). Therefore, <sup>210</sup>Pb<sub>xs</sub> result was compared with the <sup>210</sup>Pb<sub>xs</sub> record from the nearby multi-core PS97/068-2, located in the southern area of the East Bransfield Basin (Fig. 5.1), at a similar water depth (~800 m) and sediment composition (Vorrath et al., 2020). This resulted in an inferred age of ~1880 CE (70 yr BP), indicating a substantial sediment loss during coring. In TG02, the surface <sup>210</sup>Pb<sub>xs</sub> value was 41.9 mBq/g (Fig. S5.1 in supplementary material). This value, compared with the obtained <sup>210</sup>Pb<sub>xs</sub> record of the nearby multi-core PS97/072-2 (~2200 water depth) (Vorrath et al., 2020), also resulted in an inferred age of ~1880 CE (70 yr BP).

The <sup>210</sup>Pb-inferred ages were then used to estimate the overall correction to <sup>14</sup>C measurements. Total corrections of 2320 yr (2390-70 yr) for TG03 and 2107 yr (2177-70 yr) for TG02 were injected as prior parameter into rBacon to calibrate adequately the core-tops ages to be in agreement with <sup>210</sup>Pb core-top ages. Dead carbon fraction was estimated to be 1118 yr (2320-1202 yr) for TG03 and 905 yr (2107-1202 yr) for TG02. These values are in agreement with previous regional studies (Nie et al., 2022). For TG03, the calibration resulted in a core-top age of 76 cal yr BP and a core-bottom age of 969.7 cal yr BP (Fig. 5.3A). For TG02, the final age model shows that the core covers the period from 75.7 cal yr BP to 820.3 cal yr BP (Fig. 5.3B). In both cores, rBacon model is almost linear, with very similar mean sedimentation rates of 0.48 cm/yr for TG02 and 0.5 cm/yr for TG03.

			TG02						
				rBacon age model					
#	Depth (cm)	<sup>14</sup> C age (yr BP ± 1σ)	Calibrated <sup>14</sup> C age (cal yr BP)	Age model (cal yr BP)	Confidence interval (cal yr BP)				
				(caryr br)	(Min)	(Max)			
1	36	2326 ± 16	10	148	33	187			
2	137	2847 ± 16	490	362	223	394			
3	178	2721 ± 16	400	445	294	472			
4	205	2909 ± 15	530	501	342	527			
5	223	2956 ± 16	560	537	373	564			
6	240	2756 ± 16	430	571	400	598			
7	270	3077 ± 16	660	634	451	663			
8	296	3133 ± 16	710	688	494	719			
9	336	3068 ± 14	660	769	557	805			
10	361	3398 ± 14	970	820	596	860			

**Table 5.1.** Results of AMS <sup>14</sup>C dating of bulk organic matter taken from core TG02. Final adopted age model is shown in Figure 5.3A.

			TG03					
		14		rBacon age model				
#	Depth (cm)	Measured <sup>14</sup> C age (yr BP ± 1σ)	Calibrated <sup>14</sup> C age (cal yr BP)	Age model (cal yr BP)	Confidence interval (cal yr BP)			
		10)		(caryr br)	(Min)	(Max)		
1	4	2734 ± 13	280	84	0	205		
2	25	2468 ± 14	10	125	7	241		
3	78	2735 ± 14	290	231	123	338		
4	105	2579 ± 13	120	285	182	338		
5	158	2733 ± 14	280	396	298	488		
6	218	3109 ± 14	620	533	437	625		
7	288	3117 ± 14	620	685	589	782		
8	318	3410 ± 15	900	754	654	853		
9	357	3259 ± 15	720	838	731	940		
10	384	3574 ± 15	1050	899	784	1005		
11	417	3611 ± 14	1090	970	847	1085		

**Table 5.2.** Results of AMS <sup>14</sup>C dating of bulk organic matter taken from core TG03. Final adopted age model is shown in Figure 5.3B.

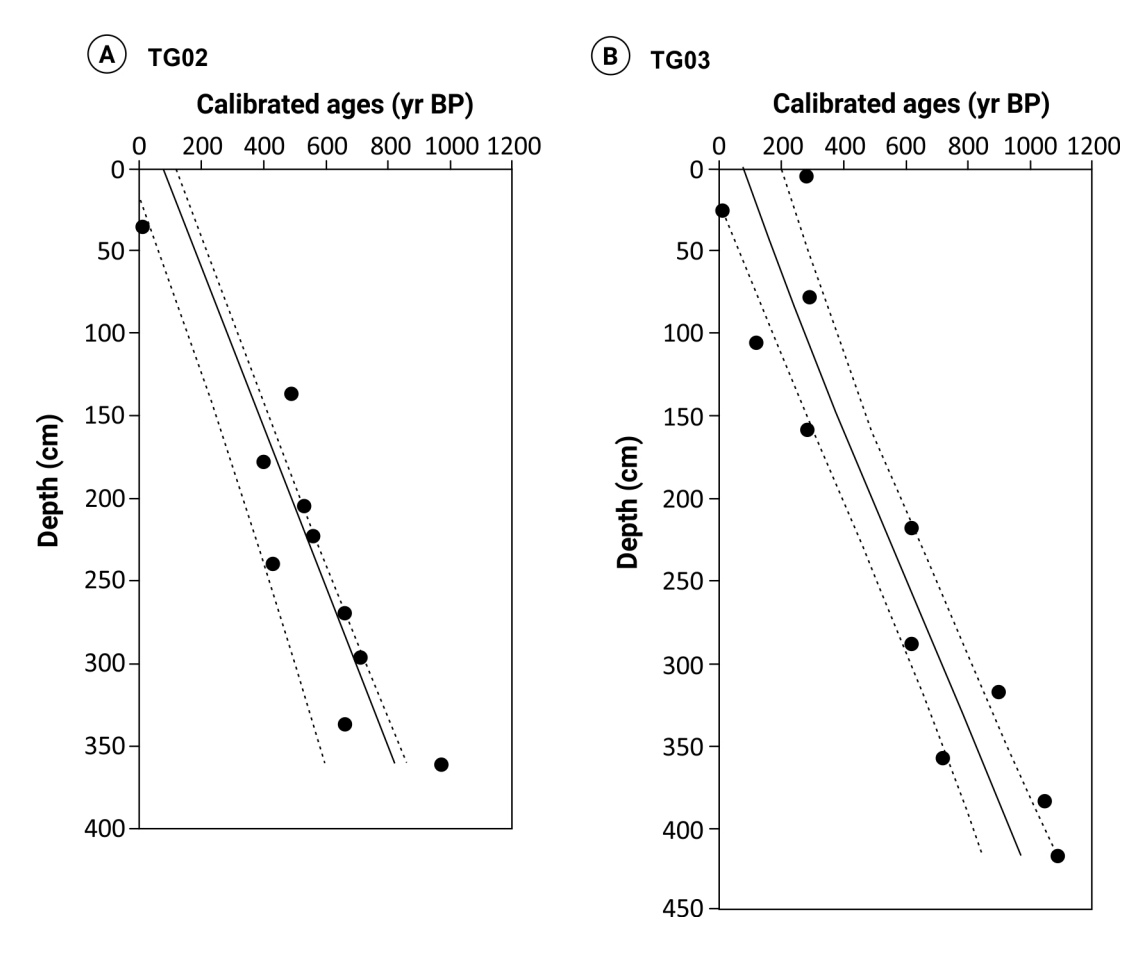


**Figure 5.3.** Age models for TG02 (A) and TG03 (B). The dashed lines represent the minimum and maximum confidence interval of the resulting model and the solid lines represent the adopted age model for this study.

#### 5.4.2. Sediment textures and structures

Visual description of the cores revealed alternations between laminated intervals, characterized by centimeter-to-millimeter-scale laminations, and intervals where laminations are diffused or apparently absent (Figs. 5.4 and 5.5). CT-Scan images allowed a precise recognition of laminated intervals and other internal structures of the cores (Fig. 5.4B and 5.4C). Sediment colors vary between very dark gray (almost black) and lighter greenish-gray layers (Figs. 5.4 and 5.5). Three main sedimentary facies are differentiated based on sedimentological (visual observation, grain-size), physical properties (CT-Scan images, GRD, MS) and geochemical (XRF-core scanning) data. It is worth noting that each facies is defined based on grouping the dominant indicators that characterizes it in a given interval.

Facies 1 (F1) is present in both TG02 and TG03 and is composed of diatom-rich medium to coarse silty sediments (Tables S5.3 and S5.4 in supplementary materials) characterized by an intense alternation of centimeter to millimeter-thick greenish to black laminae. Lamination is commonly planar with the occasional presence sedimentary structures (e.g., ripples at 60 cm in TG02). Bioturbation is generally scarce within F1 (Figs. 5.4 and 5.5). Generally, grain size distribution curves are asymmetrical and occasionally bimodal (e.g., few samples from TG03; Fig. 5.6B). F1 shows very low density values ( $\sim$ 1.10 g/cm³), is dominated by dark blue laminae on CT Scan images (Figs. 5.4 and 5.5), has the lowest magnetic susceptibility (< 50 instrumental units, iu) and high Br<sub>norm</sub> values. On the other hand, the Zr/Rb ratio and  $\overline{\rm SS}$  do not show substantially different values between F1 and Facies 2, but they are clearly lower compared to Facies 3.

Facies 2 (F2) is recorded in TG02 and TG03 and also consists of diatom-rich medium to coarse laminated silty sediments (Tables S5.3 and S5.4 in supplementary materials). However, as reflected in CT-scans, sediments have higher density values than F1. Thin dark laminations are less frequent, while centimeter-thick beds are more common than in F1 (Figs. 5.4 and 5.5). F2 is characterized by slightly higher GRD (up to ~1.20 g/cm³) and MS values (~50 to 70 iu), when compared to F1, corresponding to greenish, yellowish and pinkish colors in CT-Scan images. Br<sub>norm</sub> values are significantly lower in F2 compared to F1. Zr/Rb values are similar to F1 with higher values recorded in TG03 than TG02. Within F2, a sub-facies F2\* has been differentiated based on the presence of slightly coarser sediments, a bigradational pattern on the MS data (with values up to 85 iu), and higher GRD (~1.24 g/cm3) values, compared to F2.

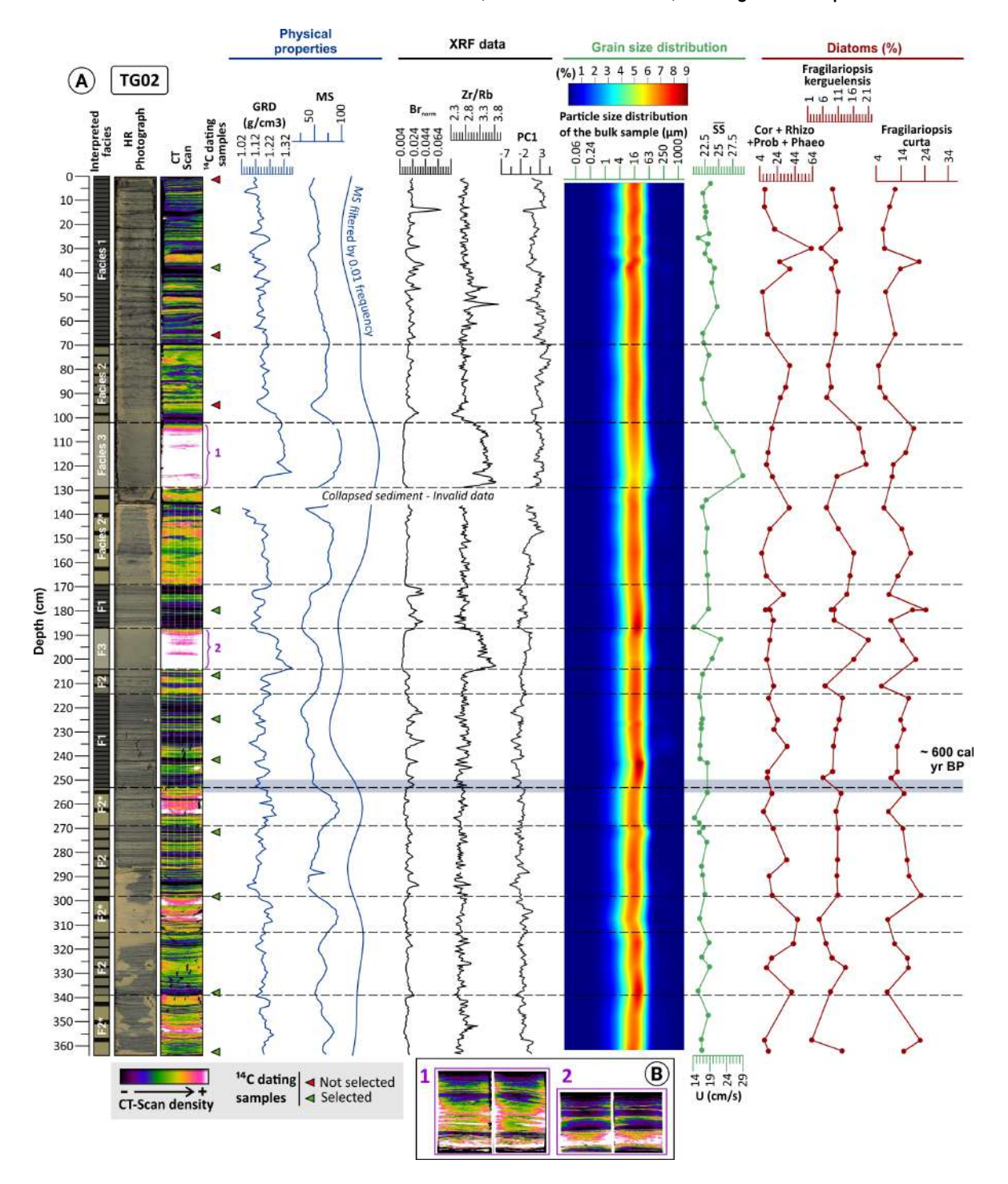


**Figure 5.4.** A) Used proxies in the study of TG02. From left to right: synthetic core with interpreted facies; high-resolution digital image; CT-Scan image; location of  $^{14}$ C dating samples; selected physical properties and XRF data; bulk grain size distribution, measured  $\overline{SS}$  fraction ( $\mu$ m) and calculated current intensity (U); diatom abundance of selected species. B) CT-Scan images of Facies 3 with relative color scale adjusted for denser values.

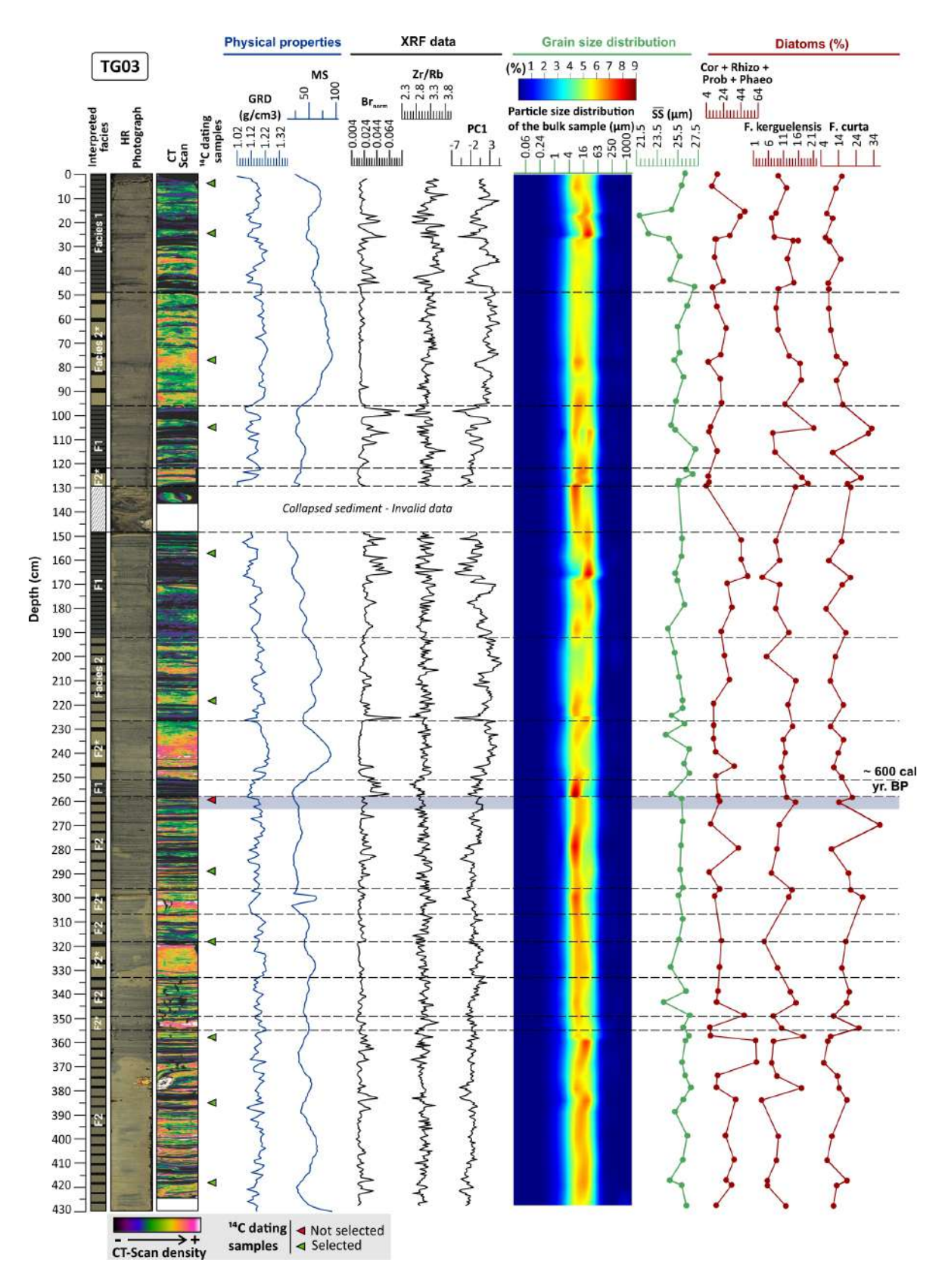


**Figure 5.5.** Used proxies in the study of TG02. From left to right: synthetic core with interpreted facies; high-resolution digital image; CT-Scan image; location of  $^{14}C$  dating samples; selected physical properties and XRF data; bulk grain size distribution, measured  $\overline{SS}$  fraction; diatom abundance of selected species.

Facies 3 (F3) consists of diatom-rich coarse and very fine sandy coarse silt sediments (Tables S5.3 and S5.4 in supplementary materials). F3 has only been identified at TG02. Grain-size distribution curves (Fig. 5.6) exhibit a near symmetrical pattern with lower kurtosis values than F1 and F2. F3 is characterized by its apparent massive appearance, without lamination to the naked eye, but occasional/common pink to white color laminae evident in CT-Scan images (Fig. 5.4b and 5.4c). Dark laminae are however absent in F3. F3 is the densest facies in these cores with GRD values reaching up to  $1.38 \text{ g/cm}^3$  (Fig. 5.4). The MS values in F3 also reach maximum values (100 iu) and show a marked bi-gradational pattern. The Br norm content in F3 is the lowest compared with the other facies. In contrast, there is a sharp increase in Zr/Rb ratio and  $\overline{\text{SS}}$  values within F3 (Fig. 5.4).

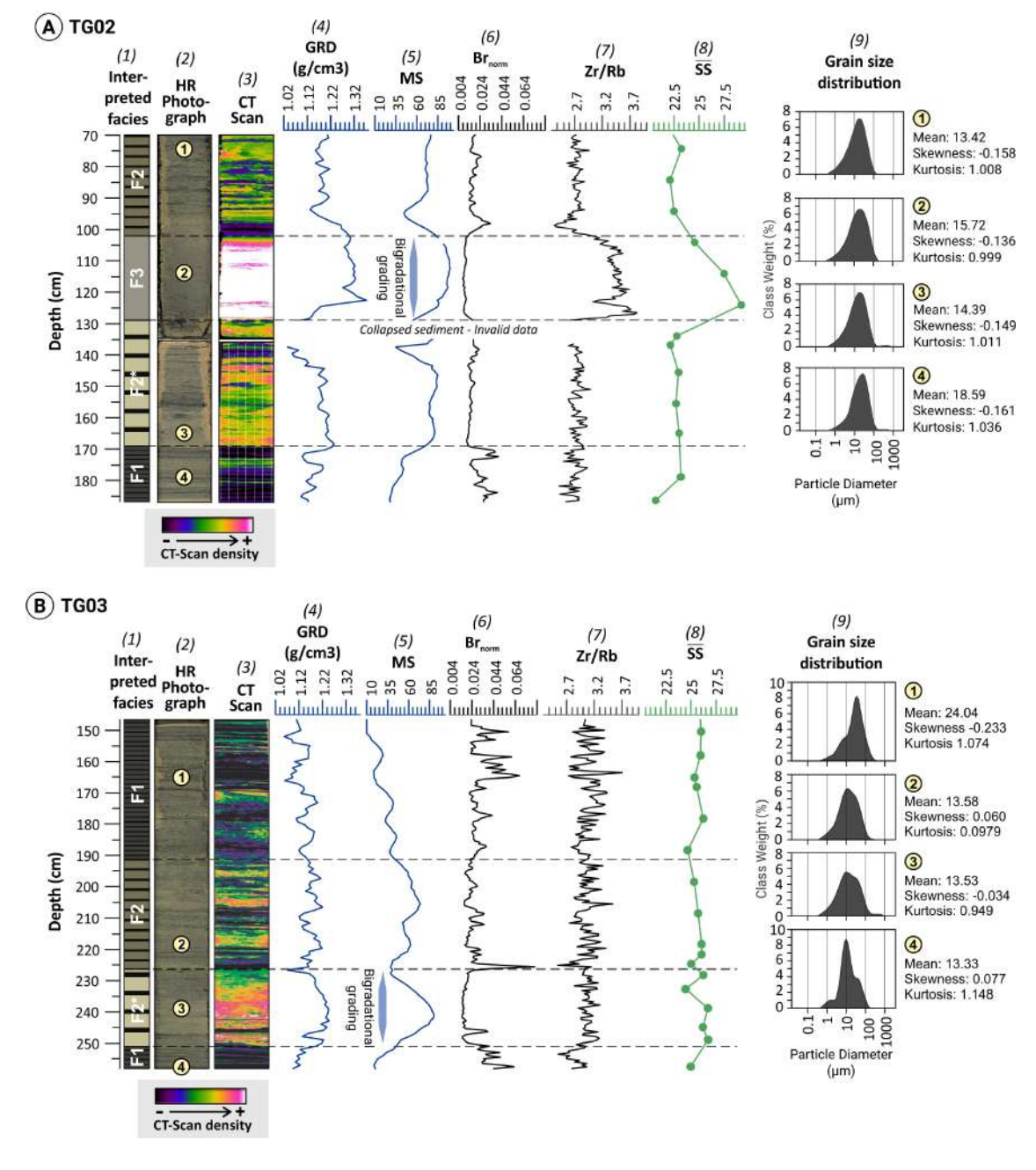


**Figure 5.6.** Detailed facies characterization of (1) two representative sections for TG02 (A) and TG03 (B) using: (2) high-resolution digital images of the core sections; (3) CT-Scan images; (4) Gamma-Ray

Density (GRD); (5) Magnetic Susceptibility (MS); (6) Br  $_{norm}$ ; (7) Zr/Rb; (8) weighted mean of the sortable silt fraction ( $\overline{SS}$ ); (9) the grain size distribution of representative samples of each facies in each core.

Although we have identified similar facies in both cores, we observe significant differences between the TG02 and TG03 bulk grain size distribution. Facies 3 is only present in core TG02. In addition, TG02 exhibits a homogeneous coarse silt grain size throughout the core (Fig. 5.4 and Table S5.3 in supplementary materials). Only a few samples are in the range of medium silt and very fine coarse silt. All the TG02 samples show unimodal distribution and present negative values of skewness, from -0.02 to -0.26, i.e., from symmetrical to skewness toward the fines (Table S5.3 in supplementary materials). In TG03, the grain size distribution of the bulk samples shows greater variability with slightly larger sizes in the range of very fine sand - very coarse silt range (Fig. 5.5 and Table S5.4 in supplementary materials). Most samples are unimodal, although some samples display bimodal distribution and the skewness varies from 0.14 to -0.24 (Table S5.4 in supplementary materials). In both cases the sorting stays in the range of poorly sorted.

## 5.4.3. Statistical analysis

# 5.4.3.1 Principal Component Analysis (PCA)

A PCA was conducted on z-scores of the elemental data obtained by XRF-scan from TG02 and TG03 cores. Three main principal components (PCs), which together account for 82.82% (TG02) and 80.33% (TG03), explains the variance of the XRF data (Table 5.3). The successive PCs have not been taken into account as they represent less than 10% of the variability. The PCA scores show a similar elemental association in both cores, with PC1 confronting biogenic elements (Si, S, and Br) in the negative load and detrital elements (e.g., Ti, Fe) in the positive load (Fig. 5.7A and 5.7D). PC2 separates S and Br (elements associated with organic matter) in the positive load versus Si, K, and Ti in the negative load (Fig. 5.7B and 5.7E). In this case, the Si is associated with the K and the Ti and, therefore, is therefore interpreted as a non-biogenic siliciclastic fraction. Finally, PC3 contributes 12-16 % of the variance, and is dominated by Ca (Fig. 5.7C and 5.7F). However, as we found no correlation with other elemental data or physical properties, we are not able to propose any interpretation for PC3 signal.

	TG03											
PC	Eigenvalue	Cumulative										
	Ligerivalae	(%)	variance (%)									
1	5.27	47.93	47.93									
2	2.24	20.35	68.28									
3	1.32	12.04	80.32									

	TG02											
PC	Eigenvalue	Variance	Cumulative									
PC	Eigeilvalue	(%)	variance (%)									
1	5.05	45.89	45.89									
2	2.29	20.82	66.71									
3	1.78	16.11	82.82									

**Table 5.3.** Principal components (PC) of the TG02 and TG03 cores.

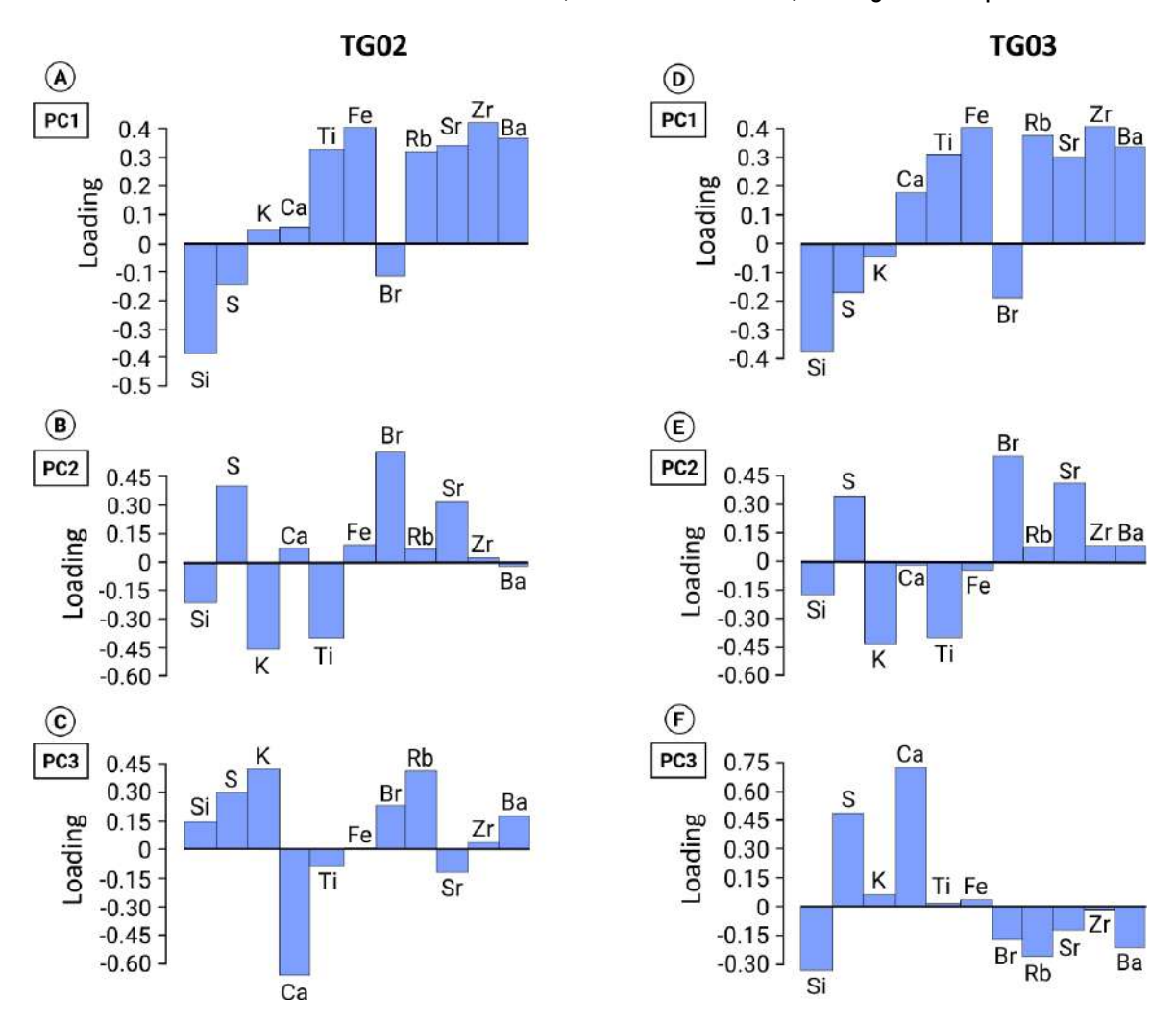


**Figure 5.7.** The three most significant Principal Components (PC) of TG02 core (A-C) and TG03 core (D-F)

## 5.4.3.2. Spectral analysis

MS data from the TG02 core shows one clear and statistically significant (>99 %) cycle of 100 yr (frequency at 0.01) (Fig. 5.8). By filtering the MS data by the frequency found in TG02, we can distinguish successive periods of higher and lower MS. This periodicity coincides with an alternation between high MS periods correlating with the formation of F2\* and F3, and low MS periods correlating mainly with F1 and F2 (Figure 5.4).

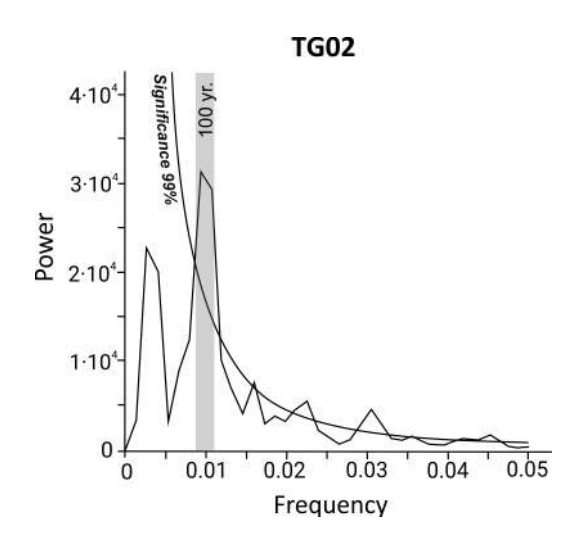


**Figure 5.8.** Spectral analysis results of the MS data in TG02. The shaded horizontal bar indicates the discussed cycle.

## 5.4.4. Sortable silt and flow speed reconstruction

In core TG02,  $\overline{SS}$  values vary between 20 and 29 µm, with higher values recorded in F3. In this core,  $\overline{SS}$  and SS% show a significant positive correlation (r = 0.63, p-value < 0.05 , n=55) (Fig. 5.9A). With this result, we can rely on the  $\overline{SS}$  as a proxy for flow speed reconstruction and convert the  $\overline{SS}$  values into scalar flow speed (U, cm/s), following the methodology proposed by McCave & Hall (2006). The obtained current flow speed variation along the core TG02 presents maximum values of 29 cm/s and minimum values of 14 cm/s (Fig. 5.4). As  $\overline{SS}$  and U are proportional, the maximum flow speeds also occur in F3. Additionally, the  $\overline{SS}$  data and Zr/Rb ratio also show a significant positive correlation in core TG02 (r = 0.74, p-value < 0.05, n=55) (Fig. 5.9B), which supports the assumption that the Zr/Rb ratio in this core is strongly related to the current strength as observed in previous studies (Salabarnada et al., 2018; Toyos et al., 2020; Wu et al., 2020).

In contrast, in TG03,  $\overline{SS}$  values range between 22 and 27 µm.  $\overline{SS}$  and SS% show no significant correlation between them (r = 0.12, p-value > 0.05, n= 64) (Fig. 5.9C). No significant correlation is observed between the  $\overline{SS}$  data and the Zr/Rb ratio (r= 0.24, p-value > 0.05, n= 64) (Fig. 5.9D). Therefore, the current flow speed cannot be estimated.

#### 5.4.5. Diatom assemblage

During sample treatment for the measurement of the sortable silt fraction, the amount of biogenic silica was estimated to be 30% on average for both cores. Diatom assemblage counts show that Chaetoceros resting spores (CRS) are predominant in both cores, accounting for about 75% of the total diatom assemblage. Main accompanying species are presented herein on a CRS-basis free. Large size and elongated species (Chaetoceros subg. Phaeoceros, Corethron pennatum, Proboscia inermis, Proboscia alata, Proboscia spp., Rhizosolenia antennata f. semispina, Rhizosolenia antennata f. antennata, and Rhizosolenia spp.) (Alley et al., 2018) were grouped together. In both cores there is a

greater presence of this group in F1 and F2, representing the 21-26% of the assemblage, and decreasing in F2\* (18%) and in F3 (15%). *Fragilariopsis curta (F. curta)*, the main sea ice related species here, shows maximum mean relative abundances coinciding with F3 and F2\* (15%) and minimum within F1 and F2 ( $\sim$ 12%). *Fragilariopsis kerguelensis (F. kerguelensis)* shows an average value along the cores of  $\sim$  10%. However, in TG02, coinciding with Facies 3, there is clear increase of *F. kerguelensis* with an average relative abundance of 18% for the six counts of F3 (Fig. 5.4).

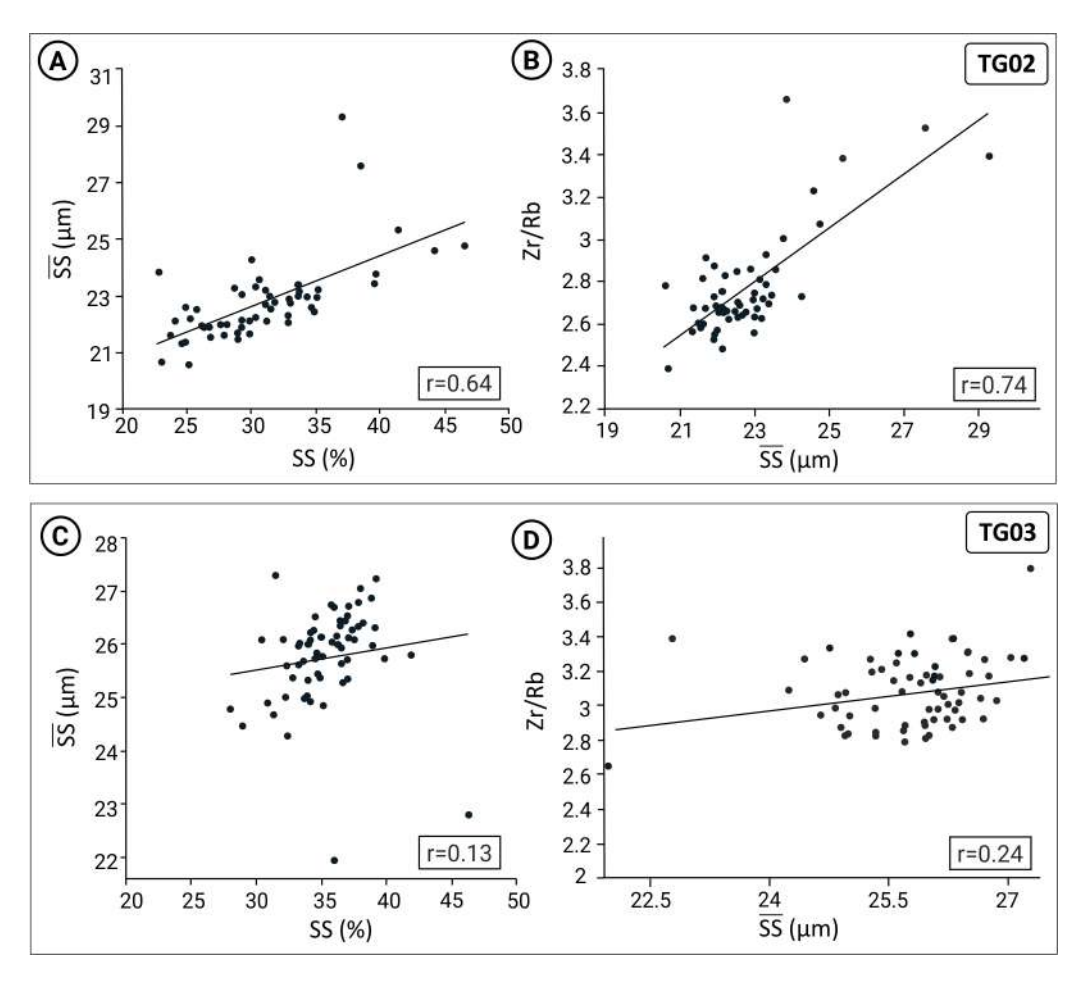


**Figure 5.9.** A) Linear regression between  $\overline{SS}$  ( $\mu m$ ) and SS% and B) between  $\overline{SS}$  ( $\mu m$ ) and Zr/Rb ratio in TG02. C) Linear regression between  $\overline{SS}$  ( $\mu m$ ) and SS% and D) between  $\overline{SS}$  ( $\mu m$ ) and Zr/Rb ratio in TG03 grain size samples.

# 5.4.6. Proxies variability throughout the cores

In both cores, there is a noticeable change in the dominant facies and alternation of facies at around 600 cal yr BP (255 cm in TG02 and 260 cm in TG03). Sediments older than 600 yr BP dominantly consist of finely laminated sediments intervals of F2 and F2\* (Figs. 5.4 and 5.5). Younger than 600 yr BP, sediments include the appearance of F1 in TG02 and TG03, and F3 in TG02 (Figs. 5.4 and 5.5). Above this depth, there is also a greater variability of some measured parameters, such as the MS, the Br, and PC1 associated with the alternation between the different facies (Figs. 5.4 and 5.5). The ratio between *F. curta/F. kerguelensis* shows a tendency towards lower values at the top in both cores (Fig. 5.10). PC1 in both cores tends towards more positive values. However, PC1 in TG03 show greater

variability than in TG02, exhibiting a reversal of the overall trend between 300 and 400 yr cal BP (Fig. 5.5 and 5.10).

## 5.5. Discussion

## 5.5.1. Interpretation of diatom, elemental ratio, and grain-size proxies

Diatoms contribute 75% of primary production in the Southern Ocean. Their study provides insights into factors driving their distribution: nutrient availability, grazing pressure, temperature, sea ice, and water column stability (Armand et al., 2005; Crosta et al., 2005). *F. kerguelensis* is generally recognized as an open-ocean species, usually absent from regions where sea ice persists during the summer (Crosta et al., 2005; Esper et al., 2010). *F. curta* is the most common diatom taxa used in reconstructing Antarctic sea ice (Allen & Weich, 2022; Armand et al., 2005). High values of the *F. curta/F. kerguelensis* ratio reflect high sea ice conditions (Denis et al., 2009). In addition to primary production, diatoms can be affected by secondary processes, such as aggregate formation and lateral and bottom transport, which can modify the original community and change the sedimentary assemblage (Burckle, 1981; Burckle & Humphreys, 1986; Leventer, 1991). For that reason, we grouped large, elongated diatoms including *Rhizosolenia*, *Proboscia*, *Phaeoceros*, and *Corethron* species (Fig. 5.4 and 5.5), all of which could be susceptible to remobilization.

The PC1 distinguishes between the biogenic versus detrital inputs (e.g., Bahr et al., 2014; van den Berg et al., 2018; de Castro et al., 2021). PC1 can be interpreted, at both sites, as a proxy for the variation between biogenic silica content and detrital input. The relatively higher values of PC1 in the denser intervals indicates a greater concentration of detrital elements. In PC2, the Si is associated with the detrital elements in opposition to Br. Therefore, in this case, it is interpreted as the non-biogenic siliciclastic fraction. Br dominates the PC2, which can be linked to organic matter content (Bahr et al., 2014; Nieto-Moreno et al., 2011; Ziegler et al., 2008). Therefore, the Br<sub>norm</sub> is selected as a proxy for organic matter variability. In the study carried out by Bahr et al. (2014), the presence of organic matter-bound Br in contourite deposits was not significantly affected by changes in the lithology. However, in this study, we observe that the distribution of Br<sub>norm</sub> closely linked to the different facies. Low Br<sub>norm</sub> content is associated with high-density facies developed under higher intensity bottom currents, and maximum Br<sub>norm</sub> peaks present in the low-density intervals (Figs. 5.4 and 5.5).

The  $\overline{SS}$  is an indicator of the grain size sorting that occurs during deposition (McCave et al., 2014). Current winnowing of pelagic/hemipelagic deposits and the removal of the fine-grained fraction has been reported to produce a higher accumulation of heavy minerals (Fralick & Kronberg, 1997; Salabarnada et al., 2018; Toyos et al., 2020; Wu et al. 2020). The Zr is representative of heavy minerals and is associated with coarse grain size, while the Rb represents the clay minerals and is associated with clay and fine silt (Fralick & Kronberg, 1997; Taylor, 1965). Therefore, we interpret the changes in  $\overline{SS}$  values and Zr/Rb ratio as proxies for grain size variability (Dypvik & Harris, 2001). This variability is, in turn, related to the current strength (Wu et al., 2020; Toyos et al., 2020) and can be

converted into scalar flow speed (U, cm/s) when the  $\overline{SS}$  and SS% show a positive significant correlation (Toyos et al., 2020).

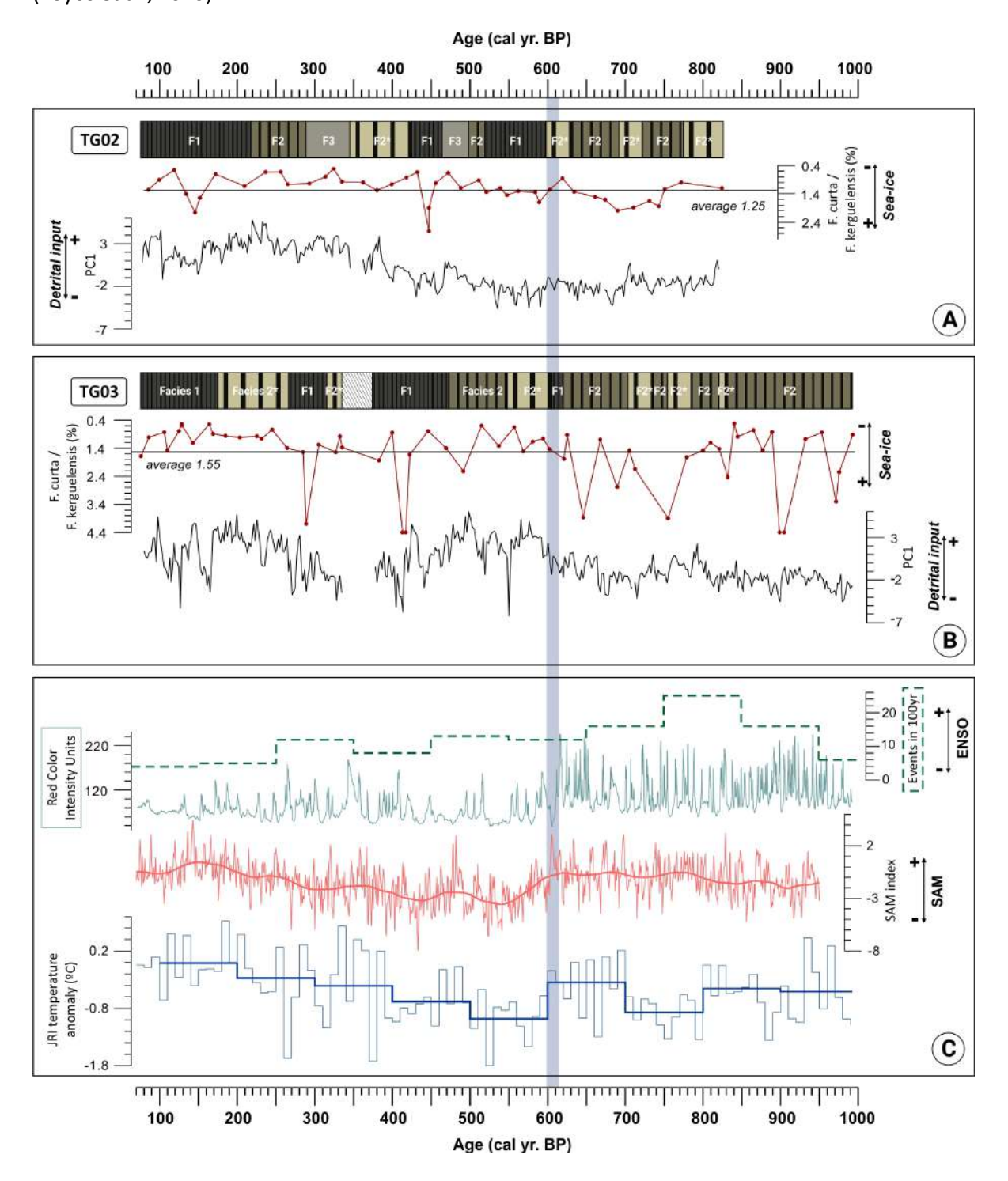


**Figure 5.10.** Proxies variability throughout the cores and their correlation to regional climatic records. Coincident trends in diatoms and PC1 results of TG02 (A) and TG03 (B) are displayed together. C) The proxies' variability correlates with regional temperature anomaly from James Ross Island (JRI) ice core (Mulvaney et al., 2012), and global climatic records, the ENSO (Moy et al., 2002) and SAM (Abram et al., 2014) variability.

The MS variability can be associated with changes in terrigenous input and has also been used to differentiate bottom current deposits (Pudsey, 2000; Hepp, 2007; Salabarnada et al., 2018). In this study, we observed that the MS varies along with the proxies of current intensity (Zr/Rb and  $\overline{SS}$ ). Also, bi-gradational grading in the MS data is present (Fig. 5.6), which has been previously identified in contourite deposits), as a result of an increase followed by a decrease in the current intensity (Martín-Chivelet et al., 2008; Rebesco et al., 2014; Salabarnada et al., 2018).

## 5.5.2. Influence of contour currents on sedimentation in the East Bransfield Basin (EBB)

The mounded morphologies and moats observed in the TOPAS profiles (Fig. 5.2) aling with an eastward BBW in the northern EBB and a westward BDW in the southern EBB (Fig. 5.1), influenced by the Coriolis effect in the Southern Hemisphere. This is in line with previously described EBB oceanographic setting (García et al. 2019; Liu et al., 2022). Chaotic reflections, observed mainly in the profile where TG03 is located (Fig. 5.2B), indicate the occurrence of slumps within this contourite mound. This suggest a complex interaction between along slope and down-slope processes in the southern flank of the EBB. The high-resolution sedimentological record of the last millennium from TG02 and TG03, support these seismic observations. Sedimentation at TG02 is primarily controlled by bottom currents, based on the significant positive correlation between  $\overline{\rm SS}$  and SS%. In contrast, in TG03,  $\overline{\rm SS}$  and SS% show no significant correlation between them, suggesting an interplay of processes influencing sedimentation in the southern EBB.

Although the contourite depositional systems have been previously recognized in the Bransfield by seismic data (Casas et al., 2004; Ercilla et al., 1998; García et al., 2009; Liu et al., 2022), the influence of bottom contour currents in sedimentation has not yet been described in detail. Sediment cores collected in the last decades from these basins are reported to mainly comprise intervals of laminated diatom ooze and bioturbated diatomaceous mud, interpreted as pelagic/hemipelagic sediments with minor fine-grained turbidites (Fabrés et al., 2000; Yoon et al., 2001, Khim et al., 2002, Bahk et al., 2003). Instead, laminated sediments in cores TG02 and TG03, are interpreted to record the reworking of hemipelagic and/or fine grained turbidites by bottom currents of varying intensities. We differentiate three facies, F1 to F3, interpreted to record increasingly intense bottom currents. F1 and F2 are characterized by well-preserved lamina and sparse bioturbation, resembling the laminated diatom ooze intervals described in nearby sediment cores (Fabrés et al., 2000; Yoon et al., 2001; Khim et al., 2002; Bahk et al., 2003; Nie et al., 2022). Based on McCave et al. (2017), SS values indicate a reconstructed flow speed, only reliable in TG02, during F1 and F2 deposition normally below 20 cm/s. According to McCave & Hall (2006) this velocity would only slightly modify the original deposit. The lower density intervals predominating in these two facies exhibit thin laminations with diatom assemblages generally dominated by one or more of Rhizosolenia, Proboscia, Phaeoceros, or Corethron species (Fig. 5.4). These diatom species share long and slender structures that could facilitate the entanglement and the formation of mats, favoring the quick settlement to the seafloor during autumn, serving as a barrier against bioturbation (Gersonde & Wefer, 1987; Kemp et al., 2000; Pike & Stickley, 2013). Another possible interpretation that would need further evidence is

that the influence of the current could favor the oriented accumulation of these diatom species, similar to the deposition of elongated imbricate detrital grains observed in other contourite deposits (Bankole et al., 2020; Nichols et al., 2020). In F3, reconstructed flow speed is slightly higher, ranging between 20 and 28 cm/s. Erosional winnowing and up to sand-size particles movement can occur above 20 cm/s (McCave & Hall, 2006). As the current intensity increases, the percentage of this diatom group decreases relative to the total, being not dominant at high-density sections of F3. This decrease can be related to a decrease in primary productivity during deposition of these facies and/or to their transport away by currents as these diatoms have a strong buoyancy. We link the decrease in this diatom species abundance with this higher current intensity during F3 resulting in non-visible to naked eye laminations that are only evident in CT-scan images (Fig. 5.4).

Further evidence for reworking of original sediments by bottom contour currents during deposition of F2\* and especially F3 is the variation of the MS and Zr/Rb records. In F3, high MS values are associated with a significant increase in Zr/Rb and  $\overline{SS}$  and an increase in current intensity that would enhance winnowing of finer/lighter sediments leaving behind coarser/heavier detrital particles (Fig. 5.6A). Similar high MS values and increase in Zr/Rb in Antarctic sediments have been associated with stronger bottom current deposition (e.g., Hepp, 2008; Pudsey, 2000; Salabarnada et al., 2018). Higher velocity bottom currents could favor well-oxygenated bottom waters promoting the increase in organic matter degradation and/or removal, which could explain low Br<sub>norm</sub> values within F3 compared with F1 and F2. Lower current intensity during deposition of F1 and F2, in both TG02 and TG03, correlates with the highest Br<sub>norm</sub> values, which is associated to the organic matter content in the sediments. Br<sub>norm</sub> and Si/Ti ratio have a very similar pattern (Fig. S5.1 in supplementary material), suggesting that organic matter is associated to biogenic silica content.

An additional line of evidence for bottom contour current influence during deposition of TG02 and TG03 sediments is the calculated sedimentation rate. Contourite deposits are characterized by their high sedimentation rates due to significant sediment focusing, which can range from 5 to 65 cm/ka, reaching up to 125-376 cm/ka (Michels et al., 2002; D. Stow et al., 2008). In contrast, pelagic/hemipelagic background sedimentation generally ranges from <2 to 15 cm/ka (Stow & Tabrez, 1998). Based on our age model, TG02 and TG03 sedimentation rates are 480-500 cm/ka. Although these values exceed the typical values calculated for other contourite drifts they can hardly be explained by other types of deep-sea sedimentary processes compatible with the rest of the analyzed sedimentological and physical properties parameters. These elevated sedimentation rates provide for a unique expanded record of paleoenvironmental and paleoceanographic changes during the past millennium.

We relate the differences in current intensity observed in cores TG02 and TG03 to the influence of the different water masses in the area where they are located. The development of F3 only in TG02, suggests that the seafloor of the deep northernmost EBB has experienced episodes with stronger bottom flow intensities than the intra-slope platform from where TG03 was retrieved. In addition, grain size samples in TG03 indicate a less sorted sediment, mainly in Facies 1 (Fig. 5.6), and

record a higher variability in most parameters, reflecting the interplay of different processes. Regarding the oceanographic processes, the deep flat basin where TG02 is located is topographically restricted for water masses exchange, and is mostly influenced by the BBW. The BBW flows through the deep sills towards the NE (Gordon et al., 2000) originating a contourite drift-moat system along the northern part of the basin (García et al., 2019). In contrast, the TG03 site is located in the region where dense shelf water masses from the Weddell Sea reach the Bransfield Basin (Gordon et al., 2000; Liu et al., 2022), and undergo sinking and mixing with the intermediate depth water masses from the Powell Basin (e.g., Warm Deep Water, WDW; Zhou et al., 2006). In addition, the location of the TG03 core in the southern flank of the EBB may be influenced by the activity of gravitational processes, as imaged in the TOPAS profiles in Fig. 5.2.

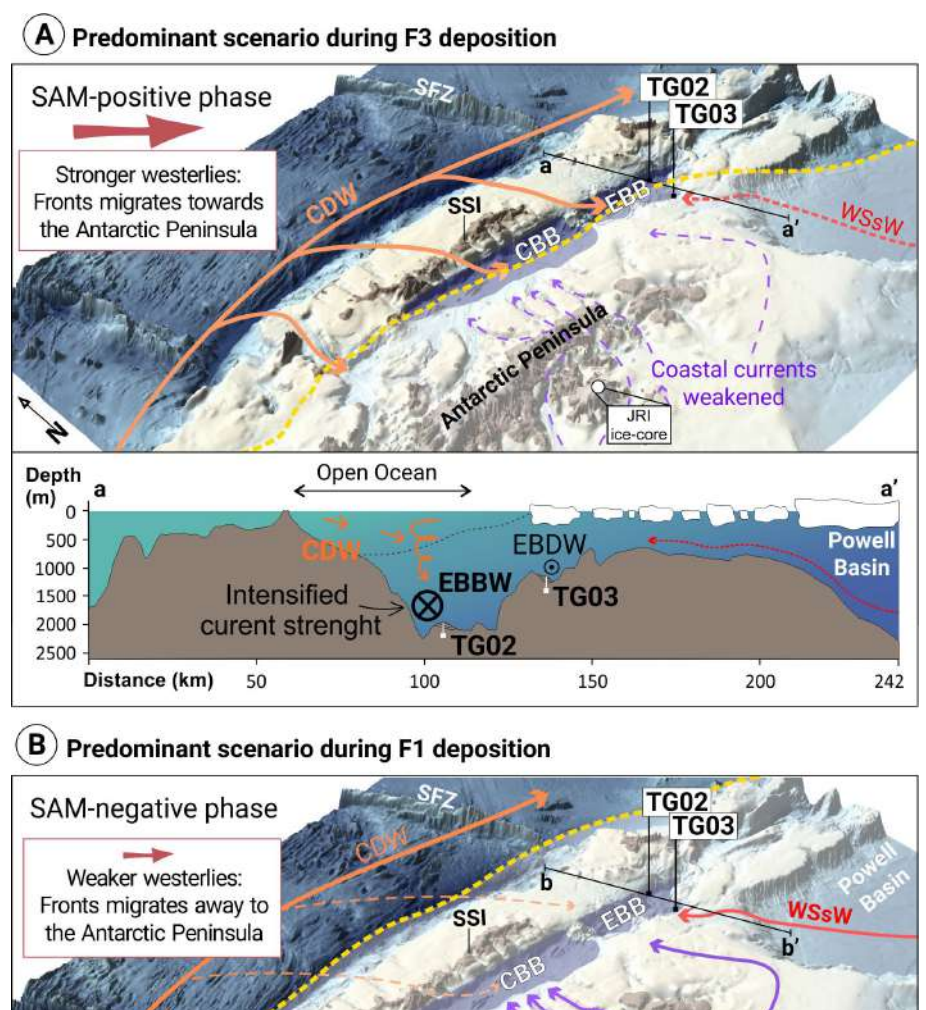
## 5.5.3. Paleoenvironmental-related changes and paleoceanographic configuration

Sediment proxies in TG02 and TG03 cores record a coetaneous change at 600 cal yr BP. These include, among other, the increase in dark lamina that define F1 when dominant, an increase in detrital input, an increase in the frequency and amplitude of the Br<sub>norm</sub>, the appearance of F3, and large shifts in the Zr/Rb in TG02. This is accompanied with a slight decreasing trend in sea ice suggested by the F. curta/F. kerguelensis ratio in sediments younger than 600 cal yr BP (Fig. 5.10). The observed trend towards decreased sea ice conditions aligns with the PC1 in both cores suggesting an increase in detrital input above 600 cal yr BP (Fig. 5.10). In TG03 this increasing trend is more pronounced after 400 cal yr BP. We tentatively link the increase in detrital input to an increase in meltwater input as ice sheets/glaciers retreated. We however observe differences between the TG02 and the TG03. While TG02 exhibits an interrupted tendency towards a decrease in sea ice, TG03 shows a reverse pattern at around 400 cal yr BP (Fig. 5.10). We attribute the observed differences between the two core sites to their different locations. TG03 is located in an intra-slope basin on the southern flank of the EBB that is likely more sensitive to ice proximal changing conditions. In contrast, TG02, located in the deep EBB, can integrate a more regional signal as it receives sediment input from all the surrounding margins (Fig. 5.1 and 5.11). Thus, our interpretation implies that the locations of TG02 and TG03 experienced a warming since 600 cal yr BP, which coincides with the described warming trend in surface air temperatures reported after 600 yr based on  $\delta D$  in the JRI ice core collected in James Ross Island (location in Fig. 5.11) (Mulvaney et al., 2012) (Fig. 5.10).

According to our age model, the development of F1 in TG03 and TG02 and F3 in TG02, also starting at 600 cal yr BP, suggest a greater fluctuation in bottom current intensity in the EBB from this period onward. The development of the F3 correlates with an increase of *F. kerguelensis* (Fig. 5.4), which is an indicator of CDW incursions to Antarctic Peninsula Continental Shelf (Allen et al., 2010; Moffat et al., 2009). The influence of the CDW in the Bransfield is closely linked to the position of the Southern Ocean fronts, conditioned by the influence of the SAM and ENSO periodic events (Damini et al., 2022; Dotto et al., 2016). Intense CDW intrusions are usually related to periods of SAM-positive phases, ENSO-negative phases, or their coupled events (Loeb et al., 2009; Ruiz Barlett et al., 2018) that shift the position of the Southern Antarctic Circumpolar Current Front (SACCF) and the Southern

Boundary (SB) of the Antarctic Circumpolar Current towards the Antarctic Peninsula (Damini et al., 2022). The variable presence of the CDW is linked in the EBB to an eddy that forms in the western strait and moves eastward (Gordon & Nowlin, 1978; Wilson et al., 1999). The TG02 location is more prone to record oceanic frontal dynamics. This would explain the presence of F3 only developing in this site and recording the incursions of CDW. When occurring, the lower stratification of water masses in the EBB (Wilson et al., 1999) may have favored the vertical propagation to the bottom of the basin through the eddy (Fig. 5.11A). As a result, higher-energy processes to the displaced oceanic front system, would affect the EBB bottom ventilation, responsible for deposition of F3. In the location of core TG03, located farther south from the area affected by the frontal migration, the SAM-positive, ENSO-negative phases result on reduced Weddell Sea shelf water masses transport. This could explain the absence of facies similar to F3 in TG03 (Fig. 5.11A). However, further studies are needed to better understand this process. On the contrary, when the CDW has no major influence in the EBB, a better water column stratification (Wilson et al., 1999) might favor the organic matter preservation allowing F1 deposition (Fig. 5.11B). In summary, F1 and F3 appear to respond to frontal system migration affecting the EBB (Fig. 5.11). This frontal variability appears to be linked with the SAM and ENSO records (Moy et al., 2002; Abram et al., 2014). The reported shifts in cores TG02 and TG03, point to three phases with different dominant SAM and ENSO conditions. Before 600 cal yr BP, global SAM positive and high ENSO variability dominated; from 600 to 400 cal yr BP SAM negative and low ENSO variability persisted; after 400 cal yr BP, global SAM positive and low ENSO variability conditions existed (Fig. 5.10), as have been described in present day records (Damini et al., 2022; Dotto et al., 2016)

TG02 MS record presents a 100-yr cyclicity (Fig. 5.8). This centennial cycle could be harmonic of the well-established 200-yr cycle associated to solar activity and reported in many records in South America and the Antarctic region (Barcena et al., 2006; Leventer et al., 1996). At Lago Argentino (Moreno et al., 2014) and Lago Cipreses (Van Wyk de Vries et al., 2023) in southern Patagonia, those cycles are related to the SAM variability. Van Wyk de Vries et al. (2023) point to the record resolution to be controlling the periodicity of the cycles, with shorter period cyclicities of 150 and 85 yr observed in shorter records of gravity cores and longer period peaks of 200 yr observed in longer timescales covered by piston cores. The high-resolution record of TG02 can, therefore, register a 100-yr periodicity of the SAM, with the higher current intensity facies developing at positive phases. Formation of F3 does not occur in every cycle and could be conditioned to especially intense SAM-positive phases, probably coupled with the ENSO-negative phases.



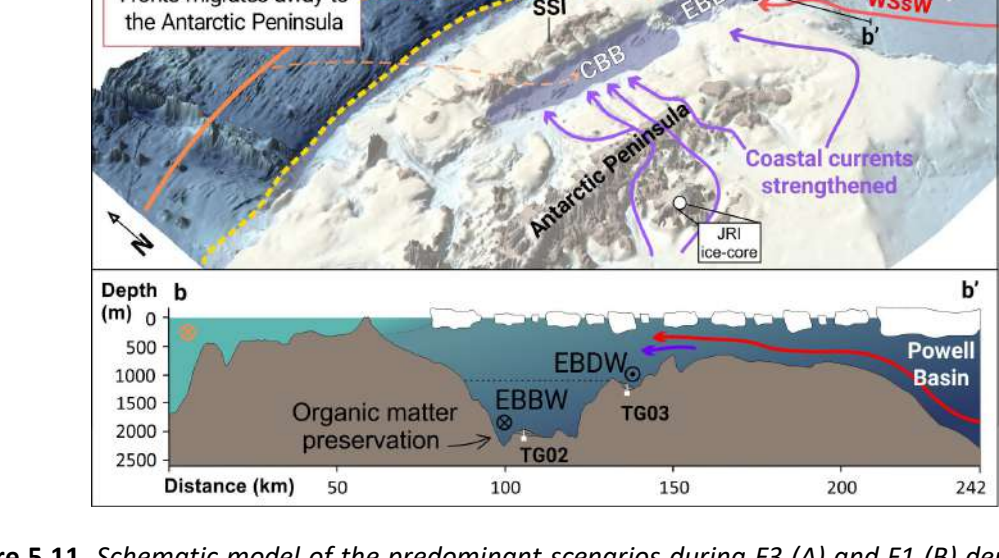


**Figure 5.11.** Schematic model of the predominant scenarios during F3 (A) and F1 (B) deposition. The summary of the effects of the SAM on the tip of the Antarctic Peninsula region is extracted from Dotto et al. (2016). The dashed yellow line represents the relative position of the fronts to the location of the sediment cores. WSsW: Weddell Sea sill Water; SFZ: Shakelton Fracture Zone, CDW: Circumpolar Deep Water; CBB: Central Bransfield Basin; EBB East Bransfield Basin; EBBW: East Bransfield Bottom Water; EBDW: East Bransfield Deep Water.

#### 5.6. Conclusions

Element geochemistry, grain size, physical properties, and paleontological analyses in sediments from cores TG02 and TG03, collected from two different contourite drifts in the EBB, show that the original pelagic/hemipelagic sediments have been reworked by the action of bottom contour currents. CT-scan images have been critical in order to detect sedimentary structures and bioturbation and non-visible lamination associated with contour currents and to define distinct facies. The development of facies F1, F2, F2\* and F3 has been linked to changes in current intensity influencing organic matter preservation, winnowing and sediment coarsening. The development of F3 only in TG02 suggests to us that its location was influenced by bottom contour currents with higher velocities than the location of TG03. We interpret the difference in current intensity between the two cores to be controlled by the different currents bathing the sites with TG02 recording the influence of the BBW, and TG03 recording the influence of the shallower BDW.

Paleontological and geochemical proxies evidence significant paleoceanographic changes in the EBB during the last millennium. Both cores indicate a major change at 600 cal yr BP towards more open water conditions. In addition, TG02 records CDW intrusions during the last 600 cal yr BP associated with negative ENSO phases and higher variability SAM. We differentiate three phases: (1) before 600 cal yr BP, characterized by global SAM positive and high ENSO variability; (2) from 600 to 400 cal yr BP characterized by SAM negative and low ENSO variability; and (3) after 400 cal yr BP, when global SAM positive and low ENSO variability conditions. Higher detrital facies (F2\* and F3) appear to be associate to high current intensity periods forced by 100-yr cycles during SAM positive phases.



Supplementary material to

CHAPTER 5

# Supplementary material to CHAPTER 5

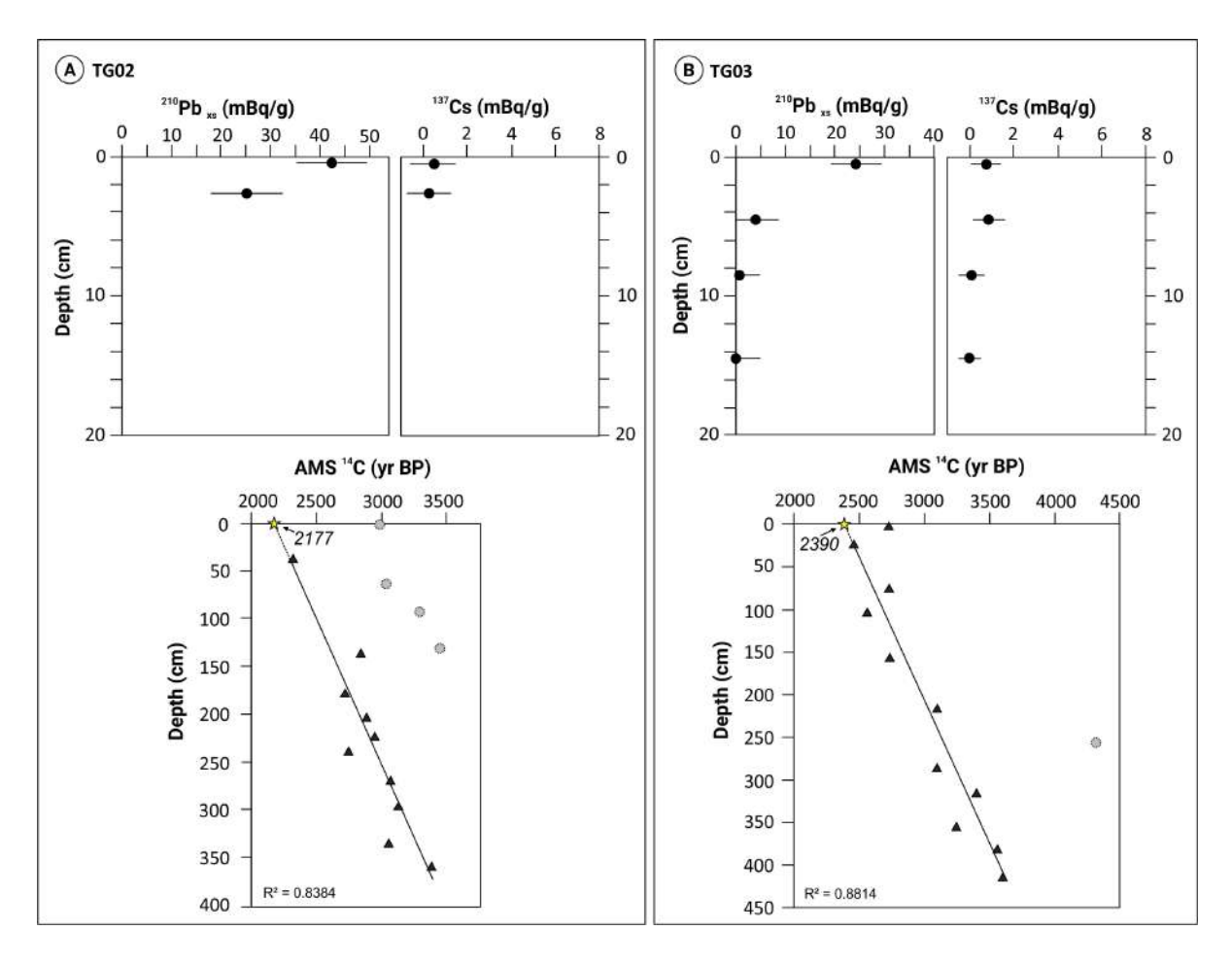


**Figure S5.1.** Resulting ages from the AMS radiocarbon dating of bulk organic matter samples and the  $^{210}Pb_{xcs}$  and  $^{137}Cs$  activities measured on the top 30 cm of in TG02 (A) and TG03 (B).

T	G02		Batch 1	Batch 2	Mean batches 1&2
Lab code	Section	Depth (cm)	Age ± 1σ (yr BP)	Age ± 1σ (yr BP)	Age ± 1σ (yr BP)
Carbonus-1043	1/3	0	2367 ± 15	3623 ± 17	2995 ± 16
Carbonus-1046	1/3	36	2318 ± 16	2335 ± 17	<b>2326</b> ± 16
Carbonus-1049	1/3	64	3046 ± 16	3046 ± 17	3046 ± 17
Carbonus-1052	1/3	93	3319 ± 16	3297 ± 17	3308 ± 17
Carbonus-1054	1/3	131	3521 ± 16	3385 ± 17	3453 ± 16
Carbonus-1041	2/3	137	2832 ± 15	2862 ± 16	<b>2847</b> ± 16
Carbonus-1044	2/3	178	2707 ± 15	2735 ± 16	<b>2721</b> ± 16
Carbonus-1047	2/3	205	2925 ± 15	2892 ± 16	<b>2909</b> ± 15
Carbonus-1050	2/3	223	2937 ± 16	2974 ± 17	<b>2956</b> ± 16
Carbonus-1051	2/3	240	2743 ± 15	2769 ± 16	<b>2756</b> ± 16
Carbonus-1053	2/3	270	3070 ± 16	3084 ± 16	<b>3077</b> ± 16
Carbonus-1042	3/3	296	3118 ± 16	3148 ± 17	<b>3133</b> ± 16
Carbonus-1045	3/3	336	3066 ± 15	3070 ± 14	<b>3068</b> ± 14
Carbonus-1048	3/3	361	3389 ± 14	3407 ± 14	<b>3398</b> ± 14

**Table S5.1.** AMS <sup>14</sup>C ages for bulk organic matter samples from TG02. The final selected ages are bold.

T	G03		Batch 1	Batch 2	Mean batches 1&2
Lab code	Section	Depth (cm)	Age ± 1σ (yr BP)	Age ± 1σ (yr BP)	Age ± 1σ (yr BP)
Carbonus-1055	1/3	4	2712 ± 13	2755 ± 14	2734 ± 13
Carbonus-1059	1/3	25	2510 ± 14	2426 ± 13	2468 ± 14
Carbonus-1062	1/3	78	2730 ± 14	2740 ± 13	2735 ± 14
Carbonus-1064	1/3	105	2588 ± 14	2571 ± 13	2579 ± 13
Carbonus-1056	2/3	158	2740 ± 14	2727 ± 14	2733 ± 14
Carbonus-1061	2/3	218	3111 ± 14	3106 ± 14	3109 ± 14
Carbonus-1065	2/3	259	4297 ± 15	4353 ± 15	4325 ± 15
Carbonus-1067	2/3	288	3109 ± 14	3125 ± 14	3117 ± 14
Carbonus-1058	3/3	318	3487 ± 15	3334 ± 14	3410 ± 15
Carbonus-1060	3/3	357	3257 ± 15	3261 ± 15	3259 ± 15
Carbonus-1063	3/3	384	3578 ± 14	3571 ± 14	3574 ± 14
Carbonus-1066	3/3	417	3601 ± 14	3620 ± 14	3610 ± 14

**Table S5.2.** AMS <sup>14</sup>C ages for bulk organic matter samples from TG03. The final selected ages are in bold.

Core	Section	Depth (cm)	Facies	Gravel	Sand	Mud	D <sub>50</sub> (mm)	D <sub>90</sub> (mm)	Sediment name	Sorting	Skewness	Skewness (μm)	Kurtosis (μm)
TG02	1/3	3	F1	0.0%	5.5%	94.5%	16.79	49.86	Coarse Silt	Poorly Sorted	Fine Skewed	-0.17	1.04
TG02	1/3	7	F1	0.0%	4.0%	96.0%	15.11	45.52	Coarse Silt	Poorly Sorted	Fine Skewed	-0.16	1.02
TG02	1/3	12.5	F1	0.0%	5.9%	94.1%	16.77	50.93	Coarse Silt	Poorly Sorted	Fine Skewed	-0.15	1.03
TG02	1/3	14.75	F1	0.0%	5.2%	94.8%	16.66	49.36	Coarse Silt	Poorly Sorted	Fine Skewed	-0.17	1.03
TG02	1/3	17	F1	0.0%	4.4%	95.6%	15.26	45.94	Coarse Silt	Poorly Sorted	Fine Skewed	-0.16	1.03
TG02	1/3	23.75	F1	0.0%	4.8%	95.2%	15.02	47.47	Coarse Silt	Poorly Sorted	Fine Skewed	-0.16	1.01
TG02	1/3	25.5	F1	0.0%	5.8%	94.2%	17.01	50.87	Coarse Silt	Poorly Sorted Poorly	Fine Skewed Fine	-0.17	1.03
TG02	1/3	28	F1	0.0%	6.2%	93.8%	16.57	51.17	Coarse Silt	Sorted Poorly	Skewed Fine	-0.16	1.04
TG02	1/3	32	F1	0.0%	4.4%	95.6%	14.46	45.78	Coarse Silt	Sorted Poorly	Skewed Fine	-0.15	1.01
TG02	1/3	35	F1	0.0%	8.1%	91.9%	18.71	56.70	Coarse Silt	Sorted Poorly	Skewed	-0.14	1.09
TG02	1/3	38	F1	0.0%	7.4%	92.6%	15.73		Medium Silt	Sorted Poorly	Symmetrical Fine		1.14
TG02	1/3	44	F1	0.0%	5.1%	94.9%	15.55	48.84	Coarse Silt	Sorted Poorly	Skewed Fine	-0.16	1.02
TG02	1/3	54	F1	0.0%	6.2%	93.8%	17.01	51.42	Coarse Silt	Sorted Poorly	Skewed Fine	-0.17	1.06
TG02	1/3	65 69	F1 F1	0.0%	<ul><li>4.4%</li><li>6.1%</li></ul>	95.6% 93.9%	15.26 15.22	46.13 50.06	Coarse Silt Coarse Silt	Sorted Poorly	Skewed Fine	-0.17 -0.14	1.02
1002	1/3			0.070	0.170	JJ.J/0	15.22	30.00	Coarse Sire	Sorted Poorly	Skewed Fine	-0.14	
TG02	1/3	74	F2	0.0%	4.3%	95.7%	14.65	45.61	Coarse Silt	Sorted	Skewed	-0.16	1.01
TG02	1/3	84	F2	0.0%	5.5%	94.5%	16.50	49.91	Coarse Silt	Poorly Sorted	Fine Skewed	-0.16	1.02
TG02	1/3	94	F2	0.0%	4.7%	95.3%	15.18	46.92	Coarse Silt	Poorly Sorted	Fine Skewed	-0.16	1.03
TG02	1/3	104	F3	0.0%	5.4%	94.6%	15.74	49.78	Coarse Silt	Poorly Sorted	Fine Skewed	-0.16	1.01
TG02	1/3	114	F3	0.0%	8.6%	91.4%	16.87	58.50	Coarse Silt	Poorly Sorted	Fine Skewed	-0.14	1.00
TG02	1/3	124	F3	0.0%	16.6%	83.4%	19.80	87.23	Very Fine Sandy Coarse Silt	Poorly Sorted	Symmetrical	-0.06	1.01

**Table S5.3.** *Grain size results of each analyzed TG02 bulk sample.* 

Core	Section	Depth (cm)	Facies	Gravel	Sand	Mud	D <sub>50</sub> (mm)	D <sub>90</sub> (mm)	Sediment name	Sorting	Skewness	Skewness (μm)	Kurtosis (μm)
TG02	1/3	134	F2*	0.0%	5.3%	94.7%	14.56	47.62	Coarse Silt	Poorly Sorted	Fine Skewed	-0.13	1.02
TG02	2/3	136.9	F2*	0.0%	7.5%	92.5%	16.18	53.56	Coarse Silt	Poorly Sorted	Fine Skewed	-0.12	1.07
TG02	2/3	145.65	F2*	0.0%	5.7%	94.3%	15.03	49.28	Coarse Silt	Poorly Sorted	Fine Skewed	-0.14	1.01
TG02	2/3	155.65	F2*	0.0%	4.6%	95.4%	16.20	48.34	Coarse Silt	Poorly Sorted	Fine Skewed	-0.16	1.03
TG02	2/3	165.15	F2*	0.0%	5.7%	94.3%	15.58	49.95	Coarse Silt	Poorly Sorted	Fine Skewed	-0.15	1.01
TG02	2/3	179.15	F1	0.0%	9.1%	90.9%	20.09	60.27	Coarse Silt	Poorly Sorted	Fine Skewed	-0.16	1.04
TG02	2/3	186.65	F1	0.0%	7.2%	92.8%	20.68	54.78	Coarse Silt	Poorly Sorted	Fine Skewed	-0.21	1.07
TG02	2/3	191.65	F3	0.0%	6.5%	93.5%	16.43	52.72	Coarse Silt	Poorly Sorted	Fine Skewed	-0.15	1.02
TG02	2/3	199.65	F3	0.0%	10.3%	89.7%	17.87	63.49	Very Fine Sandy Coarse Silt	Poorly Sorted	Fine Skewed	-0.12	1.02
TG02	2/3	206.15	F2	0.0%	5.6%	94.4%	17.25	50.81	Coarse Silt	Poorly Sorted	Fine Skewed	-0.18	1.01
TG02	2/3	215.65	F1	0.0%	5.2%	94.8%	17.09	50.10	Coarse Silt	Poorly Sorted	Fine Skewed	-0.17	1.03
TG02	2/3	224.65	F1	0.0%	7.6%	92.4%	17.04	54.92	Coarse Silt	Poorly Sorted	Fine Skewed	-0.12	1.03
TG02	2/3	226.65	F1	0.0%	8.0%	92.0%	18.79	56.51	Coarse Silt	Poorly Sorted	Fine Skewed	-0.17	1.05
TG02	2/3	228.65	F1	0.0%	6.1%	93.9%	17.11	51.67	Coarse Silt	Poorly Sorted	Fine Skewed	-0.16	1.03
TG02	2/3	235.65	F1	0.0%	11.5%	88.5%	19.28	68.73	Very Fine Sandy Coarse Silt	Poorly Sorted	Symmetrical	-0.04	1.23
TG02	2/3	241.15	F1	0.0%	8.8%	91.2%	20.94	59.49	Coarse Silt	Poorly Sorted	Fine Skewed	-0.20	1.03
TG02	2/3	242.9	F1	0.0%	7.8%	92.2%	23.37	57.54	Coarse Silt	Poorly Sorted	Fine Skewed	-0.26	1.02
TG02	2/3	255.15	F2*	0.0%	5.2%	94.8%	15.04	48.61	Coarse Silt	Poorly Sorted	Fine Skewed	-0.15	0.99
TG02	2/3	265.65	F2*	0.0%	4.1%	95.9%	14.27	45.48	Coarse Silt	Poorly Sorted	Fine Skewed	-0.15	1.00
TG02	2/3	267.65	F2*	0.0%	3.9%	96.1%	14.76	45.37	Coarse Silt	Poorly Sorted	Fine Skewed	-0.15	1.01

**Table S5.3 (cont).** *Grain size results of each analyzed TG02 bulk sample.* 

Core	Section	Depth (cm)	Facies	Gravel	Sand	Mud	D <sub>50</sub> (mm)	D <sub>90</sub> (mm)	Sediment name	Sorting	Skewness	Skewness (μm)	Kurtosis (μm)
TG02	2/3	269.65	F2	0.0%	5.6%	94.4%	16.82	51.25	Coarse Silt	Poorly Sorted	Fine Skewed	-0.15	1.00
TG02	2/3	271.65	F2	0.0%	8.9%	91.1%	18.97	59.98	Coarse Silt	Poorly Sorted	Fine Skewed	-0.15	0.98
TG02	2/3	275.65	F2	0.0%	5.1%	94.9%	15.81	49.35	Coarse Silt	Poorly Sorted	Fine Skewed	-0.15	1.00
TG02	2/3	285.65	F2	0.0%	4.0%	96.0%	15.06	45.39	Coarse Silt	Poorly Sorted	Fine Skewed	-0.15	1.03
TG02	3/3	289.3	F2	0.0%	6.1%	93.9%	16.57	51.35	Coarse Silt	Poorly Sorted	Fine Skewed	-0.14	1.02
TG02	3/3	297.3	F2	0.0%	7.0%	93.0%	17.08	53.57	Coarse Silt	Poorly Sorted	Fine Skewed	-0.14	1.03
TG02	3/3	307.3	F2*	0.0%	3.4%	96.6%	12.21	41.80	Medium Silt	Poorly Sorted	Fine Skewed	-0.11	0.98
TG02	3/3	317.3	F2	0.0%	7.3%	92.7%	18.93	55.03	Coarse Silt	Poorly Sorted	Fine Skewed	-0.18	1.04
TG02	3/3	323.3	F2	0.0%	7.5%	92.5%	17.41	54.96	Coarse Silt	Poorly Sorted	Fine Skewed	-0.14	1.03
TG02	3/3	327.3	F2	0.0%	8.3%	91.7%	17.30	57.33	Coarse Silt	Poorly Sorted	Fine Skewed	-0.13	1.03
TG02	3/3	337.3	F2	0.0%	7.8%	92.2%	21.21	56.93	Coarse Silt	Poorly Sorted	Fine Skewed	-0.22	1.04
TG02	3/3	347.3	F2*	0.0%	7.7%	92.3%	16.33	54.91	Coarse Silt	Poorly Sorted	Fine Skewed	-0.12	1.04
TG02	3/3	357.3	F2*	0.0%	6.5%	93.5%	16.14	51.97	Coarse Silt	Poorly Sorted	Fine Skewed	-0.13	1.03
TG02	3/3	361.8	F2*	0.0%	6.1%	93.9%	15.50	50.34	Coarse Silt	Poorly Sorted	Fine Skewed	-0.11	1.05

**Table S5.3 (cont).** Grain size results of each analyzed TG02 bulk sample.

Core	Section	Depth (cm)	Facies	Gravel	Sand	Mud	D <sub>50</sub> (mm)	D <sub>90</sub> (mm)	Sediment name	Sorting	Skewness	Skewness (μm)	Kurtosis (μm)
TG03	1/3	0.25	F1	0.0%	11.5%	88.5%	15.62	67.76	Very Fine Sandy Medium Silt	Poorly Sorted	Symmetrical	-0.034	0.991
TG03	1/3	5	F1	0.0%	7.0%	93.0%	13.53	53.28	Medium Silt	Poorly Sorted	Symmetrical	-0.050	0.981
TG03	1/3	15	F1	0.0%	14.3%	85.7%	21.27	77.53	Very Fine Sandy Coarse Silt	Poorly Sorted	Fine Skewed	-0.152	1.007
TG03	1/3	16.5	F1	0.0%	9.1%	90.9%	16.47	59.81	Coarse Silt	Poorly Sorted	Symmetrical	-0.091	1.014
TG03	1/3	25.5	F1	0.0%	15.4%	84.6%	26.55	77.04	Very Fine Sandy Very Coarse Silt	Poorly Sorted	Fine Skewed	-0.205	1.030
TG03	1/3	27	F1	0.0%	8.2%	91.8%	15.29	57.14	Coarse Silt	Poorly Sorted	Symmetrical	-0.087	0.965
TG03	1/3	34.5	F1	0.0%	11.1%	88.9%	16.30	65.66	Very Fine Sandy Coarse Silt	Poorly Sorted	Symmetrical	-0.088	0.952
TG03	1/3	44.75	F1	0.0%	10.1%	89.9%	14.82	62.88	Very Fine Sandy Medium Silt	Poorly Sorted	Symmetrical	-0.052	0.951
TG03	1/3	47.5	F1	0.0%	9.3%	90.7%	14.10	60.31	Medium Silt	Poorly Sorted	Symmetrical	-0.051	0.949
TG03	1/3	55	F2*	0.0%	8.9%	91.1%	14.88	59.24	Coarse Silt	Poorly Sorted	Symmetrical	-0.088	0.933
TG03	1/3	64.5	F2*	0.0%	8.8%	91.2%	14.08	58.84	Medium Silt	Poorly Sorted	Symmetrical	-0.065	0.948
TG03	1/3	75	F2*	0.0%	9.8%	90.2%	14.65	61.97	Medium Silt	Poorly Sorted	Symmetrical	-0.038	1.007
TG03	1/3	78	F2*	0.0%	6.5%	93.5%	14.25	52.00	Medium Silt	Poorly Sorted	Symmetrical	-0.064	1.003
TG03	1/3	85	F2*	0.0%	11.6%	88.4%	16.21	67.39	Very Fine Sandy Coarse Silt	Poorly Sorted	Symmetrical	-0.080	0.940
TG03	1/3	95.5	F2*	0.0%	7.7%	92.3%	15.22	55.06	Medium Silt	Poorly Sorted	Symmetrical	-0.064	1.005
TG03	1/3	105.25	F1	0.0%	9.9%	90.1%	15.90	62.34	Medium Silt	Poorly Sorted	Symmetrical	-0.037	0.949
TG03	1/3	107	F1	0.0%	10.5%	89.5%	17.63	63.71	Coarse Silt	Poorly Sorted	Symmetrical	-0.058	0.896
TG03	1/3	115	F1	0.0%	11.3%	88.7%	16.80	66.47	Very Fine Sandy Coarse Silt	Poorly Sorted	Symmetrical	-0.078	0.962

**Table S5.4.** Grain size results of each analyzed TG03 bulk sample.

Core	Section	Depth (cm)	Facies	Gravel	Sand	Mud	D <sub>50</sub> (mm)	D <sub>90</sub>	Sediment name	Sorting	Skewness	Skewness (μm)	Kurtosis (μm)
TG03	1/3	123.5	F2*	0.0%	7.7%	92.3%	16.64	55.34	Coarse Silt	Poorly Sorted	Fine Skewed	-0.109	1.016
TG03	1/3	125.25	F2*	0.0%	9.0%	91.0%	16.57	59.42	Coarse Silt	Poorly Sorted	Symmetrical	-0.068	1.011
TG03	1/3	128	F2*	0.0%	8.2%	91.8%	17.59	57.49	Coarse Silt	Poorly Sorted	Fine Skewed	-0.118	1.002
TG03	1/3	129.5	F1	0.0%	6.2%	93.8%	12.84	51.58	Medium Silt	Poorly Sorted	Symmetrical	0.028	1.005
TG03	2/3	151.5	F1	0.0%	9.7%	90.3%	18.72	61.67	Coarse Silt	Poorly Sorted	Fine Skewed	-0.125	0.950
TG03	2/3	159	F1	0.0%	11.9%	88.1%	17.38	68.23	Very Fine Sandy Coarse Silt	Poorly Sorted	Fine Skewed	-0.100	0.927
TG03	2/3	166	F1	0.0%	17.5%	82.5%	28.35	84.27	Very Fine Sandy Very Coarse Silt	Poorly Sorted	Fine Skewed	-0.233	1.074
TG03	2/3	169	F1	0.0%	9.6%	90.4%	15.96	61.37	Medium Silt	Poorly Sorted	Symmetrical	-0.060	0.998
TG03	2/3	179	F1	0.0%	13.4%	86.6%	21.00	71.82	Very Fine Sandy Very Coarse Silt	Poorly Sorted	Fine Skewed	-0.154	0.932
TG03	2/3	189	F1	0.0%	9.7%	90.3%	15.67	61.65	Medium Silt	Poorly Sorted	Symmetrical	-0.027	0.967
TG03	2/3	199	F2	0.0%	12.3%	87.7%	16.53	70.14	Very Fine Sandy Very Coarse Silt	Poorly Sorted	Symmetrical	-0.093	0.920
TG03	2/3	209	F2	0.0%	8.0%	92.0%	15.10	57.36	Coarse Silt	Poorly Sorted	Fine Skewed	-0.114	0.891
TG03	2/3	218.75	F2	0.0%	6.7%	93.3%	13.74	52.56	Medium Silt	Poorly Sorted	Symmetrical	-0.060	0.979
TG03	2/3	222	F2	0.0%	6.9%	93.1%	14.31	53.74	Medium Silt	Poorly Sorted	Symmetrical	-0.034	0.955
TG03	2/3	228.5	F2*	0.0%	10.0%	90.0%	14.89	62.59	Very Fine Sandy Medium Silt	Poorly Sorted	Symmetrical	-0.020	1.008
TG03	2/3	225	F2*	0.0%	8.7%	91.3%	17.83	58.98	Coarse Silt	Poorly Sorted	Fine Skewed	-0.134	0.958
TG03	2/3	233	F2*	0.0%	8.5%	91.5%	13.96	57.61	Medium Silt	Poorly Sorted	Symmetrical	-0.042	0.984
TG03	2/3	239	F2*	0.0%	9.8%	90.2%	13.59	61.68	Medium Silt	Poorly Sorted	Symmetrical	mmetrical -0.034	
TG03	2/3	245	F2*	0.0%	9.4%	90.6%	13.88	60.62	Medium Silt	Poorly Sorted	Symmetrical	-0.042	0.960
TG03	2/3	249	F2*	0.0%	9.5%	90.5%	15.47	60.91	Medium Silt	Poorly Sorted	Symmetrical	-0.061	0.993
TG03	2/3	257.5	F1	0.0%	6.1%	93.9%	11.85	50.11	Medium Silt	Poorly Sorted	Symmetrical	0.077	1.148

**Table S5.4 (cont).** *Grain size results of each analyzed TG03 bulk sample.* 

Core	Section	Depth (cm)	Facies	Gravel	Sand	Mud	D <sub>50</sub> (mm)	D <sub>90</sub> (mm)	Sediment name	Sorting	Skewness	Skewness (μm)	Kurtosis (μm)
TG03	2/3	259.5	F2	0.0%	9.1%	90.9%	15.69	59.82	Coarse Silt	Poorly Sorted	Symmetrical	-0.065	0.991
TG03	2/3	269	F2	0.0%	10.1%	89.9%	16.16	62.79	Very Fine Sandy Medium Silt	Poorly Sorted	Symmetrical	-0.044	1.004
TG03	2/3	279	F2	0.0%	6.1%	93.9%	12.59	51.18	Medium Silt	Poorly Sorted	Symmetrical	0.068	1.014
TG03	2/3	289	F2	0.0%	10.5%	89.5%	15.66	63.74	Very Fine Sandy Medium Silt	Poorly Sorted	Symmetrical	-0.020	0.944
TG03	2/3	296.5	F2*	0.0%	9.2%	90.8%	14.84	59.90	Medium Silt	Poorly Sorted	Symmetrical	-0.025	1.001
TG03	3/3	299.751	F2*	0.0%	7.7%	92.3%	12.86	54.35	Medium Silt	Poorly Sorted	Symmetrical	0.033	1.045
TG03	3/3	309.5	F2*	0.0%	9.0%	91.0%	14.56	59.01	Medium Silt	Poorly Sorted	Symmetrical	-0.019	1.011
TG03	3/3	318	F2	0.0%	7.9%	92.1%	14.63	55.42	Medium Silt	Poorly Sorted	Symmetrical	-0.061	0.995
TG03	3/3	329.5	F2*	0.0%	7.5%	92.5%	15.88	55.20	Coarse Silt	Poorly Sorted	Symmetrical	-0.086	0.973
TG03	3/3	339.5	F2	0.0%	8.9%	91.1%	14.43	58.86	Medium Silt	Poorly Sorted	Symmetrical	-0.042	0.978
TG03	3/3	344	F2	0.0%	9.8%	90.2%	14.26	61.69	Medium Silt	Poorly Sorted	Symmetrical	-0.007	0.996
TG03	3/3	349.5	F2*	0.0%	9.1%	90.9%	14.64	59.41	Medium Silt	Poorly Sorted	Symmetrical	-0.050	0.996
TG03	3/3	354.5	F2	0.0%	13.0%	87.0%	17.76	72.65	Very Fine Sandy Coarse Silt	Poorly Sorted	Symmetrical	-0.050	0.979
TG03	3/3	358	F2	0.0%	12.8%	87.2%	16.53	72.76	Very Fine Sandy Medium Silt	Poorly Sorted	Symmetrical	-0.008	0.995
TG03	3/3	360	F2	0.0%	8.7%	91.3%	19.55	59.00	Coarse Silt	Poorly Sorted	Fine Skewed	-0.189	0.998
TG03	3/3	369	F2	0.0%	9.2%	90.8%	15.23	59.81	Coarse Silt	Poorly Sorted	Symmetrical	-0.058	1.022
TG03	3/3	374.5	F2	0.0%	9.2%	90.8%	14.73	59.88	Medium Silt	Poorly Sorted	Symmetrical	-0.055	0.960
TG03	3/3	379.5	F2	0.0%	8.2%	91.8%	14.94	56.93	Medium Silt	Poorly Sorted	Symmetrical	-0.045	0.990
TG03	3/3	384.5	F2	0.0%	9.0%	91.0%	18.94	59.84	Coarse Silt	Poorly Sorted	Fine Skewed	-0.148	0.982

**Table S5.4 (cont).** Grain size results of each analyzed TG03 bulk sample.

Core	Section	Depth (cm)	Facies	Gravel	Sand	Mud	D <sub>50</sub> (mm)	D <sub>90</sub>	Sediment name	Sorting	Skewness	Skewness (μm)
TG03	3/3	389.5	F2	0.0%	7.3%	92.7%	14.87	53.43	Coarse Silt	Poorly Sorted	Symmetrical	-0.091
TG03	3/3	399.5	F2	0.0%	6.4%	93.6%	14.35	51.86	Medium Silt	Poorly Sorted	Symmetrical	-0.087
TG03	3/3	409.5	F2	0.0%	8.4%	91.6%	16.67	58.01	Coarse Silt	Poorly Sorted	Fine Skewed	-0.123
TG03	3/3	418	F2	0.0%	8.2%	91.8%	16.61	57.07	Coarse Silt	Poorly Sorted	Fine Skewed	-0.105
TG03	3/3	420	F2	0.0%	8.7%	91.3%	16.65	58.69	Coarse Silt	Poorly Sorted	Symmetrical	-0.096
TG03	3/3	428.5	F2	0.0%	13.4%	86.6%	16.08	78.82	Very Fine Sandy Medium Silt	Very Poorly Sorted	Coarse Skewed	0.121

**Table S5.4 (cont).** Grain size results of each analyzed TG03 bulk sample.

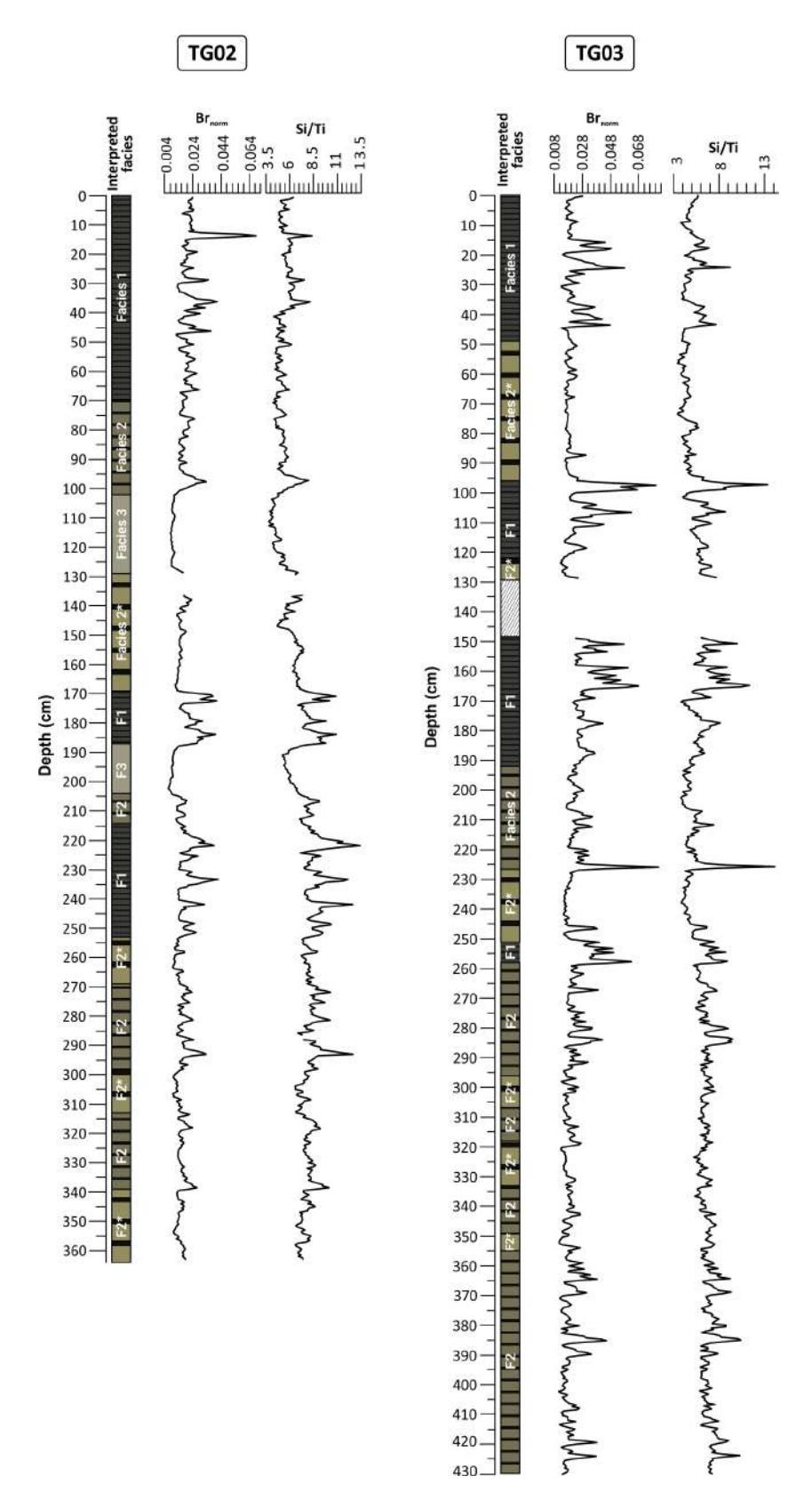


Figure S5.2. Comparison between Br norm and Si/Ti in cores TG02 (left) and TG03 (right).



General discussion and future perspectives

#### General discussion

The findings presented in this PhD thesis cover a broad temporal scope, employing multiple methodologies. These investigations have focused on elucidating unresolved questions concerning the opening of the Scotia Arc at its southern boundary and the subsequent paleoceanographic reorganization until recent times.

#### 6.1. The South Orkney Microcontinent key to Scotia Arc development and Southern Ocean circulation

## 6.1.1 The South Orkney Microcontinent as a keystone in the development of the southern Scotia Arc

The South Orkney Microcontinent (SOM) played an essential role during the development of the Scotia Arc by disrupting the land connection between Antarctica and South America during the opening of the Powell Basin (King & Barker, 1988). Chapter 3 presents the first 3D geophysical and geological model of this continental block that demonstrates that its deep structure and the distribution and orientation of its inner sedimentary basins result from the regional tectonic evolution, providing new insights for paleogeographic reconstructions (Riley et al., 2023). The particularity of this study lies the integration of several datasets, as previous studies had utilized single data sets and examined distinct structural characteristics separately (e.g., Harrington et al., 1976; King & Barker, 1988; Bussetti et al., 2001). The model results confirm the existence of two, northern and southern, structural domains in the SOM, in line with previous studies (King & Barker, 1988; Bussetti et al., 2001). The northern domain, located south of the South Orkney Islands, is characterized by a N-S extension that led to the opening of the Newton Basin as a back-arc basin (Trouw et al., 1997). The 3D modeling results point to the Newton basin having the most extensive sedimentary fill of the inner basins of the SOM, with a thickness of up to 3.5 km, slightly less than the 4 km previously described by Harrington et al. (1977).

Compared to previous studies, further differentiation has been made in the southern domain. 3D modeling has allowed the detailing of the geometry of the N-S elongated sedimentary basins (Pratt, Airy, Bouguer, and Eötvos). In this study, the westernmost sedimentary basin, tentatively named as Pratt Basin, is characterized for the first time. The Pratt Basin was previously recognized by Bussetti et al. (2001), but a detailed characterization was not possible due to the lack of quality seismic data in the area. Gravity modeling made it possible, which has proven to be a very valuable methodology for characterizing sedimentary basins. The four basins (Pratt, Airy, Bouguer, and Eötvos basins) sharing the same N-S elongation direction record a progressive east-west deformation reflected in the basement deformation and the final sedimentary geometry. This contrasts with previous knowledge of the southern domain of the SOM, which has been described as a central horst with two extended zones on either side (King & Barker, 1988). A proto-Powell basin would have initiated its extension

concurrently with these N-S elongated basins as a conjugated basin. Subsequently, extension focuses on the Powell basin that deepens and widens to produce a crustal neck prior to seafloor extension.

Based on previous studies (Amenábar et al., 2020; Bijl et al., 2013a; López-Quirós et al., 2021; Montes et al., 2019a) and the inferred ages in Chapter 3, the E-W extensional stress causing the formation of the Pratt, Airy, Bouguer and Eotvös sedimentary basins occurred between 50 and 35 Ma, before the final separation of the SOM from the Antarctic Peninsula. Results from Chapter 3 and 4 show that the sedimentary basins located in the southern domain of the SOM have acted as large sediment depocenters. However, in the northern domain, the Newton basin could hold an even longer record, as it has been open for a longer time period and hosts a greater sediment thickness. Thus, the sedimentary fill in this basin likely holds the record of the two phases of SOM deformation. Further investigation into the Newton Basin is warranted due to its extended opening and substantial sediment fill, yet limited seismic data quality inhibits detailed analysis.

Joint forward and inversion modeling of gravity and magnetic data allowed accurate mapping of the intrusive igneous rocks causing the magnetic anomalies in the southern domain of the SOM, linked to the Pacific Margin Anomaly (PMA). Previous studies, based on scattered 2D magnetic models, had described the intrusion of the igneous rock with a wide variety of sizes and magnetic susceptibilities within the SOM crust (Garrett et al., 1986/87; Harrington et al., 1972; Martos et al., 2014). However, the results of the 3D model report a single interruption in the continuity of this body, coinciding with a crustal thinning and the position of the broader and deeper Bouguer and Eötvös sedimentary basins in the southeastern sector of the SOM. This leads us to think that the location of basic rocks in the southern domain could favor the opening of the basins precisely in this zone due to the brittle behavior of the crust compared to the northern domain. However, no clear evidence of deformation linked to E-W extension is observed in the northern domain. In the absence of data, it is only possible to hypothesize about a boundary between the two sectors for which data would be needed for further investigation.

The better characterization of the intrusive igneous rocks causing the magnetic anomalies provides more insights for the paleogeographic reconstruction of the former land connection between Antarctica and South America. The elongation of the igneous rocks in the SOM is compatible with the attachment to the Antarctic Peninsula from the west. However, the continuity of this body to the east is still unknown. Since the most significant deformation is observed east of the SOM, its associated block to the east should also concentrate high deformation rates. There are different models for reconstructing the closure of the Drake Passage. To further investigate its paleogeographic configuration, similar studies as the one presented in Chapter 3 in the Herdman and Discovery banks might provide further evidence for deformation patterns observed east of the SOM, as magnetic anomalies have also been reported in these continental fragments (Martos et al., 2014).

## 6.1.2 The South Orkney Microcontinent as a keystone in the early oceanic connection between the Weddell and the Scotia Seas

The opening of the Drake Passage and the development of the Scotia Sea occurred in many stages. One of these stages involved the separation of the SOM from the Antarctic Peninsula, which resulted in the opening of the Powell Basin. Today, the Powell Basin and the SOM play an important role in the Weddell-Scotia Confluence (WSC), an important boundary zone for the northward outflow of cold, dense water from the Weddell Sea into the Scotia Sea (Franco et al., 2007). A small number of studies have concentrated on the post-Oligocene tectonic evolution of the northern Scotia Arc region, pointing to the complex paleogeographic changes (i.e., from deep marine basins to shallow ridges and emerged regions) leading to today's general oceanic circulation and global climate (Lagabrielle et al., 2009). In the southern Scotia region, interpretations of seismic reflection data from the Weddell Sea region also point to the role of topography (i.e., controlled by subsidence and margin progradation) on paleo-ocean circulation in the region (Huang et al., 2017). Our study in Chapter 4 shows that the opening and deepening of the Powell Basin, as the SOM detached from the Antarctic Peninsula, played a crucial role in reshaping current paths between the Weddell Sea and the South Scotia Sea.

The characterization of the Bouguer and Eotvös basins in Chapter 3 showed them to be the deepest basins of the southern domain in the SOM and to have opened in the early Eocene (Morales-Ocaña et al., 2023). Chapter 4 shows these basins to be filled with pre-rift and syn-rift deposits of inferred early to late Eocene age. The chronostratigraphic framework in Chapter 4 dates the earliest evidence for the influence of current flow from the Weddell Sea around the margins of the SOM to likely occur during the middle-late Eocene. This is based on the local development of a contourite drift in the southern self-break below the Eocene-Oligocene Transition (EOT) horizon D4 (i.e., top of the syn-rift unit SU5 dated younger than 37.6 Ma, Chapter 4). At Site 696, the oldest sediments below the EOT show that the SOM was submerged, albeit shallow (Barker et al., 1988). In addition, the presence of a proto-Weddell Sea gyre flowing northward along the Antarctic Peninsula was interpreted based on the presence of endemic transantarctic dinocysts in middle-late Eocene sediments from Site 696 (Houben et al., 2019), which might have reached the edges of the SOM.

A change from a neritic deposition to a glauconitic terrigenous unit with low sedimentation rates at around 35.5 Ma has been interpreted as the time when the SOM separated from the sedimentary sources of the Antarctic Peninsula (López-Quirós et al., 2021). This separation, causing the opening of the Powell Basin, has been linked with a decrease in mean annual temperatures by around 1.4 °C (Thompson et al., 2022). At this time, Site 696 has been reported to have remained under the influence of Antarctic-derived surface currents, also associated with phases of invigorated bottom water circulation (Houben et al., 2019), which could be responsible for the growth of the drifts described in the SOM in Chapter 4. The progressive subsidence of the SOM as the separation continued, also favored by thermal subsidence of the Wedddell Sea (Huang et al., 2014), continued to deepen the SOM. As the SOM deepened, the southern continental margin was placed in a deeper position, allowing a mounded drift to continue its growth during the Oligocene and early Miocene. Coincidentally, during this early phase, the seismostratigraphic analysis denotes the formation of

another mounded drift in this area, disconnected from the contourite deposits in the southern margin. As these mounds cannot be explained by the influence of the same water masses, we suggest the likely influence of the proto-CDW in the middle SOM. However, we acknowledge that evidence for a shallow flow of a proto-CDW in the SOM is very limited. Further studies are needed in the area to determine its presence and distribution.

During the middle Miocene, as the Powell continued to open and the SOM to deepened, current circulation increased and contourite mounds grew in the interior of the Bouguer and Eötvös basins, both spatially and in thickness. As described in Chapter 4, previous studies in the southern Scotia Sea reported a significant regional paleoceanographic reorganization attributed to the northward outflow of the Weddell Sea Deep Water (WSDW) into the Scotia Sea (Maldonado et al., 2006, 2014; Martos et al., 2013; Pérez et al., 2019, 2021). The timing of this reorganization marked by the regional Reflector-c ranges between 8 and 14 Ma (Pérez et al., 2021; Weber et al., 2019). In the SOM, however, the development of contourite mounds ceased in the late Miocene. We hypothesize that a change in the distribution of currents was forced by the opening of the Jane Basin, which has been proposed to occur at 14 Ma (Bohoyo et al., 2002). The initiation of the interaction between the Weddell Sea source waters and the Scotia Sea has been described as occurring through the Scan Basin. This has been demonstrated by the description of a contour fan. The formation of this depositional body was only possible when the opening of the Bruce Passage was initiated and once this passage was deep enough for deep water circulation (Hernández-Molina, 2007).

During the earliest Late Miocene, a recent study showed that the Antarctic Circumpolar Current acquired its modern characteristics (i.e., a strong and deep current) (Evangelinos et al., 2024). Several tectonic changes have been known to be active during this period and might have controlled paleogeographic changes leading to the current configuration of the Southern Ocean. The triple junction zone that conforms to the Scotia-Antarctic-South Shetland Block represents one of the most active tectonic areas. The uplift of the Shackelton Fracture Zone (SFZ) ridge occurred since 12 Ma. SFZ became an effective barrier to bottom flows in the southern Drake Passage, shifting northward to the ACC and the Polar Front and contributing to the thermal isolation of Antarctica and more polar conditions from 8 Ma (Martos et al., 2013). The northward displacement of the Lower Circumpolar Deep Water and the opening of passages along the South Scotia Ridge favored the insertion of WSDW flows along the southern part of the Drake Passage, westward into the Pacific Ocean, and northward into the abyssal plain of the southwestern Scotia Sea (Martos, 2013). Although no univocal correlation can be established, all these findings point to the early Late Miocene when the southern Scotia Sea's continental blocks and oceanic pathways reached a paleogeographic and oceanographic configuration similar to the modern one. Long sediment cores with sediments ranging from the middle Miocene to recent from key basins in the Southern Scotia Sea are needed to test this hypothesis and determine the switching of current pathways between the Weddell Sea and the Scotia Sea.

#### 6.2. Recent climatic variability from contourite deposits

The opening of Bransfield Strait as a back-arc basin represents one recent tectonic event in the Scotia Arc development (Galindo-Zaldívar et al., 2004; Jabaloy et al., 2003). Its opening is linked to the triple junction zone of the Scotia-Antarctic-South Shetland Block. The South Shetland Block constitutes a continental fragment that has been separated from the Antarctic Peninsula since the Pliocene (3.3 Ma) (Galindo-Zaldívar et al., 2004). At present, the basin is still under a generally extensional setting. Evidence of the recent tectonic influence in the region is the Quaternary deformation that has been reported from Elephant Island (Galindo-Zaldívar et al., 2006). Changing paleogeographic configurations during the opening of the Bransfield Strait forced the re-distribution of ocean water masses until the oceanic circulation began to resemble the present after a period of volcanic activity, possibly around the middle Pleistocene (Liu et al., 2022). Today, the warm CDW enters the Bransfield Strait from the South Shetlands Islands while the cold Weddell Sea Surface Water enters from the Powell Basin and the (Wilson et al., 1999). However, there is little knowledge about how varying climatic conditions in the past have controlled the circulation in the Bransfield Basin.

The two gravity cores (TG02 and TG03) from the Eastern Bransfield Basin (EBB) analyzed in Chapter 5 span the last millennium, which does not allow for the determination of long-term tectonic controlled changes in ocean circulation but provides new insights into past variability of the regional oceanic frontal systems. Complementary to interpretations from nearby marine sediment cores (Fabrés et al., 2000; Yoon et al., 2001; Khim et al., 2002; Bahk et al., 2003), we interpret sediments in cores TG02 and TG03 to record the influence of different bottom currents bathing the EBB. We show that, similar to studies from other margins (e.g., Bahr et al., 2014; Salabarnada et al., 2018; Smillie et al., 2019), contourite deposits in the EBB contain a high-resolution record of past ocean circulation that we can link to climate change. In Chapter 5, changes in sedimentation result from the changing influence of the CDW and Weddell Sea waters, consistent with forcing by the ENSO and SAM highlatitude climate modes. Before 600 cal yr BP, the ocean circulation in the EBB was forced by a global SAM positive and high ENSO variability. After 600 cal yr BP, an overall warming trend is interpreted based on decreased sea ice diatoms in the EBB. This change coincides with a warming trend observed in the eastern Antarctic Peninsula (Mulvaney et al., 2012). From 600 to 400 cal yr BP, the record shows the influence of a SAM-positive and low ENSO variability. After 400 cal yr BP, the EBB ocean currents are influenced by global SAM-positive and low ENSO variability conditions.

Similar to other Antarctic contourite deposits (i.e., Evangelinos et al., 2018; Salabarnada et al., 2018), higher detrital content appears to be associated with high current intensity periods. Diatom assemblages retrieved from the deeper parts of the EBB confirm that CDW reaches the EBB during times of high current intensities. In addition, high currents intensity facies are forced by 100-year cycles, probably related to SAM-positive phases.

The findings in Chapter 5 are relevant in the context of the ongoing global change, especially when considering the Antarctic Peninsula as one of the Antarctic regions most affected by warming. Indeed, changes are already being reported. For example, sea ice overall extension has decreased, the

volume of AABW has contracted, and the pH has decreased (e.g., Purkey et al., 2010; Rintoul et al., 2018). Our results provide insights into how the migration of frontal systems to the south forced by warming can result in more frequent CDW incursions into the Bransfield Basin.

#### Future perspectives

Completing this PhD thesis has raised new questions and avenues for future research. Results from the 3D model of the South Orkney Microcontinent (SOM) have revealed different stress accommodation between the northern and southern domains, probably due to the presence of the Cretaceous-age basement rock intrusion in the southern domain. However, the E-W deformation linked to the early stages of the Scotia Arc opening is not discernible in the northern domain. Therefore, a better characterization of the northern domain could help to understand the mechanism that coupled the differential deformation. In addition, the Newton basin, located in the northern domain of the SOM, hosts the largest sedimentary cover. This basin developed during the earlier stages of Scotia Arc evolution before the opening of the Pratt, Airy, Bouguer, and Eötvös basins in the southern domain. This basin is not well characterized due to sparse seismic data. Therefore, its study with high-quality MCS profiles validated with sedimentary data from deep ocean drilling, could provide a better understanding of the earlier tectonic stages in the evolution of the SOM.

In addition, our study has modeled the position and geometry of intrusive igneous rocks in the southern SOM that correlate with the Pacific Margin Anomaly (PMA) on the Antarctic Peninsula. However, the continuity of these intrusive igneous rocks to the east of the SOM needs to be demonstrated, which nowadays is prevented by a lack of data. 3D modeling of magnetic anomalies of adjacent continental blocks with related magnetic anomalies, such as the Herdman and Discovery blocks, could help elucidate their position before the opening of the Scotia Arc, contributing to improved paleogeographic reconstructions.

The study of the sedimentary fill of the SOM has provided unprecedented insights into the separation of the SOM from the Antarctic Peninsula and the opening of the Powell basin. We have shown how the early paleogeographic configurations forced the redistribution of ocean current paths in the region. These results point to a critical time in the development of the Scotia Arc when the connections of the Weddell Gyre and the Antarctic Circumpolar Current became similar to the present. However, more information is required from the Powell, Jane, and Scan basins to determine the timing and nature of the paleogeographic changes leading to present configurations. The Powell Basin contains a thick sedimentary cover above the acoustic basement that likely includes a valuable paleoceanographic record. The available seismic profiles recently acquired in oceanographic campaigns conducted by the Spanish R/V Hesperides offer the opportunity to analyze its sedimentary fill, which likely records the main events in its evolution. The sedimentary fill above is expected to range from syn-rift phases to recent oceanographic changes, allowing us to correlate with observations from the work in this thesis and previous studies from the western margin of the Powell Basin (e.g., Shaldril program cores). The study of the Powell Basin sedimentary fill could also provide information of the timing of the first influence of the CDW on sedimentation during the early phases of the Drake Passage opening.

The validation of interpretations based on seismic studies with sediment cores obtained during deep ocean drilling expeditions is highly desirable from the Powell basin and other critical

basins in the opening of the Scotia Arc. The scarce sedimentary material in the area precludes more complete work that interrelates the different sedimentary basins. Efforts such as those of the recent International Ocean Drilling Program Leg 382 drilling in the Dove Basin and central Scotia demonstrate the importance of new coring to provide a chronostratigraphic framework to the interpreted tectonic and climatic events based on seismic stratigraphic studies. New sedimentological data is key to advancing knowledge of unexplored areas. Still, as the result of this thesis proves, there is value in the study of sedimentary legacy sections. We show how sedimentary sections collected previously by scientific drilling expeditions, such as the ODP Leg 113 drilled in 1987, can still provide high-level science and valuable information for understanding the dynamics and evolution of the Scotia Arc. Nevertheless, improving the age models of the already collected sediments is essential.

Given the critical role that the Southern Ocean plays in the global climate system and the ongoing climate warming, it is very relevant to better understand how climate forcing impacts the dynamics of the frontal systems. In this thesis, we have focused on the changes in sedimentation in the EBB, where warm CDW interacts with the cold Weddell Sea Surface Water. Our study has provided insights into changing paleoenvironmental conditions in the EBB forced by different ENSO and SAM high-latitude climate modes during the last millennium. Further investigations are necessary to constrain the spatial and temporal variability of contour currents in the region by comparing sediment cores along the different basins of the Bransfield Strait (i.e., West and Central basins) and at similar depths. Key to this research is targeting mounded deposits, which have proven to contain valuable high-resolution paleoceanographic and paleoclimatic records. In this context, in addition to the two cores presented in this thesis, sediment cores collected from mounded deposits along the Bransfield Strait during the Powell 2020 and the PENANT 2024 oceanographic cruises provide an opportunity to tackle this challenge. For example, comparisons with other cores along the Bransfield Strait can provide further constraints on the forcing for intrusions of CDW in the different Bransfield Basins and its impact on siliceous phytoplankton ecosystems.

Also relevant for future studies is to constrain how the connections between the Weddell Sea and the Bransfield Straits are affected by climate variability. This could be achieved by comparing cores strategically located along the sill connecting the Powell and the Bransfield Basins. Finally, these sediment core analyses can benefit from emerging techniques such as hyperspectral analysis, which offers novel possibilities for providing continuous results on physical properties and geochemical composition much more efficiently. Although the application of this methodology to sediment cores remains limited, it presents promising possibilities for future research work.



Conclusions

#### CHAPTER 7: Conclusions

To achieve the three main objectives of this thesis, presented in the Context and Motivation section, a multi-methodological approach has been carried out, including geophysical modeling, seismic stratigraphic analysis, and sedimentary core analyses. Studies have focused mainly on two areas: The South Orkney Microcontinent (SOM), as a key piece in the development of the Scotia Arc and the Southern Ocean circulation, and the Bransfield Basin, as a key area to study recent climate variability. The results presented in Chapters 3, 4, and 5 provide important new insights into the evolution of the southern Scotia Arc, from the tectonic processes linked to the early stages of the opening of the Drake Passage to the subsequent paleoceanographic reorganization and variability of the oceanic configuration during the last millennium, influenced by El Niño-Southern Oscillation (ENSO) and the Southern Annular Mode (SAM).

Thus, the overall objective of this thesis - to determine the major tectonic events that led to the rifting and subsidence of the SOM due to the opening of the surrounding basins and the establishment of the subsequent paleoceanographic and paleoenvironmental evolution - has been addressed, with the following main findings related to each specific objective:

## 1. Characterization of the deep structure of the SOM through 3D potential field data modeling (i.e., gravity and magnetic anomalies) and multichannel seismic data

Chapter 3 provides a 3D geological and geophysical modeling of the SOM. The resulting model has provided valuable insights into the structural configuration of the SOM, resulting from the Scotia Arc development. In addition, the correlation of the multichannel seismic data with the Ocean Drilling Program Site 696 in Chapter 4 has provided some unprecedented constraints on the time of successive tectonic events during the separation of the SOM from the Antarctic Peninsula. Main conclusions include:

- Two previously inferred domains that divide the SOM into northern and southern domains are confirmed. The differentiation between both domains is related to the intrusion of igneous rocks in the southern area. We interpret that this intrusion conditioned the rheology of the crust, facilitating its brittle deformation and leading to the opening of the N-S elongated basins (i.e., Pratt, Airy, Bouguer, and Eötvös Basins) during the initial stages of the opening of the Scotia Arc. In contrast, the northern shows no signs of deformation related to this E-W extension.
- In the southern domain, a progressive deformation is observed coherent with great extensional stress to the east of the SOM during the early stages of the Scotia Arc fragmentation, propagating westward thereafter. This resulted in the opening of the N-S elongated basins (Pratt, Airy, Bouguer, and Eötvös Basins). Among them, the Bouguer and Eötvös Basins, located in the southeasternmost area of the SOM, are inferred to be the most affected by the deformation. As a result, they are the broadest sedimentary basins in the

southern domain, and their location coincides with the fragmentation of the intrusive igneous rocks and crustal thinning. Model results suggest that the Powell Basin may develop parallel to the N-S elongated basins west of the Pratt Basin. As the opening of the N-S basins of the SOM ceased, the Powell basin would have progressed further, leading to its oceanization.

- 3D modeling of gravity anomalies allows a detailed characterization of the geometry of the SOM inner sedimentary basins. This is especially relevant for the Newton Basin since its previous characterization was less constrained due to the sparse Multichannel Seismic Reflection (MCS) profiles over the basin. Also, it was possible to define for the first time the geometry of a well-developed N-S elongated sedimentary basin, tentatively named Pratt Basin, in the southwestern sector of the SOM. Our results show that 3D geophysical and geological modeling is a powerful tool for characterizing sedimentary basins in regions with scarce direct data, such as Antarctica.
- Correlation of the MCS data with Ocean Drilling Program Site 696 allows us to determine that
  the age of the sedimentary fill in the Eötvös Basin is older than 37 Ma. We tentatively assigned
  an age between 45 and 50 Ma for the sediments resting directly above the basement based
  on the comparison with sedimentary rates of the conjugated sedimentary basins in the
  Seymour Island. In this time frame, the initial development of the N-S elongated basins may
  be related to an early stage of the Scotia Arc formation before or around 50 Ma.
- We suggest that regional extension affected the SOM and Powell Basin simultaneously based on: (1) our inferred ages for the start of the sedimentation on the Eötvös Basin; (2) the ages of dredged alkali basalts from the Antarctic Peninsula margin, conjugated to the western SOM (47.7 and 49 Ma; Barber et al., 1991); and (3) the age of separation of the SOM from Antarctic Peninsula sediment sources (35.5 Ma; López-Quirós et al., 2021).

## 2. Identification of key thresholds in the paleoceanographic, paleoenvironmental, and climatic evolution of the SOM

Chapter 4 analyzes the sedimentary fill of the Eötvös and Bouguer Basins, the widest sedimentary basins of the SOM, where the greater extension has been described in Chapter 3. The correlation of the MCS profiles with the Ocean Drilling Program (ODP) Sites 695 and 696 provides an unprecedented chronostratigraphic framework for the identified seismic units. It allows us to determine the main events and key thresholds in their development. Main conclusions include:

- Five seismic units are identified in the MCS profiles (i.e., SU5 to SU1) separated by four regional discontinuities (D4 to D0/seafloor). Correlation between the MCS seismic data and the ODP Sites 695 and 696 allows us to provide a chronostratigraphic framework to the different units that span from the Eocene-Oligocene Transition (EOT at ~34 Ma) to recent.
- Contour current influence the deposition in the southern margin of the SOM since at least the late Eocene. The first stages of the development are mainly restricted to the shelf break/uppermost slope, with a more significant development during the Oligocene and

possibly the early Miocene. This activity is coherent with the influence of a proto-Weddell flow reaching the southern margin of the SOM. During these first stages, the seismic stratigraphic analysis also depicts an inferred influence of the northern contour current affecting the SOM, possibly related to the influence of a proto-CDW. However, the characterization of the resulting drift could not be addressed due to the poor quality of the MCS profiles in this area.

- A widespread development of contour current-related deposits during the middle Miocene is linked to the deepening of the SOM as a result of the early stages of the surrounding Powell and Jane basins tectonic opening. Both extensional processes placed the southern margin of the SOM progressively at greater depths, likely facilitating the intrusion of deeper water masses in the SOM. Inferred current directions are coherent with a Weddell-sourced current entering the SOM with a clockwise direction in the basins. Resulting contour current deposits are mainly developed where the current interacts with the topography of the basement highs surrounding the basins.
- The SOM experienced a cessation of major current influence in deposition during the middle Miocene (~11.7-9.8 Ma). The timing coincides with the reported onset of major development of contourite drifts in the Scotia Sea (~8-14 Ma). We suggest that the complete opening of new current pathways surrounding the SOM (e.g., the Jane and Scan basins) led to decreased current influence in the SOM as the onset of Weddell Sea Deep Water intrusion into the Scotia Sea occurred.
- Between the late Miocene and the early Pliocene, there was a marked shift in both the character of the seismic units and the sediments recovered from Sites 696 and 695. Contourite deposits are not evident, and instead, there is localized evidence of downslope processes coeval with a change from biogenic to detrital-dominated sedimentation. We interpret this change to result from more proximal sediment sources to where the sites are located associated with glacial expansion across the relatively shallow SOM continental shelf. This is consistent with the reported onset of more persistent glaciations in the region between 5.3—3.6 Ma.
- Our interpretations lead us to determine tectonic subsidence as the main control in sedimentation at the SOM from the early Eocene to the latest Miocene/early Pliocene. From the early Pliocene, the climate has been the main controlling factor in sedimentation at the SOM.

#### 3. Reconstruction of recent paleoceanographic and climatic changes in the Bransfield Basin

Chapter 5 describes the climatic control on the position of oceanic fronts that directly impact sedimentation in the Bransfield Basin. Sedimentological, geochemical, and biostratigraphic analyses of two sediment cores (TG02 and TG03) collected from mounded deposits in the East Bransfield Basin (EBB) allow the drawing of these conclusions:

- Analysis of the two finely laminated sediment cores conclusively validates the significant role
  of bottom contour currents in their deposition over the past millennium, affirming the
  contourite nature of the two mounded deposits within the EBB area from which the cores
  were extracted.
- Both cores record varying current intensity, increasing from interpreted Facies 1 to Facies 3.
   The inferred current intensity variability controls the organic matter preservation, winnowing, and sediment coarsening.
- The highest intensity currents (Facies 3) are only recorded in TG02, pointing to different currents bathing both sites. TG02, located in the deep waters of the EBB, records the influence of the Bransfield Bottom Water (BBW). TG03, situated on the southern slope of the EBB, records the influence of the shallower Bransfield Deep Water (BDW).
- The distinct positioning of these two cores within the EBB area also serves as a record of varied depositional processes: TG02 captures the variability of contour currents, while TG03 documents an intricate interplay between along-slope and downslope processes.
- Physical properties, paleontological, and geochemical proxies evidence significant
  paleoceanographic changes in the EBB during the last millennium. Both cores indicate a
  significant change at 600 cal yr BP towards more open water conditions. In addition, TG02
  records several CDW intrusions into the EBB during the last 600 cal yr BP that are associated
  with negative ENSO phases and higher variability SAM.
- In addition, shifts in the trends of different indicators in each core suggest three main intervals with different forcing by the ENSO and SAM high-latitude climatic patterns: (1) before 600 cal yr BP, characterized by global SAM positive and high ENSO variability; (2) from 600 to 400 ca yr BP characterized by SAM negative and low ENSO variability; and (3) after 400 ca yr BP, when global SAM positive and low ENSO variability conditions.

#### CAPÍTULO 7: Conclusiones

Para alcanzar los tres objetivos principales de esta tesis, presentados en la sección de Contexto y Motivación, se ha llevado adoptado una metodología multidisciplinar que incluye la modelización geofísica, el análisis de estratigrafía sísmica de perfiles de sísmica multicanal y el análisis sedimentario de testigos de gravedad. El trabajo realizado se ha centrado principalmente en dos áreas: el Microcontinente de las Orcadas del Sur (MOS), que representa una pieza clave en el desarrollo del arco de Scotia y la posterior reorganización de la circulación del Océano Austral, y la Cuenca de Bransfield, que actualmente es un área clave para el estudio de la variabilidad climática. Los resultados, presentados en los capítulos 3, 4 y 5 proporcionan nuevas perspectivas importantes sobre la evolución del sur del arco de Scotia, desde los procesos tectónicos en las etapas iniciales de la apertura del Pasaje de Drake, hasta la reorganización paleoceanográfica subsiguiente que llevó a la configuración oceánica actual, y la influencia de los fenómenos de El Niño (ENSO) y el Modo Anular del Sur (SAM) en la variabilidad de la configuración oceánica durante el último milenio.

De este modo, se ha abordado el objetivo general de esta tesis - determinar los principales eventos tectónicos que condujeron al rifting y subsidencia del MOS debido a la apertura de las cuencas circundantes y al establecimiento de la posterior evolución paleoceanográfica y paleoambiental – obteniendo las siguientes conclusiones relacionadas con cada objetivo específico:

## 1. Caracterización de la estructura profunda del MOS mediante la modelización 3D de anomalías gravimétricas y magnéticas, y el análisis de perfiles de sísmica multicanal

En el Capítulo 3, la modelización geológica y geofísica 3D del MOS, ha proporcionado nuevos conocimientos sobre su estructura interna, derivada de las diferentes fases tectónicas en el desarrollo del arco de Scotia. Además, en el capítulo 4, la correlación de los perfiles de sísmica multicanal con los testigos sedimentarios 695 y 696 obtenidos por el Programa de Perforación Oceánica, ha permitido acotar las edades a la que ocurrieron los diferentes eventos tectónicos durante y tras la separación del MOS de la Península Antártica. Entre las principales conclusiones cabe destacar:

- Existen dos dominios estructurales que dividen el MOS en dominios septentrional y meridional, tal y como apuntaban previamente diferentes autores. La diferenciación entre ambos dominios se atribuye a la intrusión de rocas ígneas en el dominio meridional. De esta forma, la presencia de rocas ígneas intrusivas condicionaría la reología de la corteza, facilitando la apertura de las cuencas sedimentarias alargadas en dirección N-S (Pratt, Airy, Bouguer y Eötvös) en la parte meridional del SOM. Por el contrario, el dominio septentrional no muestra signos evidentes de deformación relacionada con la extensión E-O vinculada a las etapas iniciales de la apertura del arco de Scotia.
- En el dominio meridional, se observa una deformación progresiva cada vez mayor de oeste a
  este. Esta deformación es coherente con un esfuerzo extensional al este del MOS, producido
  durante las primeras etapas de la fragmentación del arco de Scotia, que se habría propagado
  posteriormente hacia el oeste. De este modo, los resultados del modelo 3D evidencian que

las cuencas de Bouguer y Eötvös, situadas en la zona más sudoriental del MOS, fueron las más afectadas por la deformación. En consecuencia, ambas cuencas sedimentarias presentan mayor profundidad y extensión. Además, su ubicación coincide con la fragmentación de las rocas ígneas intrusivas y un pronunciado adelgazamiento cortical. Los resultados del modelo también sugieren que la cuenca Powell podría haberse desarrollado en paralelo a estas cuencas alargadas en dirección N-S, al oeste de la cuenca Pratt. Sin embargo, la cuenca Powell habría proseguido su apertura, llegando a su oceanización, quedando abortadas las cuencas Pratt, Airy, Bouguer y Eötvös.

- La modelización 3D de las anomalías gravimétricas ha permitido una caracterización detallada de la geometría de las cuencas sedimentarias internas del MOS. Esto es especialmente relevante en el caso de la cuenca de Newton, ya que su anterior caracterización había estado condicionada por los escasos perfiles de sísmica multicanal que cruzan la cuenca. Además, ha sido posible definir por primera vez la geometría de una cuenca sedimentaria situada en el sector más suroccidental del MOS, denominada provisionalmente en este trabajo como cuenca Pratt. Nuestros resultados demuestran que la modelización geofísica y geológica 3D es una valiosa herramienta para caracterizar cuencas sedimentarias en regiones con escasos datos directos como es la Antártida.
- La correlación de los perfiles de sísmica multicanal con los testigos de sedimento de los pozos 695 y 696 permite determinar la edad del relleno sedimentario de la cuenca de Eötvös, siendo ésta superior a 37 millones de años. A partir de la comparación con las tasas de sedimentación de las cuencas sedimentarias de la isla Seymour, se puede asignar una edad entre 45 y 50 millones de años a los sedimentos situados directamente sobre el basamento de la cuenca Eötvös. En este marco temporal, el desarrollo inicial de las cuencas alargadas en dirección N-S se puede relacionar con etapas tempranas de la formación del arco de Scotia.
- La extensión regional en dirección E-W, habría afectado simultáneamente al MOS y a la cuenca Powell. Esto se concluye en base a: (1) las edades inferidas para el inicio de la sedimentación en la cuenca Eötvös; (2) las edades de los basaltos alcalinos dragados del margen occidental conjugado de la Península Antártica (47,7 y 49 Ma; Barber et al., 1991); y (3) la edad de separación del MOS de las fuentes sedimentarias de la Península Antártica (35,5 Ma; López-Quirós et al., 2021).

## 2. Identificación de umbrales clave en la evolución paleoceanográfica, paleoambiental y climática del MOS

En el Capítulo 4 se realiza un análisis de estratigrafía sísmica en el relleno sedimentario de las cuencas de Eötvös y Bouguer. La correlación de los perfiles de sísmica multicanal con los testigos de sedimento de los pozos 695 y 696 proporciona un marco cronoestratigráfico para las unidades sísmicas identificadas, permitiendo determinar los principales umbrales y eventos tectónicos y climáticos que acontecieron en la zona. Se destacan las siguientes conclusiones:

- Se han identificado cinco unidades sísmicas en los perfiles de sísmica multicanal (SU5 a SU1, de muro a techo) separadas por cuatro discontinuidades regionales (D4 a D0). Las diferentes unidades, en el tramo correlacionable con los testigos de sedimento de los pozos 695 y 696, abarcan desde la Transición Eoceno-Oligoceno (EOT; ~34 millones de años) hasta la actualidad.
- El margen sur del MOS ha estado afectado por la influencia de corrientes de contorno desde, al menos, el Eoceno tardío. En sus primeras etapas de desarrollo, los cuerpos contorníticos se encuentran restringidos principalmente al límite sur de la plataforma continental, con un mayor desarrollo durante el Oligoceno y el Mioceno temprano, probablemente producidos por la influencia de una proto-corriente proveniente del mar de Weddell. Durante estas primeras etapas, el análisis de estratigrafía sísmica también muestra evidencias de depósitos contorníticos en la zona norte de la cuenca de Bouguer. Estos depósitos podrían estar asociados a la influencia de una proto-corriente de contorno ligada a la CDW. Sin embargo, la caracterización detallada de estos cuerpos no ha sido posible debido a la escasa calidad de los perfiles de sísmica multicanal en esta zona.
- El desarrollo más generalizado de depósitos contorníticos en las cuencas de Bouguer y Eötvös se produce durante el Mioceno medio y puede estar vinculado con la profundización del MOS tras la apertura las cuencas de Powell y Jane. La apertura de ambas cuencas habría situado el margen meridional del MOS progresivamente a mayor profundidad, facilitando la intrusión de masas de agua cada vez más profundas en las cuencas estudiadas. Los resultados apuntan a la influencia de una corriente en el sentido de las agujas del reloj procedente del mar de Weddell que, al interactuar con la topografía, da lugar a depósitos contorníticos localizados principalmente en los altos estructurales que rodean las cuencas.
- En el Mioceno tardío (11.7-9.8 millones de años) se observa el cese de la influencia de las corrientes de contorno en la sedimentación de las cuencas de Bouguer y Eötvös. El análisis de la estratigrafía sísmica y su correlación con las edades de los pozos 695 y 696 sugiere que este cese estaría producido por la apertura de nuevas vías alrededor del MOS, como la completa apertura de las cuencas de Jane y Scan, que desviarían las corrientes procedentes del mar de Weddell hacia el mar de Scotia. Además, este evento coincide con el inicio del desarrollo generalizado de depósitos contorníticos en zona sur del mar de Scotia (~8-14 millones de años).
- Entre el Mioceno tardío y Plioceno temprano se produce un marcado cambio tanto en las facies sísmicas en los perfiles de sísmica multicanal estudiados como en los sedimentos recuperados de los pozos 695 y 696. Estos cambios serían resultado de la expansión glaciar en la plataforma continental del MOS. De este modo, las cuencas de Bouguer y Eötvös quedarían en una posición más proximal a la fuente sedimentaria. Esto concuerda con el inicio descrito de glaciaciones más persistentes en la región entre 5,3 y 3,6 millones de años.

• Los resultados del Capítulo 4 sugieren que la subsidencia tectónica fue el principal factor de control sedimentario en el MOS entre el Eoceno temprano y el Mioceno tardío/Plioceno temprano. A partir de ese punto, el clima pasa a ser el principal factor de control en la sedimentación de las cuencas de Bouguer y Eötvös.

### 3. Reconstrucción de los cambios paleoceanográficos y climáticos recientes en la cuenca de Bransfield

El Capítulo 5 describe el control de la variabilidad de la posición de los frentes oceánicos en la sedimentación de la cuenca Este de Bransfield (EBB). Los resultados obtenidos a partir de los análisis sedimentológicos y geoquímicos realizados en dos testigos de gravedad (TG02 y TG03) recogidos en depósitos contorníticos de la EBB permiten extraer las siguientes conclusiones:

- Los resultados obtenidos de los análisis realizados a los dos testigos de sedimento confirman una influencia significativa de las corrientes de contorno durante la deposición el último milenio.
- Ambos testigos (TG02 y TG03) registran una variabilidad en la intensidad de corriente. Esta
  intensidad es mínima durante el depósito de las Facies 1 y máxima durante el depósito de las
  Facies 3. La intensidad de la corriente controla la preservación de la materia orgánica, el
  aventamiento y la ordenación de las partículas del sedimento.
- El desarrollo de las Facies 3, relacionadas con una mayor intensidad de la corriente, sólo se registra en el TG02. Las diferencias observadas entre ambos testigos parecen estar relacionadas con las diferencias entre las corrientes de contorno que bañan ambos emplazamientos. El TG02, situado en el fondo de la EBB, registra principalmente la influencia de una masa de agua profunda. Sin embargo, el TG03, situado en el flanco sur de la EBB, registra tanto la influencia de una masa de agua menos profunda, como su interacción con otros procesos deposicionales, probablemente la influencia de trasporte turbidítico.
- Las propiedades físicas y los indicadores geoquímicos y paleontológicos evidencian importantes cambios paleoceanográficos en la EBB durante el último milenio. Ambos testigos muestran un cambio importante en la sedimentación hacia condiciones de aguas más abiertas en torno a 600 cal yr BP. Además, a partir de este momento, en el TG02 se registran varias intrusiones de la CDW en la EBB, que podrían estar asociadas a fases negativas de El Niño y a una mayor variabilidad de la SAM.
- Los cambios en las tendencias de los diferentes indicadores en ambos testigos de sedimento sugieren tres etapas diferenciadas: (1) antes de 600 cal yr BP, caracterizada por condiciones de SAM positiva y una alta variabilidad de El Niño; (2) de 600 a 400 cal yr BP caracterizada por condiciones de SAM negativa y una baja variabilidad de El Niño; y (3) después de 400 cal yr BP, cuando se dan condiciones de SAM positiva y baja variabilidad de El Niño.



## REFERENCES

- **Abram, N. J.**, Mulvaney, R., Vimeux, F., Phipps, S. J., Turner, J., & England, M. H. (2014). Evolution of the Southern Annular Mode during the past millennium. *Nature Climate Change*, 4(7), 564–569. https://doi.org/10.1038/nclimate2235
- Allen, C. S., Oakes-Fretwell, L., Anderson, J. B., & Hodgson, D. A. (2010). A record of Holocene glacial and oceanographic variability in Neny Fjord, Antarctic Peninsula. *Holocene*, 20(4), 551–564. https://doi.org/10.1177/0959683609356581
- Allen, C. S., & Weich, Z. C. (2022). Variety and distribution of diatom-based sea ice proxies in Antarctic marine sediments of the past 2000 years. *Geosciences*, 12(8), 282. https://doi.org/10.3390/geosciences12080282
- Alley, R. B., Anandakrishnan, S., Christianson, K., Horgan, H. J., Muto, A., Parizek, B. R., ... & Walker, R. T. (2015). Oceanic forcing of ice-sheet retreat: West Antarctica and more. *Annual Review of Earth and Planetary Sciences*, 43, 207-231.
- Alley, K., Patacca, K., Pike, J., Dunbar, R., & Leventer, A. (2018). Iceberg Alley, East Antarctic Margin: Continuously laminated diatomaceous sediments from the late Holocene. *Marine Micropaleontology*, 140, 56–68. https://doi.org/10.1016/j.marmicro.2017.12.002
- **Alvey, A.**, Gaina, C., Kusznir, N. J., & Torsvik, T. H. (2008). Integrated crustal thickness mapping and plate reconstructions for the high Arctic. *Earth and Planetary Science Letters*, *274*(3–4), 310–321. https://doi.org/10.1016/j.epsl.2008.07.036
- Amenábar, C. R., Montes, M., Nozal, F., & Santillana, S. (2020). Dinoflagellate cysts of the la Meseta Formation (middle to late Eocene), Antarctic Peninsula: Implications for biostratigraphy, palaeoceanography and palaeoenvironment. *Geological Magazine*, 157(3), 351–366. https://doi.org/10.1017/S0016756819000591
- Anderson, J. B., Warny, S., Askin, R. A., Wellner, J. S., Bohaty, S. M., Kirshner, A. E., Livsey, D. N., Simms, A. R., Smith, T. R., Ehrmann, W., Lawver, L. A., Barbeau, D., Wise, S. W., Kulhenek, D. K., Weaver, F. M., & Majewski, W. (2011a). Progressive Cenozoic cooling and the demise of Antarctica's last refugium. Proceedings of the National Academy of Sciences of the United States of America, 108(28), 11356–11360. https://doi.org/10.1073/pnas.1014885108
- **Armand, L. K.**, Crosta, X., Romero, O., & Pichon, J. J. (2005). The biogeography of major diatom taxa in Southern Ocean sediments: 1. Sea ice related species. *Palaeogeography, Palaeoclimatology, Palaeoecology*, 223 (1–2), 93–126. https://doi.org/10.1016/j.palaeo.2005.02.015
- Arndt, J. E., Schenke, H. W., Jakobsson, M., Nitsche, F. O., Buys, G., Goleby, B., ... & Wigley, R. (2013). The International Bathymetric Chart of the Southern Ocean (IBCSO) Version 1.0—A new bathymetric compilation covering circum-Antarctic waters. *Geophysical Research Letters*, 40 (12), 3111-3117.

- Bahr, A., Jiménez-Espejo, F. J., Kolasinac, N., Grunert, P., Hernández-Molina, F. J., Röhl, U., Voelker, A. H. L., Escutia, C., Stow, D. A. V., Hodell, D., & Alvarez-Zarikian, C. A. (2014). Deciphering bottom current velocity and paleoclimate signals from contourite deposits in the Gulf of Cádiz during the last 140 kyr: An inorganic geochemical approach. *Geochemistry, Geophysics, Geosystems*, 15(8), 3145–3160. https://doi.org/10.1002/2014GC005356
- **Bankole, S.**, Buckman, J., & Stow, D. (2020). Unusual components within a fine-grained contourite deposit: Significance for interpretation of provenance and the contourite budget. *Minerals*, 10 (6). https://doi.org/10.3390/min10060488
- **Barber, P. L.**, Barker, P. F., & Pankhurst, R. J. (1991). Dredged rocks from Powell basin and the South Orkney microcontinent. In *International symposium on Antarctic earth sciences. 5*, pp. 361-367.
- **Barcena, M. Á.**, Fabrés, J., Isla, E., Flores, J. A., Sierro, F. J., Canals, M., & Palanques, A. (2006). Holocene neoglacial events in the Bransfield Strait (Antarctica). Palaeocenographic and palaeoclimatic significance. *Scientia Marina*, 70(4), 607–619. https://doi.org/10.3989/scimar.2006.70n4607
- **Barcena, M. Á.**, Gersonde, R., Ledesma, S., Fabrés, J., Calafat, A., Canals, M., Sierro, F. J., & Flores. (1998). Record of Holocene glacial oscillations in Bransfield Basin as revealed by siliceous microfossil assemblages. *Antarctic Science*, 10(3), 269–285.
- **Barlett, E. M. R.**, Tosonotto, G. V., Piola, A. R., Sierra, M. E., & Mata, M. M. (2018). On the temporal variability of intermediate and deep waters in the Western Basin of the Bransfield Strait. *Deep Sea Research Part II: Topical Studies in Oceanography*, 149, 31-46. https://doi.org/10.1016/j.dsr2.2017.12.010
- **Barker, P. F.**, & Griffiths, D. H. (1972). A Discussion on volcanism and the structure of the Earth-The evolution of the Scotia Ridge and Scotia Sea. Philosophical Transactions of the Royal Society of London. *Series A, Mathematical and Physical Sciences*, 271(1213), 151-183. https://doi.org/10.1098/rsta.1972.0005
- **Barker, P. F.**, & Burrell, J. (1977). The opening of Drake passage. *Marine geology*, 25(1-3), 15-34. https://doi.org/10.1016/0025-3227(77)90045-7
- **Barker, P. F.,** & Dalziel, I. W. (1983). Progress in geodynamics in the Scotia Arc region. *Geodynamics of the eastern Pacific region, Caribbean and Scotia Arcs*, 9, 137-170. https://doi.org/10.1029/gd009p0137
- **Barker, P. F.**, & Camerlenghi, A. (1999). An approach to Antarctic glacial history: the aims of Leg 178. *Barker, PF, Camerlenghi, A., Acton, GD, et al., 1999. Proc. ODP, Init. Repts, 178*, 1-44.
- Barker, P. F., Kennett, J.P., & Participating Scientist (1988). Procedings of the Ocean Drilling Program. Initial Reports, 113. *Ocean Drilling Program*, College Station, Texas. https://doi:10.2973/odp.proc.ir.113.1988

- **Barker, P. F.**, & Kennett, J. P. (1990). Climatic and oceanographic developments in the Weddell Sea, Antarctica, since the latest Cretaceous: an ocean-drilling perspective. *Proceedings, Ocean Drilling Program, scientific results 113*, 113, 937–962.
- **Barker, P. F.**, Dalziel, I. W. D., & Storey, B. C. (1991). Tectonic development of the Scotia arc region. *The Geology of Antarctica*, 215–248.
- **Bart, P. J.** (2001). Did the Antarctic ice sheets expand during the early Pliocene? *Geology*, 29(1), 67-70.
- **Bart, P. J.**, & Anderson, J. B. (2000). Relative temporal stability of the Antarctic ice sheets during the late Neogene based on the minimum frequency of outer shelf grounding events. *Earth and Planetary Science Letters*, 182(3-4), 259-272.
- **Bart, P. J.**, Egan, D., & Warny, S. A. (2005). Direct constraints on Antarctic Peninsula Ice Sheet grounding events between 5.12 and 7.94 Ma. *Journal of Geophysical Research: Earth Surface*, 110(4), 1–13. https://doi.org/10.1029/2004JF000254
- **Bentley, M. J.**, Hodgson, D. A., Smith, J. A., Cofaigh, C. Ó., Domack, E. W., Larter, R. D., Roberts, S. J., Brachfeld, S., Leventer, A., Hjort, C., Hillenbrand, C. D., & Evans, J. (2009). Mechanisms of Holocene palaeoenvironmental change in the Antarctic Peninsula region. *Holocene*, 19(1), 51–69. https://doi.org/10.1177/0959683608096603
- **Bijl, P. K.**, Sluijs, A., & Brinkhuis, H. (2013). A magneto- and chemostratigraphically calibrated dinoflagellate cyst zonation of the early Palaeogene South Pacific Ocean. *Earth-Science Reviews*, 124, 1–31. https://doi.org/10.1016/j.earscirev.2013.04.010
- Blaauw, M., & Christen, J. A. (2013). Bacon Manual v2. 3.3. Queens University: Belfast, UK.
- **Blott, S. J.**, & Pye, K. (2001). Gradistat: A grain size distribution and statistics package for the analysis of unconsolidated sediments. Earth Surface Processes and Landforms, 26(11), 1237–1248. https://doi.org/10.1002/esp.261
- **Blum, P.** (1997). Moisture and Density (by Mass and Volume), in Physical Properties Handbook: A Guide to the Shipboard Measurement of Physical Properties of Deep-Sea Cores. *ODP Technical Notes*, 26, 2-1-2-15.
- **Bohoyo, F.** (2004). Fragmentación continental y desarrollo de cuencas oceánicas en el sector meridional del Arco de Scotia, Antártica. Doctoral Thesis, University of Granada
- **Bohoyo, F.**, Galindo-Zaldívar, J., Maldonado, A., Schreider, A. A., & Suriñach, E. (2002). Basin development subsequent to ridge-trench collision: The Jane Basin, Antarctica. *Marine Geophysical Research*, 413–421. https://doi.org/10.1023/B:MARI.0000018194.18098.0d

- **Bohoyo, F.**, Galindo-Zaldívar, J., Jabaloy, A., Maldonado, A., Rodríguez-Fernández, J., Schreider, A., & Suriñach, E. (2007). Extensional deformation and development of deep basins associated with the sinistral transcurrent fault zone of the Scotia-Antarctic plate boundary. *Geological Society Special Publication*, 290, 203–217. https://doi.org/10.1144/SP290.6
- **Bohoyo, F.**, Larter, R. D., Galindo-Zaldívar, J., Leat, P. T., Maldonado, A., Tate, A. J., Flexas, M. M., Gowland, E. J. M., Arndt, J. E., Dorschel, B., Kim, Y. D., Hong, J. K., López-Martínez, J., Maestro, A., Bermúdez, O., Nitsche, F. O., Livermore, R. A., & Riley, T. R. (2019). Morphological and geological features of Drake Passage, Antarctica, from a new digital bathymetric model. *Journal of Maps*, 15(2), 49–59. https://doi.org/10.1080/17445647.2018.1543618
- **Bonotto, D. M.**, & Garcia-Tenorio, R. (2014). A comparative evaluation of the CF: CS and CRS models in 210Pb chronological studies applied to hydrographic basins in Brazil. *Applied Radiation and Isotopes*, *92*, 58-72.
- **Busetti, M.**, Zanolla, M., & Marchetti, A. (2000). Geological structure of the South Orkney microcontinent. *Terra Antartica*, *8*(2), 1-8.
- **Calcagno, P.**, Chilès, J. P., Courrioux, G., & Guillen, A. (2008). Geological modelling from field data and geological knowledge. Part I. Modelling method coupling 3D potential-field interpolation and geological rules. *Physics of the Earth and Planetary Interiors*, 171(1–4), 147–157. https://doi.org/10.1016/j.pepi.2008.06.013
- Camerlenghi, A., Domack, E., Rebesco, M., Gilbert, R., Ishman, S., Leventer, A., Brachfeld, S., & Drake, A. (2001). Glacial morphology and post-glacial contourites in northern Prince Gustav Channel (NW Weddell Sea, Antarctica). *Marine Geophysical Research*, 22(5–6), 417–443. https://doi.org/10.1023/A:1016399616365
- Carter, L., McCave, I. N., & Williams, M. J. M. (2008). Chapter 4 Circulation and Water Masses of the Southern Ocean: A Review. *Developments in Earth and Environmental Sciences*, 8(08), 85–114. https://doi.org/10.1016/S1571-9197(08)00004-9
- Casas, D., Ercilla, G., Estrada, F., Alonso, B., Baraza, J., Lee, H., Kayen, R., & Chiocci, F. (2004). Physical and geotechnical properties and assessment of sediment stability on the continental slope and basin of the Bransfield Basin (Antarctica Peninsula). *Marine Georesources and Geotechnology*, 22(4), 253–278. https://doi.org/10.1080/10641190490900853
- Casas, D., García, M., Bohoyo, F., Maldonado, A., & Ercilla, G. (2018). The Gebra–Magia Complex: mass-transport processes reworking trough-mouth fans in the Central Bransfield Basin (Antarctica). *Geological Society, London, Special Publications*, 461(1), 61–75. https://doi.org/10.1144/SP461.10
- Catalán, M., Martos, Y. M., Galindo-Zaldivar, J., Perez, L. F., & Bohoyo, F. (2020). Unveiling Powell Basin's Tectonic Domains and Understanding Its Abnormal Magnetic Anomaly Signature. Is Heat the Key? *Frontiers in Earth Science*, 8. https://doi.org/10.3389/feart.2020.580675

- **Chen, L.** (2014). Stretching factor estimation for the long-duration and multi-stage continental extensional tectonics: Application to the Baiyun Sag in the northern margin of the South China Sea. *Tectonophysics*, *611*, 167–180. https://doi.org/10.1016/j.tecto.2013.11.026
- **Chow, J. M.**, & Bart, P. J. (2003). West Antarctic Ice Sheet grounding events on the Ross Sea outer continental shelf during the middle Miocene. *Palaeogeography, Palaeoclimatology, Palaeoecolog,* 198 (1–2), 169–186. https://doi.org/10.1016/S0031-0182(03)00400-0
- **Civile, D.**, Lodolo, E., Vuan, A., & Loreto, M. F. (2012). Tectonics of the Scotia-Antarctica plate boundary constrained from seismic and seismological data. *Tectonophysics*, 550–553, 17–34. https://doi.org/10.1016/j.tecto.2012.05.002
- **Clowes, C. D.** (1985). Stoveracysta, a new gonyaulacacean dinoflagellate genus from the upper Eocene and lower Oligocene of New Zealand. *Palynology*, 9(1), 27–35. https://doi.org/10.1080/01916122.1985.9989286
- **Colleoni, F.**, De Santis, L., Siddoway, C. S., Bergamasco, A., Golledge, N. R., Lohmann, G., Passchier, S., & Siegert, M. J. (2018). Spatio-temporal variability of processes across Antarctic ice-bed-ocean interfaces. *Nature Communications*, *9*(1), 1–14. https://doi.org/10.1038/s41467-018-04583-0
- Cook, C. P., Van De Flierdt, T., Williams, T., Hemming, S. R., Iwai, M., Kobayashi, M., Jimenez-Espejo, F. J., Escutia, C., González, J. J., Khim, B. K., McKay, R. M., Passchier, S., Bohaty, S. M., Riesselman, C. R., Tauxe, L., Sugisaki, S., Galindo, A. L., Patterson, M. O., Sangiorgi, F., ... Yamane, M. (2013). Dynamic behaviour of the East Antarctic ice sheet during Pliocene warmth. *Nature Geoscience*, 6(9), 765–769. https://doi.org/10.1038/ngeo1889
- **Coxall, H. K.**, Wilson, P. A., Pälike, H., Lear, C. H., & Backman, J. (2005). Rapid stepwise onset of Antarctic glaciation and deeper calcite compensation in the Pacific Ocean. *Nature*, *433*(7021), 53–57.
- Crosta, X., Romero, O., Armand, L. K., & Pichon, J. J. (2005). The biogeography of major diatom taxa in Southern Ocean sediments: 2. Open ocean related species. *Palaeogeography, Palaeoclimatology, Palaeoecology,* 223(1–2), 66–92. https://doi.org/10.1016/j.palaeo.2005.03.028
- **Dalziel, I. W.** (1984). *Tectonic evolution of a forearc terrane, southern Scotia Ridge, Antarctica* (200). Geological Society of America. https://doi.org/10.1029/eo067i007p00080
- Dalziel, I. W., Lawver, L. A., Pearce, J. A., Barker, P. F., Hastie, A. R., Barfod, D. N., Schenke, H. W., & Davis, M. B. (2013). A potential barrier to deep antarctic circumpolar flow until the late miocene? *Geology*, 41(9), 947–950. https://doi.org/10.1130/G34352.1
- **Damini, B. Y.**, Kerr, R., Dotto, T. S., & Mata, M. M. (2022). Long-term changes on the Bransfield Strait deep water masses: Variability, drivers and connections with the northwestern Weddell Sea. *Deep-Sea Research Part I: Oceanographic Research Papers*, 179(April 2021), 103667. https://doi.org/10.1016/j.dsr.2021.103667

- **Davies, B. J.**, Hambrey, M. J., Smellie, J. L., Carrivick, J. L., & Glasser, N. F. (2012). Antarctic Peninsula Ice Sheet evolution during the Cenozoic Era. *Quaternary Science Reviews*, *31*, 30–66. https://doi.org/10.1016/j.quascirev.2011.10.012
- **DeConto, R.** & Pollard, D. (2003). A coupled climate--ice sheet modeling approach to the early Cenozoic history of the Antarctic ice sheet. *Palaeogeography, Palaeoclimatology, Palaeoecology,* 198(1–2), 39–52.
- **DeConto, R.**, Pollard, D., & Harwood, D. (2007). Sea ice feedback and Cenozoic evolution of Antarctic climate and ice sheets. *Paleoceanography*, *22*(3).
- Denis, D., Crosta, X., Schmidt, S., Carson, D. S., Ganeshram, R. S., Renssen, H., Bout-Roumazeilles, V., Zaragosi, S., Martin, B., Cremer, M., & Giraudeau, J. (2009). Holocene glacier and deep water dynamics, Adélie Land region, East Antarctica. *Quaternary Science Reviews*, 28 (13–14), 1291–1303. https://doi.org/10.1016/j.quascirev.2008.12.024
- **Dentith, M.** & Mudge, S. T. (2014). *Geophysics for the mineral exploration geoscientist*. Cambridge University Press. https://doi.org/10.1017/cbo9781139024358
- **Dickens, W. A.**, Graham, A. G. C., Smith, J. A., Dowdeswell, J. A., Larter, R. D., Hillenbrand, C. D., Trathan, P. N., Erik Arndt, J., & Kuhn, G. (2014). A new bathymetric compilation for the South Orkney Islands region, Antarctic Peninsula (49°-39°W to 64°-59°S): Insights into the glacial development of the continental shelf. *Geochemistry, Geophysics, Geosystems*, 15(6), 2494–2514. https://doi.org/10.1002/2014GC005323
- **Diester-Haass, L.** & Zahn, R. (1996). Eocene-Oligocene transition in the Southern Ocean: History of water mass circulation and biological productivity. *Geology*, 24(2), 163–166. https://doi.org/10.1130/0091-7613(1996)024<0163:EOTITS>2.3.CO;2
- **Dinniman, M. S.**, Klinck, J. M., & Hofmann, E. E. (2012). Sensitivity of circumpolar deep water transport and ice shelf basal melt along the west antarctic peninsula to changes in the winds. *Journal of Climate*, 25(14), 4799–4816. https://doi.org/10.1175/JCLI-D-11-00307.1
- **Divine, D. V.**, Koç, N., Isaksson, E., Nielsen, S., Crosta, X., & Godtliebsen, F. (2010). Holocene Antarctic climate variability from ice and marine sediment cores: Insights on ocean-atmosphere interaction. *Quaternary Science Reviews*. 29 (1–2), 303–312. https://doi.org/10.1016/j.quascirev.2009.11.012
- **Doo, W. B.**, Hsu, S. K., Tsai, C. H., & Huang, Y. S. (2009). Using analytic signal to determine magnetization/density ratios of geological structures. *Geophysical Journal International*, *179*(1), 112-124. https://doi.org/10.1111/j.1365-246X.2009.04297.x
- **Dotto, T. S.**, Kerr, R., Mata, M. M., & Garcia, C. A. E. (2016). Multidecadal freshening and lightening in the deep waters of the Bransfield Strait, Antarctica. *Journal of Geophysical Research: Oceans*, 121(5), 3741–3756. https://doi.org/10.1002/2015JC011228

- **Duliu, O. G.** (1999). Computer axial tomography in geosciences: an overview. *Earth-Science Reviews*, 48(4), 265–281. https://doi.org/https://doi.org/10.1016/S0012-8252(99)00056-2
- **Eagles, G.** & Jokat, W. (2014). Tectonic reconstructions for paleobathymetry in Drake Passage. *Tectonophysics*, 611, 28–50. https://doi.org/10.1016/j.tecto.2013.11.021
- **Eagles, G.** & Livermore, R. A. (2002). Opening history of Powell Basin, Antarctic Peninsula. *Marine Geology*, 185(3–4), 195–205. https://doi.org/10.1016/S0025-3227(02)00191-3
- Eagles, G., Livermore, R. A., Fairhead, J. D., & Morris, P. (2005). Tectonic evolution of the west Scotia Sea. *Journal of Geophysical Research: Solid Earth*, 110(2), 1–19. https://doi.org/10.1029/2004JB003154
- **Eagles, G.** & Eisermann, H. (2020). The Skytrain plate and tectonic evolution of southwest Gondwana since Jurassic times. *Scientific Reports*, *10*(1), 1–17. https://doi.org/10.1038/s41598-020-77070-6
- **Ercilla, G.**, Baraza, J., Alonso, B., & Canals, M. (1998). Recent geological processes in the Central Bransfield Basin (Western Antarctic Peninsula). *Geological Society Special Publication*, 129, 205–216. https://doi.org/10.1144/GSL.SP.1998.129.01.13
- Escutia, C., Bárcena, M. A., Lucchi, R. G., Romero, O., Ballegeer, A. M., Gonzalez, J. J., & Harwood, D. M. (2009). Circum-Antarctic warming events between 4 and 3.5 Ma recorded in marine sediments from the Prydz Bay (ODP Leg 188) and the Antarctic Peninsula (ODP Leg 178) margins. *Global and Planetary Change*, 69(3), 170-184. https://doi.org/10.1016/j.gloplacha.2009.09.003
- **Escutia, C.** & Brinkhuis, H. (2014). From greenhouse to icehouse at the Wilkes Land Antarctic margin: IODP Expedition 318 synthesis of results. In *Developments in marine geology* (Vol. 7, pp. 295-328). Elsevier. https://doi.org/https://doi.org/10.1016/B978-0-444-62617-2.00012-8
- **Escutia, C.**, Brinkhuis, H., & Klaus, A. (2011). IODP Expedition 318: From greenhouse to icehouse at the Wilkes Land Antarctic margin. *Scientific Drilling*, *12*, 15-23.
- Esper, O., Gersonde, R., & Kadagies, N. (2010). Diatom distribution in southeastern Pacific surface sediments and their relationship to modern environmental variables. *Palaeogeography, Palaeoclimatology, Palaeoecology, 287*(1-4), 1-27. https://doi.org/10.1016/j.palaeo.2009.12.006
- Evangelinos, D., Escutia, C., Etourneau, J., Hoem, F., Bijl, P., Boterblom, W., van de Flierdt, T., Valero, L., Flores, J. A., Rodriguez-Tovar, F. J., Jimenez-Espejo, F. J., Salabarnada, A., & López-Quirós, A. (2020). Late Oligocene-Miocene proto-Antarctic Circumpolar Current dynamics off the Wilkes Land margin, East Antarctica. *Global and Planetary Change*, 191(May), 103221. https://doi.org/10.1016/j.gloplacha.2020.103221

- Evangelinos, D., Escutia, C., van de Flierdt, T., Valero, L., Flores, J. A., Harwood, D. M., Hoem, F. S., Bijl, P., Etourneau, J., Kreissig, K., Nilsson-Kerr, K., Holder, L., López-Quirós, A., & Salabarnada, A. (2022). Absence of a strong, deep-reaching Antarctic Circumpolar Current zonal flow across the Tasmanian gateway during the Oligocene to early Miocene. *Global and Planetary Change*, 208. https://doi.org/10.1016/j.gloplacha.2021.103718
- Evangelinos, D., Etourneau, J., van de Flierdt, T., Crosta, X., Jeandel, C., Flores, J. A., Harwood, D. M., Valero, L., Ducassou, E., Sauermilch, I., Klocker, A., Cacho, I., Pena, L. D., Kreissig, K., Benoit, M., Belhadj, M., Paredes, E., Garcia-Solsona, E., López-Quirós, A., ... Escutia, C. (2024). Late Miocene onset of the modern Antarctic Circumpolar Current. *Nature Geoscience*, *17* (February). https://doi.org/10.1038/s41561-023-01356-3
- **Faugères, J. C.**, Stow, D., Imbert, P., & Viana, A. (1999). Seismic features diagnostic of contourite drifts. *Marine Geology*, 162(1), 1–38. https://doi.org/10.1016/S0025-3227(99)00068-7
- Ferris, J. K., Vaughan, A. P. M., & Storey, B. C. (2000). Relics of a complex triple junction in the Weddell Sea embayment, Antarctica. In *Earth and Planetary Science Letters* (Vol. 178, Issues 3–4, pp. 215–230). https://doi.org/10.1016/S0012-821X(00)00076-5
- **Flower, B. P.** & Kennett, J. P. (1994). The middle Miocene climatic transition: East Antarctic ice sheet development, deep ocean circulation and global carbon cycling. *Palaeogeography, Palaeoclimatology, Palaeoecology*, 108(3–4), 537–555.
- **Foldvik, A.**, Gammelsrød, T., Østerhus, S., Fahrbach, E., Rohardt, G., Schröder, M., Nicholls, K. W., Padman, L., & Woodgate, R. A. (2004). Ice shelf water overflow and bottom water formation in the southern Weddell Sea. *Journal of Geophysical Research: Oceans*, 109(C2).
- **Foster, T. D.** & Carmack, E. C. (1976). Frontal zone mixing and Antarctic Bottom Water formation in the southern Weddell Sea. *Deep Sea Research and Oceanographic Abstracts*, 23(4), 301–317.
- **Francis, J. E.**, Marenssi, S., Levy, R., Hambrey, M., Thorn, V. C., Mohr, B., Brinkhuis, H., Warnaar, J., Zachos, J., Bohaty, S., & others. (2008). From greenhouse to icehouse-the Eocene/Oligocene in Antarctica. *Developments in Earth and Environmental Sciences*, *8*, 309–368.
- **Freeman, N. M.**, Lovenduski, N. S., & Gent, P. R. (2016). Temporal variability in the Antarctic polar front (2002--2014). *Journal of Geophysical Research: Oceans, 121*(10), 7263–7276.
- Fretwell, P., Pritchard, H. D., Vaughan, D. G., Bamber, J. L., Barrand, N. E., Bell, R., Bianchi, C., Bingham, R. G., Blankenship, D. D., Casassa, G., Catania, G., Callens, D., Conway, H., Cook, A. J., Corr, H. F. J., Damaske, D., Damm, V., Ferraccioli, F., Forsberg, R., ... Zirizzotti, A. (2013). Bedmap2: improved ice bed, surface and thickness datasets for Antarctica. *The Cryosphere*, 7(1), 375–393. https://doi.org/10.5194/tc-7-375-2013
- **Folk, R. L.** & Ward, W. C. (1957). Brazos River bar [Texas]; a study in the significance of grain size parameters. *Journal of Sedimentary Research*, 27(1), 3–26. https://doi.org/10.1306/74D70646-2B21-11D7-8648000102C1865D

- **Fouinat, L.**, Sabatier, P., Poulenard, J., Reyss, J.-L., Montet, X., & Arnaud, F. (2017). A new CT scan methodology to characterize a small aggregation gravel clast contained in a soft sediment matrix. *Earth Surface Dynamics*, 5(1), 199–209. https://doi.org/10.5194/esurf-5-199-2017
- **Galindo-Zaldívar, J.**, Gamboa, L., Maldonado, A., Nakao, S., & Bochu, Y. (2004). Tectonic development of the Bransfield Basin and its prolongation to the South Scotia Ridge, northern Antarctic Peninsula. *Marine Geology*, 206(1–4), 267–282. https://doi.org/10.1016/j.margeo.2004.02.007
- **Galindo-Zaldívar, J.**, Bohoyo, F., Maldonado, A., Schreider, A., Suriñach, E., & Vázquez, J. T. (2006). Propagating rift during the opening of a small oceanic basin: The Protector Basin (Scotia Arc, Antarctica). *Earth and Planetary Science Letters*, *241*(3–4), 398–412. https://doi.org/10.1016/j.epsl.2005.11.056
- **Galindo-Zaldívar, J.**, Maestro, A., López-Martínez, J., & de Galdeano, C. S. (2006). Elephant Island recent tectonics in the framework of the Scotia-Antarctic-South Shetland Block triple junction (NE Antarctic Peninsula). *Antarctica: contributions to global earth sciences*, 271-276.
- García, M., Hernández-Molina, F. J., Llave, E., Pérez, L., Escutia, C., Bohoyo, F., Salabarnada, A., López-Quirós, A., & Lobo, F. J. (2019). Contourite features distribution and water masses circulation in the Eastern Bransfield Basin (Antarctic Peninsula). http://hdl.handle.net/10261/207515
- **García, M.**, Ercilla, G., & Alonso, B. (2009). Morphology and sedimentary systems in the Central Bransfield Basin, Antarctic Peninsula: Sedimentary dynamics from shelf to basin. *Basin Research*, 21(3), 295–314. https://doi.org/10.1111/j.1365-2117.2008.00386.x
- **Garrett, S. W.**, Renner, R. G. B., Jones, J. A., & McGibbon, K. J. (1986/87). Continental magnetic anomalies and the evolution of the Scotia arc. *Earth and Planetary Science Letters* (Vol. 81, Issues 2–3, pp. 273–281). https://doi.org/10.1016/0012-821X(87)90163-4
- **Garrett, S. W.**, & Storey, B. C. (1987). Lithospheric extension on the Antarctic Peninsula during Cenozoic subduction. *Geological Society Special Publication*, 28, 419–431. https://doi.org/10.1144/GSL.SP.1987.028.01.26
- **Garrett, S. W.** (1990). Interpretation of reconnaissance gravity and aeromagnetic surveys of the Antarctic Peninsula. *Journal of Geophysical Research*, 95(B5), 6759–6777. https://doi.org/10.1029/JB095iB05p06759
- **GEBCO Compilation Group (2020),** GEBCO 2020 Gridded Bathymetry Data Dataset. https://doi:10.5285/a29c5465-b138-234d-e053-6c86abc040b9
- **Gemperle, M.**, Conrad, G., Sargen, M. y. Starr, S. (1991): Geosoft GM-SYS v. 1.8. [Software] *Northwest Geoph. Ass.* Inc. 65 pags
- **Gersonde, R.** & Wefer, G. (1987). Sedimentation of biogenic siliceous particles in Antarctic waters from the Atlantic sector. *Marine Micropaleontology*, 11(4), 311–332. https://doi.org/10.1016/0377-8398(87)90004-1

- **Gersonde, R.** & Burckle, L. H. (1990). Neogene diatom biostratigraphy of ODP Leg 113, Weddell Sea (Antarctic Ocean). *Proc., Scientific Results, ODP, Leg 113*, June, 761–789. https://doi.org/10.2973/odp.proc.sr.113.126.1990
- **Gille, S. T.** (2014). Meridional displacement of the Antarctic circumpolar current. *Philosophical Transactions of the Royal Society A: Mathematical, Physical and Engineering Sciences, 372* (2019), 20130273.
- **Gille, S. T.**, McKee, D. C., & Martinson, D. G. (2016). Temporal changes in the Antarctic circumpolar current: Implications for the Antarctic continental shelves. *Oceanography*, 29(4), 96–105. https://doi.org/10.5670/oceanog.2016.102
- **Gonthier, E. G.**, Faugères, J. C., & Stow, D. A. V. (1984). Contourite facies of the Faro Drift, Gulf of Cadiz. *Geological Society Special Publication*, 15, 275–292. https://doi.org/10.1144/GSL.SP.1984.015.01.18
- Gordon, A. L. (2009). Bottom water formation. Ocean Currents, 263, 269.
- **Gordon, A. L.**, Huber, B., McKee, D., & Visbeck, M. (2010). A seasonal cycle in the export of bottom water from the Weddell Sea. *Nature Geoscience*, 3(8), 551–556. https://doi.org/10.1038/ngeo916
- **Gordon, A. L.**, Mensch, M., Dong, Z., Smethie, W. M., & De Bettencourt, J. (2000). Deep and bottom water of the Bransfield Strait eastern and central basins. *Journal of Geophysical Research: Oceans*, 105(C5), 11337–11346. https://doi.org/10.1029/2000jc900030
- **Gordon, A. L.** & Nowlin, W. D. (1978). The basin waters of the Brandsfield Strait. *Journal of Physical Oceanography*, 8(1), 258–264.
- **Gràcia, E.**, Canals, M., Farràn, M., Sorribas, J., & Pallàs, R. (1997). Central and eastern Bransfield basins (Antarctica) from high-resolution swath-bathymetry data. *Antarctic Science*, 9(2), 168–180. https://doi.org/10.1017/s0954102097000229
- **Griener, K. W.**, Warny, S., Askin, R., & Acton, G. (2015). Early to middle Miocene vegetation history of Antarctica supports eccentricity-paced warming intervals during the Antarctic icehouse phase. *Global and Planetary Change*, *127*, 67–78.
- Hammer, Ø., Harper, D. A. T., & Ryan, P. D. (2001). PAST: PALEONTOLOGICAL STATISTICS SOFTWARE PACKAGE FOR EDUCATION AND DATA ANALYSIS. Palaeontologia Electronica, 4(1), 9pp. http://palaeo-electronica.org/2001\_1/past/issue1\_01.htm
- **Harrington, P.K.**, Barker, P.F., & Griffiths, D.H. (1972) *Crustal structure of the South Orkney Islands area from seismic refraction and magnetic measurements*. Paper presented at Symposium on Antarctic Geology and Solid Earth Geophysics in August 1970, Oslo.

- **Hartman, J. D.**, Sangiorgi, F., Salabarnada, A., Peterse, F., Houben, A. J. P., Schouten, S., Brinkhuis, H., Escutia, C., & Bijl, P. K. (2018). Paleoceanography and ice sheet variability offshore Wilkes Land, Antarctica--Part 3: Insights from Oligocene-Miocene TEX 86-based sea surface temperature reconstructions. *Climate of the Past*, *14*(9), 1275–1297.
- **Hepp, D. A.**, Mörz, T., & Grützner, J. (2006). Pliocene glacial cyclicity in a deep-sea sediment drift (Antarctic Peninsula Pacific Margin). *Palaeogeography, Palaeoclimatology, Palaeoecology,* 231(1–2), 181–198. https://doi.org/10.1016/j.palaeo.2005.07.030
- **Hepp, D. A.** (2008). Late Miocene-Pliocene glacial cyclicity in a deep-sea sediment drift on the Antarctic Peninsula continental margin: Sedimentary and diagenetic processes (Doctoral dissertation, Bremen, Univ., Diss., 2007).
- Hernandez-Molina, F. J., Bohoyo, F., Galindo-zaldivar, J., & Jabaloy, A. (2008). Tectonic, sedimentary and paleoceanographic implications of a regional discontinuity (Reflector- c) in the Scotia and Weddell Seas (Antarctica). *Geo-Temas*, 10 (July).
- Hernández-Molina, F. J., Larter, R. D., Rebesco, M., & Maldonado, A. (2006). Miocene reversal of bottom water flow along the Pacific Margin of the Antarctic Peninsula: Stratigraphic evidence from a contourite sedimentary tail. *Marine Geology*, 228, (1–4), 93–116. https://doi.org/10.1016/j.margeo.2005.12.010
- Hernández-Molina, F. J., Llave, E., Somoza, L., Fernández-Puga, M. C., Maestro, A., León, R., Medialdea, T., Barnolas, A., García, M., del Río, V. D., Fernández-Salas, L. M., Vázquez, J. T., Lobo, F., Dias, J. M. A., Rodero, J., & Gardner, J. (2003). Looking for clues to paleoceanographic imprints: A diagnosis of the Gulf of Cadiz contourite depositional systems. *Geology*, 31(1), 19–22. https://doi.org/10.1130/0091-7613(2003)031<0019:LFCTPI>2.0.CO;2
- **Hillenbrand, C. D.**, & Ehrmann, W. (2005). Late Neogene to Quaternary environmental changes in the Antarctic Peninsula region: Evidence from drift sediments. *Global and Planetary Change*, *45*(1-3 SPEC. ISS.), 165–191. https://doi.org/10.1016/j.gloplacha.2004.09.006
- Hochmuth, K., Gohl, K., Leitchenkov, G., Sauermilch, I., Whittaker, J. M., Uenzelmann-Neben, G., Davy, B., & De Santis, L. (2020). The Evolving Paleobathymetry of the Circum-Antarctic Southern Ocean Since 34 Ma: A Key to Understanding Past Cryosphere-Ocean Developments. *Geochemistry, Geophysics, Geosystems*, 21(8), 1–28. https://doi.org/10.1029/2020GC009122
- **Hoem, F. S.**, Valero, L., Evangelinos, D., Escutia, C., Duncan, B., McKay, R. M., Brinkhuis, H., Sangiorgi, F., & Bijl, P. K. (2021). Temperate Oligocene surface ocean conditions offshore of Cape Adare, Ross Sea, Antarctica. *Climate of the Past*, *17*(4), 1423–1442.
- **Hojnacki, V.**, Lepp, A., Horowitz Castaldo, J., States, A., Li, X., & Passchier, S. (2022). Impact of Eocene-Oligocene Antarctic Glaciation on the Paleoceanography of the Weddell Sea. *Paleoceanography and Paleoclimatology*, 37(12). https://doi.org/10.1029/2022PA004440

- Houben, A., Bijl, P. K., Pross, J., Bohaty, S. M., Passchier, S., Stickley, C. E., Röhl, U., Sugisaki, S., Tauxe, L., Flierdt, T. van de, Olney, M., Sangiorgi, F., Sluij, A., Escutia, C., & Brinkhuis, H. (2013). Reorganization of Southern Ocean Plankton Ecosystem at the Onset of Antarctic Glaciation. *Science*, 340 (April), 341–345.
- **Houben, A.**, Bijl, P. K., Sluijs, A., Schouten, S., & Brinkhuis, H. (2019). Late Eocene Southern Ocean Cooling and Invigoration of Circulation Preconditioned Antarctica for Full-Scale Glaciation. *Geochemistry, Geophysics, Geosystems*, 20(5), 2214–2234. https://doi.org/10.1029/2019GC008182
- **Hsu, S. K.**, Coppens, D., & Shyu, C. T. (1998). Depth to magnetic source using the generalized analytic signal. *Geophysics*, *63*(6), 1947-1957. https://doi.org/10.1190/1.1444488
- **Huang, X.**, Gohl, K., & Jokat, W. (2014). Variability in Cenozoic sedimentation and paleo-water depths of the Weddell Sea basin related to pre-glacial and glacial conditions of Antarctica. *Global and Planetary Change*, 118, 25–41. https://doi.org/10.1016/j.gloplacha.2014.03.010
- **Huang, X.**, Stärz, M., Gohl, K., Knorr, G., & Lohmann, G. (2017). Impact of Weddell Sea shelf progradation on Antarctic bottom water formation during the Miocene. *Paleoceanography*, 32(3), 304–317. https://doi.org/10.1002/2016PA002987
- **Huber, M.**, Brinkhuis, H., Stickley, C. E., Döös, K., Sluijs, A., Warnaar, J., Schellenberg, S. A., & Williams, G. L. (2004). Eocene circulation of the Southern Ocean: Was Antarctica kept warm by subtropical waters? *Paleoceanography*, *19*(4), 1–12. https://doi.org/10.1029/2004PA001014
- **Hutchinson, D. K.**, Coxall, H. K., Lunt, D. J., Steinthorsdottir, M., De Boer, A. M., Baatsen, M., von der Heydt, A., Huber, M., Kennedy-Asser, A. T., Kunzmann, L., & others. (2020). The Eocene-Oligocene transition: a review of marine and terrestrial proxy data, models and model-data comparisons. *Climate of the Past Discussions*, 2020, 1–71.
- **Hutchinson, D. K.**, Coxall, H. K., O'Regan, M., Nilsson, J., Caballero, R., & de Boer, A. M. (2019). Arctic closure as a trigger for Atlantic overturning at the Eocene-Oligocene Transition. *Nature Communications*, *10*(1). https://doi.org/10.1038/s41467-019-11828-z
- Ingólfsson, Ó., Hjort, C., Berkman, P. A., Björck, S., Colhoun, E., Goodwin, I. D., ... & Prentice, M. L. (1998). Antarctic glacial history since the Last Glacial Maximum: an overview of the record on land. *Antarctic science*, 10(3), 326-344.
- **Ivany, L. C.**, Van Simaeys, S., Domack, E. W., & Samson, S. D. (2006). Evidence for an earliest Oligocene ice sheet on the Antarctic Peninsula. *Geology*, 34(5), 377–380. https://doi.org/10.1130/G22383.1
- Jabaloy, A., Balanyá, J. C., Barnolas, A., Galindo-Zaldívar, J., Hernández-Molina, F. J., Maldonado, A., Martínez-Martínez, J. M., Rodríguez-Fernández, J., de Galdeano, C. S., Somoza, L., Surinach, E., & Váquez, J. T. (2003). The transition from an active to a passive margin (SW end of the South Shetland Trench, Antarctic Peninsula). *Tectonophysics*, 366(1–2), 55–81. https://doi.org/10.1016/S0040-1951(03)00060-X

- **Jacobs, S. S.** (2004). Bottom water production and its links with the thermohaline circulation. *Antarctic Science*, *16*(4), 427–437.
- **Jenkins, A.**, Dutrieux, P., Jacobs, S., Steig, E. J., Gudmundsson, G. H., Smith, J., & Heywood, K. J. (2016). Decadal ocean forcing and Antarctic ice sheet response: Lessons from the Amundsen Sea. *Oceanography*, 29(4), 106-117.
- Jones, J. M., Gille, S. T., Goosse, H., Abram, N. J., Canziani, P. O., Charman, D. J., Clem, K. R., Crosta, X., Lavergne, C. De, Eisenman, I., England, M. H., Fogt, R. L., Frankcombe, L. M., Marshall, G. J., Masson-delmotte, V., Morrison, A. K., Orsi, A. J., Raphael, M. N., Renwick, J. A., ... Vance, T. R. (2016). Assessing recent trends in high-latitude Southern Hemisphere surface climate. *Nature*, 6(October), 917–926. https://doi.org/10.1038/nclimate3103
- Katz, M. E., Cramer, B. S., Toggweiler, J. R., Esmay, G., Liu, C., Miller, K. G., Rosenthal, Y., Wade, B. S., & Wright, J. D. (2011). Impact of antarctic circumpolar current development on late paleogene ocean structure. *Science*, 332 (6033), 1076–1079. https://doi.org/10.1126/science.1202122
- **Kavoun, M.** & Vinnikovskaya, O. (1994). Seismic stratigraphy and tectonics of the northwestern Weddell Sea (Antarctica) inferred from marine geophysical surveys. *Tectonophysics*, *240*(1-4), 299-341. https://doi.org/10.1016/0040-1951(94)90277-1
- **Kemp, A. E. S.**, Pike, J., Pearce, R. B., & Lange, C. B. (2000). The "Fall dump" a new perspective on the role of a "shade flora" in the annual cycle of diatom production and export flux. *Deep Sea Research Part II: Topical Studies in Oceanography*, 47(9), 2129–2154. https://doi.org/https://doi.org/10.1016/S0967-0645(00)00019-9
- **Kemp, A. E. S.**, Grigorov, I., Pearce, R. B., & Garabato, A. C. N. (2010). Migration of the Antarctic Polar Front through the mid-Pleistocene transition: evidence and climatic implications. *Quaternary Science Reviews*, *29*(17–18), 1993–2009.
- **Kennett, J. P.** (1977). Cenozoic evolution of Antarctic glaciation, the circum-Antarctic Ocean, and their impact on global paleoceanography. *Journal of Geophysical Research*, *82*(27), 3843–3860.
- Kennett, J. P., & Barker, P. F. (1990). Latest Cretaceous to Cenozoic climate and oceanographic developments in the Weddell Sea, Antarctica: an ocean-drilling perspective. Proc., Scientific Results, ODP, Leg 113, Weddell Sea, Antarctica, 937–960. https://doi.org/10.2973/odp.proc.sr.113.195.1990
- Khim, B. K., Yoon, H. II, Kang, C. Y., & Bahk, J. J. (2002). Unstable climate oscillations during the late Holocene in the eastern Bransfield Basin, Antarctic Peninsula. *Quaternary Research* (Vol. 58, Issue 3, pp. 234–245). https://doi.org/10.1006/qres.2002.2371
- **King, E. C.** & Barker, P. F. (1988). The margins of the South Orkney microcontinent. *Journal of the Geological Society*, 145(2), 317-331. https://doi.org/10.1144/gsjgs.145.2.0317

- **King, E. C.**, Leitchenkov, G., Galindo-Zaldivar, J., Maldonado, A., & Lodolo, E. (1997). Crustal structure and sedimentation in Powell Basin. *Geology and Seismic Stratigraphy of the Antarctic Margin,* 2, 71, 75-93. https://doi.org/10.1029/ar071p0075
- **Kirby, S. H.** (1983). Rheology of the lithosphere. *Reviews of Geophysics*, 21(6), 1458-1487. https://doi.org/10.1029/RG021i006p01458
- **Kotov, S.** & Pälike, H. (2018, December). QAnalySeries-a cross-platform time series tuning and analysis tool. In *AGU Fall Meeting Abstracts* (Vol. 2018, pp. PP53D-1230). https://doi.org/10.1002/essoar.10500226.1
- **Lajaunie, C.**, Courrioux, G., & Manuel, L. (1997). Foliation fields and 3D cartography in geology: Principles of a method based on potential interpolation. *Mathematical Geology*, 29(4), 571–584. https://doi.org/10.1007/bf02775087
- Larter, R. D., Vanneste, L. E., Morris, P., & Smythe, D. K. (2003). Structure and tectonic evolution of the South Sandwich arc. *Geological Society, London, Special Publications*, *219*(1), 255–284.
- **Lawver, L. A.**, Sclater, J. G., & Meinke, L. (1985). Mesozoic and Cenozoic reconstructions of the South Atlantic. *Tectonophysics*, *114*(1-4), 233-254.
- **Lear, C. H.**, Bailey, T. R., Pearson, P. N., Coxall, H. K., & Rosenthal, Y. (2008). Cooling and ice growth across the Eocene-Oligocene transition. *Geology*, *36*(3), 251–254. https://doi.org/10.1130/G24584A.1
- **Lee, D. Y.**, Petersen, M. R., & Lin, W. (2019). The Southern Annular Mode and Southern Ocean Surface Westerly Winds in E3SM. *Earth and Space Science*, *6*(12), 2624–2643. https://doi.org/10.1029/2019EA000663
- **Lesur, V.**, Hamoudi, M., Choi, Y., Dyment, J., & Thébault, E. (2016). Building the second version of the World Digital Magnetic Anomaly Map (WDMAM) *Earth, Planets and Space*, 68(1), 1-13. https://doi.org/10.1186/s40623-016-0404-6
- **Leventer, A.**, Domack, E. W., Ishman, S. E., Brachfeld, S., McClennen, C. E., & Manley, P. (1996). Productivity cycles of 200-300 years in the Antarctic Peninsula region: Understanding linkages among the sun, atmosphere, oceans, sea ice, and biota. *Bulletin of the Geological Society of America*, 108(12), 1626–1644. https://doi.org/10.1130/0016-7606(1996)108<1626:PCOYIT>2.3.CO;2
- Levy, R. H., Meyers, S. R., Naish, T. R., Golledge, N. R., McKay, R. M., Crampton, J. S., DeConto, R. M., De Santis, L., Florindo, F., Gasson, E. G. W., Harwood, D. M., Luyendyk, B. P., Powell, R. D., Clowes, C., & Kulhanek, D. K. (2019). Antarctic ice-sheet sensitivity to obliquity forcing enhanced through ocean connections. *Nature Geoscience*, 12(2), 132–137. https://doi.org/10.1038/s41561-018-0284-4

- Liebrand, D., Beddow, H. M., Lourens, L. J., Pälike, H., Raffi, I., Bohaty, S. M., Hilgen, F. J., Saes, M. J. M., Wilson, P. A., Van Dijk, A. E., & others. (2016). Cyclostratigraphy and eccentricity tuning of the early Oligocene through early Miocene (30.1--17.1 Ma): Cibicides mundulus stable oxygen and carbon isotope records from Walvis Ridge Site 1264. Earth and Planetary Science Letters, 450, 392–405.
- **Liebrand, D.**, de Bakker, A. T. M., Beddow, H. M., Wilson, P. A., Bohaty, S. M., Ruessink, G., Pälike, H., Batenburg, S. J., Hilgen, F. J., Hodell, D. A., & others. (2017). Evolution of the early Antarctic ice ages. *Proceedings of the National Academy of Sciences*, *114*(15), 3867–3872.
- Liu, S., Hernández-Molina, F. J., Yang, C., Zhang, C., Huang, X., Yin, S., García, M., Rooij, D. Van, Wang, C., Zhuo, H., Chen, H., Lei, Y., Lin, Z., Luo, K., & Su, M. (2022). Oceanographic consequences of the Bransfield Strait (Antarctica) opening. *Geology*, 50(12), 1403–1408. https://doi.org/10.1130/G50389.1
- **Livermore, R.**, Nankivell, A., Eagles, G., & Morris, P. (2005). Paleogene opening of Drake Passage. *Earth and Planetary Science Letters*, 236(1–2), 459–470. https://doi.org/10.1016/j.epsl.2005.03.027
- **Livermore, R.**, Hillenbrand, C. D., Meredith, M., & Eagles, G. (2007). Drake Passage and Cenozoic climate: An open and shut case? *Geochemistry, Geophysics, Geosystems*, 8(1). https://doi.org/10.1029/2005GC001224
- **Loeb, V. J.**, Hofmann, E. E., Klinck, J. M., Holm-Hansen, O., & White, W. B. (2009). ENSO and variability of the Antarctic Peninsula pelagic marine ecosystem. *Antarctic Science*, 21(2), 135–148.
- **Lodolo, E.**, Civile, D., Vuan, A., Tassone, A., & Geletti, R. (2010). The Scotia-Antarctica plate boundary from 35°W to 45°W. *Earth and Planetary Science Letters*, 293(1–2), 200–215. https://doi.org/10.1016/j.epsl.2009.12.045
- **Lodolo, E.**, Donda, F., & Tassone, A. (2006). Western Scotia Sea margins: improved constraints on the opening of the Drake Passage. *Journal of Geophysical Research: Solid Earth*, 111(B6).
- López-Quirós, A., Escutia, C., Etourneau, J., Rodríguez-Tovar, F. J., Roignant, S., Lobo, F. J., Thompson, N., Bijl, P. K., Bohoyo, F., Salzmann, U., Evangelinos, D., Salabarnada, A., Hoem, F. S., & Sicre, M. A. (2021). Eocene-Oligocene paleoenvironmental changes in the South Orkney Microcontinent (Antarctica) linked to the opening of Powell Basin. *Global and Planetary Change*, 204(July). https://doi.org/10.1016/j.gloplacha.2021.103581
- Maestro, A., López-Martínez, J., & Bohoyo, F. (2013). Mesozoic to recent evolution of intraplate stress fields under multiple remote stresses: The case of signy island (south orkney microcontinent, antarctica). *Geological Society Special Publication*, 381(1), 45–65. https://doi.org/10.1144/SP381.4

- Maldonado, A., Zitellini, N., Leitchenkov, G., Balanyá, J. C., Coren, F., Galindo-Zaldívar, J., Lodolo, E., Jabaloy, A., Zanolla, C., Rodríguez-Fernández, J., & Vinnikovskaya, O. (1998). Small ocean basin development along the Scotia-Antarctica plate boundary and in the northern Weddell Sea. *Tectonophysics* (Vol. 296, Issues 3–4, pp. 371–402). https://doi.org/10.1016/S0040-1951(98)00153-X
- Maldonado, A., Barnolas, A., Bohoyo, F., Escutia, C., Galindo-Zaldívar, J., Hernández-Molina, J., Jabaloy, A., Lobo, F. J., Hans Nelson, C., Rodríguez-Fernández, J., Somoza, L., Suriñach, E., & Vázquez, J. T. (2006). Ocean basins near the Scotia–Antarctic plate boundary: Influence of tectonics and paleoceanography on the Cenozoic deposits. *Antarctica*, 441–446. https://doi.org/10.1007/3-540-32934-x\_56
- Maldonado, A., Barnolas, A., Bohoyo, F., Escutia, C., Galindo-Zaldívar, J., Hernández-Molina, J., ... & Vázquez, J. T. (2005). Miocene to recent contourite drifts development in the northern Weddell Sea (Antarctica). *Global and Planetary Change*, 45 (1-3), 99-129. https://doi.org/10.1016/j.gloplacha.2004.09.013
- Maldonado, A., Barnolas, A., Bohoyo, F., Galindo-Zaldívar, J., Hernández-Molina, J., Lobo, F., Rodríguez-Fernández, J., Somoza, L., & Vázquez, J. T. (2003). Contourite deposits in the central Scotia Sea: The importance of the Antarctic Circumpolar Current and the Weddell Gyre flows. *Palaeogeography, Palaeoclimatology, Palaeoecology*, 198(1–2), 187–221. https://doi.org/10.1016/S0031-0182(03)00401-2
- Maldonado, A., Bohoyo, F., Galindo-Zaldívar, J., Hernández-Molina, F. J., Lobo, F. J., Lodolo, E., Martos, Y. M., Pérez, L. F., Schreider, A. A., & Somoza, L. (2014). A model of oceanic development by ridge jumping: Opening of the Scotia Sea. *Global and Planetary Change*, *123*, 152–173. https://doi.org/10.1016/j.gloplacha.2014.06.010
- Mallet, J.L. (2002). Geomodeling. Oxford University Press.
- Martos, Y. M., Maldonado, A., Lobo, F. J., Hernández-Molina, F. J., & Pérez, L. F. (2013). Tectonics and palaeoceanographic evolution recorded by contourite features in southern Drake Passage (Antarctica). *Marine Geology*, 343, 76–91. https://doi.org/10.1016/j.margeo.2013.06.015
- Martos, Y. M., Catalán, M., Galindo-Zaldívar, J., Maldonado, A., & Bohoyo, F. (2014). Insights about the structure and evolution of the Scotia Arc from a new magnetic data compilation. *Global and Planetary Change*, 123, 239–248. https://doi.org/10.1016/j.gloplacha.2014.07.022
- Masqué, P., Isla, E., Sanchez-Cabeza, J. A., Palanques, A., Bruach, J. M., Puig, P., & Guillén, J. (2002). Sediment accumulation rates and carbon fluxes to bottom sediments at the Western Bransfield Strait (Antarctica). *Deep Sea Research Part II: Topical Studies in Oceanography*, 49(4–5), 921–933.
- McCave, I. N. & Tucholke, B. E. (1986). Deep current-controlled sedimentation in the western North Atlantic.

- **McCave, I. N,** & Hall, I. R. (2006). Size sorting in marine muds: Processes, pitfalls, and prospects for paleoflow-speed proxies. *Geochemistry, Geophysics, Geosystems*, 7(10). https://doi.org/10.1029/2006GC001284
- **McCave, I. N.**, Manighetti, B., & Robinson, S. G. (1995). Sortable silt and fine sediment size/composition slicing: Parameters for palaeocurrent speed and palaeoceanography. *Paleoceanography*, 10(3), 593–610. https://doi.org/10.1029/94PA03039
- McCave, I. N., Thornalley, D. J. R., & Hall, I. R. (2017). Relation of sortable silt grain-size to deep-sea current speeds: Calibration of the 'Mud Current Meter.' *Deep-Sea Research Part I: Oceanographic Research Papers*, 127(July), 1–12. https://doi.org/10.1016/j.dsr.2017.07.003
- **McKenzie, D.** (1978). Some remarks on the development of sedimentary basins. *Earth and Planetary Science Letters*, 40(1), 25–32. https://doi.org/10.1016/0012-821X(78)90071-7
- Mena, A., Francés, G., Pérez-Arlucea, M., Aguiar, P., Barreiro-Vázquez, J. D., Iglesias, A., & Barreiro-Lois, A. (2015). A novel sedimentological method based on CT-scanning: Use for tomographic characterization of the Galicia Interior Basin. *Sedimentary Geology*, 321, 123–138. https://doi.org/https://doi.org/10.1016/j.sedgeo.2015.03.007
- Michels, K. H., Kuhn, G., Hillenbrand, C. D., Diekmann, B., FÜtterer, D. K., Grobe, H., & Uenzelmann-Neben, G. (2002). The southern Weddell Sea: combined contourite-turbidite sedimentation at the southeastern margin of the Weddell Gyre. *Geological Society Memoir*, 22(1), 305–323. https://doi.org/10.1144/GSL.MEM.2002.022.01.22
- **Moffat, C.**, Owens, B., & Beardsley, R. C. (2009). On the characteristics of Circumpolar Deep Water intrusions to the west Antarctic Peninsula Continental Shelf. Journal of Geophysical Research: Oceans, 114(5), 1–16. https://doi.org/10.1029/2008JC004955
- **Montes, M.**, Beamud, E., Nozal, F., & Santillana, S. N. (2019). Late Maastrichtian-Paleocene chronostratigraphy from Seymour Island (James Ross Basin, Antarctic Peninsula). Eustatic controls on sedimentation. *Advances in Polar Science*, 30(2), 1–12. https://doi.org/10.13679/j.advps.2019.2.00
- Morales-Ocaña, C., Bohoyo, F., Escutia, C., Marín-Lechado, C., Rey-Moral, C., Druet, M., Galindo-Zaldívar, J., & Maestro, A. (2023). 3D Geophysical and Geological Modeling of the South Orkney Microcontinent (Antarctica): Tectonic Implications for the Scotia Arc Development. *Tectonics*, 42(4), 1–20. https://doi.org/10.1029/2022TC007602
- Moreno, P. I., Vilanova, I., Villa-Martínez, R., Garreaud, R. D., Rojas, M., & De Pol-Holz, R. (2014). Southern Annular Mode-like changes in southwestern Patagonia at centennial timescales over the last three millennia. *Nature communications*, *5*(1), 4375. https://doi.org/10.1038/ncomms5375

- Moy, C. M., Seltzer, G. O., Rodbell, D. T., & Anderson, D. M. (2002). Variability of El Niño/Southern Oscillation activity at millennial timescales during the Holocene epoch. *Nature*, 420(6912), 162–165. https://doi.org/10.1038/nature01194
- **Mudelsee, M.**, Bickert, T., Lear, C. H., & Lohmann, G. (2014). Cenozoic climate changes: A review based on time series analysis of marine benthic  $\delta$ 18O records. *Reviews of Geophysics*, *52*(3), 333–374.
- **Mulder, T.** & Alexander, J. (2001). The physical character of subaqueous sedimentary density flows and their deposits. *Sedimentology*, 48(2), 269–299.
- Mulvaney, R., Abram, N. J., Hindmarsh, R. C. A., Arrowsmith, C., Fleet, L., Triest, J., Sime, L. C., Alemany, O., & Foord, S. (2012). Recent Antarctic Peninsula warming relative to Holocene climate and iceshelf history. *Nature*, 489(7414), 141–144. https://doi.org/10.1038/nature11391
- **Naish, T.**, Powell, R., Levy, R., Wilson, G., Scherer, R., Talarico, F., ... & Williams, T. (2009). Obliquity-paced Pliocene West Antarctic ice sheet oscillations. *Nature*, 458(7236), 322-328.
- Nakayama, Y., Menemenlis, D., Zhang, H., Schodlok, M., & Rignot, E. (2018). Origin of Circumpolar Deep Water intruding onto the Amundsen and Bellingshausen Sea continental shelves. Nature Communications, 9(1), 1–9. https://doi.org/10.1038/s41467-018-05813-1
- Naveira Garabato, A. C., McDonagh, E. L., Stevens, D. P., Heywood, K. J., & Sanders, R. J. (2002). On the export of Antarctic Bottom Water from the Weddell Sea. *Deep-Sea Research Part II: Topical Studies in Oceanography*, 49(21), 4715–4742. https://doi.org/10.1016/S0967-0645(02)00156-X
- Nichols, M. D., Xuan, C., Crowhurst, S., Hodell, D. A., Richter, C., Acton, G. D., & Wilson, P. A. (2020). Climate-Induced Variability in Mediterranean Outflow to the North Atlantic Ocean During the Late Pleistocene. *Paleoceanography and Paleoclimatology*, 35(9), 1–17. https://doi.org/10.1029/2020PA003947
- **Nielsen, T. A. P. M.**, Knutz, P. C., & Kuijpers, A. (2008). Seismic expression of contourite depositional systems. *Developments in Sedimentology*, *60*, 301-321.
- Nieto-Moreno, V., Martínez-Ruiz, F., Giralt, S., Jiménez-Espejo, F., Gallego-Torres, D., Rodrigo-Gámiz, M., García-Orellana, J., Ortega-Huertas, M., & de Lange, G. J. (2011). Tracking climate variability in the western Mediterranean during the Late Holocene: a multiproxy approach. Climate of the Past, 7(4), 1395–1414. https://doi.org/10.5194/cp-7-1395-2011
- **Northwest Geophysical Associates** (2004), *GM-SYS gravity/magnetic modeling software. User's guide, Version 4.9*, Northwest Geophysical Associates, 101 pp
- **Orsi, A. H.**, Johnson, G. C., & Bullister, J. L. (1999). Circulation, mixing, and production of Antarctic Bottom Water. *Progress in Oceanography*, *43*(1), 55–109.

- Orsi, A. H., Whitworth III, T., & Nowlin Jr, W. D. (1995). On the meridional extent and fronts of the Antarctic Circumpolar Current. *Deep Sea Research Part I: Oceanographic Research Papers*, 42(5), 641–673.
- Palike, H., Norris, R. D., Herrle, J. O., Wilson, P. A., Coxall, H. K., Lear, C. H., Shackleton, N. J., Tripati, A. K., & Wade, B. S. (2006). The heartbeat of the Oligocene climate system. *Science*, *314*(5807), 1894–1898.
- **Payton, C. E.** (1977). Seismic Stratigraphy Applications to Hydrocarbon Exploration. American Association of Petroleum Geologists. https://doi.org/10.1306/M26490
- **Peck, V. L.**, Allen, C. S., Kender, S., McClymont, E. L., & Hodgson, D. (2015). Oceanographic variability on the West Antarctic Peninsula during the Holocene and the influence of upper circumpolar deep water. *Quaternary Science Reviews*, 119, 54–65. https://doi.org/10.1016/j.quascirev.2015.04.002
- **Pérez, L. F.**, Lodolo, E., Maldonado, A., Hernández-Molina, F. J., Bohoyo, F., Galindo-Zaldívar, J., Lobo, F. J., & Burca, M. (2014). Tectonic development, sedimentation and paleoceanography of the Scan Basin (southern Scotia Sea, Antarctica). *Global and Planetary Change*, 123, 344–358. https://doi.org/10.1016/j.gloplacha.2014.06.007
- **Pérez, L. F.**, Hernández-Molina, F. J., Esteban, F. D., Tassone, A., Piola, A. R., Maldonado, A., Preu, B., Violante, R. A., & Lodolo, E. (2015). Erosional and depositional contourite features at the transition between the western Scotia Sea and southern South Atlantic Ocean: links with regional water-mass circulation since the Middle Miocene. *Geo-Marine Letters*, 35(4), 271–288. https://doi.org/10.1007/s00367-015-0406-6
- Pérez, L. F., Maldonado, A., Hernández-Molina, F. J., Lodolo, E., Bohoyo, F., & Galindo-Zaldívar, J. (2017). Tectonic and oceanographic control of sedimentary patterns in a small oceanic basin: Dove Basin (Scotia Sea, Antarctica). Basin Research, 29, 255-276. https://doi.org/10.1111/bre.12148
- **Pérez, L. F.**, Hernández-Molina, F. J., Lodolo, E., & Bohoyo, F. (2019). Oceanographic and climatic consequences of the tectonic evolution of the southern scotia sea basins, Antarctica. *Earth-Science Reviews*, 198 (August), 102922. https://doi.org/10.1016/j.earscirev.2019.102922
- Pérez, L. F., Martos, Y. M., García, M., Weber, M. E., Raymo, M. E., Williams, T., Bohoyo, F., Armbrecht, L., Bailey, I., Brachfeld, S., Glüder, A., Guitard, M., Gutjahr, M., Hemming, S., Hernández-Almeida, I., Hoem, F. S., Kato, Y., O'Connell, S., Peck, V. L., ... Zheng, X. (2021). Miocene to present oceanographic variability in the Scotia Sea and Antarctic ice sheets dynamics: Insight from revised seismic-stratigraphy following IODP Expedition 382. Earth and Planetary Science Letters, 553, 116657. https://doi.org/10.1016/j.epsl.2020.116657
- **Pike, J.** & Stickley, C. E. (2013). Diatom fossil records from marine laminated sediments. In S. A. Elias & C. J. Mock (Eds.), Encyclopedia of Quaternary Science (Second Edition) (554–561). Elsevier. https://doi.org/https://doi.org/10.1016/B978-0-444-53643-3.00226-0

- **Pollard, D.** & DeConto, R. M. (2009). Modelling West Antarctic ice sheet growth and collapse through the past five million years. *Nature*, *458*(7236), 329–332.
- **Pritchard, H. D.**, Ligtenberg, S. R. M., Fricker, H. A., Vaughan, D. G., Van Den Broeke, M. R., & Padman, L. (2012). Antarctic ice-sheet loss driven by basal melting of ice shelves. *Nature*, 484(7395), 502–505. https://doi.org/10.1038/nature10968
- Pross, J., Houben, A. J. P., van Simaeys, S., Williams, G. L., Kotthoff, U., Coccioni, R., Wilpshaar, M., & Brinkhuis, H. (2010). Umbria-Marche revisited: A refined magnetostratigraphic calibration of dinoflagellate cyst events for the Oligocene of the Western Tethys. In *Review of Palaeobotany and Palynology* (Vol. 158, Issues 3–4, pp. 213–235). https://doi.org/10.1016/j.revpalbo.2009.09.002
- **Pross, J.**, Contreras, L., Bijl, P. K., Greenwood, D. R., Bohaty, S. M., Schouten, S., Bendle, J. A., Röhl, U., Tauxe, L., Raine, J. I., & others. (2012). Persistent near-tropical warmth on the Antarctic continent during the early Eocene epoch. *Nature*, *488*(7409), 73–77.
- **Pudsey, C. J.** (2000). Sedimentation on the continental rise west of the Antarctic Peninsula over the last three glacial cycles. *Marine Geology*, 167(3–4), 313–338.
- **Pudsey, C. J.** & Howe, J. A. (2002). Mixed biosiliceous-terrigenous sedimentation under the Antarctic Circumpolar Current, Scotia Sea. *Geological Society Memoir*, 22(1), 325–336. https://doi.org/10.1144/GSL.MEM.2002.022.01.23
- **Ranalli, G.** & Murphy, D. C. (1987). Rheological stratification of the lithosphere. *Tectonophysics*, 132(4), 281–295. https://doi.org/10.1016/0040-1951(87)90348-9
- **Rebesco, M.**, Richard, C. S., Cocks, L. R. M., & Ian, R. P. (2005). Sedimentary Environments: Contourites, Encyclopedia of Geology. https://doi.org/https://doi.org/10.1016/B0-12-369396-9/00497-4
- **Rebesco, M.**, & Stow, D. (2001). Seismic expression of contourites and related deposits: A preface. *Marine Geophysical Research* (Vol. 22, Issues 5–6, pp. 303–308). https://doi.org/10.1023/A:1016316913639
- **Rebesco, M.**, Hernández-Molina, F. J., Van Rooij, D., & Wåhlin, A. (2014). Contourites and associated sediments controlled by deep-water circulation processes: State-of-the-art and future considerations. *Marine Geology*, *352*, 111-154. https://doi.org/10.1016/j.margeo.2014.03.011
- **Rebesco, M.**, Larter, R. D., Barker, P. F., Camerlenghi, A., & Vanneste, L. E. (1997). The history of sedimentation on the continental rise west of the Antarctic Peninsula. *Geology and seismic stratigraphy of the Antarctic margin, 2, 71,* 29-49. https://doi.org/10.1029/ar071p0029
- **Rebesco, M.** & Stow, D. (2001). Seismic expression of contourites and related deposits: A preface. In *Marine Geophysical Research* (Vol. 22, Issues 5–6, pp. 303–308). https://doi.org/10.1023/A:1016316913639

- **Reguzzoni, M.**, & Sampietro, D. (2015). International Journal of Applied Earth Observation and Geoinformation GEMMA: An Earth crustal model based on GOCE satellite data. *International Journal of Applied Earth Observations and Geoinformation*, 35, 31–43. http://doi.org/10.1016/j.jag.2014.04.002
- **Reinardy, B. T. I.**, Escutia, C., Iwai, M., Jimenez-Espejo, F. J., Cook, C., van de Flierdt, T., & Brinkhuis, H. (2015). Repeated advance and retreat of the East Antarctic Ice Sheet on the continental shelf during the early Pliocene warm period. *Palaeogeography, Palaeoclimatology, Palaeoecology,* 422, 65–84.
- Renner, R. G. B., Dikstra, B. J., & Martin, J. L. (1982). *Aeromagnetic Surveys over the Antarctic Peninsula*. Paper presented at Symposium on Antarctic Geology and Geophysics in 1977, Madison, Wisconsin.
- Renner, A. H. H., Thorpe, S. E., Heywood, K. J., Murphy, E. J., Watkins, J. L., & Meredith, M. P. (2012). Advective pathways near the tip of the Antarctic Peninsula: Trends, variability and ecosystem implications. *Deep-Sea Research Part I: Oceanographic Research Papers*, 63, 91–101. https://doi.org/10.1016/j.dsr.2012.01.009
- **Rignot, E.**, Mouginot, J., Morlighem, M., Seroussi, H., & Scheuchl, B. (2014). Widespread, rapid grounding line retreat of Pine Island, Thwaites, Smith, and Kohler glaciers, West Antarctica, from 1992 to 2011. *Geophysical Research Letters*, *41*(10), 3502–3509.
- **Rignot, E.**, Mouginot, J., Scheuchl, B., Van Den Broeke, M., Van Wessem, M. J., & Morlighem, M. (2019). Four decades of Antarctic ice sheet mass balance from 1979–2017. *Proceedings of the National Academy of Sciences of the United States of America*, 116(4), 1095–1103. https://doi.org/10.1073/pnas.1812883116
- Riley, T. R., Carter, A., Burton-Johnson, A., Leat, P. T., Hogan, K. A., & Bown, P. R. (2022). Crustal block origins of the South Scotia Ridge. *Terra Nova*, 34(6), 495-502. http://doi.org/10.1111/ter.12613
- **Rintoul, S. R.** (2018). The global influence of localized dynamics in the Southern Ocean. *Nature*, 558(7709), 209–218. https://doi.org/10.1038/s41586-018-0182-3
- **Robinson, S. G.** (1992). Lithostratigraphic applications for magnetic susceptibility logging of deep-sea sediment cores: Examples from ODP Leg 115. *Geological Society Special Publication*, 70(70), 65–98. https://doi.org/10.1144/GSL.SP.1993.070.01.06
- **Rodrigues, S.**, Roque, C., Hernández-Molina, F. J., Llave, E., & Terrinha, P. (2020). The sines contourite depositional system along the SW Portuguese margin: Onset, evolution and conceptual implications. *Marine Geology*, *430*. https://doi.org/10.1016/j.margeo.2020.106357
- Rodriguez-Fernandez, J., Balanya, J. C., Galindo-Zaldivar, J., & Maldonado, A. (1997). Tectonic evolution of a restricted ocean basin: The Powell Basin (Northeastern Antarctic Peninsula). *Geodinamica Acta*, 10(4), 159-174. https://doi.org/10.1080/09853111.1997.11105300

- **Roest, W. R.**, Verhoef, J., & Pilkington, M. (1992). Magnetic interpretation using the 3-D analytic signal. *Geophysics*, 57(1), 116–125. https://doi.org/10.1190/1.1443174
- **Roest, W. R.**, & Pilkington, M. (1993). Identifying remanent magnetization effects in magnetic data. *Geophysics*, 58(5), 653–659. https://doi.org/10.1190/1.1443449
- **Salabarnada, A.** (2020). Oligocene-Miocene Ice Sheet and Paleoceanographic Evolution of the Eastern Wilkes Land Margin. http://hdl.handle.net/10481/62873
- Salabarnada, A., Escutia, C., Bijl, P. K., Houben, A. J. P., Hartman, J. D., Pross, J., & Sangiorgi, F. (2018). Paleoceanography and ice sheet variability offshore Wilkes Land, Antarctica Part 2: Insights from Oligocene-Miocene dinoflagellate cyst assemblages. *Climate of the Past*, 14(7), 1015–1033. https://doi.org/10.5194/cp-14-1015-2018
- **Sandwell, D. T.**, Müller, R. D., Smith, W. H. F., Garcia, E. and Francis, R. (2014). New global marine gravity model from Cryo-Sat-2 and jason-1 reveals buried tectonic structure. *Science*, 346(6205), 65-67. http://doi.org/10.1126/science.1258213
- Sangiorgi, F., Bijl, P. K., Passchier, S., Salzmann, U., Schouten, S., McKay, R., Cody, R. D., Pross, J., Van De Flierdt, T., Bohaty, S. M., Levy, R., Williams, T., Escutia, C., & Brinkhuis, H. (2018). Southern Ocean warming and Wilkes Land ice sheet retreat during the mid-Miocene. *Nature Communications*, 9(1), 1–11. https://doi.org/10.1038/s41467-017-02609-7
- **Sarkar, S.**, Basak, C., Frank, M., Berndt, C., Huuse, M., Badhani, S., & Bialas, J. (2019). Late Eocene onset of the proto-Antarctic circumpolar current. *Scientific reports*, *9*(1), 10125.
- **Scher, H. D.** & Martin, E. E. (2006). Timing and Climatic Consequences of the Opening of Drake Passage. *Science*, 312(5772), 428–430. https://doi.org/10.1126/science.1120044
- Scherer, R. P., Bohaty, S. M., Dunbar, R. B., Esper, O., Flores, J.-A., Gersonde, R., Harwood, D. M., Roberts, A. P., & Taviani, M. (2008). Antarctic records of precession-paced insolation-driven warming during early Pleistocene Marine Isotope Stage 31. *Geophysical Research Letters*, 35(3).
- **Schmidt, S.**, Howa, H., Diallo, A., Martín, J., Cremer, M., Duros, P., ... & Mulder, T. (2014). Recent sediment transport and deposition in the Cap-Ferret Canyon, South-East margin of Bay of Biscay. *Deep Sea Research Part II: Topical Studies in Oceanography*, 104, 134-144.
- **Schodlok, M. P.**, Hellmer, H. H., & Beckmann, A. (2002). On the transport, variability and origin of dense water masses crossing the South Scotia Ridge. *Deep Sea Research Part II: Topical Studies in Oceanography*, 49(21), 4807–4825.
- **Schreider, A. A.**, Schreider, A. A., Galindo-Zaldivar, J., Maldonado, A., Sazhneva, A. E., & Evsenko, E. I. (2017). Age of the scan basin (Scotia Sea). *Oceanology*, *57*, 328–336.
- **Schreider, A. A.**, Schreider, A. A., Galindo-Zaldivar, J., Maldonado, A., Sazhneva, A. E., & Evsenko, E. I. (2018). Age of the floors of the protector and dove basins (Scotia Sea). *Oceanology*, *58*, 447–458.

- Schreider, A. A., Sazhneva, A., Kluyev, M. S., Brekhovskikh, A. L., Bohoyo, F., Galindo-Zaldivar, J., Morales, C., & Evsenko, E. I. (2022). Kinematic Model of the Development of the Bottom of the Powell Basin (Weddell Sea). *Processes in GeoMedia*, 5. https://doi.org/10.1007/978-3-030-85851-3 22
- **Shanmugam, G.** (2016). Submarine fans: a critical retrospective (1950-2015). *Journal of Palaeogeography*, 5(2), 110–184.
- **Shevenell, A. E.**, Kennett, J. P., & Lea, D. W. (2004). Middle Miocene southern ocean cooling and Antarctic cryosphere expansion. *Science*, *305*(5691), 1766–1770.
- **Schulz, M.** & Mudelsee, M. (2002). REDFIT: estimating red-noise spectra directly from unevenly spaced paleoclimatic time series. *Computers & Geosciences*, 28(3), 421–426. https://doi.org/https://doi.org/10.1016/S0098-3004(01)00044-9
- **Shukla, S. K.**, Crespin, J., & Crosta, X. (2016). Thalassiosira lentiginosa size variation and associated biogenic silica burial in the Southern Ocean over the last 42 kyrs. *Marine Micropaleontology*, 127, 74–85.
- **Sijp, W. P.**, England, M. H., & Huber, M. (2011). Effect of the deepening of the Tasman Gateway on the global ocean. *Paleoceanography*, 26(4), 1–18. https://doi.org/10.1029/2011PA002143
- **Simpson, R. W.**, Jachens, R. C., & Blakely, R. J. (1983). *AIRYROOT; a FORTRAN program for calculating the gravitational attraction of an Airy isostatic root out to 166.7 km* (No. 83-883). US Geological Survey. https://doi.org/10.3133/ofr83883
- **Sjunneskog, C.** & Taylor, F. (2002). Postglacial marine diatom record of the Palmer Deep, Antarctic Peninsula (ODP Leg 178, Site 1098) 1 . Total diatom abundance. *Paleoceanography*, 17(3), 1–8.
- Smellie, J. L., McIntosh, W. C., Whittle, R., Troedson, A., & Hunt, R. J. (2021). A lithostratigraphical and chronological study of Oligocene-Miocene sequences on eastern King George Island, South Shetland Islands (Antarctica), and correlation of glacial episodes with global isotope events. *Antarctic Science*, 33(5), 502–532. https://doi.org/10.1017/S095410202100033X
- **Smith, W.** & Sandwell, D. (1997). Global sea floor topography from satellite altimetry and sparse shipboard bathymetry. *Science*, 277, 1956-1961.
- Smith, R. C., Ainley, D., Baker, K., Domack, E., Emslie, S., Fraser, B., Kennett, J., Leventer, A., Mosley-Thompson, E., Stammerjohn, S., & Vernet, M. (1999). Marine ecosystem sensitivity to climate change. *BioScience*, 49(5), 393–404. https://doi.org/10.2307/1313632
- **Sokolov, S.**, & Rintoul, S. R. (2009). Circumpolar structure and distribution of the Antarctic Circumpolar Current fronts: 1. Mean circumpolar paths. *Journal of Geophysical Research: Oceans, 114*(C11). https://doi.org/10.1029/2008JC005108

- **Sterken, M.**, Roberts, S. J., Hodgson, D. A., Vyverman, W., Balbo, A. L., Sabbe, K., Moreton, S. G., & Verleyen, E. (2012). Holocene glacial and climate history of Prince Gustav Channel, northeastern Antarctic Peninsula. *Quaternary Science Reviews*, 31, 93–111. https://doi.org/10.1016/j.quascirev.2011.10.017
- Stickley, C. E., Brinkhuis, H., Schellenberg, S. A., Sluijs, A., Röhl, U., Fuller, M., Grauert, M., Huber, M., Warnaar, J., & Williams, G. L. (2004). Timing and nature of the deepening of the Tasmanian Gateway. *Paleoceanography*, 19(4), 1–18. https://doi.org/10.1029/2004PA001022
- **Stow, D.** & Tabrez, A. R. (1998). Hemipelagites: processes, facies and model. *Geological Society Special Publication*, 129, 317–337. https://doi.org/10.1144/GSL.SP.1998.129.01.19
- **Stow, D.** & Faugères, J. C. (2008). Contourite facies and the facies model. *Developments in sedimentology*, 60, 223-256. https://doi.org/10.1016/S0070-4571(08)10013-9
- **Stow, D.** & Smillie, Z. (2020). Distinguishing between deep-water sediment facies: Turbidites, contourites and hemipelagites. In *Geosciences (Switzerland)* (Vol. 10, Issue 2). https://doi.org/10.3390/geosciences10020068
- **Stow, D.**, Faugères, J. C., Howe, J. A., Pudsey, C. J., & Viana, A. R. (2002). Bottom currents, contourites and deep-sea sediment drifts: Current state-of-the-art. *Geological Society Memoir*, 22(1), 7–20. https://doi.org/10.1144/GSL.MEM.2002.022.01.02
- **Stow, D.**, Hunter, S., Wilkinson, D., & Hernández-Molina, F. J. (2008). The nature of contourite deposition. *Developments in sedimentology*, 60, 143-156. https://doi.org/10.1016/S0070-4571(08)10009-7
- **Stuiver, M.**, & Reimer, P. J. (1993). Extended 14C data base and revised CALIB 3.0 14C age calibration program. *Radiocarbon*, *35*(1), 215-230.
- Suriñach, E., Galindo-Zaldivar, J., Maldonado, A., & Livermore, R. (1997). Large Amplitude Magnetic Anomalies in the Northern Sector of the Powell Basin, NE Antarctic Peninsula. *Marine Geophysical Research*, 19(1), 65–80. https://doi.org/10.1023/A:1004240931967
- **Tamsitt, V.**, England, M. H., Rintoul, S. R., & Morrison, A. K. (2021). Residence time and transformation of warm Circumpolar Deep Water on the Antarctic continental shelf. *Geophysical Research Letters*, 48(20), e2021GL096092.
- Telford, W. M., Geldart, L. P., & Sheriff, R. E. (1990). Applied geophysics. Cambridge university press.
- **Thompson, N.**, Salzmann, U., López-Quirós, A., Bijl, P. K., Hoem, F. S., Etourneau, J., Sicre, M. A., Roignant, S., Hocking, E., Amoo, M., & Escutia, C. (2022). Vegetation change across the Drake Passage region linked to late Eocene cooling and glacial disturbance after the Eocene-Oligocene transition. *Climate of the Past*, 18(2), 209–232. https://doi.org/10.5194/cp-18-209-2022

- **Tibbett, E. J.**, Warny, S., Tierney, J. E., Wellner, J. S., & Feakins, S. J. (2022). Cenozoic Antarctic Peninsula Temperatures and Glacial Erosion Signals from a Multi-Proxy Biomarker Study. *Paleoceanography and Paleoclimatology*, 37(9). https://doi.org/10.1029/2022PA004430
- **Toggweiler, J. R.**, & Samuels, B. (1995). Effect of Drake Passage on the global thermohaline circulation. *Deep Sea Research Part I: Oceanographic Research Papers*, 42(4), 477–500.
- **Toyos, M. H.**, Lamy, F., Lange, C. B., Lembke-Jene, L., Saavedra-Pellitero, M., Esper, O., & Arz, H. W. (2020). Antarctic Circumpolar Current Dynamics at the Pacific Entrance to the Drake Passage Over the Past 1.3 Million Years. *Paleoceanography and Paleoclimatology*, 35(7), 1–20. https://doi.org/10.1029/2019PA003773
- **Troedson, A. L.** & Riding, J. B. (2002). Upper Oligocene to lowermost Miocene strata of King George Island, South Shetland Islands, Antarctica: Stratigraphy, facies analysis, and implications for the glacial history of the Antarctic Peninsula. *Journal of Sedimentary Research*, 72(4), 510–523. https://doi.org/10.1306/110601720510
- **Trouw, R. A. J.**, Passchier, C. W., Simões, L. S. A., Andreis, R. R., & Valeriano, C. M. (1997). Mesozoic tectonic evolution of the South Orkney Microcontinent, Scotia arc, Antarctica. *Geological Magazine*, 134(3), 383–401. https://doi.org/10.1017/S0016756897007036
- van de Lagemaat, S. H. A., Swart, M. L. A., Vaes, B., Kosters, M. E., Boschman, L. M., Burton-Johnson, A., Bijl, P. K., Spakman, W., & van Hinsbergen, D. J. J. (2021). Subduction initiation in the Scotia Sea region and opening of the Drake Passage: When and why? *Earth-Science Reviews*, 215, 103551. https://doi.org/10.1016/j.earscirev.2021.103551
- Van Wyk de Vries, M., Ito, E., Romero, M., Shapley, M., & Brignone, G. (2023). Periodicity of the Southern Annular Mode in Southern Patagonia, insight from the Lago Argentino varve record. *Quaternary Science Reviews*, 304. https://doi.org/10.1016/j.quascirev.2023.108009
- Vaughan, A. P. M., Wareham, C. D., Johnson, A. C., & Kelley, S. P. (1998). A Lower Cretaceous, synextensional magmatic source for a linear belt of positive magnetic anomalies: the Pacific Margin Anomaly (PMA), western Palmer Land, Antarctica. *Earth and Planetary Science Letters*, 158(3–4),143–155. https://doi.org/10.1016/S0012-821X(98)00054-5
- Vaughan, D. G., Marshall, G. J., Connolley, W. M., Parkinson, C., Mulvaney, R., Hodgson, D. A., King, J. C., Pudsey, C. J., & Turner, J. (2003). Recent rapid regional climate warming on the Antarctic Peninsula. In *Climatic Change* (Vol. 60, Issue 3, pp. 243–274). https://doi.org/10.1023/A:1026021217991
- Vorrath, M. E., Müller, J., Rebolledo, L., Cárdenas, P., Shi, X., Esper, O., Opel, T., Geibert, W., Munoz, P., Haas, C., Kuhn, G., Lange, C. B., Lohmann, G., & Mollenhauer, G. (2020). Sea ice dynamics in the Bransfield Strait, Antarctic Peninsula, during the past 240 years: A multi-proxy intercomparison study. *Climate of the Past*, 16(6), 2459–2483. https://doi.org/10.5194/cp-16-2459-2020

- Villa, G., Fioroni, C., Pea, L., Bohaty, S., & Persico, D. (2008). Middle Eocene-late Oligocene climate variability: Calcareous nannofossil response at Kerguelen Plateau, Site 748. *Marine Micropaleontology*, 69(2), 173–192. https://doi.org/10.1016/j.marmicro.2008.07.006
- **Warnock, J. P.**, & Scherer, R. P. (2015). A revised method for determining the absolute abundance of diatoms. *Journal of Paleolimnology*, *53*, 157-163.
- **Weber, M. E.**, Raymo, M. E., Peck, V. L., & Williams, T. (2019). International Ocean Discovery Program Expedition 382 Preliminary Report. In *Integrated Ocean Drilling Program: Preliminary Reports*, 366, 1–40. https://doi.org/10.14379/iodp.pr.371.2018
- Whitehead, J. M., & Bohaty, S. M. (2003). Pliocene summer sea surface temperature reconstruction using silicoflagellates from Southern Ocean ODP Site 1165. *Paleoceanography*, *18* (3).
- Whitworth, T., Nowlin, W. D., Orsi, A. H., Locarnini, R. A., & Smith, S. G. (1994). Weddell Sea shelf water in the Bransfield Strait and Weddell-Scotia Confluence. In *Deep-Sea Research Part I* (Vol. 41, Issue 4, pp. 629–641). https://doi.org/10.1016/0967-0637(94)90046-9
- Wei, W. & Wise, S.W. (1990). Middle Eocene to Pleistocene calcareous nannofossils recovered by Ocean Drilling Program Leg 113 in the Weddell Sea. In *Proc., scientific results, ODP, Leg 113, Weddell Sea, Antarctica* (pp. 639–666). https://doi.org/10.2973/odp.proc.sr.113.125.1990
- **Williams, M.**, Nelson, A. E., Smellie, J. L., Leng, M. J., Johnson, A. L. A., Jarram, D. R., Haywood, A. M., Peck, V. L., Zalasiewicz, J., Bennett, C., & others. (2010). Sea ice extent and seasonality for the Early Pliocene northern Weddell Sea. *Palaeogeography, Palaeoclimatology, Palaeoecology,* 292(1–2), 306–318.
- **Wilson, C.**, Klinkhammer, G. P., & Chin, C. S. (1999). Hydrography within the central and east basins of the Bransfield Strait, Antarctica. *Journal of Physical Oceanography*, 29(3), 465–479. https://doi.org/10.1175/1520-0485(1999)029<0465:HWTCAE>2.0.CO;2
- Wu, L., Wilson, D. J., Wang, R., Yin, X., Chen, Z., Xiao, W., & Huang, M. (2020). Evaluating Zr/Rb Ratio from XRF Scanning as an Indicator of Grain-Size Variations of Glaciomarine Sediments in the Southern Ocean. *Geochemistry, Geophysics, Geosystems*, 21(11), 1–26. https://doi.org/10.1029/2020GC009350
- **Wu, Q.**, Xu, H., & Zou, X. (2005). An effective method for 3D geological modeling with multi-source data integration. *Computers and Geosciences*, 31(1), 35–43. https://doi.org/10.1016/j.cageo.2004.09.005
- **Yuan, X.** (2004). ENSO-related impacts on Antarctic sea ice: A synthesis of phenomenon and mechanisms. *Antarctic Science*, *16*(4), 415–425. https://doi.org/10.1017/S0954102004002238
- **Zachos, J.**, Dickens, G. R., & Zeebe, R. E. (2008). An early Cenozoic perspective on greenhouse warming and carbon-cycle dynamics. *Nature*, 451(7176), 279–283. https://doi.org/10.1038/nature06588

- **Zachos, J.**, Pagani, H., Sloan, L., Thomas, E., & Billups, K. (2001). Trends, rhythms, and aberrations in global climate 65 Ma to present. *Science*, *292*(5517), 686–693. https://doi.org/10.1126/science.1059412
- **Zhang, Y. F.**, Sun, Z., Zhou, D., Guo, X. W., Shi, X. Bin, Wu, X. J., & Pang, X. (2008). Stretching characteristics and its dynamic significance of the northern continental margin of South China Sea. *Science in China, Series D: Earth Sciences*, *51*(3), 422–430. https://doi.org/10.1007/s11430-008-0019-2
- **Zhou, M.**, Niiler, P. P., Zhu, Y., & Dorland, R. D. (2006). The western boundary current in the Bransfield Strait, Antarctica. *Deep Sea Research Part I: Oceanographic Research Papers*, 53(7), 1244–1252.
- **Ziegler, M.**, Jilbert, T., De Lange, G. J., Lourens, L. J., & Reichart, G. J. (2008). Bromine counts from XRF scanning as an estimate of the marine organic carbon content of sediment cores. *Geochemistry, Geophysics, Geosystems*, 9(5). https://doi.org/10.1029/2007GC001932







